Federal University of Rio Grande do Sul
Engineering School
Graduate Program of Civil Engineering

Molding conditions effect on the geomechanical behavior of uncemented and cemented iron ore tailings under low and high confining stresses

Giovani Jordi Bruschi

Porto Alegre
2023

GIOVANI JORDI BRUSCHI

MOLDING CONDITIONS EFFECT ON THE GEOMECHANICAL BEHAVIOR OF UNCEMENTED AND CEMENTED IRON ORE TAILINGS UNDER LOW AND HIGH CONFINING STRESSES

Thesis presented to the Graduate Program in Civil Engineering of Federal University of Rio Grande do Sul as part of the requirements for the Degree of Doctor in Engineering.

Porto Alegre
2023

CIP - Catalogação na Publicação

Bruschi, Giovani Jordi
Molding conditions effect on the geomechanical behavior of uncemented and cemented iron ore tailings under low and high confining stresses / Giovani Jordi Bruschi. -- 2023.
235 f.
Orientador: Nilo Cesar Consoli.

Tese (Doutorado) -- Universidade Federal do Rio Grande do Sul, Escola de Engenharia, Programa de Pós-Graduação em Engenharia Civil, Porto Alegre, BR-RS, 2023.

1. Iron ore tailings. 2. Cemented mining tailings. 3. Dry stacking. 4. Multiaxial behavior. 5. Grain breakage analysis. I. Consoli, Nilo Cesar, orient. II. Título.

Elaborada pelo Sistema de Geração Automática de Ficha Catalográfica da UFRGS com os dados fornecidos pelo(a) autor(a).

GIOVANI JORDI BRUSCHI

MOLDING CONDITIONS EFFECT ON THE GEOMECHANICAL BEHAVIOR OF UNCEMENTED AND CEMENTED IRON ORE TAILINGS UNDER LOW AND HIGH CONFINING STRESSES

This doctoral thesis was considered suitable for obtaining the title of DOCTOR IN ENGINEERING, Geotechnics, and was approved in its final form by the advisor professor and by the Graduate Program in Civil Engineering at the Federal University of Rio Grande do Sul.

Porto Alegre, June 02nd, 2023.

Prof. Nilo Cesar Consoli
Ph.D. by Concórdia University
Advisor

Prof. Lucas Festugato
Coordinator of PPGEC/UFRGS

EXAMINATION COMITEE

Prof. Karla Salvagni Heineck (UFRGS)
Dr. by Universidade Federal do Rio Grande do Sul

Prof. Michéle Dal Toé Casagrande (UnB)
Dr. by Universidade Federal do Rio Grande do Sul

Prof. Monica Prezzi (Purdue University)
PhD. by University of California Berkeley

Dr. João Paulo de Sousa Silva (VALE)
Dr. by University of Brasilia

ACKNOWLEDGEMENTS

I am immensely grateful to my parents, Gerson and Itamara, and also to my brother, Júnior, for all the support and unconditional love. You are, and always will be, my foundation. Thank you for always being there for me. I love you guys.

I would like to thank Prof. Nilo Cesar Consoli for always being available and doing everything in his power for the development of this research. I am very grateful for the exchange of experiences and for the opportunity to share a work environment.

To my great friend and ex-roommate Marina Paula Secco, a special thanks is needed. Thank you for being part of my life. Our experience in Royal Village will definitely be forever in my mind. Never forget, when God closes a door, he also closes the windows and turns off the lights.

This research would not have been possible without the help of Carolina Pereira dos Santos. Thank you for all the assistance you have provided during the development of this research (really really really early in the mornings) and, of course, thank you for being my friend.

To my great friends Guilherme Medina and Helena Farenzena (also known as Gui and Lena), thank you for having welcomed me into your lives. Our great times in Porto Alegre will always be part of my fondest memories, including Pipa Maria and Pandora. It would be fitting to finish this paragraph with a quote from sensitive Márcia, but we better leave it like this.

I would like to thank my great friend, Fernando Fante. Thank you for all the support, companionship, and, of course, many hours of study and discussion invested during these long years.

I would like to thank the eggshell lime girls, Suéllen Tonatto Ferrazzo and Mariana Tonini de Araújo. Our time together has made me grow not only as a researcher, but also, as a person. I am grateful for the connection we have developed during this time.

I would like to thank the big grill girls, Camila Martinatto and Maria Mariana de Sousa Rocha, you guys definitely made my time in Porto Alegre way more fun. This acknowledgement extends to Luana Rutz Schulz, Débora Thais Mesavilla, and Rodrigo Zorzal Velten, thank you guys for all our moments together.

To my oldest friends, Levino Bertochi Júnior and Júlia Arcego, thank you for always being there for me. I love you guys.

I would like to thank the postdoc fellows Sérgio Filipe Marques and Hugo Carlos Scheuermann Filho for always being available and helping me in the development of this research.

A special thanks is also owed to Yuri Gugel, who made the execution time of this research run more smoothly. Thank you for being present in the bad times, tirelessly listening to all the cries and complaints, and honoring, even if from a distance, the good times.

Finally, I would like to thank all professors and postgraduate colleagues who in some way contributed to the execution of this research.

“Normal is not something to aspire to, it's something to get away from”

Jodie Foster

ABSTRACT

BRUSCHI, G. J. **Molding conditions effect on the geomechanical behavior of uncemented and cemented iron ore tailings under low and high confining stresses**. 2023. Thesis (Doctor degree in Civil Engineering) – Graduate Program in Civil Engineering, UFRGS, Porto Alegre.

The safety of mining structures has grown in interest after the several dam failures reported worldwide. Filtered tailings have been gaining special attention, considering that they represent a lower-physical-risk option compared to conventional or paste tailings. Nevertheless, mining tailings are known to have extremely variable and difficult-to-predict geotechnical behavior/strength parameters; this variability results in several uncertainties associated with the design conception of projects, independently of the storage technique utilized. With that in mind, techniques such as soil stabilization may aid in the improvement and predictability of the geotechnical behavior of mining tailings. Extensive research has been developed for conventional geotechnical materials, such as clays, sands, and silts. However, regarding mining tailings, studies are still scarce, especially studies on the molding conditions and stress state of the mixtures. Thus, this research sought to analyze the influence of different molding conditions [i.e., dry side of the compaction curve, optimum moisture content (max. density), optimum moisture content (red. density), and wet side of the compaction curve] on the geotechnical behavior of both uncemented and cemented iron ore tailings under low (p' = 300kPa) and high confining stresses (p' = 3000kPa). To this extent, the following tests were executed: unconfined compressive strength (*UCS*), initial shear stiffness (*G0*), hydraulic conductivity, compressibility, axial compression triaxial, and grain breakage analysis. The results have shown that the geomechanical behavior of mining tailings is directly affected by the molding condition. For *UCS* tests, optimum moisture content (max. density) specimens resulted in the highest strength, followed by optimum moisture content (red. density), dry-side and wet-side ones; however, this behavior was not repeated for stiffness, in which dry-side specimens resulted in the highest values, followed by optimum moisture content (max. density), optimum moisture content (red. density), and wet-side ones. As for permeability tests, the increase in water presence led to a decrease in hydraulic conductivity for all specimens. The same behavior depicted for *UCS* tests was seen on compressibility tests, in which optimum moisture content specimens resulted in the highest strength and lowest settlement, followed by optimum moisture content (red. density), dry-side and wet-side ones. As for the triaxial testing, the strength results

follow the pattern presented for *UCS*, while the stiffness results alluded to the behavior depicted for *G0*. Grain size analysis revealed that the most influential factor on the grains breakage of iron ore tailings is the shearing movement of particles and not the consolidation, as reported for conventional soils. Finally, from the data gathered in this research, it was possible to see that the initial molding conditions play a fundamental role in the general mechanical behavior of both cemented and uncemented iron ore tailings.

Key-words: *Initial moisture content; molding compaction energy; iron ore tailings; cemented mining tailings; grain breakage analysis*

RESUMO

BRUSCHI, G. J. **Efeito das condições de moldagem no comportamento geomecânico de rejeitos de mineração de ferro cimentados e não cimentados sob baixas e altas tensões de confinamento.** 2023. Tese (Doutorado em Engenharia Civil) – Programa de Pós-graduação em Engenharia Civil, UFRGS, Porto Alegre.

A segurança de estruturas de contenção da área minerária é um tópico de discussão recorrente, que tem sido impulsionado ainda mais após os inúmeros acidentes relacionados com barragens de rejeito. Os rejeitos filtrados vêm ganhando atenção especial por representarem uma opção de menor risco físico em relação aos rejeitos convencionais ou pastosos. No entanto, os rejeitos de mineração ainda são conhecidos pela grave imprevisibilidade no que diz respeito a seu comportamento geotécnico; essa variabilidade resulta em diversas incertezas associadas à concepção dos projetos, independentemente da técnica de contenção utilizada. Assim, técnicas como a estabilização de solo podem auxiliar na melhoria e previsibilidade do comportamento geotécnico dos rejeitos de mineração. Diversas pesquisas vêm sendo desenvolvidas para materiais geotécnicos convencionais, como argilas, areias e siltes. No entanto, em relação aos rejeitos de mineração, os estudos ainda são escassos, principalmente estudos sobre as condições de moldagem e estado de tensão das misturas. Com isso, esta pesquisa buscou analisar a influência de diferentes condições de moldagem [lado seco da curva de compactação, teor de umidade ótimo (densidade máxima), teor de umidade ótimo (densidade reduzida) e lado úmido da curva de compactação] no comportamento geotécnico de rejeitos de minério de ferro não cimentados e cimentados sob baixas (p' = 300kPa) e altas tensões de confinamento (p' = 3000kPa). Para tanto, foram executados os seguintes ensaios: resistência à compressão não confinada (*UCS*), rigidez inicial (*G0*), condutividade hidráulica, compressibilidade, compressão axial triaxial e análise de quebra de grãos. Os resultados mostraram que o comportamento geomecânico dos rejeitos de mineração é diretamente afetado pela condição de moldagem. Para os ensaios *UCS*, as amostras de teor de umidade ótimo (densidade máxima) resultaram na maior resistência, seguidas pelas do teor de umidade ótimo (densidade reduzida), lado seco e do lado úmido; no entanto, esse comportamento não se repetiu para a rigidez, onde os corpos de prova do lado seco apresentaram os maiores valores, seguidos dos teores de umidade ótimos (máxima e reduzida) e do lado úmido. Por sua vez, nos testes de permeabilidade, o aumento da presença de água levou a uma diminuição da condutividade

hidráulica para todos os corpos de prova analisados. O mesmo comportamento descrito para os ensaios *UCS* foi observado nos ensaios de compressibilidade, nos quais os corpos de prova com teor de umidade ótimo (densidade máxima) resultaram na maior resistência e menor deformação, seguidos pelos corpos de prova com teor de umidade ótimo (densidade reduzida), lado seco e lado úmido. Já nos ensaios triaxiais, os resultados de resistência seguem o padrão apresentado para *UCS*, enquanto os resultados de rigidez aludem ao comportamento descrito para *G0*. A análise granulométrica revelou que o fator mais influente na quebra dos grãos de rejeitos de minério de ferro é o movimento de cisalhamento das partículas e não a consolidação, como relatado para solos convencionais. Finalmente, a partir dos dados obtidos nesta pesquisa foi possível constatar que as condições iniciais de moldagem desempenham um papel fundamental no comportamento mecânico de rejeitos de minério de ferro cimentados e não cimentados.

Palavras chave: *Teor de umidade inicial; energia de compactação; rejeitos de mineração de ferro; rejeitos de mineração cimentados; análise de quebra de grãos.*

FIGURES

TABLES

ACRONYMS AND SYMBOLS

A	Cross-sectional area of the specimen
Ac	Area of the specimen
Al_2O_3	Aluminum oxide
$Ca(OH)_2$	Calcium hydroxide
$C–A–H$	Calcium aluminate hydrate
CH	Calcium hydroxide
Civ	Cement content
$C–S–H$	Calcium silicate hydrate
CSL	Critical state line
d	Deformation reading at various times
d_a	Apparatus deformation correction
DAQ	Data acquisition board
DID	Terrestrial detrital iron deposits
d_o	Initial deformation reading
DSO	Direct shipping ore
e	Void ratio
$E0$	Initial Young's modulus
e_f	Final void ratio
e_o	Initial void ratio
Es	Secant Young's modulus
Et	Tangent Young's modulus
F	Maximum force
Fe_3O_4	Magnetite
G	Specific gravity of the solids
g	Gravity
$G0$	Initial shear modulus
h	Hydraulic head
H_f	Final specimen height
H_o	Initial specimen height
H_s	Height of solids

IOCG	Iron oxide Cu–Au
IOTs	Iron ore tailings
k	Hydraulic conductivity
L	Length of the specimen
LEGG	Laboratory of Geotechnical Engineering and Environmental Geotechnology
LVDT	Linear variable differential transformer
M	Slope of the critical state
M_a	Mass of apparatus resting on specimen
Md	Dry mass of the specimen
Md	Dry mass of the specimen
M_{Tf}	Moist mass of the specimen
M_{To}	Moist mass of the specimen before testing
NCL	Normal compression line
OC	Oedometric conditions
P	Applied force
p'	Average effective stress
q	Deviatory stress
Q	Water flow rate
qu	Unconfined compression strength
R^2	Determination coefficient
S_f	Final degree of saturation
SiO_2	Silicon dioxide
S_o	Initial degree of saturation
TC	Triaxial conditions
tp	Compressive wave
ts	Travel time
u	Back pressure
UCS	Unconfined compressive strength
UFRGS	Federal Universisity of Rio Grande do Sul
v	Specific volume
V_o	Initial volume of the specimen
Vs	Shear wave
V_s	Volume of solids

V_s	Volume of solids
w_f	Final water content
w_{fp}	Water content wedge of the specimen
w_o	Initial water content
α-*FeOOH*	Oxyhydroxide
γ_d	Dry unit weight
ΔH	Change in specimen height
η	Porosity
ρ_d	Dry density of the specimen
ρ_w	Density of water filling the pore space
ρ_w	Density of water filling the pore space
$\sigma 1$	Axial stress
σ_a	Total axial stress
ψ	State parameter
Δu	Variation of back pressure
$\Delta\sigma 3$	Variation of the confining stress
εa	Axial strain
εs	Distortional strain
ϕ_{EC}	Friction angle in the critical state
$\sigma 3$	Confining pressure

INDEX

1 INTRODUCTION

The mining industry is a direct source of jobs for more than 35 million workers worldwide (Furlan et al., 2020; Nishijima and Rocha, 2020); also, it provides indirect support to approximately 200 million people. In the economy sector, goods produced in mining industries are of vital importance for society, as these materials constitute indispensable products (e.g., metals, construction materials) (Bahurudeen et al., 2015; Burris et al., 2015).

Despite the importance of the mining sector, its activities generate considerable volumes of waste, regardless of the size of the mineral extraction operations. Materials with no apparent economic value, resulting from the mining process, are known as mining tailings (Gomes et al., 2017). Among them, the iron ore tailings stand out, due to their large generation, disposal areas, and storage problems.

Mining tailings must be disposed of in properly designed environments to minimize the possible socio-environmental impacts of their production process (Davies, 2002; Gomes et al., 2017). Different disposal techniques can be found in the literature, however, the most widespread method for the disposal of mining tailings consists of damming through a structure known as a tailings dam (Lumbroso et al., 2019). This storage structure raises a series of concerns, with the most important one being safety.

The construction process of a tailings dam often requires the use of compacted material to create the starting dam. Therefore, a complete geo-mechanical and hydraulic understanding of the landfill material is essential to ensure the safety of the construction (Duchesne and Doye, 2005). Usually, the materials used in the construction system of a tailings dam are those available during the mining process or those that are at an economically viable distance from the production plant (Lumbroso et al., 2019). The use of these tailings as a construction material in dam embankments (or any other type of embankment) presents some problems associated with material variability.

The geotechnical behavior of tailings is related to the characteristics of the material, the nature of the deposit and the disposal method (Nierwinski, 2019; Schnaid et al., 2015). In addition, due to their nature, some types of tailings require extensive preventive measures to mitigate risks, alluding to worker safety, leakage in ecosystems and waterways, and structure failure (Panda et al., 2017).

Recent events, such as the failure of Tonglvshan iron Mine in China and Bloom Lake iron mine in Canada have demonstrated the fragility of these storage structures (Guimarães et al., 2022; Islam and Murakami, 2021; Piciullo et al., 2022). In a national context, the failure of Córrego de Feijão mine in Minas Gerais, led to desolating effects; the tailings wave devastated the mine's loading station, its administrative area, and two smaller sediment retention basins (B4 and B4A); it then traveled more than 7 kilometers downhill until reaching Rio Paraopeba, thereby destroying a bridge of the mine's railway branch, and spreading to parts of the local community Vila Ferteco, near the town of Brumadinho; the slurry was then carried further by Rio Paraopeba; 259 people were killed, and 11 are still reported missing (Armstrong et al., 2019; Furlan et al., 2020; Islam and Murakami, 2021). Along these lines, the failure of Germano mine also resulted in a slurry wave that flooded the town of Bento Rodrigues (province of Minas Gerais), destroying 158 homes, with at least 17 people killed and 2 reported missing; the slurry polluted North Gualaxo River, Carmel River and Rio Doce over 663 km, destroying 15 square kilometers of land along the rivers and cutting residents off from potable water supply; with a damage of at least US$ 6.7 billion (Davila et al., 2020; Gama et al., 2019; Gomes et al., 2017). Such episodes have awakened the attention of society to the catastrophic impacts of the failures of tailing dams.

With the intensification of socio-environmental concerns related to the safety of communities and the fragility of ecosystems, new and more rigorous laws and guidelines began to be implemented (Piciullo et al., 2022; Rout et al., 2013). With that in mind, the mining industry is more than ever under socio-political pressure to enforce more responsible management strategies, as well as remedy the environmental impact left in the surrounding areas (Zhang et al., 2011).

The failure of tailing dams can be associated with several different factors (e.g., seismic loading, liquefaction, environmental effects), with the most common/recurrent one being attributed to the presence of water within the facilities (Guimarães et al., 2022). With that in mind, new alternatives for the disposal techniques of conventional mining tailing facilities started being applied, such as the dewatering of the materials (i.e., thickened, paste, and filtered) and different structure types (e.g., dry stacking) (Alshawmar and Fall, 2023; Gomes et al., 2016; Liu et al., 2016; Servi et al., 2022; Xiaolong et al., 2021).

The management of tailing facilities should safely guarantee the disposal/storage of mining tailings, reducing possible associated risks, especially over long-range scenarios. In this sense, the removal of water from tailings can significantly reduce potential risks; thus, an increasing desire in dewatered tailings is being evidenced in mining industries and although dewatering

techniques are already a reality, the industry has not been able to perfect this methodology (Cox et al., 2022; Schoenberger, 2016). Although dewatered/thickened tailings have been proven to be linked to safer practices, their production is costlier than conventional tailings. Transforming slurry tailings into dewatered tailings has been a research focus for more than a decade, but it has not achieved broad acceptance in the industry, mostly due to monetary reasons (Alshawmar and Fall, 2023; Gomes et al., 2016).

Even though implementation costs weight considerably on the decision-making process of the mining industries, the safety of mining structures has grown in interest after the several dam failures reported worldwide (Ruan et al., 2021). Along these lines, filtered tailings have been gaining special attention and, as a consequence, costs are decreasing, and larger plants are being proposed (Gomes et al., 2016; Servi et al., 2022). These novelties are creating an industrial tendency towards filtered tailings, as a lower-physical-risk option compared to conventional or paste tailings. Nevertheless, aspects such site conditions, geochemical risks, long-term closure risks, environmental impacts, and social impacts, should always be considered when selecting a disposal technique (Owen et al., 2020).

The majority of the mining facilities are still handling tailings as slurry contained by dams in surface impoundments. This slurry can be defined as a by-product of ore processing, being composed of a mixture of tailings solids and water (20-40% solids content). As for the disposition, the slurry is normally disposed via pipeline for hydraulic discharge into the containment structure. Several studies can be found on conventional tailings dams, dam geometry and types, and dam design geometry options (i.e., downstream, centerline, and upstream). Other management strategies include in-pit disposal and underground backfill. If in-pit disposal or underground backfill are viable, they can be effective strategies and should be considered with their strengths and limitations for mining projects (Adiansyah et al., 2015; Edraki et al., 2014; Watson et al., 2010; Yilmaz and Fall, 2017).

Different terms are utilized to describe dewatered tailings; however, for this study the mining tailings were categorized in three groups, according to their storage method (Alshawmar and Fall, 2023; Yilmaz and Fall, 2017): (i) conventional tailing structures (unthickened or thickened slurry tailings, contained by dams); (ii) high-density thickened/paste tailings structures (thickened or paste tailings, generally contained by engineered dams); and (iii) filtered tailings structures (dewatered tailings with soil-like behavior arranged in self-supporting piles).

According to what has been presented so far, it becomes clear that new disposal techniques may contribute to the safety of the containment structure of mining tailings. However, the increasing

mineral production also means that more robust structures are necessary to contain these tailings. In addition, mining tailings are known to have extremely variable and difficult to predict geotechnical behavior/strength parameters; this variability results in several uncertainties associated with the design conception of projects, independently of the storage technique utilized (Schnaid et al., 2004, 2015, 2016).

With that in mind, techniques such as soil stabilization may aid on the improvement and predictability of the geotechnical behavior of mining tailings (Bruschi et al., 2021; Servi et al., 2022). This technique is utilized to refine and improve the engineering properties of geotechnical materials. These properties include mechanical strength, permeability, compressibility, durability, and plasticity (Bruschi et al., 2021c; Consoli et al., 2012, 2019a; b, 2020b, 2021; Festugato et al., 2017; Quiñónez Samaniego et al., 2022). Extensive research has been developed for conventional geotechnical materials, such as clays, sands, and silts (Consoli et al., 2009c, 2011b; c; Diambra et al., 2018; Festugato et al., 2018; Lade and Overton, 1989; Trads and Lade, 2014). However, regarding mining tailings, studies are still scarce, especially studies on the molding conditions and stress state of the mixtures.

1.1 RESEARCH QUESTION

Give the exposed literature, this research proposes to answer the following question: “How is the geotechnical behavior of uncemented and cemented iron ore tailings affected under different molding conditions and confining stresses?”

1.2 OBJECTIVE

The objective of this research was to evaluate the effect of distinctive molding conditions on the geotechnical behavior of uncemented and cemented iron ore tailings under low and high confining stresses.

1.3 SPECIFIC OBJECTIVES

In view of the general objective and the problem proposed in this research, the following specific objectives are required:

a) Characterize the chemical, physical-mechanical, and microstructural behavior of iron ore tailings;
b) Assess the influence of distinctive molding conditions (i.e., initial moisture content, dry unit weight and compaction energy) on the mechanical behavior (i.e., unconfined compressive strength, initial shear stiffness, hydraulic conductivity, compressibility, stress-strain) of iron ore tailings;
c) Evaluate the influence of cement addition on the mechanical behavior (i.e., unconfined compressive strength, initial shear stiffness, hydraulic conductivity, compressibility, stress-strain) of iron ore tailings;
d) Analyze the influence of different stress conditions (i.e., low and high confining stresses) on the triaxial stress-strain behavior of both cemented and uncemented iron ore tailings;
e) Investigate the influence of different boundary conditions (i.e., oedometric and triaxial) under high stresses (i.e., 6.4 MPa for oedometric conditions and 3.0 MPa for triaxial conditions) on the grain breakage of both cemented and uncemented iron ore tailings.

1.4 JUSTIFICATION

More than 221 incidents/failures have been reported throughout the world regarding tailings storage facilities (Edraki et al., 2014). In this sense, effective reduction of the cost of risk and failure can only be achieved by a commitment from owners to the adequate and enforced application of available engineering technology to the design, construction, and closure of tailings dams and impoundments over the entire period of their operating life (Armstrong et al., 2019). Despite the clear problem associated with tailing dams, failures continue to occur, resulting in consequences both to human life and to the downstream environment.

Depending on how tailings are processed, transported, discharged, and stored, different types of tailing store facilities are generated, which have significant variations in terms of cost, volume, and type of materials required for construction, rate of construction, and inherent stability (Guimarães et al., 2022). The current practice of tailings management is mostly associated with tailings deposits known as conventional type, due to their lower cost and simpler implementation. The conventional system of tailings disposal consists of one or several dams that confine and retain the saturated loose, hydraulically deposited tailings and process water in an impoundment. The retaining component of tailings facilities is usually constructed

using the sandy fraction of the tailings, which may be accomplished using cyclones or, more often, conventional earthmoving equipment (Piciullo et al., 2022).

According to the construction procedure used, it is possible to distinguish between upstream, downstream, and centerline methods of construction. The upstream method of construction requires a minimum volume of coarser tailings (or borrow material) for embankment construction, but the geotechnical properties of the tailings, sometimes including the finer fractions, are involved in the overall stability of the facility. On the other hand, tailings facilities constructed using the downstream method are supported on the foundation soil and tailings only act as a load against the retaining embankment. The centerline option is an intermediate structure, with the downstream shoulder resting on the foundation soil and supporting the lateral forces generated by the retained tailings and water (Vick, 1999). Although many upstream tailings facilities have performed satisfactorily for many years and continue to do so, it is noted that analyses of the performance of tailings store facilities generally identify the upstream construction method as the least reliable one (Guimarães et al., 2022; Rout et al., 2013).

Despite various recycling initiatives around the world, demand for most minerals remains almost insatiable. The volume of tailings produced annually is increasing significantly, as the grade of available ore bodies declines. Every couple of years the volume of tailings worldwide increases about ten-fold, the area covered by tailings storage facilities increases five-fold and the average height of tailing storage facilities doubles (Islam and Murakami, 2021).

In this sense, the understanding of the geotechnical behavior of mine tailings will continue to be imperative, and to evolve to include the effect of increasingly high confining stresses on tailings characteristics. Furthermore, it is estimated that more than 50,000,000,000 m^3 of tailings will require storage until 2023 (Carmignano et al., 2021), in other words mining tailings storage will remain a necessity for the foreseeable future.

Tailing dam failures can be attributed to the effects excess water. Over the past decades, significant advances have been made in technologies that utilize less water to transport tailings to the tailings storage facilities. Most operational tailings storage facilities today would classify as conventional tailings, with no measurable yield stress of the as-deposited tailings (Berger, 2017; Edraki et al., 2014). Additional thickening, using much deeper thickeners than previously used, results in higher solids concentrations and thus higher yield stresses, requiring much more attention to detail of tailings transportation, as the higher solids concentration may sometimes require the use of positive displacement pumps rather than conventional centrifugal pumps (Boger, 2013).

There are also implications for deposition practices when using high-density thickened tailings. Added impetus to the adoption of increased dewatering has been provided by recommendations arising from some of the forensic investigations of major tailings storage facilities failures to minimize storage of water on tailings storage facilities. Further thickening requires use of filters, producing a cake-like material when successful. The production of filtered tailings usually comes at significantly increased cost, particularly operational costs due to increased energy use (Alshawmar and Fall, 2023; Cox et al., 2022; Edraki et al., 2014).

As a result, it is essential that these previously non-existent scenarios (e.g., behavior of materials at high tensions, influence of different deposition/disposition conditions, and molding conditions) are studied in depth, in order to guarantee the safety of the new proposed methodologies.

1.5 RESEARCH ORGANIZATION

This research is structured into five chapters. The first is composed of introductory features. It presents a delimitation of the universe to be studied, the research problem, the general and specific objectives, as well as, a presentation of the theoretical justification and practical relevance of the theme.

In chapter two the theoretical background is presented with five sections. The first reflects the conceptualizations about iron ore and its characteristics. The second section explores the aspects inherent to the generation of mining tailings from mineral processing. Then, concepts related to the chemical stabilization of mining tailings are presented. This chapter ends with the presentation of perceptions regarding the Critical State Theory applied to soil mechanics.

The third chapter covers the methodological determinations of this study. Therefore, the chapter consists of the research design and specification of the research problem at first. Also exposed are the explanations inherent to the decision-making processes, as well as the description of the tests performed.

The fourth chapter exposes the results of the materials studied and provides for the analysis and discussion of the obtained data.

Finally, the fifth chapter contains final considerations about the results, as well as, suggestions for future work.

2 BACKGROUND RESEARCH

This chapter aims to theoretically support the main aspects of this research. Therefore, to allow a reasonable understanding of the concepts herein, this section explores the characteristics of the iron ore, the tailings generated in mineral processing, the chemical stabilization of mining tailings, as well as, the Critical State Theory applied to conventional and unconventional geotechnical materials.

2.1 IRON ORE

Iron is estimated to constitute up to 32% of the Earth's mass and its elemental abundance varies between about 5% of the Earth's crust and as much as 80% of the planet's core (Galvão et al., 2018). Thus, several iron ore minerals and iron ore deposits can be commonly found at the surface of the Earth. Morris (1985) states that just one of the iron-enrichment deposit types alone, derived from iron formations, and represents the largest and most concentrated accumulation of any single metalliferous element in the Earth's crust.

The most common iron ore minerals are: (i) magnetite, (ii) hematite, and (iii) goethite. Magnetite (Fe_3O_4) is normally found in iron ore deposits of metasedimentary and magmatic origin; presenting an inverse spinel structure and is moderately altered in near-surface environments to hematite or kenomagnetite (Araujo et al., 2003).

As for hematite, this mineral is frequently formed from oxidation of magnetite in the near-surface environment. The transformation of magnetite to hematite or vice versa can also be achieved via a non-redox reaction. Martite is a commonly used textural term to denote hematite pseudomorphs after primary magnetite where the outlines of many of the original magnetite grains are preserved (Araujo et al., 2003; Fernández-González et al., 2017).

Finally, goethite is characterized as an iron oxyhydroxide (α-$FeOOH$), being the most common iron ore mineral in sedimentary and near-surface, and altered metasedimentary iron ore deposits. This mineral can be found in three forms: brown, yellow ochreous, and dark brown vitreous goethite. Several seaborne-traded iron ores are amalgamations of hard brown goethite and yellow ochreous goethite with hematite. Yellow ochreous goethite and vitreous goethite normally are composed of amorphous material and high (up to 9%) levels of aluminum oxide (Al_2O_3) and silicon dioxide (SiO_2). Ochreous goethite is typically highly microporous (20–40%

total porosity), is normally fine grained, and often contains considerable sub-micron crystallites of goethite (D′Azeredo Orlando et al., 2020).

The mineralogy of iron ore deposits is rather simple; however, the ore textures are complex and directly linked to deposit ore genesis. In addition, these multifarious textures also influence the metallurgical process performance from crushing to screening, beneficiation, and agglomeration (sintering or pelletizing) of fine ores or concentrates, and lump burden behavior in the blast furnace. Divergences in iron ore chemistry, texture, mineralogy, and physical properties are associated with iron deposit types and their vertical mineralogical and textural zonation (Ferreira and Leite, 2015; Srivastava et al., 2001).

A broad range in chemical composition is evidenced for iron ores and concentrate products; notably for iron (55-65%), silicon dioxide (2.5-5%) and aluminum oxide (0.5-4%). However, if the analysis is normalized to correct for loss on ignition (crystal-bound water) from goethite during sintering or pelletizing, the calcined fine ore values for traded iron ores and concentrates vary within a remarkably narrow range of 4.3–10.5% for (silicon dioxide + aluminum oxide) and 61.8–66.3% for *Fe* (Lu, 2021; Morris, 1985).

Also, the chemical composition of beneficiated iron ores can be divided into high-grade hematite ores and high-loss of ignition iron ores. The first group is characterized by iron contents between 62% and 65%, with low content of aluminum oxide and silicon dioxide (normally found in Brazil and South Africa). On the other hand, in the second group iron content varies between 56% to 61% (normally found in India and Australia) (Lu, 2021; Ma, 2012).

Higher grades of iron are found in magnetite and hematite concentrates, with low contents of contaminants when used for direct reduction purposes; this emulates a more extensive beneficiation process, normally with fine grinding tailed by magnetic separation and also with reverse flotation or gravity concentration to reduce silica content (Srivastava et al., 2001; Srivastava and Kawatra, 2009).

Considering that the quality of the available iron ore deposits is degrading with time, the chemical composition of many fine iron ore products is also being affected. Thus, it expected that the current iron ore raw materials to be substituted by beneficiated fine ores and magnetite concentrates (Lu, 2021).

Several mineral and elements (e.g., sideritic carbonates, alkalis, clays, luminism oxide, and silicon oxide) may present deleterious effect on downstream iron processing. A classic technique for the reduction in deleterious materials concentration consists in the dilution through blending at the steel mill; this technique enables the use of what might otherwise seem

to be an unacceptable iron ore. However, it is important to highlight that limits but does not eliminate the adverse effects of a deleterious element (Araujo et al., 2003; Dauce et al., 2019). More than 90% of the currently exploited iron ore deposits originated as chemical precipitates from ocean water (*i.e.*, sedimentary origin). Among these deposits, iron formation-hosted iron ores are characterized as the most commonly found. Although most of the exploitable iron deposits are from sedimentary origin, it is important to highlight that several other less significant sources can be found, such as: (i) terrestrial detrital iron deposits (*DID*); (ii) detrital marine placer titanomagnetite deposits (iron sands); (iii) oolitic goethite deposits of Minette/Salzgitter type; (iv) iron oxide Cu–Au (*IOCG*) deposits; and (v) contact metamorphic ores formed by replacement of carbonate rocks in the aureoles of granitoid intrusions (Fernández-González et al., 2017; Ma, 2012).

With that in mind, the next section discusses the world representation of iron ore, considering the above-mentioned information on iron ore deposits.

2.1.1 World representation

Iron ore is the raw material for steel, which is used in the production of tools, machines, vehicles, electricity transmission lines, as a structural element for the construction of buildings and houses, in addition to having an infinity of other applications. Usable iron ore production from the top 16 iron ore producing countries in millions of tons per annum (Mt/a) is summarized in Table 2.1. These countries are spread around the globe with the geographic distribution of the major iron ore producing countries shown in Figure 2.1.

Table 2.1. Iron ore production worldwide.

Country	Mine production				Reserves (million metric tons)	
	Usable ore		Iron content			
	2020	2021	2020	2021	Crude ore	Iron content
United States	38,100	46,000	24,100	29,000	3,000	1,000
Australia	912,000	900,000	565,000	560,000	51,000	25,000
Brazil	388,000	380,000	247,000	240,000	34,000	15,000
Canada	60,1000	68,000	36,100	41,000	6,000	2,300
Chile	15,600	19,000	9,890	12,000	NA	NA
China	360,000	360,000	225,000	220,000	20,000	6,900
India	204,000	240,000	127,000	150,000	5,500	3,400
Iran	49,500	50,000	32,500	33,000	2,700	1,500
Kazakhstan	62,900	64,000	12,00	13,000	2,500	900
Mexico	14,900	17,000	9,380	11,000	NA	NA
Peru	13,30	16,000	8,890	11,000	2,600	1,500
Russia	100,000	100,000	69,500	71,000	25,000	14,000
South Africa	55,600	61,000	35,400	39,000	1,000	670
Sweden	35,800	40,000	25,400	28,000	1,300	600
Turkey	15,400	16,000	8,570	8,900	130	38
Ukraine	78,800	81,000	49,300	51,000	6,500	2,300

Country	Mine production				Reserves (million metric tons)	
	Usable ore		Iron content			
	2020	2021	2020	2021	Crude ore	Iron content
Other countries	69,500	90,000	40,000	58,000	18,000	9,500
World total	2,470,000	2,600,000	1,520,000	1,600,000	180,000	85,000

Source: Moraes and Ribeiro, (2019) and Niu et al., (2022).

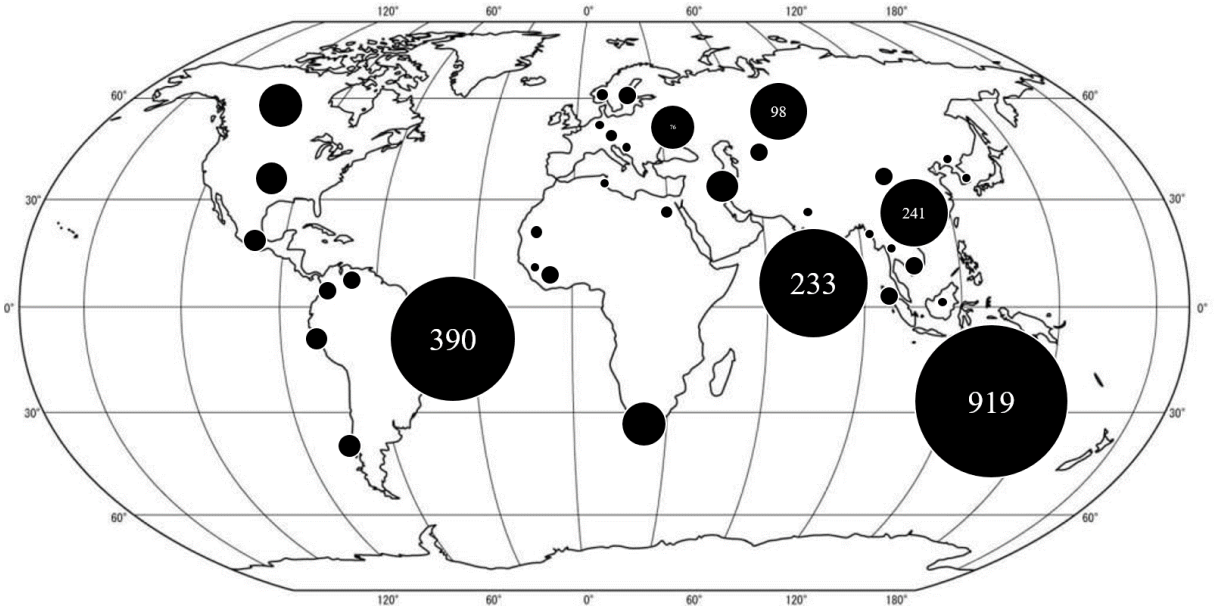

Figure 2.1. Geographic distribution of the major iron ore producing countries (Source: Adapted from Hagemann et al., 2015; Moraes and Ribeiro, 2019).

Although sixteen countries stand out as the major iron ore producers (Table 2.1), especial attention must be paid to Australia, Canada, China, India, Russia, South Africa, Ukraine, the United States of America, and Brazil; considering their expressive influence on the worldwide economy. Thus, the next paragraphs present information on each of these countries (Lu, 2021; Niu et al., 2022).

Australia has been a major iron ore exporter since the 1960s and continues to do so, by increasing its production to fulfil China's market requests for iron ore. Major efforts have been carried out for the optimization and automation of the country's mining operations to further enhance its iron production. Australia is endowed with large iron ore resources from the Western Pilbara region, which currently accounts for over 90% of its iron ore production; this plethora led to expressive infrastructure/groundwork development in Australia's environment. The iron ore reserves and resources of the country have suffered extensive changes over the expansion of the iron ore industry. New goethite/hematite deposits were discovered (e.g., Marra Mamba, Channel Iron Deposits, Detrital Iron Ore Deposits) and are now being explored as

alternatives to the traditional reserves. However, it is important to highlight that, these new deposits are lower in grade, i.e., require more processing to be marketable (Mohr et al., 2015; Yellishetty et al., 2010).

As for the types, Australia's iron ore mines are mostly open cut, in which the ore is extracted through conventional drilling or blast mining methods. Nevertheless, surface mining can also be applied, considering that some mines have deposits that are soft and of free digging. The extracted iron ore is normally utilized as a direct shipping ore (*DSO*); *DSOs* require minimum processing, with most stages involving crushing and screening and, as a result, lump and sinter fines are produced. These materials are later stockpiled and blended either on-site and/or at the port prior to exportation. Regarding the new ore types (goethite/hematite deposits), additional processing is required to produce a material with the required grade, involving more complex processes. As a consequence, several nonmagnetic physical separation methods (e.g., scrubbers, jigs, spirals, hydrocyclones, heavy medium drums, and cyclones) are being utilized. While magnetic separation is also used for the hematitic ores, its performance is limited due to the nature of the ores (Ferenczi, 2001; Mohr et al., 2015; Watson et al., 2010).

Although Canada is seen as a medium-size country, its reserves of crude iron ore reach values up to 6.0 billion tons, containing more than 2.0 Bt of iron. The most important iron ore deposits are located in western Labrador and northeastern Quebec, comprising a geological region known as the Labrador Trough. Hematite and magnetite are key ore types, including coarse-grained specular hematite, with lesser amounts of goethite and limonite (Thistle and Langston, 2016; Wansbrough, 2014). Regarding production aspects, the Canadian mining industry produced more than 58.0 mega tons of usable iron ore in 2019 (Vallejo and Dimitrakopoulos, 2019).

On the other hand, China is known as the "Giant of iron ore", currently occupying the place of largest importer and consumer of this good, with more than 1000 million tons imported in 2022. In 2011 China reached its peak of domestic production, with values up to 660 Mt; this climax was driven by rapid increase in demand for iron in the country. Yet, this level of production was proven unsustainable, considering the high costs associated with iron production due to the low-grade nature of the country's unprocessed ore reserves. Since then, China has been featured in the market as a main importer (Mustafa et al., 2022; Wu et al., 2016; Zhang et al., 2022).

The Chinese Geological Survey (*CGS*) it estimated to be higher than 70 billion tons, however, its crude ore reserves are 20 billion tons. The goods in these crude ore reserves are classified as low-grade (averaging 34% Fe content) and, thus, China's reserves are actually estimated to be 6.9 Bt. China diverges from the other main iron ore producing countries mainly because it also

exploits a wide range of different ore types (e.g., magnetite, hematite, V–Ti magnetites, limonite, siderite); in this sense, magnetite is the most common type, accounting for more than 60% of China's reserves, hematite, V–Ti magnetite, siderite, limonite, and other complex ore types (Lu, 2021). As previously mentioned, iron ore deposits in China are classified as low-grade, with iron grades varying from 30% to 50%; this results in expressive processing challenges. Considering the low-grade and polymetallic nature of the majority of the country's iron ore deposits, complex beneficiation processes are needed for most of the mining operations in order to produce useable iron ore concentrates high enough in grade for subsequent sintering and pelletizing to provide feed materials for the country's steel industry (Mustafa et al., 2022; Wu et al., 2016).

The iron ore beneficiations plants in China are normally designed not only to recover the iron minerals, but also all other marketable ones, aiming to fully harness the available iron ore deposits. For instance, the beneficiation plants for V–Ti magnetite ores segregate the primary process stream into separate streams for sub sequential extraction vanadium/titanium. The applied beneficiation methods are directly linked to the chemistry and mineralogy of the ore deposit, varying case-by-case. Among these methods, low intensity magnetic separation is applied to recover magnetite, wet high intensity magnetic separation for hematite both forward and reverse flotation, respectively, for recovering the iron minerals or removing the gangue (Mustafa et al., 2022; Zhang et al., 2022).

The crude iron ore reserves of India are estimated to be 5.5 Bt, with more than 3.4 Bt of iron. The most important iron ore deposits are scattered across the country into five main zones: (a) Singhbhum in Jharkhand and Cuttack in Odisha; (b) Dantewara and Durg in Chhattisgarh and Chandrapur and Gadchiroli in Maharashtra; (c) Bellary–Hospet belt in Karnataka; (d) Goa, Ratnagiri in Maharashtra, and North Karnataka; and (e) Metamorphosed BIF along the west coast in Karnataka and Kerala (Park et al., 2021; Sahu et al., 2022). The first four zones consist in hematite/goethite mineralization, while the last zone accounts for the magnetite mineralization. Most of the current iron ore processing in the country is the result of hematite/goethite reserves exploitation. Although India presents significant magnetite resources, these reserves are not fully explored considering their sensitive location (environmental and ecological preservation areas) (Krishnamurthy, 2022).

Regarding Russia, the country's iron ore reserves reach values up to 25 Bt, with roughly 14 Bt of exploitable iron. Most of Russia's reserves (>60%) are based in the Kursk magnetic anomaly in European Russia. With that in mind, more than half Russia's iron ore production comes from

this area, with the remaining production coming from the Urals and Siberia. In regard to the iron ore production, the country produced approximately 97 Mt of usable ore in 2019, occupying the place of fifth largest iron ore producer (after Australia, Brazil, China, and India); Its production is expected to grow to about 125 Mt/a in 2023 (Galitskaya and Zhdaneev, 2022; Hao and An, 2022; Tishkov et al., 2022).

In relation to South Africa, the country's iron ore reserves are around 1.1 Bt, with more than 690 Mt of iron. Most of these iron ore deposits are located in the Northern Cape, adjacent to the Kalahari Desert. The country's production of usable iron ore in 2019 reached values of 72.4 Mt. The ore bodies being mined are renowned for their dense hematitic ore types, and high-grade products are produced using both dense medium separation and jigs (Fan and Friedmann, 2021; Geymond et al., 2022; Liu et al., 2019).

As for Ukraine, the country's estimated iron ore reserves are about 6.5 Bt, with 2.3 Bt of iron. Ukraine's iron ore deposits are mostly located in Kryvyi Rih, Kremenchuk, Kerch, Mariupol, and Belozersky. The deposits are classified as average-graded, with 45-55% Fe, with a large portion of the iron ore being extracted by open cut mining. The largest iron ore deposit is Krivoy Rih in the Dnepropetrovsk region between Kremenchuk and Zaporizhzhya in central Ukraine, where most of the ore reserves and projects are located, including the Canadian owned Black Iron Shymanivske iron ore project under development near Kryvyi Rih which is 330 km southeast of Kiev. The area accounts for more than 80% of all Ukraine's iron ore fines, concentrate, and pellet production (Bazaluk et al., 2021).

Finally, the United States of America (USA) is endowed with iron ore reserves of about 3 Bt, Bt containing around 1 Bt of iron. Most of the country's iron ore deposits and operations are in Michigan and Minnesota located in the Lake Superior district; accounting for more than 97% the country's usable iron ore production. Iron ores in USA are classified as low-graded, with Fe contents between 25% and 30%, with distinctive proportions of hematite and magnetite, requiring beneficiation and pelletizing prior to utilization. Magnetite is normally recovered by rushing and grinding, followed by magnetic separation; hematite can also be recovered as a separate concentrate when it is economic viable (Fonteneau et al., 2019; Gielen et al., 2020; Lu, 2021; Zhu et al., 2019).

After exposing the global representation of iron ore industry and its deposits, the next section is focused on providing a local context, exploring the nuances of the topic in Brazil.

2.1.2 Local representation

As presented in the last section, Brazil is the world's second largest usable iron ore producer. The iron ore deposits of the country are mostly located in the Amazon basin in the state of Para and the Quadrilátero Ferrífero in the state of Minas Gerais. The largest iron ore mine is located in Carajás (see Figure 2.2), state of Para; this mine is owned and operated by VALE S.A. The second largest one is the Samarco Alegria mine (Figure 2.3), in the state of Minas Gerais; this mine is owned and operated as a 50:50 Joint Venture between VALE S.A. and BHP Billiton companies (Saes and Bisht, 2020; Santos and Milanez, 2015; Vasques Freitas et al., 2022).

Figure 2.2. Carajá mine in Brazil (Source: https://www.ihu.unisinos.br/categorias/188-noticias-2018/582222-e-quando-carajas-acabar).

Figure 2.3. Samarco Alegria mine in Brazil (source: https://revistamineracao.com.br/2018/10/02/samarco-inicia-obras-de-preparacao-da-cava-alegria-sul).

VALE is the largest mining company of Brazil, with total iron ore reserves of more than 14 Bt in terms of contained iron, and, up to 2015, was the largest one in the world. However, this position was lost due to two main failures that happened in Brazil: the collapse of Samarco's Fundão tailings dam at the Alegria mine and the failure of Vale's Brumadinho tailings dam at the Córrego do Feijão mine (Armstrong et al., 2019; Furlan et al., 2020).

Such failures posed a devastating impact on VALE S.A. along Brazil's iron ore production. To this extent, usable iron ore production in Brazil fell from 460 Mt/a in 2018 to 300 Mt/a in 2020.

Nevertheless, the company is slowly recovering and is expected to return to 340 Mt/a in 2023. Vale also produced about 42 Mt of iron ore pellets in 2019 (VALE, 2019), accounting for more than 80% of Brazil's total iron ore pellet exports. Production of iron ore pellets by Samarco, following the tailings dam collapse, finally recommenced in late 2020 after massive remediation work. Other important iron ore mining companys in Brazil are Companhia Siderurgica Nacional (annual production capacity of 33 Mt/a) and Mineração USIMINAS (annual production capacity of 7.4 Mt/a).

Brazil's iron ore resources and reserves are mostly classified as high-grade. For instance, Carajás mine in the Northern System consists of about 18 Bt of hematite ore with an average iron ore content of around 65–66% Fe (Almada et al., 2022). Nevertheless, the iron ore reserves in the southern state of Minas Gerais in the Southern/South-Eastern Systems contain high levels of itabirite and have average in situ iron contents of only 35–50% Fe. Itabirite is a banded-quartz hematite and consequently requires beneficiation, usually using a combination of cyclones and reverse flotation to achieve shipping grades of around 63% Fe (Moraes and Ribeiro, 2019).

The mining operations of VALE S.A. are divided in four fronts: (i) Northern, (ii) Southeastern, (iii) Southern, and (iv) Midwestern. The first system is located in the high-graded mines (Carajás) which produce lump ore, sinter fines, pellet feed, and special feed for direct reduction. The Quadrilátero Ferrífero in the state of Minas Gerais is home to the Southeastern Systems, including three mining complexes at Itabira (two mines with three major beneficiation plants), Minas Centrais (two mines with two major beneficiation plants and one secondary plant), and Mariana (three mines with three major beneficiation plants); the products of this system include sinter fines, lump ore, and pellet feed. The Southern System mines are also located in the Iron Quadrangle and comprise two major mining complexes, namely, Vargem Grande (five mines and five major beneficiation plants and Paraopeba (five mines and three major beneficiation plants), producing mainly sinter fines, lump ore, and pellet feed. As for the last system, it is composed by two high-graded mines in Corumbá, producing lump ore and sinter fines (VALE, 2022). The iron ore production of the aforementioned mines can be seen in Table 2.2, while the capacity of the plants is summarized in Table 2.3.

Table 2.2. Iron ore production VALE S.A.

Northern	2019 (Mt)	2020 (Mt)
Serra Norte and Serra leste	115.3	109.4

Northern	2019 (Mt)	2020 (Mt)
Serra Sul	73.4	82.9
Southeastern System	2019 (Mt)	2020 (Mt)
Itabira	35.9	23.9
Minas Centrais	25.9	15.7
Mariana	11.3	17.7
Southern system	2019 (Mt)	2020 (Mt)
Vargem Grande	13.1	25.1
Paroeba	24.7	23.3
Midwestern system	2019 (Mt)	2020 (Mt)
Corumbá	2.4	2.5
Total	302.0	300.4

Source: VALE (2023).

Table 2.3. Nominal production pellet plants VALE S.A.

Southeastern System	Production capacity (Mt/a)
Tubarão Itabrasco Hispanobras Kobrasco Nibrasco	36.7
Southern System	Production capacity (Mt/a)
Vargem Grande	7.0
Fábrica	4.5
Northern System	Production capacity (Mt/a)
São Luis	7.5
Oman	9.0
Total	64.7

Source: VALE (2023).

Regarding the Alegria mine in Minas Gerais, the 2.1 Bt available ore can be beneficiated in the Germano concentrator; the resulting concentrate is pumped as a slurry down a 396 km pipeline to Ponta Ubu where it is dewatered and pelletized in one of four straight-grate pelletizing machines with production capacities of 30.5 Mt/a (see Figure 2.4). However, production ceased in November 2015 following the failure of the Fundão tailings dam. After the completion of substantial remedial work, production recently recommenced in December 2020 at about 7.8 Mt/a, that is, at about 26% of capacity (VALE, 2022).

Figure 2.4. Pelletizing process in Alegria mine (Source: https://www.datamarnews.com/noticias/vale-halts-operation-at-alegria-mine/).

From the abovementioned information is possible to conclude that the mining sector is an important source of income, acting as a financial and economic support for Brazil. This sector is responsible for more than 2 million jobs in the country, contributing for a significant portion of the Brazilian economy; as a result, a multiplier effect on the economy is evidenced (Machado and Figueirôa, 2022). Besides, the sector can also offer products widely applied in different types of industries, such as metallurgy, fertilizers, steel, and petrochemicals. The impacts of the sector are strong in culture and also in the economic market since a large part of the investments made in Brazil are aimed at this sector of the market and many government initiatives are also aimed at stimulating these investments (Duarte and Lameiras, 2022; Santos and Milanez, 2015). Based on the knowledge acquired from the global and local representation of iron ore (sections 2.1.1 and 2.1.2), the next section seeks to provide information on the processing and production of iron and steel.

2.1.3 Steel production

The frontier between iron and steel was defined in the Industrial Revolution, through the invention of furnaces that allowed not only to correct impurities in iron, but also to add properties such as resistance to wear, impact, and corrosion. Considering these new properties

and the associated cost, steel now represents over 85% of all consumed metals by the current industrial civilization (Cristelo et al., 2021; Mcnab et al., 2009; Yellishetty et al., 2010).

Steel can be seen as an alloy of iron and carbon, with iron being a material that can be found throughout the Earth's crust, being strongly associated with oxygen and silica. Iron ore is basically iron oxide mixed with fine sand. As for carbon, the material is also relatively abundant in nature and can be found in many forms. Carbon is also relatively abundant in nature and can be found in many forms. In the steel industry, coal is used, and in some cases, charcoal (Ma, 2012; de Moraes and Ribeiro, 2019).

Coal and charcoal are both carbon-containing compounds. Coal is a sedimentary rock, being primarily composed of carbon and other elements such as hydrogen, sulfur, and nitrogen. Charcoal, on the other hand, is an impure form of carbon that is obtained by partial burning of carbonaceous materials in the presence of limited oxygen. The main difference between coal and charcoal is that coal is a naturally occurring fossil fuel whereas charcoal is formed as a result of burning carbonaceous materials (Cadore et al., 2019; Sahu et al., 2022).

Coal plays a dual role in the manufacturing of steel. As a fuel, it allows reaching high temperatures (about 1,500º Celsius) necessary for the melting of the ore. As a reducer, it combines with the oxygen that is released from the ore at high temperature, leaving the iron free. The process of removing oxygen from iron to bond to carbon is called reduction and takes place inside a blast furnace (Fernández-González et al., 2017).

Before being taken to the blast furnace, the iron ore and coal are previously prepared to improve the yield and economy of the process. The ore is transformed into pellets and the coal is distilled to obtain coke, which also produces carbon-chemical by-products. In the reduction process, the iron liquefies and is called pig iron or first melting iron. Impurities (e.g., limestone, silica) compose the slag, which is the raw material for the manufacturing of cement (Sahu et al., 2022).

The next step in the iron-making process is known as refining. The pig iron is taken to the melting station, still in a liquid state, to be transformed into steel, by burning impurities and additions. Steel is refined in oxygen or electric furnaces.

Finally, the third classic phase of the steelmaking process is rolling. Steel, in the process of solidification, is mechanically deformed and transformed into steel products used by the transformation industry, such as thick and thin plates, coils, rebars, wires, profiles, bars, among others (Fernández-González et al., 2017; Sahu et al., 2022; Vasques Freitas et al., 2022).

With the evolution of technology, the stages of reduction, refining and rolling are being enhanced and upgraded, ensuring greater speed in production. Steel mills around the world are classified according to their production process: (i) integrated, which operate with three basic phases: reduction, refining and lamination; (ii) semi-integrated, which operate in two stages: refining and lamination. These plants start from pig iron, sponge iron or metallic scrap purchased from third parties to transform them into steel in electric melt stations and their subsequent lamination. In addition, depending on the products that predominate in the production lines, plants can also be classified as: (i) semi-finished products (slabs, blooms and billets); (ii) flat carbon steel (plates and coils); (iii) special/alloyed flat steel (plates and coils); (iv) long carbon steel (bars, profiles, wire rod, rebar, wire and seamless tubes); and (v) long special/alloyed steels (bars, wire rod, wires and seamless tubes). In addition, there are also the so-called non-integrated production units, which operate only one phase of the process: processing (rolling or drawing) or reduction (Fernández-González et al., 2017).

Metallurgy is a division of the Transformation Industries section. It is in this economic activity that the conversion of ferrous and non-ferrous ores into metallurgical products and intermediate products of the process takes place. Steelmaking, the sector in which steel is manufactured in the form of semi-finished, laminated, re-rolled, drawn and seamless tubes, is classified as a specific group in the metallurgy division, a section in which other related activities are included. Within metallurgy, independent producers of pig iron and ferroalloys make up another group.

Steel is basically produced from iron ore, coal and lime. Steelmaking can be divided into four stages: preparation, reduction, refining and rolling (Fernández-González et al., 2017).

a) Preparation: the fine iron ore is agglomerated using lime and coke fines. The resulting product is called sinter. Coal is processed in the coke plant and turns into coke.

b) Reduction: these raw materials, now prepared, are loaded into the blast furnace. Oxygen heated to a temperature of 1000°C is blown from the bottom of the blast furnace. Coal, in contact with oxygen, produces heat that melts the metallic charge and starts the process of reducing the iron ore into a liquid metal.

c) Refining: oxygen or electric steel mills are used to transform liquid or solid pig iron and iron and steel scrap into liquid steel. In this step, part of the carbon contained in the pig iron is removed along with impurities. Most molten steel is solidified in continuous casting equipment to produce semi-finished products, ingots and blooms.

d) Lamination: the semi-finished items, ingots and blocks are processed by equipment called rolling mills and transformed into a wide variety of steel products, whose nomenclature depends on their shape and/or chemical composition.

After understanding the basics of iron ore extraction and steel production, the next section thoroughly explores the concepts regarding the wastes generated during these processes.

2.2 IRON ORE TAILINGS

The mineral extraction process generates high amounts of materials that have no economic value and that need an adequate destination (Davies, 2002). These inputs are industrially produced and, therefore, tend to present behavior characteristics that are different from the natural materials normally analyzed in engineering (i.e., natural soils) (Shackelford et al., 2010).

In search of acquiring a commercially viable product, the mining industry performs several crushing, pulverizing and processing processes in a high number of rocks (Hua et al., 2017). Sterile material, consisting of solid waste (e.g., piles of poor ores, rocks, sediments and soils), is seen as the input for the aforementioned process (Tishkov et al., 2022). Furthermore, a large amount of fine rock particles, whose granulometry normally varies between fine sand and clay, is produced during the beneficiation process. These fine and ultrafine particles, with no commercial value, are named mining tailings (Gomes et al., 2017). Mining tailings are generally mixtures containing high moisture contents as a function of the washing process to separate the fine fraction from the coarse fraction, which generally contains the ore (Machado and Figueirôa, 2022).

According to Vick, (1999), the main aspect for understanding the behavior of tailings is to know the nature of the disposal process that the tailings undergo. The consistency of the tailings when disposed can be defined as a function of the solids content and, consequently, of their moisture content. When disposed in the form of pulp, the tailings have a low solids content, are pumpable and require a structure for their containment. In this consistency, greater segregation of particles can occur and the control of percolation is more complex, however it is the operating system with the lowest associated cost. In the consistency known as “cake”, the tailings have a high solids content, making the material not pumpable, which increases the cost of the operation. In addition to these two consistencies, the material can still have two other intermediate consistencies: thickened tailings and paste tailings (Davies, 2002). Often, tailings are transported hydraulically and are deposited in hydraulic landfills (Benzaazoua et al., 2008; Vick, 1999).

According to Lima et al., (2020) and Soares Fortes et al., (2022) Ribeiro (2015), pulp is the most common concentration of processing plants in Brazil. Iron ore tailings are commonly classified according to their granulometry, being classified as fine tailings, known as mud and coarse tailings, also known as sandy or granular (Duarte and Lameiras, 2022; Vick, 1999). Regarding particle size, Dauce et al., (2019) presents granular tailings with particles larger than 50 μm, sludge consisting of particles smaller than 10 μm, and a third classification called fine tailings with particles between 10 μm and 50 μm. This granulometric separation can be performed by hydrocyclones installed close to the disposal system and the classified tailings are named according to the location of their outlet in the hydrocyclone, with the mud referred to as overflow and the granular tailings as underflow (Magalhães et al., 2020; Valenzuela et al., 2020). There is also the possibility of installing hydrocyclones inside the beneficiation plant, in which, part of the ore is reused before disposal, with the overflow portion being the tailings sludge and directed directly to the disposal system and the underflow forwarded to subsequent stages of ore beneficiation, whose tailings produced will be classified as granular (Vick, 1999). When classified, fine and granular tailings have different properties and behavior, mainly in relation to compressibility, permeability and shear strength (Ruan et al., 2021; Schoenberger, 2016). When the tailings are part of the structure of the disposal system, such as, for example, construction material for a dam or foundation material for elevations, the type of tailings commonly used is granular tailings (Lima et al., 2020; Vick, 1999).

To fully understand the structures that contain/are composed by iron ore tailings, it is relevant to understand the tailings disposal process. Thus, the next sub-section discusses the disposal of tailings. To this end, basic concepts regarding the disposal, transport and discharge of these materials are introduced.

2.2.1 Disposal, transportation, and discharge

Tailings can come from the processing unit in solid or liquid form (water pulp with solids or mud). Once the tailings are made available by the processing plant, they can be classified according to their solids content and percentage of water in one of the groups below: (a) conventional (unthickened and thickened tailings); (b) paste tailings; and (c) filtered tailings (Edraki et al., 2014; Ruan et al., 2021; Tishkov et al., 2022; Watson et al., 2010). Table 2.4 depicts the state, equipment, and transport methods for the above-mentioned classification.

Table 2.4. Mining tailings dewatering process technologies.

State	Yield strength (Pa)	Processing	Transportation
Unthickened	0	None	Pipelines, typically using centrifugal pumps
Thickened	0-40	Conventional thickeners and flocculants	Pipelines, typically using centrifugal pumps
High-density thickened	40-200	High-density thickeners and flocculants	Pipelines, typically using centrifugal or positive-displacement pumps
Paste	>200	Deep cone thickener or a combination of thickening and filtering	Pipelines, typically using positive-displacement pumps
Filtered	N/A	Vacuum or pressure filters	Trucks or conveyors

Source: Adapted from Fernandes (2017).

Boger (2013) studied the characteristic curve of yield strength variation as a function of solids concentration. Due to the low concentration of solids, pulp tailings behave like Newtonian fluids. With thickening, the concentration of solids increases and the tailings start to behave as non-Newtonian fluids and present yield point stress. This tension increases exponentially with the concentration and is accentuated from the paste concentration, as shown in Figure 2.5.

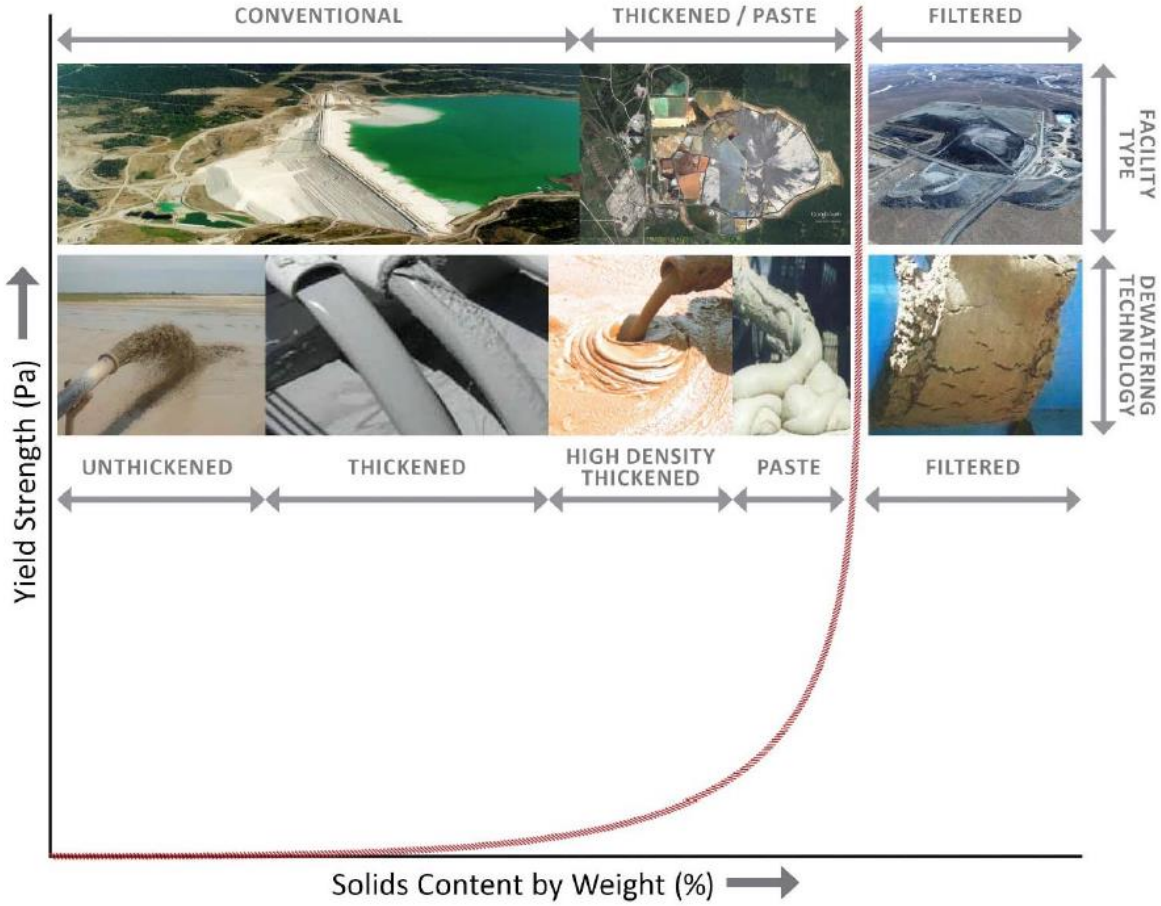

Figure 2.5. Characteristic curve of yield strength for mining tailings as a function of solids content (Source: Boger, 2013).

Conventional tailings (Figure 2.6) have a high content of suspended solid particles and lower solids content than the other groups presented. Vick, (1999) adds that pulp tailings have a solids percentage between 15% and 55%.

Figure 2.6. Conventional tailings example (Source: https://www.patersoncooke.com/the-impact-of-ore-body-variability-on-mine-waste-tailings-disposal-systems/).

Thickened tailings (Figure 2.7) have a solids content in the range between 50% and 60% (FELL et al., 2015) and behave similarly to highly viscous fluids (Vick, 1999). These contents of solid particles are usually obtained through high compression ratio thickeners or thickeners combined with filter presses.

Figure 2.7. Thickened tailings example (Source: https://www.srk.com/en/publications/srk-new-thickened-tailings-deposition-for-closure).

Regarding paste tailings (Figure 2.8), these can be described as a mixture of water with solids of dense consistency and with high proportions of fine particles and low amount of water

(Edraki et al., 2014; Watson et al., 2010; Yilmaz and Fall, 2017). This material is dewatered in such a way that it releases minimal amounts of water after being discharged and does not segregate when deposited. The solids content range that characterizes tailings in paste comprises between 70% and 85% (Helinski et al., 2011).

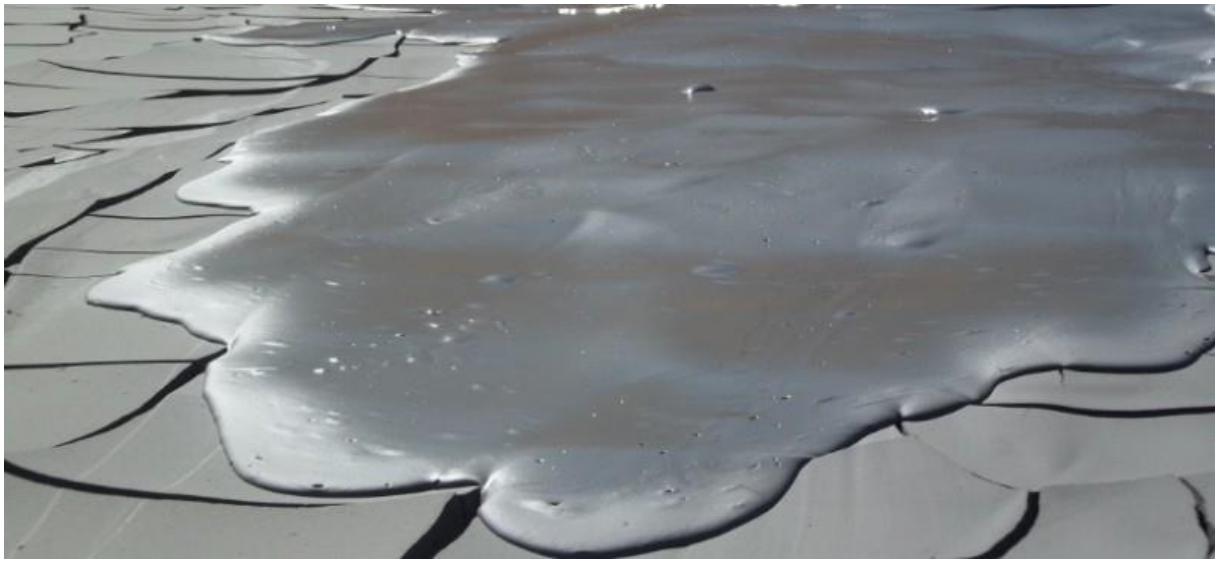

Figure 2.8. Paste tailings example (Source: http://delf-ing.com/know-how/paste-tailings/).

Finally, the filtered tailings (Figure 2.9) consist of unsaturated materials, with low compressibility and low hydraulic conductivity. The filtered material has a solids content greater than 85% (Servi et al., 2022; Watson et al., 2010).

Figure 2.9. Filtered tailings example (Source: https://www.takraf.com/news/detail/takraf-addresses-the-role-of-dry-stack-tailings/).

Regarding management strategies, tailing structures can be divided in three groups: (a) storage of unthickened/thickened slurry tailings; (b) high-density thickened and/or paste tailings and (c) filtered tailings (Piciullo et al., 2022).

A standard tailings disposition setup consists in the transport/delivery of unthickened or thickened slurry (up to 60% solids content) from the ore processing facility or thickener to the tailings facility (Alshawmar and Fall, 2023; Edraki et al., 2014). These tailings are disposed of hydraulically in tailing facilities (i.e., containment dams), normally in a loose density; in this type of disposition the material is segregated by particle size, in which the material near the deposition point is coarser while the fine grains are transported further from the discharge point. A significant amount of water is liberated from the deposition of the tailings, accumulating in a surface pond; three processes can be evidenced for this accumulated water: (i) natural evaporation; (ii) discharging from the facility; and (iii) reclamation to the ore processing facility via a reclaim pond (Vick, 1999). The aforementioned process is thoroughly detailed in Figure 2.10, showing a typical schematic view of a conventional tailings facility.

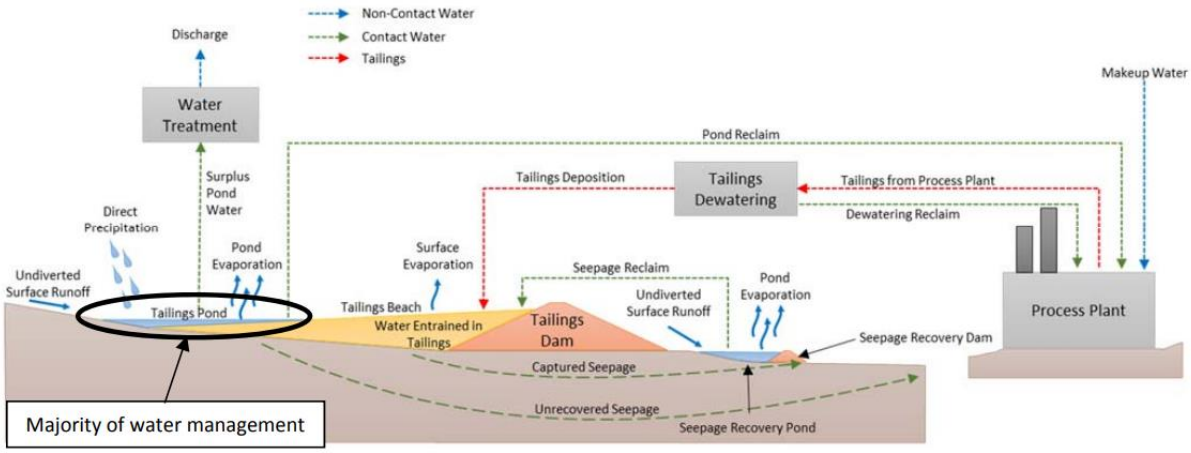

Figure 2.10. Conventional tailings facility (Source: Berger, 2017).

Natural and local materials (e.g., mine waste rock, tailings) can be utilized in the construction of tailings dams; the mining tailings are deposited in these structures in an initially saturated state and may remain saturated or desiccate/drain-down becoming partially saturated. The final saturation state of the deposited tailings is directly dependent of the local climate and hydrogeological conditions of the facility. As previously mentioned, tailings segregate, accumulating coarser particles near the deposition point and finer particles being deposited further away (Berger, 2017). A positive point from this segregation is that a well-drained zone close to the dam can be created, which may enhance the overall stability. Some negative aspects can also be associated with the segregation, dusting of dry, sandy beaches, concentration of sulphides, and poor consolidation and low strength of the slime areas. Nevertheless, the coarser tailings can be applied as compacted filling for dam construction (Edraki et al., 2014; Piciullo et al., 2022).

As for high-density thickened/paste tailings, the setup also involves the delivery of the materials to the tailings facility, normally through a pipeline (Yilmaz and Fall, 2017). Considering that paste tailings present a high yield stress, sometimes displacement pumps are necessary to transport the material. Similar to conventional tailings, paste tailings are hydraulically discharged; however, steeper slopes than unthickened slurry can be applied (Edraki et al., 2014). As shown in Figure 2.11, these facilities are usually operated with no or minimal ponds on the tailings surface. Due to the initial moisture condition of the material, less water is released from the deposited tailings as they consolidate. All the water involved in the process is collected in ponds here it may be reclaimed to the ore processing facility or discharged (Berger, 2017).

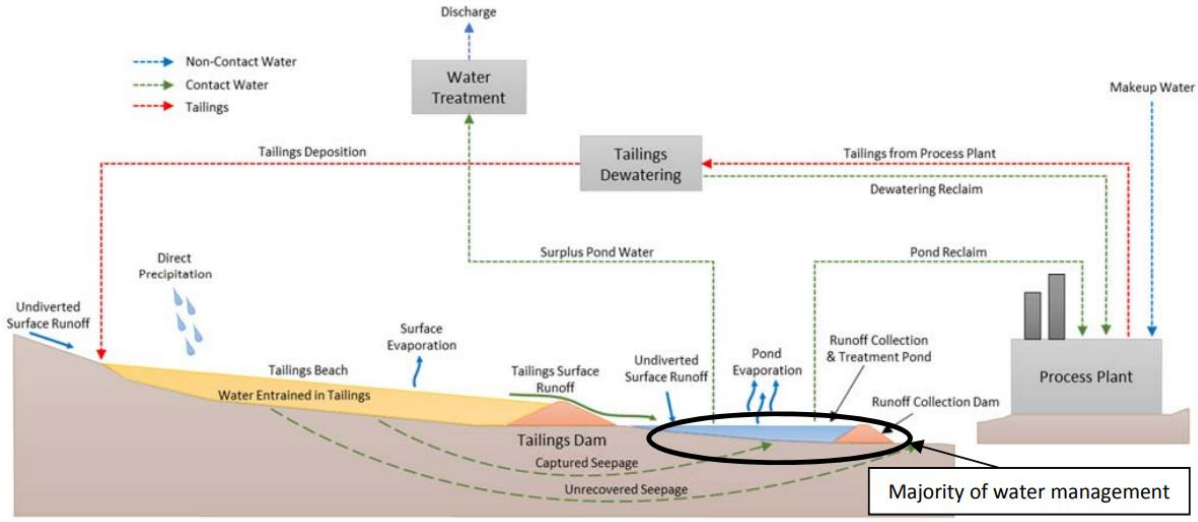

Figure 2.11. Thickened/paste tailings storing facility (Source: Berger, 2017).

Alluding to the conditions of conventional tailings, thickened tailings are also deposited in a loose, saturated state and, depending on climate and hydrogeological conditions, may remain saturated or desiccate/drain-down and become partially saturated. As their name indicates, thickened tailings are denser than conventional tailings. Nevertheless, over-time due to the consolidation process both types of tailings achieve a similar final density at depth and this reduces the often-cited advantage that paste facilities require significantly less storage than slurry tailings (Berger, 2017). There are even cases in which high-density thickened/paste tailings facilities require a larger space than a conventional tailings facility to allocate a lower perimeter dam height. As previously stated, steeper slopes can be applied to projects of thickened tailing dams; this premise allows the storage above dam elevation, reducing the footprint and height of the dam (Watson et al., 2010).

For filtered tailings, unlike conventional and thickened materials, the disposition is made by trucks or conveyors; considering that these materials are partially saturated and act more like a natural soil rather than a fluid. Filtered tailings are known to be composed of more than 80% solids content, often presenting moisture contents near the optimum content from compaction tests. These materials form the containment structure, creating the structural zones. Facility seepage and runoff are collected and managed in external collection ponds (Watson et al., 2010; Yilmaz and Fall, 2017). Figure 2.12 shows a schematic of a typical filtered tailings facility.

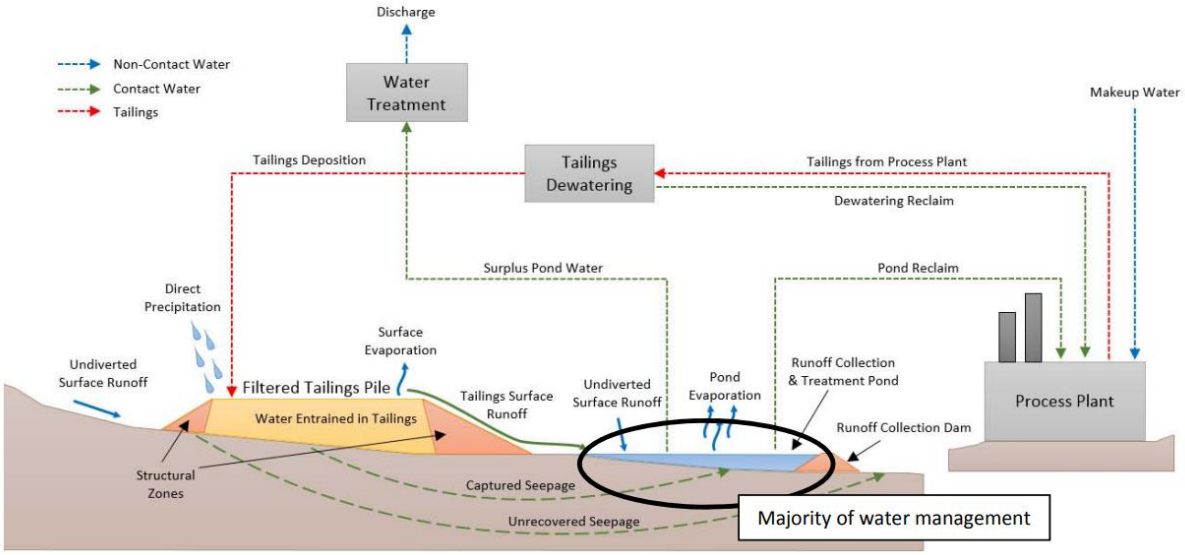

Figure 2.12. Filtered tailings facility (Source: Berger, 2017).

If deposited in a dry-stacking form (pile/stack), structural stability must be guaranteed over both conventional and seismic loading conditions (Servi et al., 2022; Watson et al., 2010). In addition, to prevent the liquefaction phenomenon, the materials must be well-compacted and drained. Finally, it is important to determine at the start of pile construction what the final geometry is so that the zone of compaction is well-defined (Berger, 2017).

Through the exposed information, it is noted that the generation of tailings, by either disposal methodology, is extremely high when compared to the number of processed ore. The aforementioned mining tailings have geotechnical characteristics that are different from the usual materials used in engineering practice. With that, the following subsection aims to clarify such behavioral aspects.

2.2.2 Geotechnical properties

The geotechnical properties of mining tailings depend on a number of factors, such as: (a) the origin of the mined ore; (b) the type of processing; (c) the refinery typology; (d) disposal and storage, among others (Souza Villar et al., 2009).

The properties of mining tailings are similar to those of a soil, that is, parameters such as: grain size distribution, grain density, chemical composition, consistency limits, compaction, hydraulic conductivity, compressibility, compaction performance, and shear strength are often analyzed (Reddy and Rao, 2016).

2.2.2.1 Grain size distribution

The grain size distribution is a fundamental geotechnical property for understanding the behavior of a material. According to Schnaid et al. (2015), the determination of the grain size distribution curve of mining tailings is loaded with uncertainties, and it is only possible to define a range of variation that normally presents particles with the size of silts.

Iron ore tailings, specifically, present grain size distributions that are dependent on the source of the source rock, the ore extraction process, processing and type of deposition (Armstrong et al., 2019). Thus, the definition of a standardized curve for this type of material is difficult to obtain, being more commonly defined a range of variation (Brunori et al., 2005; Nath et al., 2015). In studies involving iron ore tailings, several researchers (Figure 2.13) verify different granulometric distribution curves, with granular, intermediate and/or fine materials.

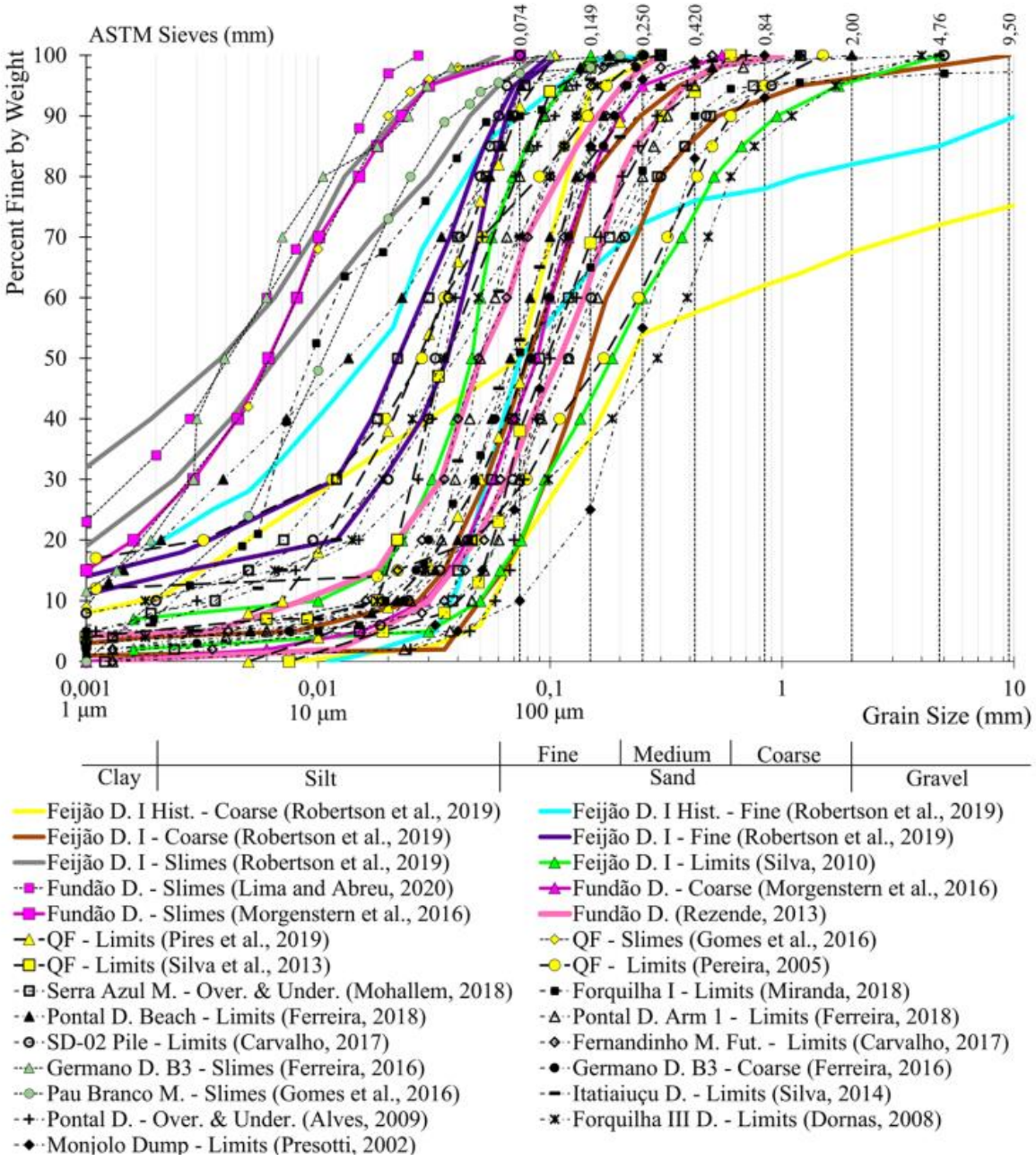

Figure 2.13. Grain size distribution for different iron ore tailings (Source: Carneiro et al., 2022)

As expected, the grain size distribution of different iron ore tailings (Figure 2.13) is extremely variable and highly dependent on the processing method applied to the mining facility. In addition, the disposition method also plays a fundamental role in the final grain shape and size; the more processed the material is the finer it gets (Gomes et al., 2016).

2.2.2.2 Specific unit weight of grains

The specific unit weight of grains (γs) is a characteristic of solids, being defined as the ratio between weight and volume of solid particles (Pinto, 2006). For conventional soils, the real specific weight values of the grains show small variations depending on the constituent minerals of the soil, being verified in the range of 25 to 28 kN/m³ (Lambe and Whitman, 1979).

Mining tailings, due to the high presence of iron oxides, commonly result in specific weight of grain values higher than those verified for conventional soils (Hu et al., 2017; Vick, 1999). Table 2.5 highlights the actual specific weight of grains for different iron ore tailings found in literature.

Table 2.5. Specific unit weight of grains for different iron ore tailings.

Origin	Specific unit weight of grains (kN/m³)	Author
USA	29.9-30.4	(Tawil, 1997)
Brazil	30.0-33.0	(Araújo, 2006)
India	27.7	(Ullas et al., 2010)
Brazil	35.5	(Bastos et al., 2016)
Nigeria	33.5	(Etim et al., 2017)
China	30.8-32.3	(Hu et al., 2017)
China	31.1-33.7	(Li and Coop, 2019)
Brazil	29.2	(Servi et al., 2022)

From the data exposed in Table 2.5 is possible to conclude that iron ore tailings present a high variability regarding their specific unit weight of grains; this variability is directly affected by the percent of iron oxide present in the material, higher the iron oxide content, higher the specific unit weight of grains (Lu et al., 2020).

2.2.2.3 Chemical composition

The chemical and mineralogical composition of iron ore tailings depend mainly on the mineralogy of the processed rock, the nature of the processing fluids used in the target minerals, the efficiency of the processing, and the degree of weathering before the storage in the dam. During the exploitation of iron ore, crushing rocks generates particles of iron oxide, quartz, and clay (Corrêa-Silva et al., 2020; Fontes et al., 2018).

Depending on the granulometric classification, the tailings can be classified as fine or coarse (granular or sandy tailings). Iron ore with high clay content, for example, tends to generate fine particles. Fine tailings are usually originated from the beneficiation process that involves desliming. These tailings, in general, are extremely fine, characterized basically by size fractions corresponding to the clay (with more than 90% below 74 μm in diameter) (Bazaluk et al., 2021; Srivastava et al., 2001; Zhang et al., 2020).

Flotation produces a coarse tailing made mainly of SiO_2 with small amounts of iron oxide, hydroxide, and kaolinite with an average particle size of 150 μm. In terms of mineralogy, most coarse tailings are mainly composed of quartz and small amounts of hematite and goethite (Araujo et al., 2003; Edraki et al., 2014).

All this variation in processing results in several different final mining tailings, with different chemical and mineralogical composition. With that in mind, Table 2.6 presents a compilation of chemical composition for iron ore tailings.

Table 2.6. Chemical composition of different iron ore tailings.

Chemical composition (%)						Location	Author
Fe_2O_3	SiO_2	Al_2O_3	CaO	MgO	Other compounds		
8.38	90.40	0.43	0.06	-	0.63	Brazil	(Silva et al., 2014)
11.60	84.20	1.60	-	-	2.60	Brazil	(D′Azeredo Orlando et al., 2020)
11.31	75.23	2.64	1.47	2.10	7.25	China	(Cheng et al., 2016)
12.31	34.72	16.22	7.63	8.92	20.20	China	(Duan et al., 2016)
15.10	84.40	0.45	0.07	-	-	Brazil	(Silva et al., 2014)
18.58	36.48	11.67	16.85	5.66	10.76	China	(Yang et al., 2015)
21.20	45.60	12.10	1.79	-	19.31	China	(Zheng et al., 2016)
21.40	65.70	0.80	-	-	12.10	Brazil	(Augusto et al., 2018)
21.50	71.40	-	-	-	7.10	Brazil	(Matiolo et al., 2020)
29.35	49.20	1.46	0.12	-	19.87	Brazil	(Zuccheratte et al., 2017)
32.00	46.68	3.89	-	-	17.43	Brazil	(de Freitas et al., 2019)
35.00	63.00	1.20	-	-	0.80	Brazil	(Filho et al., 2017)
38.80	14.00	2.01	37.5	0.36	44.83	China	(Zheng et al., 2016)
42.40	47.90	5.61	0.13	-	3.86	Brazil	(Silva et al., 2014)
44.52	24.40	10.95	6.20	0.99	12.94	China	(Chen et al., 2013)
47.80	30.00	21.20	0.10	0.10	0.80	Brazil	(Galvão et al., 2018)
51.37	15.11	3.39	0.23	0.16	29.74	Brazil	(Lima and Abreu, 2020)
55.78	16.58	15.46	1.44	0.13	10.61	India	(Giri et al., 2011a)
69.21	11.42	2.38	0.49	0.11	16.39	Bosnia	(Stević et al., 2016)
71.70	20.10	2.30	0.10	-	5.80	Brazil	(Pereira and Bernardin, 2012)

The data from Table 2.6 indicates that the iron oxide and silicon oxide content on iron ore tailings are extremely variable and dependent of how many processes was the material involved in until its final form. The more processed a tailing is, lower the iron oxide content; on the other hand, less processed tailings present higher silicon dioxide content and lower iron oxide content.

2.2.2.4 Consistency limits

The understanding and measurement of consistency limits are considered relevant in predicting engineering properties (e.g., expansion, shrinkage, strength), as well as in identifying and classifying materials (Gore et al., 2016). The determination of these indexes becomes even more

imperative when the input in question is considered as a mining waste (Nierwinski, 2019). Table 2.7 presents the consistency limits of different iron ore tailings.

Table 2.7. Consistency limits for different iron ore tailings.

Consistency limits (Atterberg limits)*			Origin	Author
LL (%)	LP (%)	IP (%)		
10	15	5	Brazil	(Oliveira et al., 2019)
NP	NP	NP	Brazil	(Oliveira et al., 2019)
NP	NP	NP	Brazil	(Silva et al., 2022)
25	18.75	6.25	Turkey	(Yüksek, 2022)
NP	NP	NP	China	(Hu et al., 2017)
28	19	9	China	(Hu et al., 2017)
NP	NP	NP	Brazil	(Consoli et al., 2022)

*NP = non-plastic

In general, iron ore tailings present little or no consistency (non-plastic behavior), considering that these materials are often composed by coarser particles. Nevertheless, depending on the processing method, some consistency can be found, especially when the material is grinded until finer particles are obtained; these fine particles (clay size) increase the intake of water molecules, contributing for the development of consistency (Aldaood, 2020).

2.2.2.5 Compaction characteristics

Compaction can be generally defined as the densification of a material, by removing the air and rearranging its particles, through the addition of mechanical energy (Pinto, 2006). The energy exerted by this process forces the material to fill the available voids, and with this, the friction forces generated improve the mechanical properties of the final product. According to Lambe and Whitman, (1979), the parameters that allude to the compaction of a material (i.e. density and optimal moisture) are directly dependent on three main factors: (i) the origin; (ii) typology; and (iii) compaction energy. Table 2.8 presents the compaction parameters for different iron ore tailings.

Table 2.8. Compaction characteristics for different iron ore tailings.

Dry unit weight (kN/m³)	Optimum moisture content (%)	Effort	Origin	Author
19.20	11.60	Standard	Brazil	(Consoli et al., 2022)
20.50	10.00	Modified	Brazil	(Consoli et al., 2022)
21.33	8.76	Standard	Brazil	(Oliveira et al., 2019)
20.73	11.40	Standard	Brazil	(Oliveira et al., 2019)
20.30	11.59	Standard	Brazil	(Oliveira et al., 2019)
19.86	10.70	Standard	Brazil	(Oliveira et al., 2019)
19.41	11.80	Standard	Brazil	(Oliveira et al., 2019)
19.90	9.55	Standard	Brazil	(Oliveira et al., 2019)
18.62	9.84	Standard	Brazil	(Oliveira et al., 2019)
17.90	7.55	Standard	Brazil	(Oliveira et al., 2019)
21.09	9.05	Intermediate	Brazil	(Oliveira et al., 2019)
20.20	10.00	Modified	Brazil	(Wagner et al., 2022)

19.30	11.50	Standard	Brazil	(Wagner et al., 2022)
18.06	14.30	Modified	Brazil	(Wagner et al., 2022)
17.62	14.82	Standard	Brazil	(Wagner et al., 2022)

From the data exposed in Table 2.8, it is clear that the compaction parameters of iron ore tailings are affected by the applied mechanical energy. Higher the effort, higher the dry unit weight and lower the optimum moisture content. The differences found in the compaction characteristics of iron ore tailings are once again associated with the processing of the material (Oliveira et al., 2019).

2.2.2.6 Hydraulic conductivity

Hydraulic conductivity alludes to several obstacles in engineering practice (e.g. surface drainage, water level lowering, flow calculation, settlement analysis and slope stability) and, therefore, it is extremely important for the characterization of a material (Lambe and Whitman, 1979). This property represents the ability of a material to allow water to flow through its voids and is determined by the parameter of the hydraulic conductivity (k).

Regarding natural soils, Fernandes (2016) states that about eight different magnitudes are found, that is, hydraulic conductivity presents itself as one of the properties with the greatest range of variation of values and difficulty of generalization. Its magnitude depends on several factors, such as: (i) granulometric distribution; (ii) void ratio; (iii) temperature; (iv) soil structure; (v) mineralogical composition; (vi) degree of saturation; and (vii) stratification.

In line with Oboni and Oboni (2020), mining tailings show variations in hydraulic conductivity coefficients in the range of 10^{-4} (for coarse sandy materials) to 10^{-10} m/s (for well-consolidated sludge with high plasticity). The increase in fines content, plasticity and deposit depth gradually decrease the hydraulic conductivity coefficient. Table 2.9 shows the variation of this property, according to the characteristics of the material.

Table 2.9. Hydraulic conductivity mining tailings.

Tailings types	Hydraulic conductivity (m/s)
Coarse, Sandy, clean, less than 15% fines content	10^{-4} to 10^{-5}
Sandy close to discharge points, more than 30% fines content	10^{-5} to $5x10^{-6}$
Low plasticity or non-plastic	10^{-7} to $5x10^{-9}$
High plasticity	10^{-6} to 10^{-10}

Source: Adapted from Oboni e Oboni (2020).

The hydraulic conductivity coefficient of mining tailings is also affected by the mechanism of input disposal and the segregation of particles. According to Oboni and Oboni (2020), high permeability materials are concentrated in the vicinity of the discharge point, followed by a transition zone between coarse and fine materials and finally the mostly fine materials. Under these conditions, the concentration ranges of coarser materials will have a higher coefficient of hydraulic conductivity, gradually reducing to the area of fine materials. Figure 2.14 exposes the values of this property for different mining tailings.

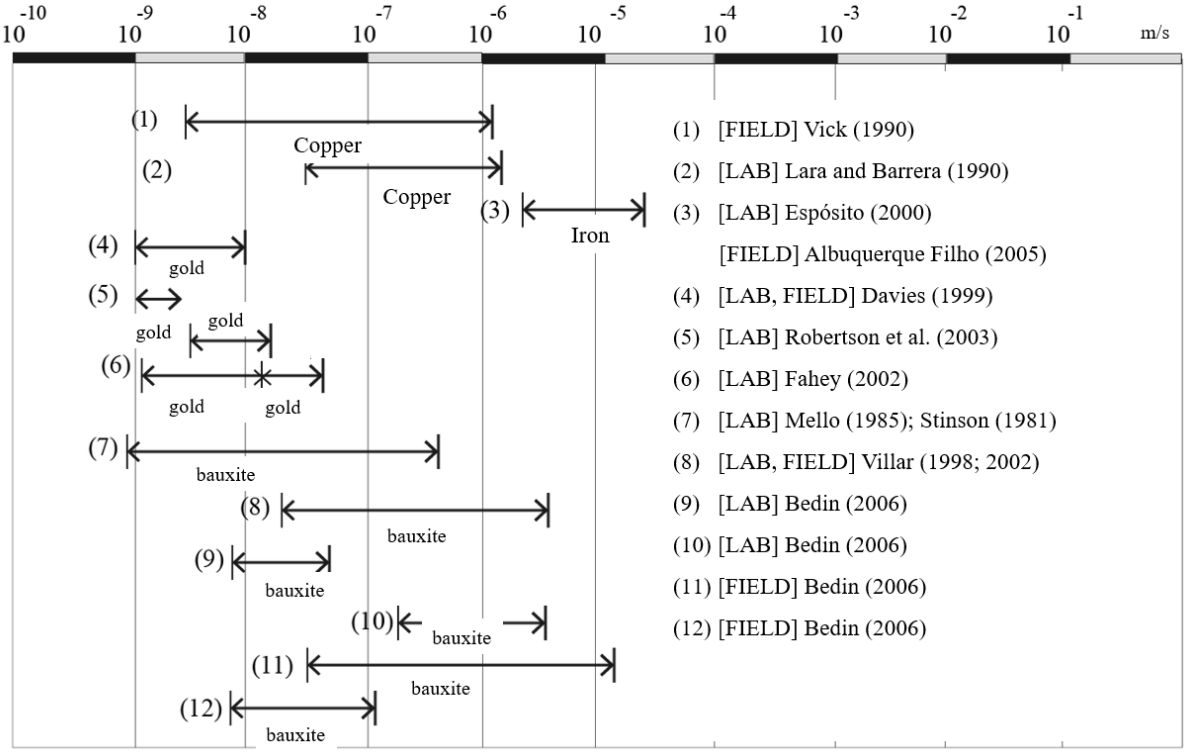

Figure 2.14. Conventional hydraulic conductivity for mining tailings (Source: adapted from Bedin and Schnaid, 2010).

Finally, as tailings are materials with an intermediate behavior (Bedin and Schnaid, 2010), the interpretation of tests on mining tailings, adopting fully drained conditions or undrained conditions, may not adequately portray the behavior of the material (Consoli et al., 2022; Helinski et al., 2011; Klahold, 2013; Nierwinski, 2019; Schnaid et al., 2014, 2016; Wagner et al., 2022).

2.2.2.7 Compressibility

The compressibility property of a material is related to the reduction of its volume under the application of an external force. This reduction is the result of a phenomenon of compaction (elimination of air from the voids) or densification (drainage of water from the voids) (Terzaghi,

1943; Terzaghi et al., 1996). Materials from tailings dams tend to have superior compressibility when compared to natural materials with the same characteristics. This premise is justified based on the interference generated by the tailings disposal procedure, which results in materials of low density and high grain angularity (Oboni and Oboni, 2020; Vick, 1999).

The interpretation of the density curve for mining tailings is of substantial difficulty, as the recompression section and the virgin straight of the material do not present a clear distinction, as in the case of clays (Bedin and Schnaid, 2010; Schnaid et al., 2014). Usual values for mining tailings compressibility parameters vary according to the type of material studied. Oboni and Oboni (2020) state that the cc parameter is contained in a range of 0.05 to 0.1, for sandy materials, and 0.20 to 0.6 for fine-grained materials. On the other hand, cv values are in the order of $5x10^{-1}$ and 10^{-2} cm²/s for materials with sandy properties and 10^{-2} to 10-7 cm²/s for fine-grained tailings. When the tailings are disposed of, consisting of a large percentage of fine particles and high moisture content, a deposition process begins that involves sedimentation together with the material's own weight consolidation, resulting in large deformations (Schnaid et al., 2015). Therefore, knowledge of compressibility and permeability laws is extremely important for solving problems inherent to geotechnics (Bedin and Schnaid, 2007).

2.2.2.8 Shear strength

The largest portion of shear strength of a soil is a consequence of the friction between the particles of the material, this resistance, contained in a parameter known as friction angle (Lambe and Whitman, 1979; Pinto, 2006). This angle is dependent on the applied normal force and consists of the maximum angle that the tangential component can exert in relation to the force normal to the plane, without slipping.

In addition to the resistance generated as a function of the friction between the particles, some soils have a resistance component due to cohesion (i.e., resistance that is independent of the applied normal stresses, generated only by the chemical attraction between the particles) (Rubinos et al., 2015). At similar stress levels, mining tailings tend to have greater effective friction angles than natural soils. Typical values of the friction angle of mining tailings are in the range of 30 to 40 degrees, and the factor that most affects this parameter is the stress level (Bedin and Schnaid, 2010; Oboni and Oboni, 2020; Schnaid et al., 2004, 2015; Vick, 1999).

2.2.3 Geotechnical applications

As previously state, iron ore tailings are known for being rich in silica, iron oxides, and other minority phases. With that in mind, several reuse applications can be found in the literature for this mining waste, as shown in Table 2.10.

Table 2.10. Geotechnical applications iron ore tailings.

Utilization	Example	Author
Mortar and concrete	Aggregate	(Almada et al., 2022; Yi et al., 2009)
Alkali-activated materials	Precursor material	(M. C. Duarte and S. Lameiras, 2022; Servi et al., 2022; Wong and Tam, 1977)
Ceramics	Tile production	(da Silva et al., 2014; Yang et al., 2015)
Pigments	Ceramic pigment	(Fontes et al., 2018; Galvão et al., 2018)
Silicates	Zeolite synthesis	(Halász et al., 2005)
Iron oxides nanoparticles	Nanoparticles synthesis	(Giri et al., 2011b)
Catalysis	Catalyst for Fenton reaction	(Augusto et al., 2018; Zheng et al., 2016)
Catalysis	Catalyst for CO oxidation reaction	(Augusto et al., 2018; Singh et al., 2018)
Catalysis	Catalyst for biodiesel	(Consoli et al., 2018a)
Catalysis	Catalyst for carbon materials synthesis	(Stević et al., 2016)
Adsorption	Adsorbent for H2S removal	(Huang et al., 2016)
Adsorption	Adsorbent for heavy metals	(Wong, 1981, 1985)
Adsorption	Adsorbent for phosphate	(Cristelo et al., 2021; Desogus et al., 2013)
Batteries	Cathodes synthesis	(Stević et al., 2016)

Most of the reuse applications of iron ore tailings (Table 2.10) can be segregated into the following sectors: (i) construction and building materials (Cristelo et al., 2021; Jiang et al., 2019; Servi et al., 2022; Zhang et al., 2020; Zuccheratte et al., 2017) (aggregates for concrete, mortar, Portland cement additives); (ii) ceramics industry (da Silva et al., 2014; Yang et al., 2015); (iii) alkali-activated materials (Kiventerä et al., 2016; Obenaus-Emler et al., 2020; Perumal et al., 2020; Servi et al., 2022; Xiaolong et al., 2021); and (iv) technological application (Bruschi et al., 2021a; c; d; Pereira dos Santos et al., 2022). Although several applications have been suggested in recent studies, the actual use of these applications on an industrial and commercial scale has been scarce due to several technological and market barriers.

After exposing the geotechnical characteristics inherent to natural iron ore tailings, as well as, the possible applications of this waste, the following subsection seeks to understand the chemical stabilization method applied to mining tailings as an alternative way to better predict the behavior of iron ore tailings.

2.3 CHEMICAL STABILIZATION OF MINING TAILINGS

In general, chemical stabilization can be seen as a widely applied soil improvement technique, utilized to increase the material's geomechanical response. In cemented geotechnical materials, a parcel of the strength and stiffness develops from the particle bonding, allowing the structured material to present states which are normally not possible for non-structured or reconstituted materials. The bonding exerts a significant influence on the stress-strain behavior independently of the soil type (e.g., fine-grained soils, granular soils, silts, and even mining tailings) (Consoli et al., 2009a, 2022; Hoch, 2023; Lirer et al., 2011; Mmbando et al., 2023; Servi et al., 2022; Silva et al., 2022; Wagner et al., 2022). From a mechanical perspective, cemented soils are located in an intermediate category of materials which behavior lies between the classical soil mechanics and the rock mechanics.

For granular and coarse grained materials, such as the case of most iron ore tailings, the structure is created as a result of both the bonding between particles and the fabric of the soil, reflecting the interaction between cementation and the arrangement of the soil matrix (Lade and Overton, 1989; Trads and Lade, 2014). This cementitious bonding refrains the relative movement between soil particles, before the bonding breakage starts to occur. Hence, the cementing matrix implies in an augment of stiffness and peak strength which are coupled with a more dilative response and post-peak brittleness in comparison to the unstructured (or untreated) soil (Atkinson, 2000; Shipton and Coop, 2015).

Even so, the role of the cementation along the shearing phase depends upon the effective state of stress prior to this stage. The response of the cemented material resembles the natural (uncemented) soil's behavior if the bonds are broken during the consolidation phase. In this context, several characteristics can be improved with the addition of cement, such as: strength, stiffness, hydraulic conductivity, and stress-strain behavior. With that in mind, the next subsections present some key information on the behavior of cemented geotechnical materials.

2.3.1 Unconfined compressive strength characteristics of stabilized mining tailings

The existence of a bonded structure in artificially cemented mining tailings results in a true cohesion parameter, in other words, a strength component which is seen even though no confining stresses are applied. In this sense, simpler strength tests (i.e., unconfined compressive

strength and split tensile strength) are valuable to analyze the effect of cement content and void ratio for compacted soil cement mixtures for low confinement levels, for example (PCA, 1992). The unconfined strength of soil-cement mixtures is primarily controlled by both the cementation and compaction degree (Consoli et al., 2007, 2009b, 2020b). In a similar manner, the same has been proven for stabilized mining tailings (Bruschi et al., 2021c; e; Chen et al., 2020; Edraki et al., 2014; Jiang et al., 2019; Newson et al., 2006; Pereira dos Santos et al., 2022), in which the cement content and void ratio play a fundamental role on the overall mechanical behavior. Higher the cement content and lower the void ratio, better are the mechanical results; the reduction in porosity induces a greater contact area between soil particles, intensifying interlocking and mobilizing friction, which increases strength; while the increase in binder content is linked to the increase in cementitious reactions, also contributing to strength development.

2.3.2 Initial shear stiffness characteristics of stabilized mining tailings

In accordance with Lambe and Whitman (1979) and Schnaid et al. (2004), as stresses are increased or decreased a material body will tend to change size and shape as strains occur, in which stiffness can be defined as the relationship between changes of stress and changes of strain. This parameter is dependent of the shape of the body, the boundary conditions, and the inherent stiffness properties of its constituent materials. In addition, the stress-strain behavior of soils is non-linear, in other words, stiffness varies as the straining progress. Figure 2.15 depicts a simplified model for stiffness and strength parameters of a soil specimen submitted to a compression triaxial test, presenting the Young's modulus: initial (*E0*), tangent (*Et*) and secant (*Es*).

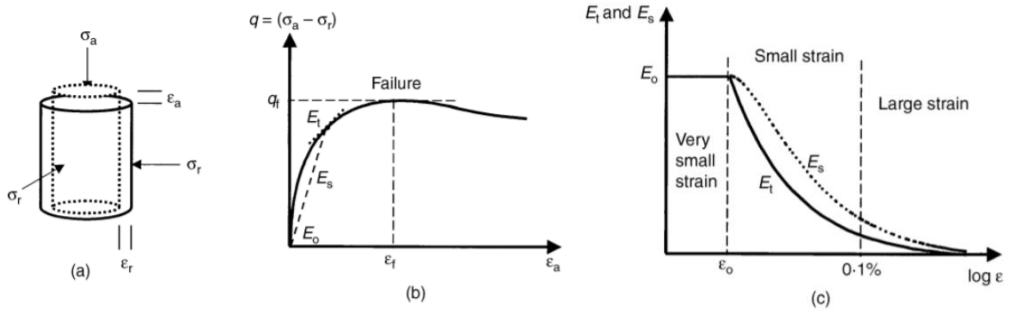

Figure 2.15. Stiffness variation during the execution of a triaxial test.

At very small strains, stiffness can be said to be constant (*Et = Es = E0*). Following this small strain zone, rapid decrements of stiffness occur as the straining progress. At large strains, *Es* is virtually constant and *Et* is zero. The same considerations are valid for cemented soils, in which

the onset of bond degradation changes the dynamics of the stiffness variation. At this region of very small strains, particle deformation is the prevailing deformation mechanism in geomaterials. Thus, the stiffness is fundamentally affected by the compaction degree, interparticle contact dynamics, and material properties (Atkinson, 2000; Consoli et al., 2017b; Diambra, 2015; Schnaid, 2005; Schnaid et al., 2004; Shipton and Coop, 2015). In this sense, the existence of a cementitious bond surrounding particle contacts ultimately modifies the load-induced stress distribution mechanism around these contacts (Atkinson, 2000).

From a micromechanical perspective, the Hertzian Contact Theory can provide important information regarding small-strain stiffness of granular materials (Yun and Santamarina, 2005). The cementation results in the increase of the contact area between the particles. Moreover, the increase in the cement content causes an increase in the yield stress, postponing the onset of the bond's degradation and enlarging the cementation controlled region. Finally, this behavior is extended to stabilized mining tailings, in which the same mechanisms presented for conventional geotechnical materials occur (Dutra, 2021; Gonçalves, 2021; Hoch, 2023)

2.3.3 Hydraulic conductivity characteristics of stabilized mining tailings

Several factors affect the hydraulic conductivity of stabilized tailings, with the main ones being: (a) water/cement ration; (b) cement content; and (iii) curing time. The schematics of both stabilized and non-stabilized mining tailings are shown in Figure 2.16.

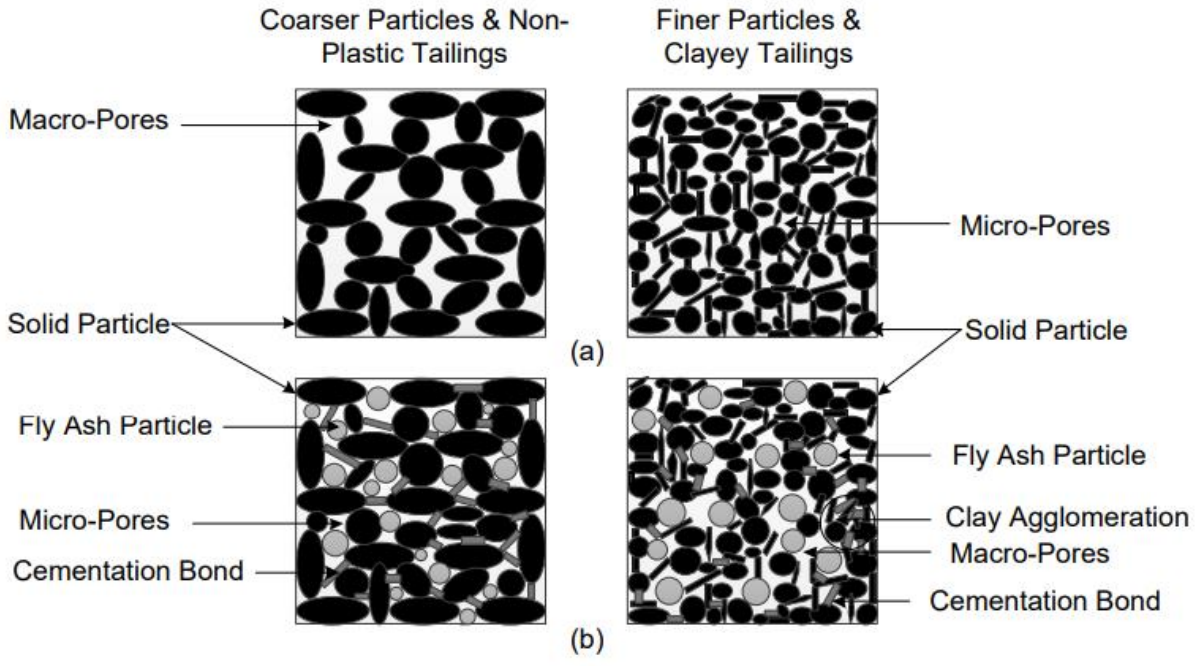

Molding conditions effect on the geomechanical behavior of uncemented and cemented iron ore tailings under low and high confining stresses. 2023.

Figure 2.16. General behavior stabilized mining tailings (Source: Adapted from Rajasekaran and Narasimha Rao, 2002).

The presence of a cementitious material results in the formation of calcium silicate/aluminate hydrates (C-S-H and C-A-S-H gels) surrounding the tailings particles (Figure 2.16b). In this sense, porosity and pores distribution play a fundamental role in the definition of the hydraulic conductivity. In uncemented coarse-grained materials (Figure 2.16a), larger pore spaces (macro-pores) between particles allow an enhanced ability to convey fluid when compared to fine-grained, uncemented materials that present smaller pore sizes (micro-pores) (Alonso and Palomo, 2001; He, 2000).

The cement effect on stabilized geotechnical materials may increase or decrease the hydraulic conductivity. For fine-grained materials, the cementitious products agglomerate the soil's particles into a cluster. The formation of these clusters is connected to the increase in the average pore size, creating a macro-pore structure (Figure 2.16b); this new macro-pore structure results in an increase in hydraulic conductivity (i.e., increases permeability). On the other hand, for coarse-grained materials (large grain sizes) the cement binds the soil particles, which decreases the average pore size, reducing the hydraulic conductivity (Alonso and Palomo, 2001; He, 2000).

Furthermore, the moisture of soil-cement mixtures is classified into three different groups: (i) capillary water, (ii) gel water, and (iii) chemically bonded water. Physically and chemically bonded water are depicted as a consequence of cement type while the amount of water that reacts with the cement, depending on the cement composition. In this sense, Brouwers (2011) states that 0.23 grams of water can become chemically bonded to 1 gram of cement and that physically bonded water adsorbed as a surface gel, accounts for approximately 19% by mass.

The ideal moisture content of any stabilized geotechnical material can be said to be the sum of chemically and physically bonded water in which no free water is evidenced. The optimum water/cement ratio is not only a function of the chemical composition of the cement but also a function of available reactive water. To this extent, Bin-Shafique et al. (2004) studied the effect of moisture content of fly-ash stabilized soils; authors reported that the highest cementitious activity and strength gains were observed for mixtures compacted at the optimum water content. In addition, any excess water shows no participation in the formation of cementitious bonds, increasing porosity (decreasing the contact area of the particles) and enlarging the pore-size network, resulting in an increase in hydraulic conductivity. Fall et al. (2009), while studying

cemented tailings, indicated that any excess water results in an increase in hydraulic conductivity.

Godbout et al. (2007) explored the effect of cement content on silty tailings; their study indicated that the increase in cement content leads to a decrease in hydraulic conductivity. Xenidis et al. (2002) also explored the effect of cement content on sulfate-rich tailings, authors indicated that the higher the cement the higher the blockage of flow paths through the amended specimen, which in turn, decreased the hydraulic conductivity. As for fine-grained materials, several authors (Diana et al., 2019; Latt and Giao, 2017; Zhao et al., 2022) indicate the opposite behavior, in which the increase in cement content leads to the increase in hydraulic conductivity. Thus, is plausible to assume that the permeability of cemented geotechnical materials (including mining tailings) is intrinsically connected to grain size distribution, in addition to cement type and moisture content.

2.3.4 Triaxial compression characteristics of stabilized geotechnical materials

For cemented geotechnical materials, three types of behavior can be evidenced during shearing under drained conditions, which are directly dependent on the initial state of the specimen concerning the yield curve of the cementitious bonds (Coop and Atkinson, 1994; Cuccovillo and Coop, 1999); this behavior can be evidenced on Figure 2.17a.

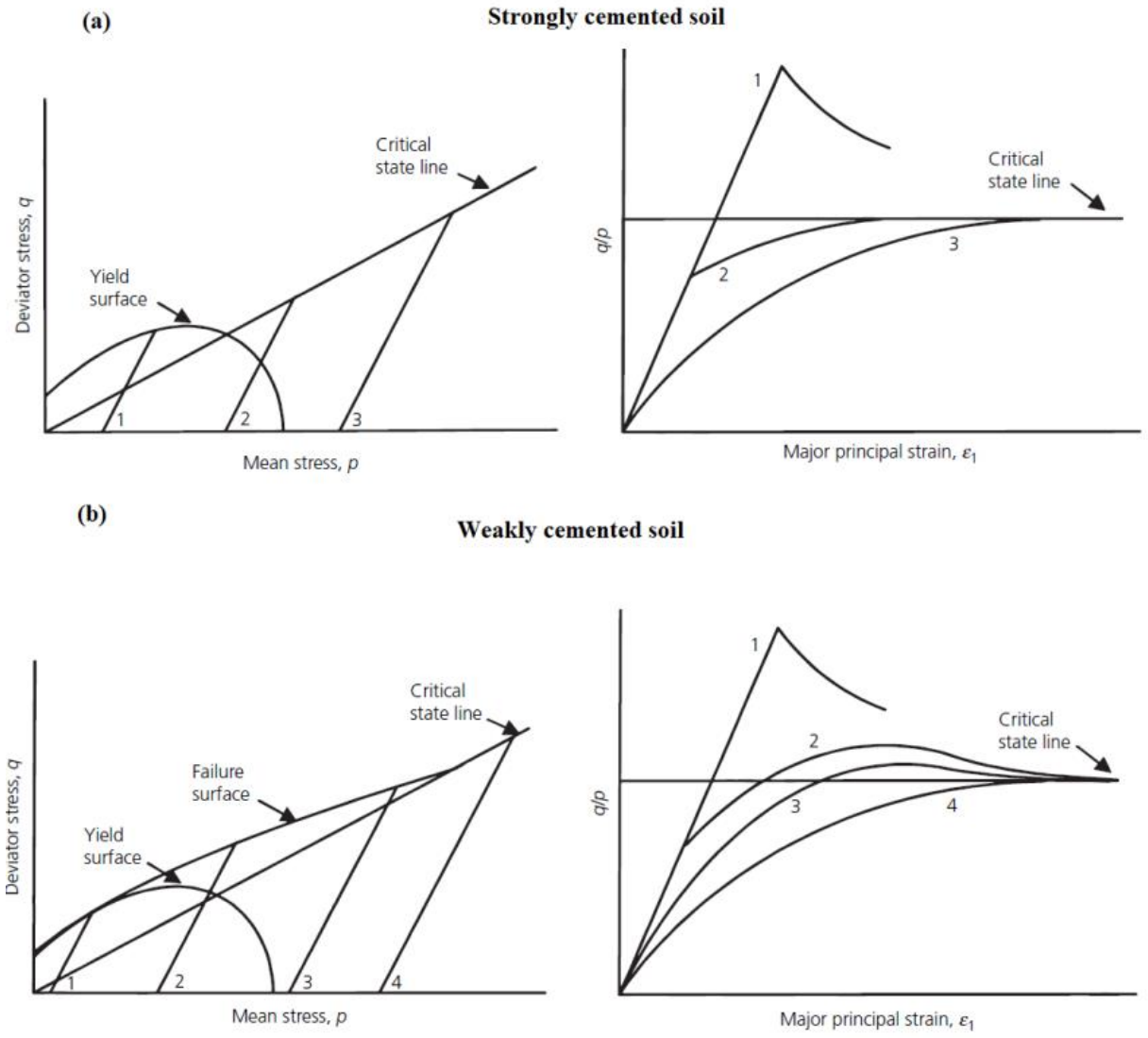

Figure 2.17. Stress-strains responses at intermediate confinement levels (Source: Adapted from Coop and Atkinson, 1994).

For low confining stresses, the stress-strain response behaves in an elastic form up to a well-defined yield point; then, a strain-softening is evidence directing towards the critical state line. At intermediate confining stresses, the yield of the material occurs before the critical state is reached, while failure is primarily frictional; nevertheless, the cementitious bonds enhance the initial stiffness. Finally, for high confining stresses, the cementitious bonds are broken during the consolidation phase and the behavior becomes purely frictional. Furthermore, strongly cemented soil and weakly cemented soils present distinctive behaviors (Figure 2.17b), encompassing two stress-strains responses at intermediate confinement levels for weakly cemented soil specimens (Trads and Lade, 2014). Both responses exhibit a slightly pronounced peak, however the one with highest deviatory stress is sheared in the yield surface of the

cement.; with the differences on the stress-strain behavior relying on the size of the cement yield surface.

In other words, the cement matrix is able to coordinate the stress-strain response up to the yield of the bonds, as the cohesive parcel is mobilized first (Lade and Trads, 2014). After this point, the friction component is mobilized. However, in the case of the yield surface of the bond being reached before the shearing phase (i.e., during consolidation) the response of the material becomes frictional, and the effects of the initial amount of cement on the effective stress parameters are negligible. In addition, once the cementitious bonds are broken, the material is not capable of returning to its original form, considering that lumps of cemented material may act as larger particles and/or the cement induced modification may not be fully erased during the shearing phase (Trads and Lade, 2014).

During the shearing phase, volume variation is directly dependent of the effective confining stress as well as the porosity of the material (Herzog and Mitchell, 1963; Lambe and Whitman, 1979; Trads and Lade, 2014). In this sense, contraction is evidenced for high stress levels and/or elevated porosities, while dilation occurs for the opposite conditions. Before the yield of the bonds, any volumetric strain should behave elastically and be contractive; afterwards, plastic dilative volume changes may occur. This behavior can be clearly seen in Figure 2.18and Figure 2.19.

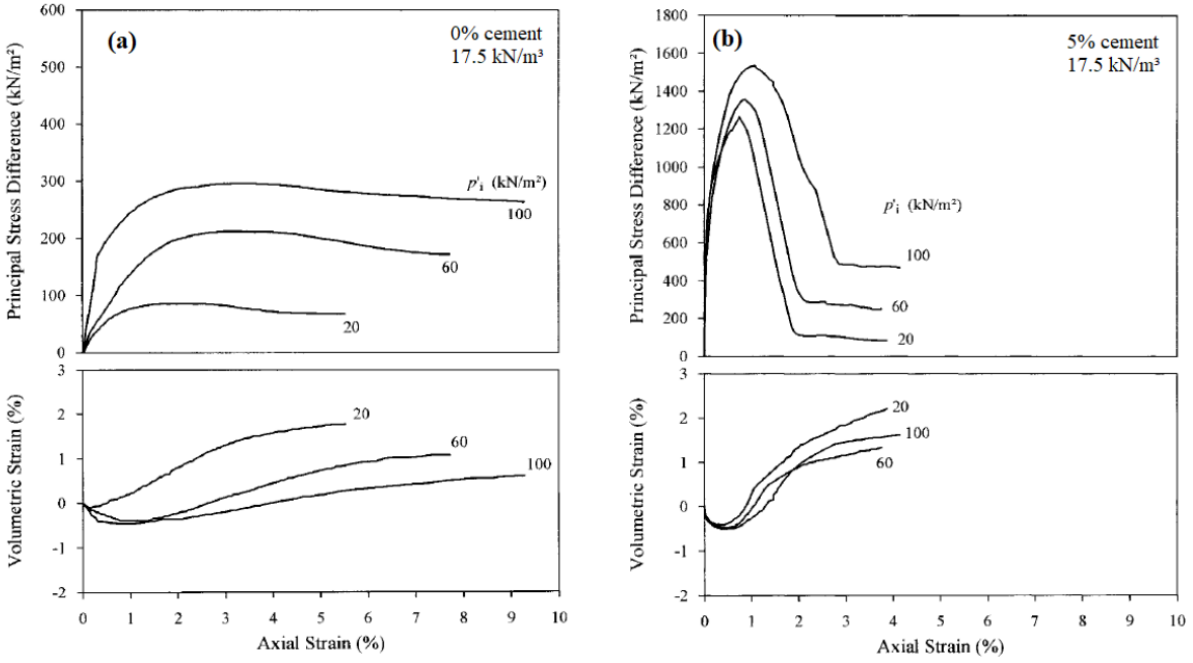

Figure 2.18. Stress-strains responses geotechnical materials (Source: Adapted from Lade and Trads 2014).

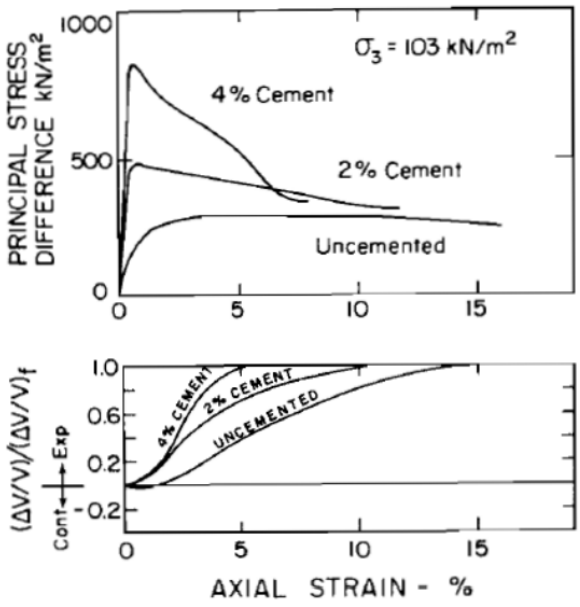

Figure 2.19. Stress-strains responses cemented and uncemented geotechnical materials (Source: Adapted from Clough et al., 1981).

2.3.5 Degradation of the bonded structure of stabilized mining tailings

The cementitious matrix wields a significant influence on the mechanical behavior of structured soils, to such an extent that authors diverge on the definition of yield/yield criteria for structured soils. Yield can be defined as the condition that sets the limit of elasticity and the beginning of plastic deformation under any possible combination of stresses, in accordance with the Classic Plasticity Theory (Malandraki and Toll, 1996). In other words, yield represents the limit between the region of recoverable strains (elastic zone) and irrecoverable/permanent strains (plastic zone). As for the graphical representation, for one-dimensional loading, the yield criterion is represented by a single point, while for two-dimensional and three-dimensional stress-states a curve and a surface are presented respectively.

Bond degradation plays a fundamental role in the understanding of the geotechnical behavior of structured materials, especially the specific point in which this degradation begins (i.e., yield point) on the stress-strain curves. Several authors (e.g., (Consoli et al., 2019c; Coop and Atkinson, 1994; Cuccovillo and Coop, 1999) indicated that the yield point is a stress state at which the material presents a discontinuity in the stress-strain response, as depicted in Figure 2.20.

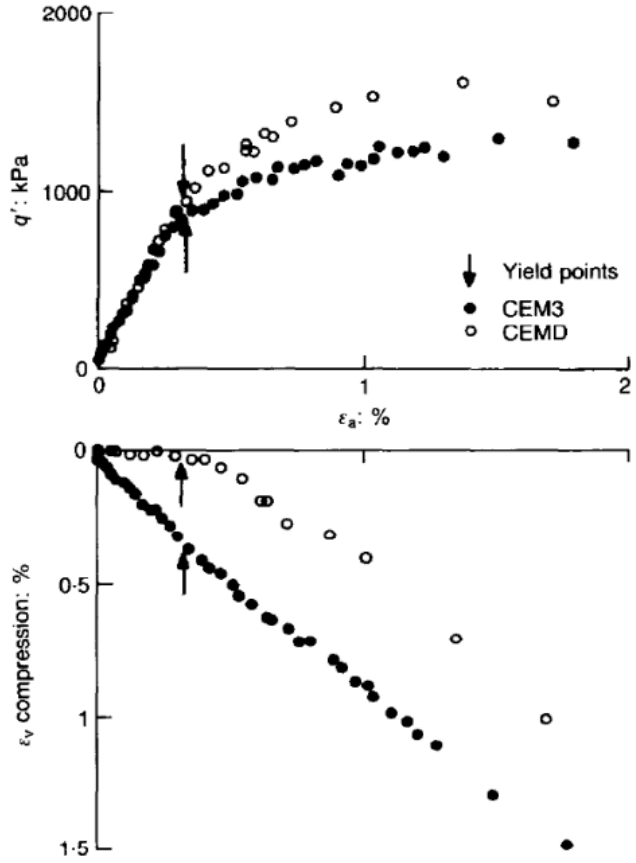

Figure 2.20. Yield points cemented soil specimens (Source: Adapted from Coop and Atkinson, 1993).

With that in mind, more than one yield point can be identified in structured materials, with these points being related to distinctive phases of the degradation of the cementitious bonds over shearing. Along these lines, two yield points were defined for structured soils by Vaughan et al. (1988); the first point represents the beginning of bond degradation, while the second point is associated with an equilibrium between the decreasing bond strength and the increasing bond stress. The second yield point, is represented by the point of maximum curvature on a log-log scale plot of the stress-strain curve; nevertheless, this point is not coincident with the complete destruction of the cementitious bonds (which normally occurs at larger strains). A different method for defining the yield point of structured materials is based on the stiffness of the material along the strain progression, as indicated in Figure 2.21.

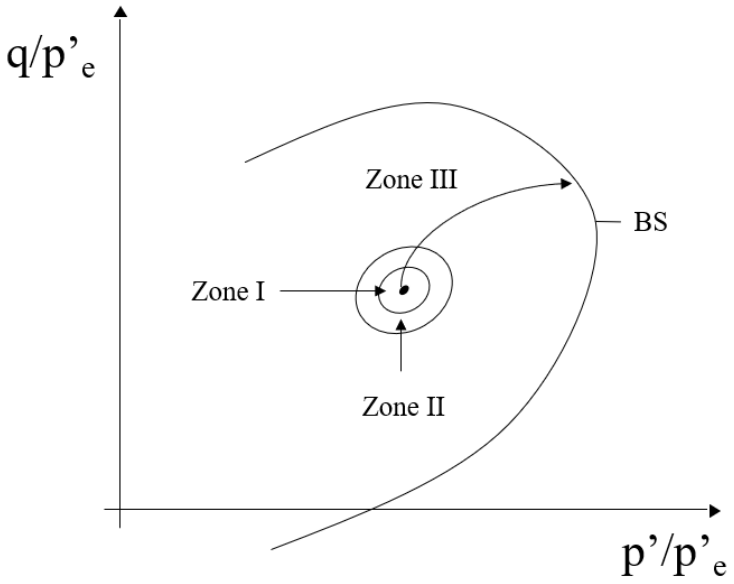

Figure 2.21. Yield point of structured materials based on the stiffness of the materials (Source: Adapted from Malandraki and Toll, 1996).

This approach tends to be more accurate, considering that it shows the specific points at which major stiffness losses begin (Malandraki and Toll, 1996). As indicated by Figure 2.21, three zones (I, II and III) that indicate three different yield conditions in the triaxial stress space are evidenced; Y1 represents the limit of the linear elastic response, Y2 delimits the recoverable (elastic) behavior zone and Y3 states the complete destruction of the bonded structure. Zones I and II are kinematic and moveable according to the stress path, whereas zone III is static and independent of the stress history.

Other authors (Malandraki and Toll, 2000) have also indicated three different yield points for structured soils (Figure 2.22): the first is represented by an initial stiffness loss, suggesting an onset structure degradation; the second is seen as a significant loss in tangential stiffness; and the third is defined as the final yield point, representing a condition of complete bond degradation.

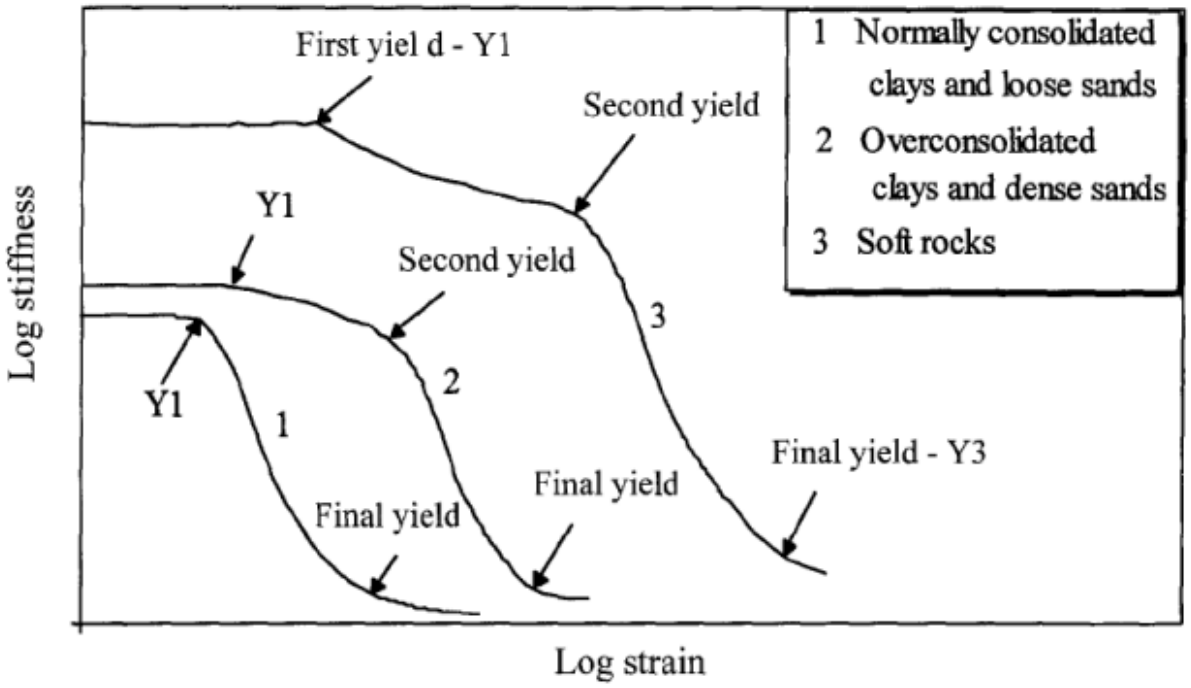

Figure 2.22. Three yield zones of cemented soil specimens (Source: Adapted from Malandraki and Toll, 1996; 2000).

Figure 2.23 further exemplifies the approach, presenting the normalized tangential stiffness, as a function of the axial strain, for triaxial tests carried out on structured soil specimens.

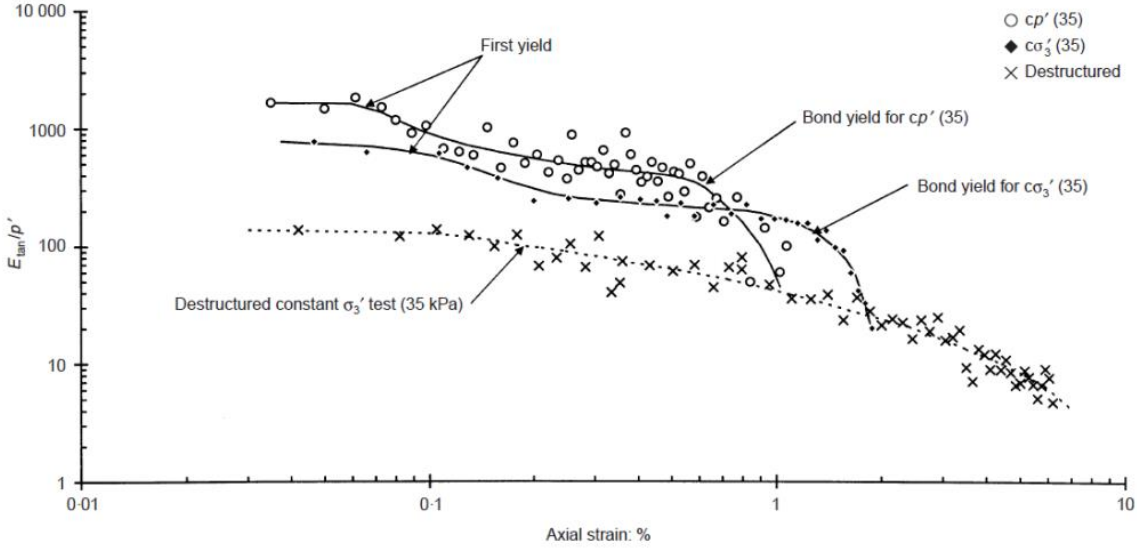

Figure 2.23. Yield point of the cemented structure for different stress paths (Source: Adapted from Malandraki and Toll, 2000).

In addition, four zones of behavior can be seen from the relative position of the failure surface and the second yield surface, as shown in Figure 24.

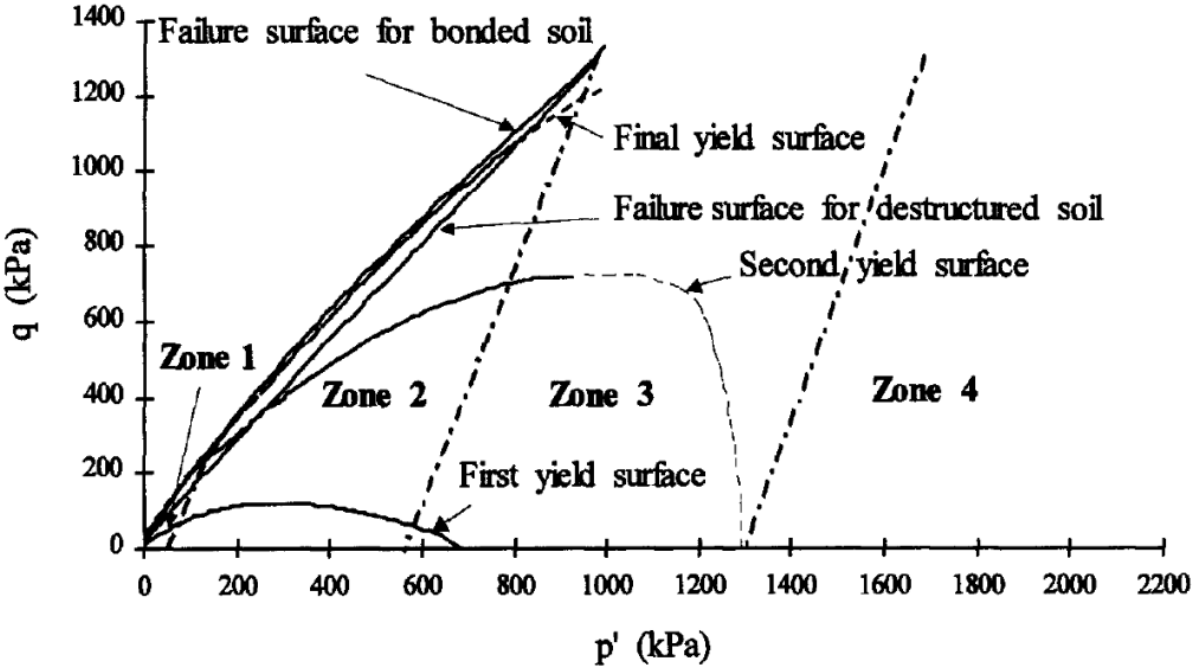

Figure 2.24. Behavior zones of structured soils (Source: Adapted from Malandraki and Toll, 1996).

For the first zone, the behavior of the material at failure is dictated by the cementitious structure, with the failure surface coinciding with the second yield surface (bonds yield surface). In the second zone, the behavior is only partially controlled by the cementitious structure and the bond yield is reached before the failure. However, he material still presents a higher maximum strength ratio than that of the de-structured soil owing to the post-yield influence of the cement matrix, such as more pronounced rates of dilation as a result of greater particle interlocking and delayed dilation (Lade and Overton, 1989; Lade and Trads, 2014; Yun and Santamarina, 2005). As the mean effective stress increases, this post yield influence decreases. In the third zone, soil behavior is now independent of the cementitious structure, which degrades in the beginning of the shearing. In the fourth zone, the behavior is analogous to that observed in the third zone, in which the cementing matrix yielding (second yield) occurs during the isotropic compression (i.e., in the consolidation phase). In the third and fourth zones, the failure surface of the structured material coincides with that of the de-structured soil.

2.4 CRITICAL STATE THEORY

Theoretical soil mechanics has always sought to explain the observed behavior of the soil in terms of mathematical and physical principles. As soils can exist for a range of void ratios and

confining stresses, the main challenge has always been to understand (and quantify) how this index can affect soil strength and stiffness (Lambe and Whitman, 1979).

The Critical State Theory, was first studied by Wroth (1968) and Atkinson and Bransby (1978). This state is defined as the moment when the soil reaches stability, which usually happens after large deformations (ε). Thus, the deviatory stress (q), the average effective stress (p') and the void ratio (e) no longer show variations, as explained in Equation (2.1). The stress invariants q (deviator stress) and p' (normal mean effective stress), used to describe the state of the sample and the specific volume ν, are defined by Equations (2.2), (2.3) and (2.4).

$$\frac{\delta q}{\delta \varepsilon_1} = \frac{\delta p'}{\delta \varepsilon_1} = \frac{\delta e}{\delta \varepsilon_1} = 0 \tag{2.1}$$

$$q = (\sigma'_1 - \sigma'_3) \tag{2.2}$$

$$p' = {}^{1}/_{3}\,(\sigma'_1 + 2 \times \sigma'_3) \tag{2.3}$$

$$v = 1 + e \tag{2.4}$$

Initially, the behavior of soil under isotropic loading is normally represented in the space of ν versus lnp', where ν is the specific volume of the soil. For most soils, compression and expansion are linear in this space, as in clays and sands, thus being a good idealization of their behavior. For granular soils, however, volumetric variations during loading are often accompanied by grain breakage, and in these cases, it is necessary to apply higher stresses (generally greater than 1000 kPa) to identify their real behavior. Figure 2.25 schematizes the behavior of materials under isotropic loading.

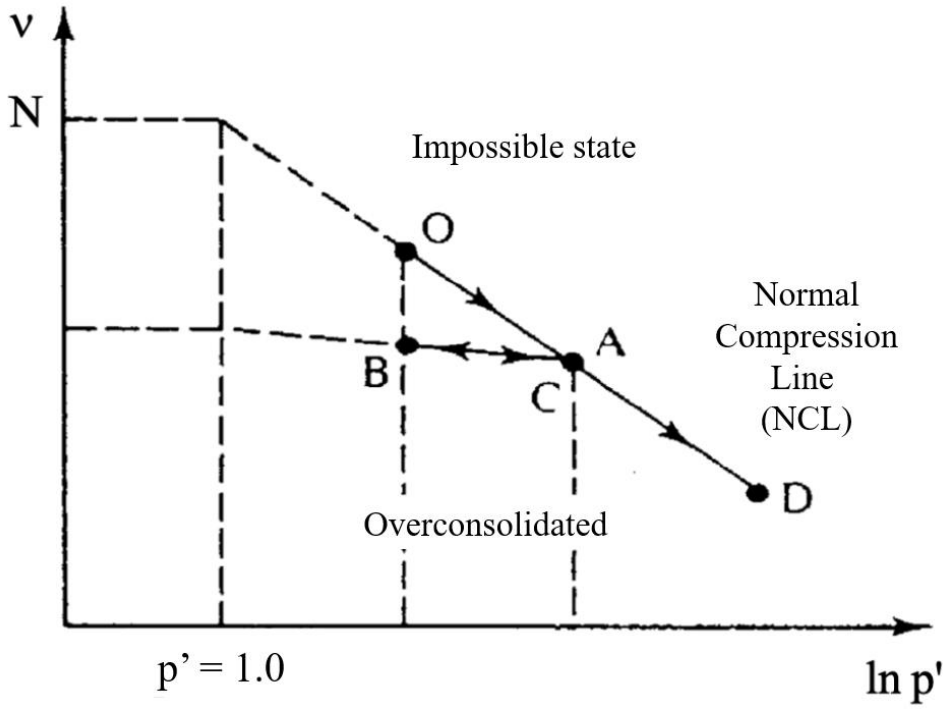

Figure 2.25. Behavior of the materials under isotropic loading conditions (Source: Adapted from Wroth 1968).

In the unloading phase (*C-B*), the soil is stiffer than in the first loading (*O-A*) since most of the deformations imposed in the first loading are plastic. The line *A-O*, corresponding to the first load, is known as the Normal Compression Line (*NCL*), expressed by Equation (2.5).

$$v = N - \lambda \times lnp' \tag{2.5}$$

Where *N* corresponds to the value of v when p' = 1 kPa and λ is the slope of the *NCL*. The parameters λ and *N* are constant for each soil, resulting in the existence of a single *NCL* defined by them.

An isotropically loaded soil specimen will follow the line *O-D* and, if unloaded, will follow a line on the line *AB*, but it will never move to a state to the right of the *NCL*. This line represents a limit state between possible states on its left and impossible states on its right. After being isotropically loaded, a soil that lies on the *O-A-D* line is considered loose. On the other hand, if the soil is in any state to the left of the *NCL*, having followed a line of expansion such as the *C-B*, it is considered a pre-consolidated soil, where point *C* corresponds to the maximum stress experienced by the soil. Based on the concept that if soil and other granular materials are continuously distorted, they will flow like a fluid of friction, they will enter a critical state

determined by equations (2.6) and (2.7) (Schofield and Wroth, 1968). Thus, in the same way as the *NCL*, the Critical State Line (*CSL*) is also represented in ν versus lnp' space by a line parallel to the *NCL*.

$$q = M \times p' \tag{2.6}$$

$$v = \Gamma - \lambda \times lnp' \tag{2.7}$$

The constants M, Γ and λ represent basic properties of the material, where Γ is defined as the value of ν corresponding to a p' of 1 kPa in the same way that N defines the location of the *NCL*. The projection of the *CSL* on the q-p' plane is a line where M is the slope and is equivalent to the friction angle in the critical state (ϕ_{EC}). For triaxial compression, the value of M is given by Equation (2.8).

$$M = \frac{6 \times sen\ \emptyset'}{3 - sen\ \emptyset'} \tag{2.8}$$

Considering a random arrangement of irregular solid particles of different sizes that interact with each other during the continuous deformation process, the entire energy dissipation process is treated as friction, neglecting the possibilities of degradation or particle orientation. The first critical state equation determines the magnitude of the deviation stress (q) required to keep the soil flowing continuously as a product of a friction constant (M) with the effective stress (p'), as illustrated in Figure 2.26. Macroscopically, the second equation states that the specific volume will decrease as the logarithm of the effective pressure increases (according to Figure 2.26b). Both equations make sense for dry sand and also saturated silty clays, where low effective stresses result in large specific volumes (i.e., more water is present in the voids) (Schofield and Wroth, 1968).

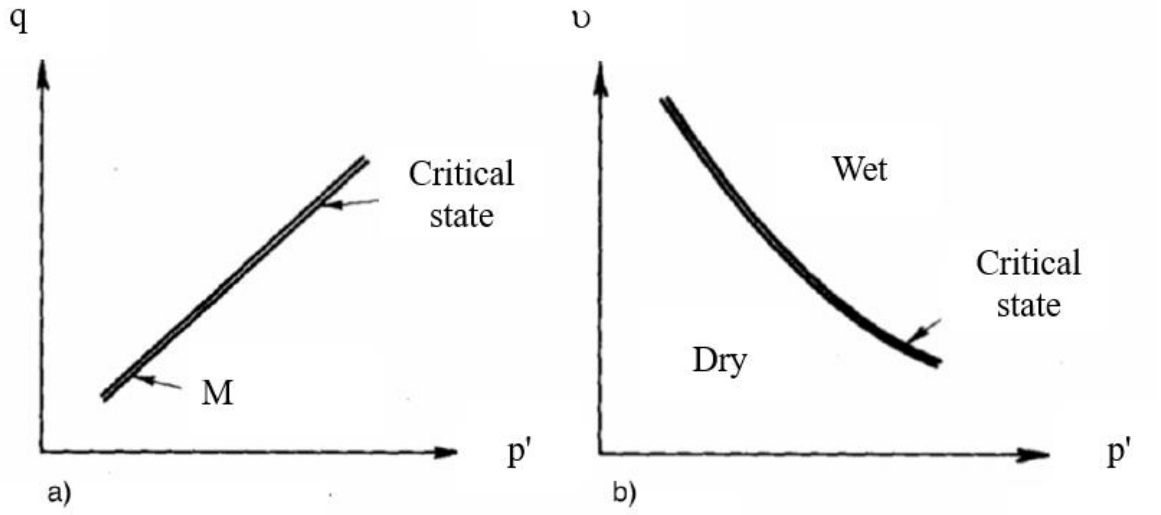

Figure 2.26. Critical state condition (Source: Adapted from Schofield and Wroth 1968).

Remolded soil specimens can be obtained in very different states by different loading conditions. The initial conditions of such specimens are complex, being difficult to define their stiffness, as well as, the mechanical behavior once the plastic strains begin to occur. However, this problem can be simplified if the soil is considered to flow as a friction fluid. Thus, the total change from any initial state to a final critical state can be accurately predicted, and the problem is reduced to calculating how much of this total change can be expected when the distortion process is not carried too far. Therefore, critical states become a baseline (Schofield and Wroth, 1968).

Combining the effective stress and the soil specific volume for any state, it is possible to plot a single point in Fig. 2.17b. At the beginning of the analysis, the first question that arises is whether the soil is looser than its critical state. In such states, the soil is called “wet”; during deformation the effective soil structure will sag and put some pressure on the pore water (depending on how far the initial state is from the critical state), and this positive pore pressure will cause water to drain out of the soil. Therefore, samples that are to the right of the *CSL* compress during shear, showing no strength peaks and correspond to normally consolidated or weakly pre-consolidated clays and soft sands. On the other hand, if the soil is denser than the critical state, it is called “dry”, and during strain the effective soil structure will expand (this expansion can be resisted by negative porepressures) and the soil will tend to absorb water. Thus, samples with initial state to the left of the *CSL* expand after a small contraction during shear and reach peak strength before reaching the ultimate state. They correspond to heavily pre-consolidated clays and dense sands. Thus, according to the Critical State Theory, the basic

mechanism of compression in soils is through grain rearrangement. In granular soils, this mechanism can be accompanied by the breaking of grains, and, in clayey soils, by the contraction or expansion of clay particles. The *NCL* represents a limit for all possible states in isotropic compression and the peak envelope should represent a limit for all possible states, as it represents the points of maximum strength, according to Figure 2.18a. Furthermore, for each specific volume value there is a peak envelope. These summed envelopes will form a peak surface in the three-dimensional space *q* versus *p'* versus *v*, as shown in Figure 2.18b.

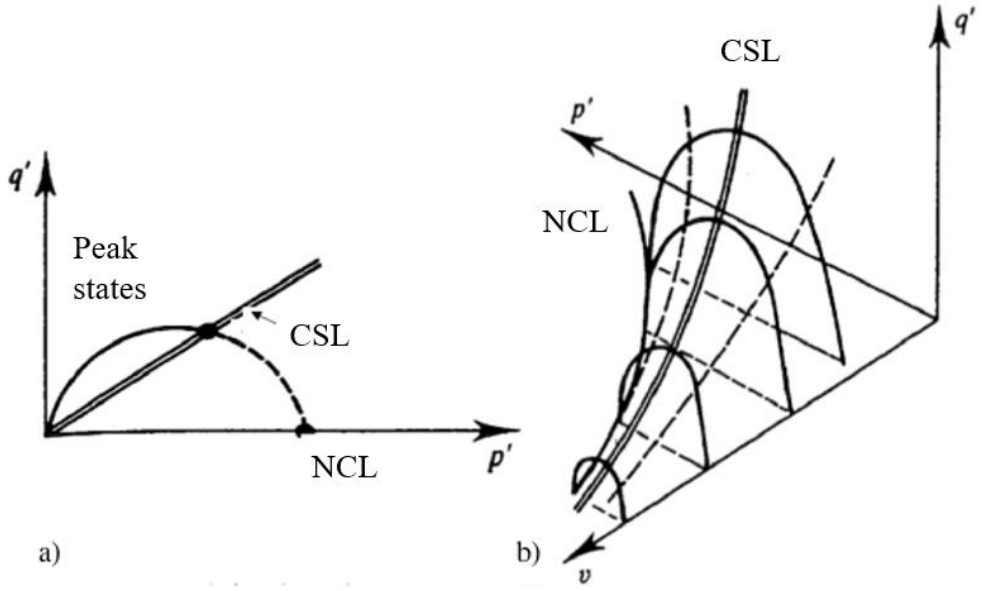

Figure 2.27. Representation of (a) peak failure envelope (b) state limit surface (source: Adapted from Atkinson, 1993).

This boundary state surface corresponds to the boundary of all possible states of a reconstituted soil, with no states being possible outside this surface. During shear, if the soil is inside this surface, the strains are elastic, while when it is on the boundary surface, both elastic and plastic strains can occur. Furthermore, all constant specific volume slices of the state boundary surface have a similar shape, but their size is related to the specific volume. Thus, it is possible to use a normalization feature with respect to an equivalent stress, to dimensionless *p'* and *q*. For normalization, the parameters used are the equivalent stress *p'e* and the critical stress *p'c*, which represent the stress in the *NCL* and in the *CSL* corresponding to the specific volume of the soil after isotropic consolidation, as shown in Figure 2.28. This equivalent stress *p'e* can be calculated during the test by Equation (2.9).

$$p'e = \exp[\frac{N - v}{\lambda}] \tag{2.9}$$

Normalizing p' and q with $p'e$, the stress paths for normally consolidated or weakly pre-consolidated soils (both for the drained and undrained case) follow the Roscoe Surface, which connects the points represented by the *NCL* and by the *CSL* in the space q versus p' versus v. Figure 2.28b illustrates this surface.

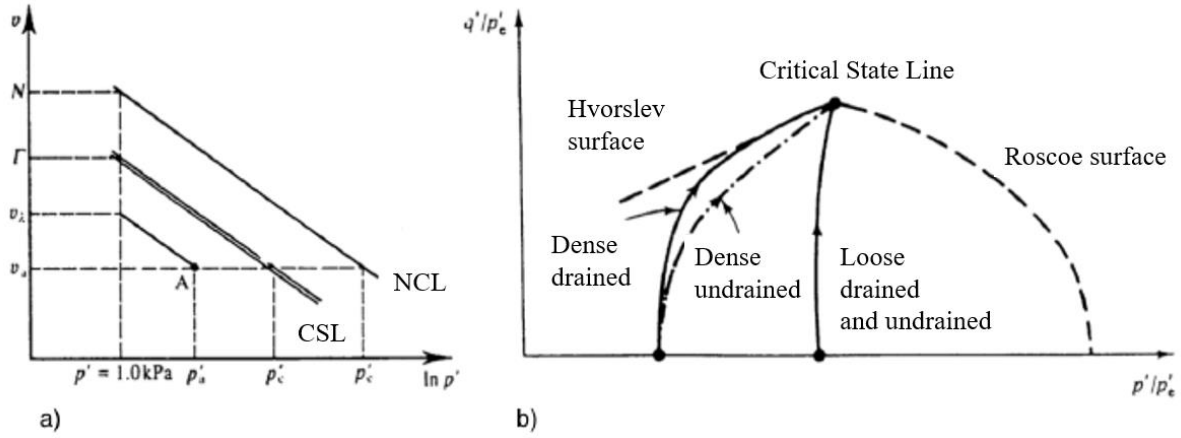

Figure 2.28. Representation of (a) normalization parameters (b) state limit surface normalized plane (source: Adapted from Atkinson, 1993).

Roscoe's surface corresponds to a state boundary, being impossible for a reconstituted soil to lie to its right in the normalized plane illustrated in Figure 2.28b. Likewise, a boundary state surface called the Hvorslev surface limits the states of heavily pre-compacted soils in the space q versus p' versus v. Figure 2.29 shows a representation of the complete state boundary surface in the normalized plane, where the *NCL* is represented by point A and the *CSL* by point B. Thus, it is necessary to determine the state of the soil with reference to the *NCL* for the application of the Critical State Theory. Figure 2.29 also shows this representation in space q versus p' versus v.

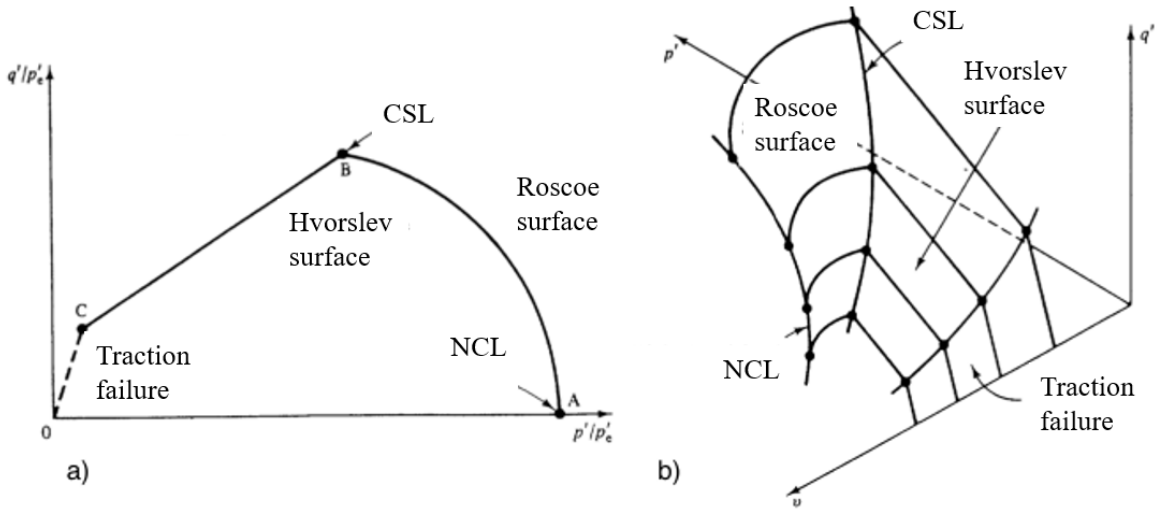

Figure 2.29. Complete state limit surface (source: Adapted from Atkinson, 1993).

Since the *CSL* is unique for a given soil, Been and Jefferies (1985) proposed the existence of a single physical parameter to measure the behavior of sand, the state parameter (ψ), which is the distance between the initial state and the ultimate state in the plane *e* versus *lnp'*, subtracting the value of the sample void ratio by the critical void ratio. The critical void ratio was identified by the practical concern to avoid failures caused by static liquefaction in hydraulic supply dams in the late 19th and early 20th centuries. The term "critical" means what is a safe void ratio for engineering works. Thus, it is sought to avoid the sudden transition from the drained condition without excessive pore pressure to a failure in an undrained condition by liquefaction (Been, 2016). The concept of critical void ratio was developed through the Casagrande tests, and it was later shown that it was dependent on the confining stress, configuring the *CSL*.

However, the stress-strain behavior of all engineering materials is ruled by The Plasticity Theory and, for various theoretical reasons, *CSL* was adopted as a central idealization in the Original Cam Clay and Modified Cam Clay models. Some authors see Cam Clay's model as overly idealized and totally useless for real soils in engineering practice. The problem became Cam Clay's link with Critical State theory and in this respect, a fundamental contribution was made by Been and Jefferies (1985). The tendencies in the behavior of sand reported in this work showed that the plasticizing surfaces (limits of elastic behavior), in general, are not located in the *CSL*, but evolve to the *CSL* with shear deformations. With respect to strength parameters, Table 2.2 shows typical values of peak and critical friction angles for some soil types.

Table 2.11. Conventional friction angles for soils (Source: Adapted from Been and Jefferies, 1985).

Soil type	Critical state friction angle (°)	Peak friction angle (°)
Gravel	30-35	35-50
Sand with gravel	28-33	30-40
Sand	27-37	32-50
Silt and Silty sand	24-32	27-35
Clay	15-30	20-30

2.4.1 Conventional soils

Critical State Theory, which is usually applied to understand the behavior of fine-grained soils, has recently been applied to sandy soils with some modifications (Coop and Lee, 1993; Been et al., 1991). However, reconstituted sands and clays behave differently when isotropically loaded. While the state of a normally isotropically consolidated clay falls on a LIC and is determined solely by the state of stress, the behavior of a sand, in turn, is not only determined by the state of stress, but also by its initial specific volume. For the same level of stress, a sand can be soft or dense, depending on the method used to mold the samples.

According to Atkinson and Bransby (1978), there will be different normal compression lines approximately linear and parallel to the p' axis for stress values below 700 kPa, which are totally dependent on the initial specific volume of the sample. From this level of stress, the *NCL* of the sand becomes unique and with a higher slope. Vesic and Clough (1968) performed isotropic compression tests on sands up to stress levels of 60 MPa, showing the convergence of these compression curves for different initial specific volumes. Therefore, sandy soils achieve a single *NCL* regardless of the initial specific volume provided the sample is loaded to a sufficiently high stress level. The position of the *NCL* and the *CSL* is different for different types of sand, being related to the breakage of the soil grains during loading and to the nature of the soil particles, which includes their granulometry, mineralogy and grain shape.

Been et al. (1991) also observed, an abrupt change in the slope of the *CSL* for stresses of 1000 kPa. According to the authors, this is indicative of the change in the shear mechanism at high stress levels, in which grain breakage becomes significant. This *CSL* breakpoint is possibly dependent on sand mineralogy, assuming it is a result of grain crushing. Analyzing the variation in the amount of fines in a previously washed sand, it was observed that with the increase of the fines content there was an increase in the slope of the *CSL* (Been and Jefferies, 1985).

In the case of silts, Phan et al. (2016) studied different percentages of fines, concluding that the greater amount of fines increased the slope of the *CSL* in the v plane versus lnp'. This behavior

can be explained by the fact that this increase in fines gradually increases the compressibility of the mixtures; since the samples were molded in an initial loose state.

Murthy et al. (2007) pointed out that the critical state is also governed by grain breakage. The less uniform the sand granulometry becomes and with increasing silt size particles, both the gradient and the intercept of the critical state line tend to decrease. At very high stresses, it was observed that the critical state line tends to curve and does not appear as a straight line in ν versus *lnp'* space.

Coop and Nocilla (2006) investigated the effect of particle breakage on the behavior of transitional soils. In the research, two poorly graded samples were used, one composed of sand and kaolin and the other of sand and smaller particles of quartz. Each sample was sieved after the tests and the sedimentation test was performed to evaluate the grain breakage. In the study, a greater amount of grain breakage was observed in samples with lower initial specific volume, which was justified by the presence of a matrix of fines between the sand particles. Thus, a larger initial specific volume reduces the possibility of contact between the sand particles and, consequently, the breakage of the grains, with the increase in tension transmitted through the fine grains. In addition to grain breakage, the content of non-plastic and plastic fines are also among the factors that interfere with the linearity of the critical state line.

The effect of a small fraction of non-plastic fines on the *CSL* of sands was first investigated by Been and Jefferies (1985). Later, other studies that also assessed the influence of fines during undrained monotonic loading (e.g., Lade and Yamamuro, 1997; Thevanayagam, 1998; Thevanayagam et al., 2002; and Ni et al., 2004). The studies showed that, for a given value of void ratio, the presence of non-plastic fines increases contraction, reducing the swelling of sands. It was observed that the addition of non-plastic fines in sands causes a clear downward translation of the *CSL* in *e* versus *p'* space. According to Coop and Nocilla (2014), research with soils of intermediate granulometry has shown that the Critical State Theory cannot be directly applied. Martins et al. (2002) verified, for reconstituted samples of poorly graded residual sand, that the normal compression curves show no conversion.

Recent advances have highlighted that many soils have so-called transitional behavior (Martins et al., 2001; Nocilla et al., 2006 and Shipton and Coop, 2012), in which different initial void ratio samples have non-unique *CSLs* in compression in shear, resulting in difficulty to characterize soil behavior through critical state theory. These soils normally present an intermediate granulometry between clean sands and clays.

Shipton and Coop (2012) addressed the behavior of transitional soils, in which consolidation and shear depend on the initial void ratio of the soil. Even under high confining stresses, the compression curves for different initial voids indices did not converge to a single *CSL*, as occurs in pure sands when their behavior is controlled by grain breakage. Furthermore, by subjecting a transitional soil to monotonic shear, a single *CSL* in the v versus lnp' plane has also not been achieved.

2.4.2 Mining tailings

Some recent research has shown that transitional behavior can also be found in specific types of tailings. Coop (2015) analyzed data from tailings trials from Stava (dam in Italy) and showed that silty tailings taken from different depths, but with similar granulometry, presented more than on *CSL*. However, Carrera et al. (2011) performed test with the same tailings, but with different granulometries, and found no indication of this transitional behavior.

Al-Tarhouni et al. (2011) performed simple shear tests on gold tailings and reported that the final states were dependent on the initial density, with no unique relationship between shear strength and void ratio, which may result from transitional behavior. Coop (2015) also reported transitional behavior in several other tailings. Generally, the break in *CSL* linearity is caused by the onset of particle breakage (Konrad 1998), which was also identified in the gold tailings tested by Bedin et al. (2012).

Thus, despite the *CSL* linearity being recommended, recent studies with soils of intermediate granulometry (e.g. mining tailings) show that the *CSL* can also present a steep slope for high stresses and low void ratios. Considering the results of triaxial tests obtained by Bedin (2010) with gold tailings, for stresses below 60 kPa there was a sharp decrease in shear stresses, and effective stresses equal to or close to zero for large deformations, which configures an unstable behavior. For greater confinement, the deflection stress grows with strains until it reaches a maximum strength value, followed by constant values for large strains. Since these tailings showed potential for liquefaction and possible grain breakage for stresses above 1000 kPa, a strong non-linearity of the *CSL* was observed, which was divided into three segments.

Praça (2019) obtained, for zinc tailings at different values of the initial specific volume (from 3.62 to 4.14), different isotropic compression curves approximately linear and almost parallel to the p' axis for stress values below 100 kPa. For stresses greater than 100 kPa, in samples with specific volume between 3.97 and 4.14, a tendency of unification of the *CSL* with a large slope was observed, similar to what occurs in sands (Figure 2.24). Extending the *CSL*, an $N = 5.17$ and a slope of the *NCL* (λ) equal to 0.24 were observed.

Comparing these results from Praça (2019) with those from Bedin (2010), it was observed that the parameters found for zinc tailings greatly exceed those for bauxite tailings, which can be justified by the fact that zinc tailings are a material with more compressible fines. Furthermore, in the critical state, the values of M = 1.09 and φ'_{EC} = 27.5° were obtained, values lower than those found for the peak trajectories. The *CSL* plotted for the samples led to values of Γ = 4.85 and slope (λ) corresponding to the slope of the *NCL*, in the value of 0.24. In the experiments by Praça (2019), the non-linearity of the *CSL* was justified by the influence of the fines content or by the occurrence of grain breakage during the shear of the samples. To carry out this analysis, granulometry tests were performed for samples of the natural material and after being sheared at effective stresses of 1000, 2500 and 4000 kPa.

Li and Coop (2018) analyzed three types of iron ore tailings with different granulometries (*PO*, *MB*, and *UB*); *PO* being the finest, *MB* a medium granulometry, and *UB* the coarsest. *M* values in the critical state were 1.40, 1.36 and 1.41 and effective friction angle values in the critical state were 34.6˚, 33.7˚ and 34.8˚, for samples *PO*, *MB* and *UB*, respectively. The similar friction angles indicate that the different grain size distribution presented little or no influence over the strength parameters on the critical state; probably due to the similar mineralogy and the particle shape of all specimens. The *NCLs* could not be easily identified even at the end of isotropic compression at higher stresses, and their tendency was estimated. The difficulty of identifying unique *NCLs* stems from the slow convergence in compression. In the critical state, however, the *CSL* was observed without the slow convergence observed in consolidation. The *CSL* of the *PO* material is still a straight line, even at low p' levels; which indicates similar behavior to clays, even though this material is not plastic. As the particle size increases from *MB* to *UB* materials, *CSLs* tend to become more curved at lower stresses, which is typical sand behavior. Since the curvature of the *CSLs* may indicate the beginning of particle breakage (Konrad 1998), Li and Coop (2018) analyzed the size distributions of sheared tailings at effective stress levels of 6 MPa and concluded that there was only a small amount of particle breakage for *UB* and *MB* materials and no particle breakage was observed for *PO* material. Authors concluded that very small amounts of rupture tend to reinforce the conclusion of Carrera et al. (2011); particle breakage is not a necessary feature of a curved *CSL*.

From the information provided in this subsection, it can be stated that the behavior of mining tailings seems to be influenced by structuring and aging effects, in addition to characteristics of void ratio and stress level, thus it becomes essential to study these types of material under different molding conditions and stresses.

3 MATERIALS, METHOD, AND RESEARCH APPROACH

This chapter scrutinizes the materials used in the research, the experimental program and method applied to carry out the tests, the design of experiments and their levels of complexity, the preparation of the specimens, and details relevant to the execution of the tests. In this sense, the chapter was divided in (i) materials and characterization approaches; (ii) methods and equipment; and (iii) research approaches.

3.1 MATERIALS

This subsection aims to provide information on the characterization of the raw materials applied in this research, as well as, the approaches behind their characterization methods.

3.1.1 Iron ore tailings

Iron ore tailings are abundant materials in the Brazilian scenario. Therefore, this research, several mining companies were contacted for the acquisition of the material. A Southeastern Brazilian company[1] was willing to respond to the research requirements and provided the material to be studied. The iron ore tailings utilized in this research can be seen in Figure 3.1.

Figure 3.1. Iron ore tailings utilized in this research.

The physical characterization of the iron ore tailings (Figure 3.2 and Table 3.1) was evaluated by determining their grain size distribution [ASTM D7928 (ASTM, 2017a)], consistency limits [ASTM D4318 (ASTM, 2017b)], and specific weight of grains [ASTM D854 (ASTM, 2014)].

[1]In view of issues beyond the control of the researcher, the name of the company supplying the materials must be kept confidential. There was a request by the institution and for ethical and legal reasons its name will remain veiled.

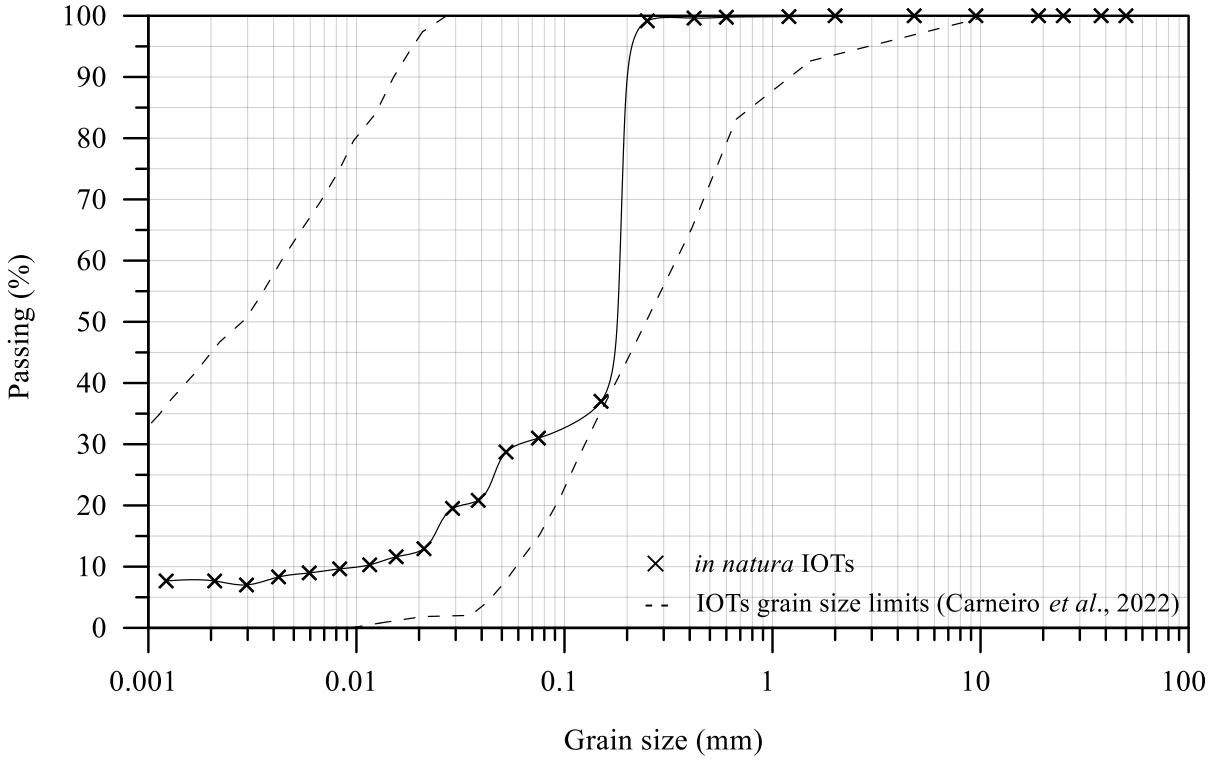

Figure 3.2. Grain size distribution - iron ore tailings.

Table 3.1. Physical properties - iron ore tailings.

Property	Iron ore tailings
Liquid limit (%)	-
Plastic limit (%)	-
Plastic index (%)	Nonplastic
Specific unit weight of grains (g.cm^{-3})	2.72
Medium sand (0.2mm < diameter < 0.6mm) (%)	30.0
Fine sand (0.06mm < diameter < 0.2mm) (%)	41.0
Silt (0.002mm < diameter < 0.06mm) (%)	22.0
Clay (diameter < 0.002mm) (%)	7.0
USCS classification (ASTM, 2017)	Silty sand (*SM*)

The iron ore tailings presented a non-plastic behavior, and based on their grain size distribution they were classified as a silty sand (*SM*), in accordance with the Unified Classification System (ASTM, 2017). The grain size distribution presented for the iron ore tailings of this research is within the limits found in literature for this material, as exposed in Item 2.2.2.1.

The mineralogical composition (Figure 2) was determined using X-ray diffraction (*XRD*), with a WDS spectrometer, equipped with a Rh X-ray tube, model RIX 2000 from Rigaku; the analysis was performed on a Siemens X-ray diffractometer (BRUKER AXS), model D-5000

(θ-2θ), equipped with a fixed copper anode tube (λ = 1.5406 Å) and operating at 40 kV and 25 mA in the primary beam and curved graphite monochromator in the secondary beam. In addition, the Reference Intensity Ratio Method (*RIR*) was used for the semi-quantification of the phases present in the sample.

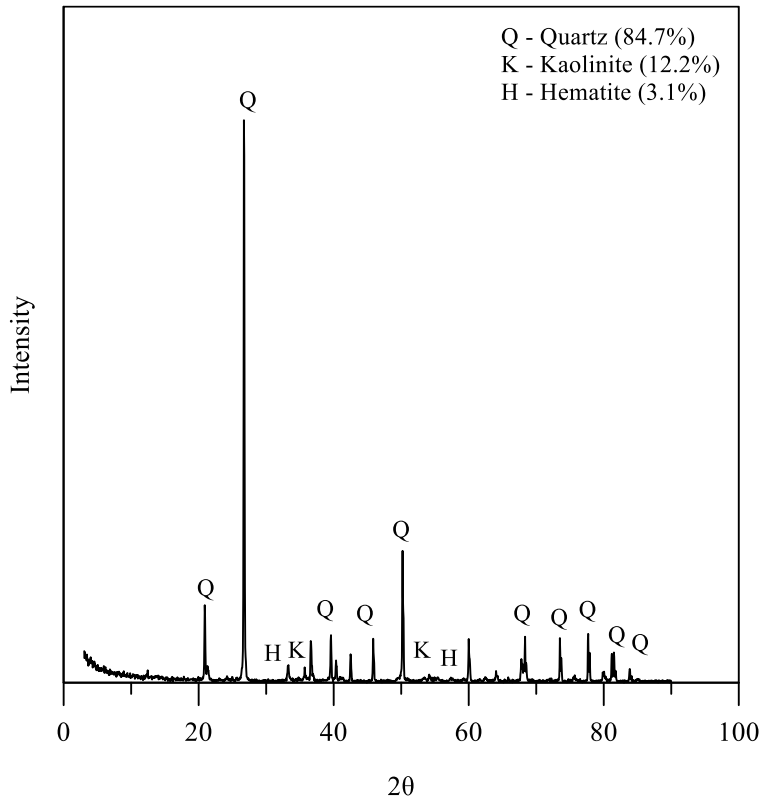

Figure 3.3. XRD - iron ore tailings.

From the mineralogical composition analysis, it was possible to see that the iron ore tailings were mainly composed of three minerals: quartz – SiO_2 (84.7%), kaolinite – $Al_2Si_2O_5(OH)_4$ (12.1%), and hematite – Fe_2O_3 (3.1%). The low quantities of hematite indicate that this material has been extensively processed. Similar mineralogical compositions have also been found by several authors (Giri et al., 2011b; Lu et al., 2020; Sahu et al., 2022; Yi et al., 2009). In addition, these results allude to the origin of the materials, as exposed in Item 2.1.

The elemental composition (Table 3.2) was determined using X-ray fluorescence spectrometry (*XRF*), through a quantitative analysis with a calibration curve based on tabulated rock patterns from Geostandards.

Table 3.2. Elemental composition - iron ore tailings.

Material	Si	Al	Ti	Fe	Mn	Mg	Ca	Na	K	P	Cl	Cd	S	Total
IOTs	88.98	1.56	0.05	9.12	0.05	0.14	-	-	0.02	0.08	-	-	-	100

As expected, the iron ore tailings were majorly composed of silicon (88.98%), followed by iron (9.12%), and aluminum (1.56%). This result corroborates the mineralogical composition found in the *XRD* analysis, in which minerals composed of silicon (quartz), iron (hematite) and aluminum (kaolinite) were identified. Furthermore, the elemental composition results are in accordance with the ones found in the literature for granular *IOTs*, as exposed in Item 2.2.2.3.

The morphology of the iron ore tailings was explored through scanning electron microscopy (SEM) analysis, with an electron beam of 20 kV voltage and gold-coated samples (Quorum Q150 and JSM-6610 models), at magnifications of 100, 500, 1,000, 2,000, and 5000 times. Figure 3.4 shows the results of the SEM analysis for the iron ore tailings.

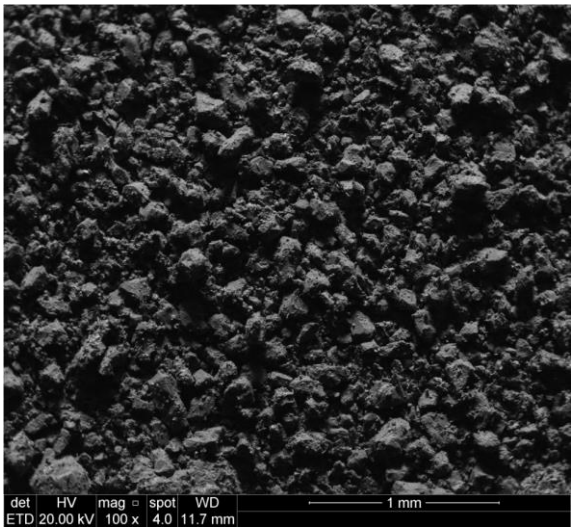

(a)

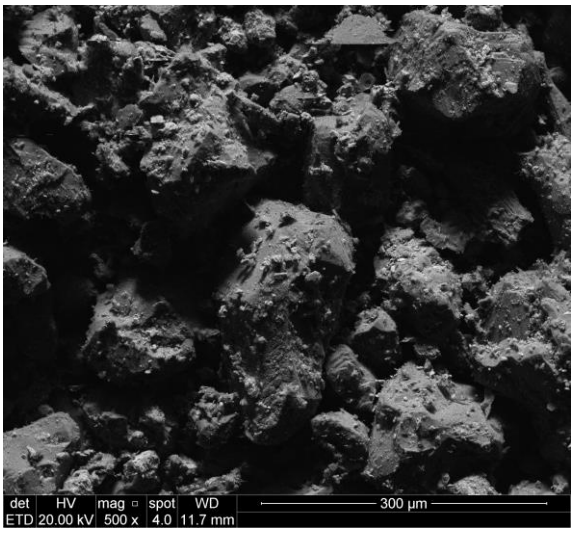

(b)

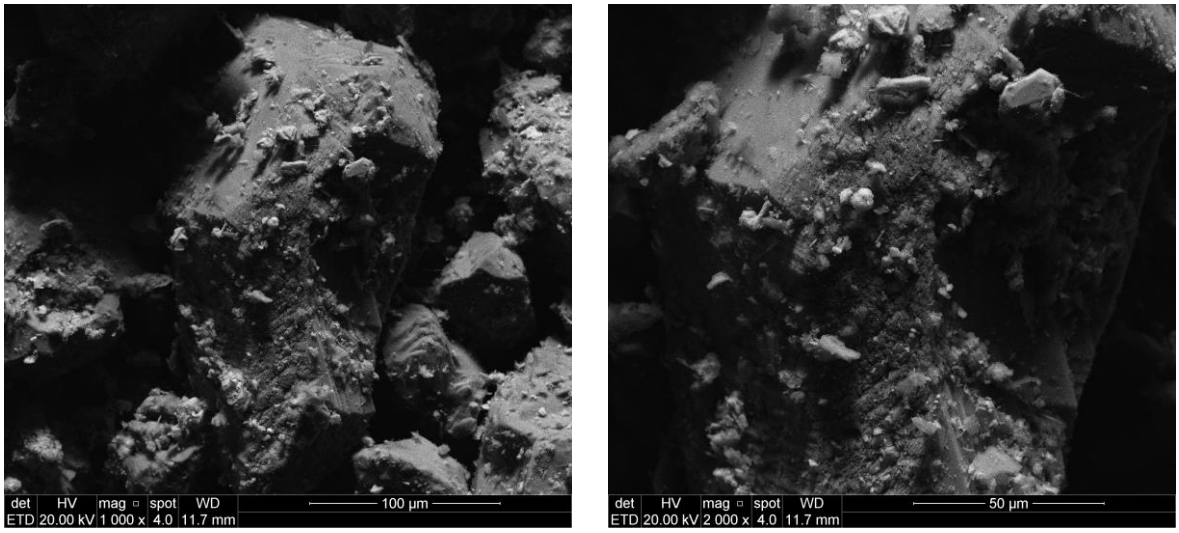

(c) (d)

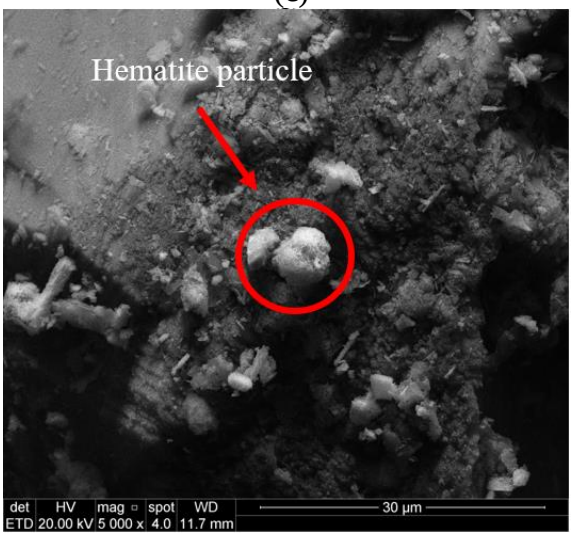

(e)

Figure 3.4. SEM analysis – iron ore tailings: (a) 100x magnification; (b) 500x magnification; (c) 1000x magnification; (d) 2000x magnification; (e) 5000x magnification.

From the data exposed in Figure 3.4 it is possible to see that the morphology of the iron ore tailings is basically composed of smaller agglomerated of hematite particles on the surface of regular flat large quartz particles. A similar behavior has been evidenced for several authors for different granular *IOTs* (Etim et al., 2017; Reid et al., 2022; Reid and Fanni, 2022; Sahu et al., 2022; Zhang et al., 2020; Zheng et al., 2016).

In addition to the basic characterization, the iron ore tailings were also characterized regarding their environmental classification. This test was carried out in accordance with the procedures indicated in NBR 10.005 (ABNT, 2004). Metals were analyzed using the Inductively Coupled Plasma Atomic Emission Spectrometry Technique (*ICP-AES*) and the other substances (volatiles) were analyzed using the Standard Method for Analyzing Water and Sewage (APHA,

AWWA and WEF, 2012). The solubilization test was used in order to characterize the solubility. For that, the procedures indicated in NBR 10.006 (ABNT, 2009) were followed. As with the samples of the leachate extract, the metals present in the solubilized extract were studied using the Inductively Coupled Plasma Atomic Emission Spectrometry Technique and the volatiles using the Standard Method of Analysis of Water and Sewage (APHA, AWWA and WEF, 2012). In this sense, Table 3.3 presents the lixiviation results while Table 3.4 presents the solubilization ones.

Table 3.3. Lixiviation results - iron ore tailings

Element	Concentration (mg/L)	Limit NBR 10,005 (ABNT, 2004)
Ag	0.00	5
Al	0.00	-
As	0.00	1
Ba	0.00	70
Cd	0.00	0.5
Cr	0.00	5
Cu	0.00	-
Fe	0.00	-
Hg	0.00	0.1
Mn	0.00	-
Na	17.33	-
Pb	0.00	1
Se	0.00	1
Zn	0.00	-
Ag	0.00	5

Table 3.4. Solubilization results - iron ore tailings

Element	Concentration (mg/L)	Limit NBR 10,005 (ABNT, 2004)
Ag	0.000	0.05
Al	0.000	0.2
As	0.000	0.01
Ba	0.000	0.7
Cd	0.000	0.005
Cr	0.000	0.05
Cu	0.000	2
Fe	0.081	0.3
Hg	0.000	0.001
Mn	0.002	0.1
Na	0.275	200
Pb	0.000	0.01
Se	0.003	0.01
Zn	0.000	5
Ag	0.000	0.05

From the data exposed in Table 3.3 (lixiviation) and Table 3.4 (solubilization), it was possible to classify the iron ore tailings as inert and non-hazardous waste (class IIB) in accordance with

NBR 10.005 (ABNT, 2004). In other words, the material presents no harmful substances such as heavy metals or chemicals, not chemically or biologically reactive. Similar results have also been found by different authors (Cristelo et al., 2020; Garbarino et al., 2020; Segui et al., 2023), in which granular *IOTs* were classified as inert and non-hazardous.

3.1.2 Portland cement

High initial strength Portland cement (type-III) was used as the stabilization agent for this research. The material was chosen due to its accelerated strength gain at low curing times and had a specific gravity of 3.15 g/cm³. The cement utilized in this research can be seen in Figure 3.5.

Figure 3.5. High initial strength Portland cement (type III)

3.1.3 Water

Distilled water was utilized for the molding process of the specimens and the saturation phase of the triaxial tests. Considering that the material for this research was provided in a low moisture condition, it was not possible to mold the specimens with the liquor from the tailing facility. This liquor consists of the liquid fraction from the processing of iron ores. Previous research has reported the application of liquor in the molding of specimens (Tomasi, 2018) and during percolation and saturation in triaxial testing (Bedin, 2010). However, due to the above-mentioned limitations, only distilled water was applied in the molding, percolation, saturation, and application of backpressure steps in the specimens of this research.

3.2 METHOD

This subsection provides information regarding the methods and equipment utilized to explore the behavior of the materials applied in this research. In this sense, the following subdivision

was proposed: (i) Unconfined compressive strength test; (ii) Initial shear modulus test; (iii) Hydraulic conductivity test; (iv) Compressibility test; (v) Triaxial compression test; and (vi) Grain breakage analysis.

3.2.1 Unconfined compressive strength test

This test was performed following the procedures of NBR 5739 (ABNT, 2018). The molding of the specimens was performed with a three-way mold of 5 cm in diameter and 10 cm in height. The preparation of the specimens was carried out through the following procedures: weighing, mixing, compacting, demolding, enveloping, storage, and curing. After weighing all materials (soil, cement, and water) with a resolution of 0.01 g, the dry materials (i.e. iron tailings and cement) were mixed until a uniform color was acquired; then, water was added to the process and mixing continued until homogeneity was obtained. After the mixing process, the specimens were produced through a three-layer compaction at the previously established moisture content and dry unit weight. Upon completion of the molding process, specimens were extracted from the mold and their mass and dimensions (diameter and height) were recorded with a resolution of 0.01 g and 0. 1 mm, respectively. Then, specimens were enveloped in hermetic bags to avoid significant variations in moisture content. Finally, specimens were then stored for the proposed curing period. The aforementioned process can be seen in Figure 3.6.

(a) (b)

(c)

(d)

(e)

(f)

(g)

(h)

(i)

(j)

(k) (l)

Figure 3.6. Molding procedures: (a) iron ore tailings; (b) 5x10cm mold; (c) initial of the molding procedure; (d) cement addition; (e) homogenization of the dry materials; (f) water addition; (g) homogenization of the wet materials; (h) weighing of the first layer; (i) molding of the specimen; (j) demolding of the specimen; (k) weighing of the specimen; (l) measurement of the specimen.

Specimens were considered suitable for testing if they met the following criteria: degree of compaction ± 1%; moisture content ± 0.5%; diameter ± 0.5 mm; and height ± 1 mm. After the stipulated curing period, specimens were removed from the hermetic bags 24 hours before testing and placed in immersion in water at room temperature to minimize the possible suction effects.

An automatic press machine was utilized for the unconfined compressive strength tests, equipped with pressure cells of 5 kN, 10 kN, and 20 kN capacity (Figure 3.7). The deformation rate was set at 1.14 mm per minute. Also, as an acceptance criterion, it was stipulated that the individual strength of the duplicates should not deviate more than 10% from the average strength.

Figure 3.7. Automatic press machine.

The unconfined compression strength (*qu*) was defined by the relation between the maximum force (*F*) and the area of the specimen (*Ac*), according to Equation (3.1).

$$qu = {}^{F}\!/_{A} \tag{3.1}$$

Unconfined compressive strength tests results were expressed as a function of the porosity/cement index proposed by (Consoli et al., 2007) and defined by Equations (3.2) and (3.3).

$$\eta = 100 - 100 \left\{ \left[\frac{\gamma_d}{\frac{IOT}{100} + \frac{PC}{100}} \right] \left[\frac{\frac{IOT}{100}}{\gamma_{s_{IOT}}} + \frac{\frac{PC}{100}}{\gamma_{s_{PC}}} \right] \right\} \tag{3.2}$$

$$C_{iv} = \frac{V_C}{V} = \frac{{}^{m_C}\!/_{\gamma_{s_C}}}{V} \tag{3.3}$$

Porosity (η) is a function of the dry unit weight (γ_d) and unit weight of solids (γs_{IOT} and γs_{PC}) of the iron ore tailings and cement. The cement content (*Civ*) results from the volume occupied by Portland cement divided by the total volume of the sample. This index allows the unification of

all experiments in a single relation, resulting in a rational dosage methodology for cemented soil mixtures. However, such equations are valid for the cemented mixtures studied herein and are only functional if the boundary conditions of the applied variables are ensured.

3.2.2 Initial shear modulus test

The initial shear modulus (*G0*) of an ideal elastic isotropic medium can be obtained by measuring the velocity of a shear wave (*Vs*) passing through its body [ASTM D8295 (ASTM, 2019)]. This parameter can be estimated through the relationship shown in Equation (3.4, where ρ represents the bulk density of the tested specimen.

$$G0 = {}^{\rho}/_{Vs^2} \tag{3.4}$$

For this research, an ultrasonic pulse device was used to measure the travel time (*ts*) of a shear wave through the cemented tailings. This wave was emitted at a frequency of 150 kHz using special transducers that were coupled to the test samples by means of a special shear gel. This device and its pieces are shown in Figure 3.8.

Figure 3.8. Pundit Lab ultrasonic device

Prior to the *ts* assessment, the travel time of a compressive wave (*tp*), emitted at a frequency of 54 kHz, was also measured. Figure 3.9 exhibits a typical outcome of the ultrasonic pulse velocity test using the Pundit Lab+ ® software. As this test is non-destructive, it was carried out on the same specimens that were submitted to the unconfined compressive strength tests, right after the specimens were retrieved from the submersion process.

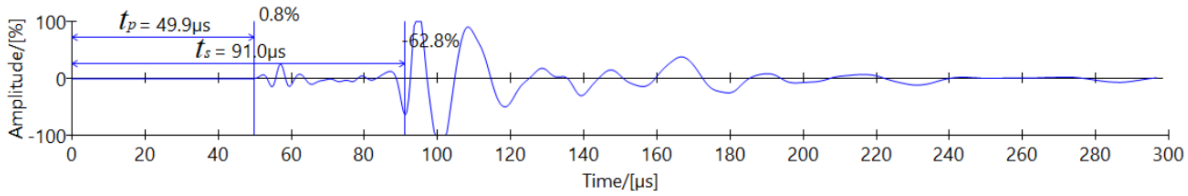

Figure 3.9: Typical signal using software Pundit Lab+ ®.

As for the unconfined compressive strength tests, the initial shear modulus test results were also correlated with the porosity/cement index, thoroughly discussed on Item 3.2.1.

3.2.3 Hydraulic conductivity test

Hydraulic conductivity tests were performed in a flexible wall permeameter. The equipment consists of a triaxial chamber, a pressure application system with a compressed air network inlet, and monitoring and data acquisition through an analog/digital converter (data logger) connected to a computer. Such equipment was developed by Cruz (2004), in accordance with D-5084-90 (ASTM, 2016b), as schematically shown in Figure 3.10.

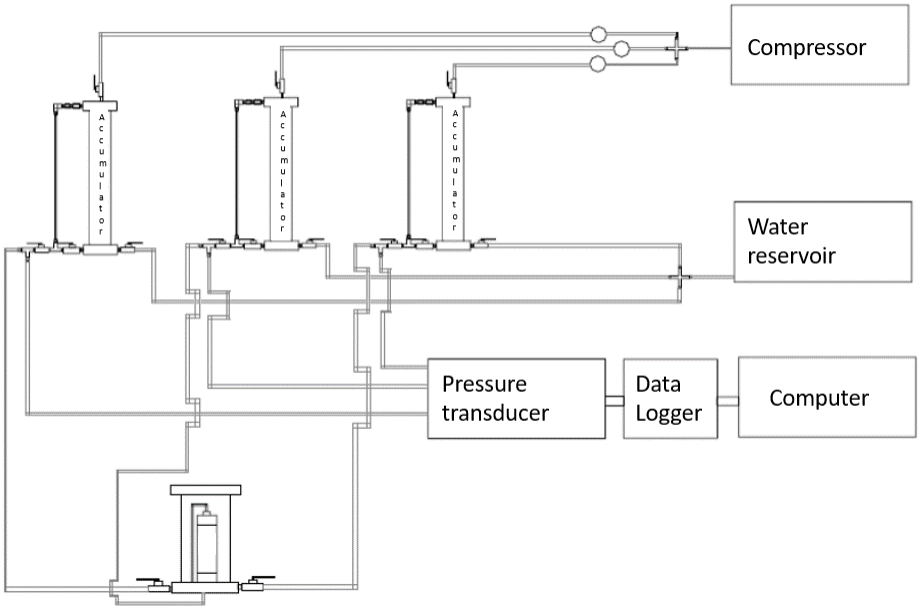

Figure 3.10. Hydraulic conductivity equipment scheme.

The molding of hydraulic conductivity specimens followed the same procedures presented on item 3.2.1 for the unconfined compressive strength specimens. As for the test procedure, the following steps were followed: (i) sample allocation; (ii) saturation; (iii) percolation; and (iv) hydraulic conductivity measurement. For the sample allocation step, the specimen was placed

inside the chamber on the pedestal, between two porous stones and filter paper (in order to avoid clogging the porous stone by possible fine particle that may be carried by the water flow), the lateral confinement was achieved through a latex membrane, which is fixed to the pedestal and the top-cap, with O-rings. After assembling this set, the chamber was filled with water and sealed. A summary of the aforementioned steps can be seen on Figure 3.11.

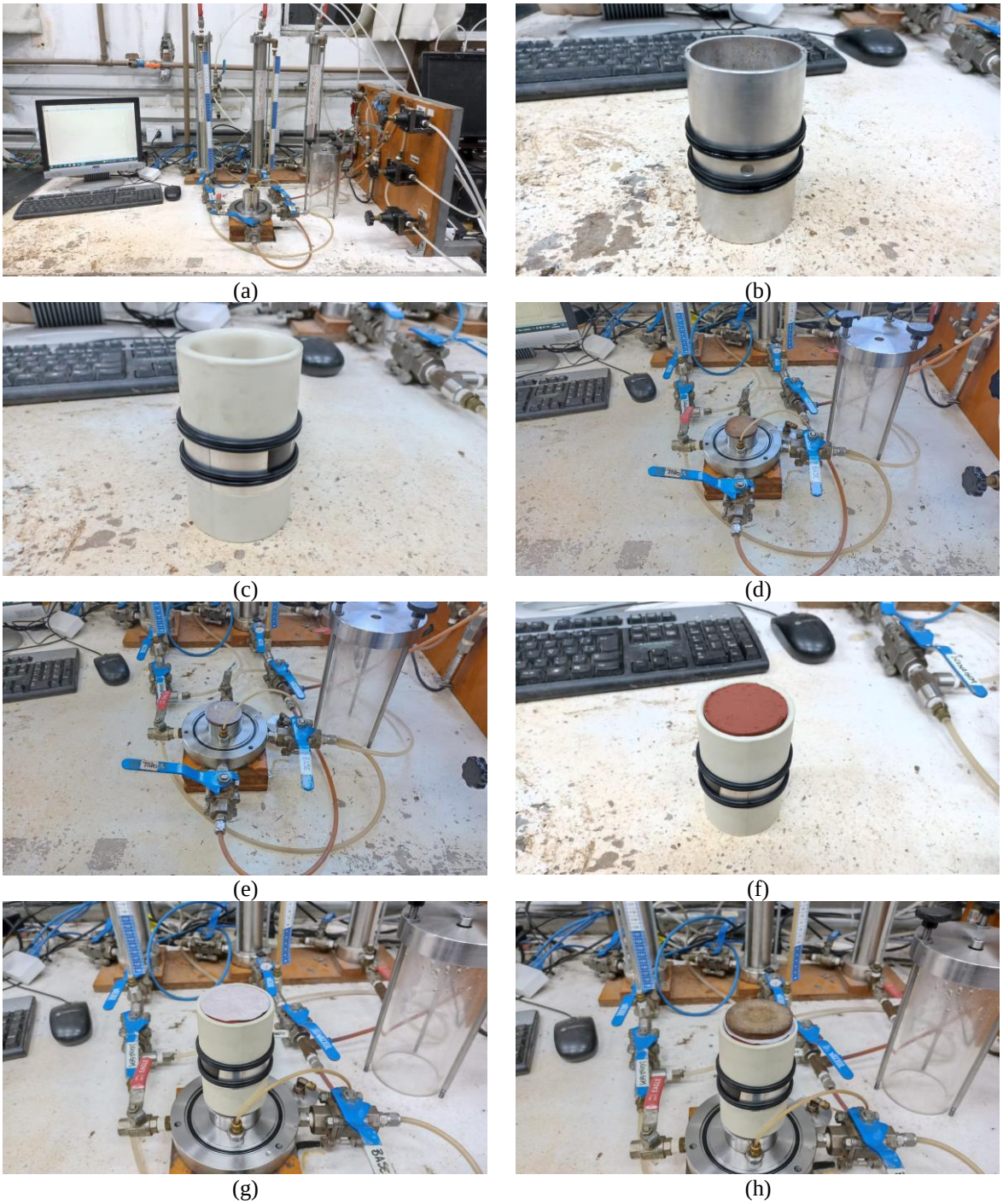

(a) (b) (c) (d) (e) (f) (g) (h)

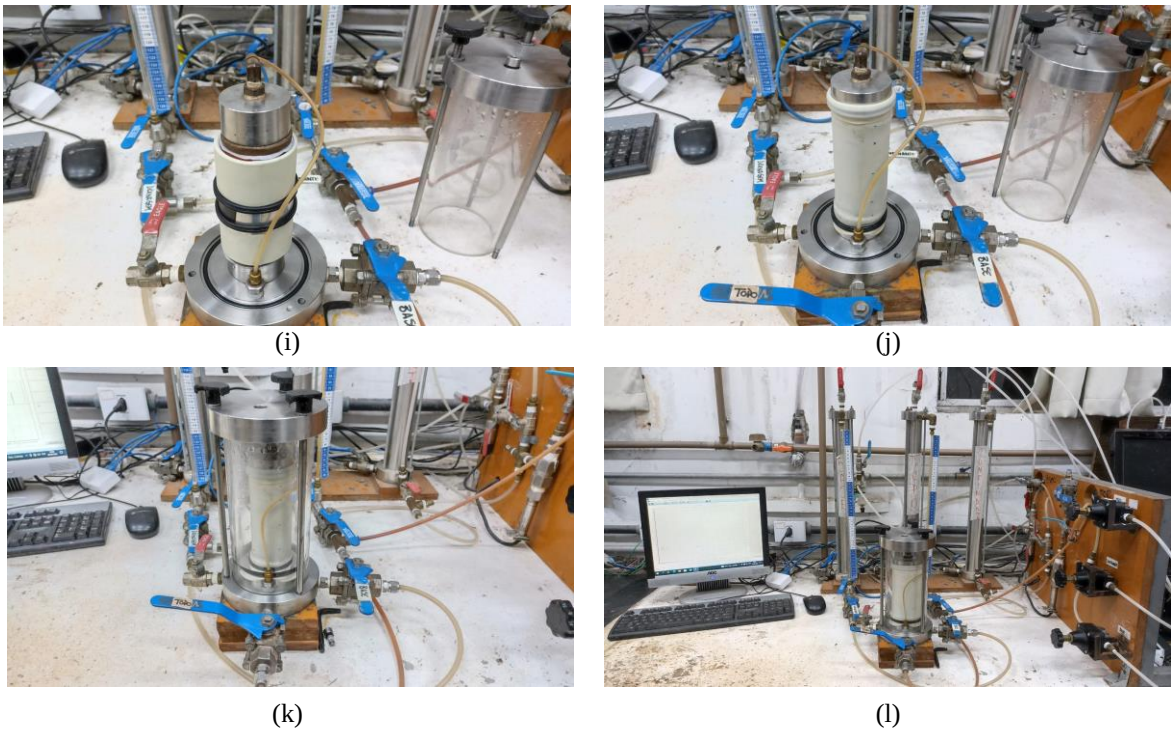

(i) (j)

(k) (l)

Figure 3.11. Hydraulic conductivity equipment: (a) unassembled test; (b) O-rings positioning; (c) membrane positioning; (d) bottom porous stone allocation; (e) bottom filter paper allocation; (f) sample allocation on the membrane; (g) top filter paper allocation; (h) top porous stone allocation; (i) sample allocation; (j) top cab and membrane allocation; (k) chamber water filling; (l) final assemble of the test.

As for the percolation step, its objective consists in eliminating air-filled voids, filling them with water, facilitating the later saturation of the specimen. A back pressure of 15 kPa (height of the suspended reservoir) was applied to the bottom of the sample, while the top was open to the atmosphere. A confining pressure of 35 kPa (20 kPa effective stress) was also applied to the sample, preventing preferential flow between the specimen and the latex membrane. Water percolation was continued until a volume equal to twice of the estimated volume of voids of the specimen was achieved.

During the saturation stage, gradual increments of 50kPa were applied both in the confining stress and in the back pressure, while maintaining an effective stress of 20 kPa. A new increment was only made after the back pressure applied to the top of the specimen was the same as the one read at the base of the specimen (i.e., after the pressure was equalized throughout the specimen). The degree of saturation was verified through parameter *B* (Skempton, 1954). This parameter is defined by the ratio between the pore-pressure variation and the corresponding variation of the applied confining stress, measured at each stress increment. In general, for conventional geotechnical materials, when the specimen is saturated, the value of *B* is equal or very close to 1. However, when soil incompressibility becomes high, as is the case of very

dense and cemented soils, the value of parameter *B*, in the saturation condition, is normally less than 1 (Lambe and Whitman, 1979). The *B* values achieved in this research ranged from 0.9 to 0.99 (Table 3.5), indicating that all specimens can be considered saturated.

Table 3.5. Skempton parameter B for the hydraulic conductivity tests.

Specimens*	B
SD-WS-C	0.93
SD-OMM-C	0.92
SD-OMR-C	0.95
SD-DS-C	0.95
MO-WS-C	0.93
MO-OMM-C	0.90
MO-OMR-C	0.92
MO-DS-C	0.94
SD-WS-U	0.99
SD-OMM-U	0.99
SD-OMR-U	0.99
SD-DS-U	0.99
MO-WS-U	0.99
MO-OMM-U	0.99
MO-OMR-U	0.98
MO-DS-U	0.99

*W-X-Y: Compaction energy [standard (SD) or modified (MD)]-Initial moisture content [dry side (DS), optimum moisture content at maximum density (OMM), optimum moisture content at reduced density (OMR), and wet side (WS)]-Cement content [uncemented (U) or cemented (C)].

The hydraulic conductivity tests of this research were carried out with a constant hydraulic load (i.e., Darcy's law is valid). The average flow was given by the quotient of the total volume of water passing through the specimens and the hydraulic conductivity was estimated through Equation (3.5). Where: *k* is the hydraulic conductivity; *L* is the length of the specimen; *Q* is the water flow rate passing through the sample; *A* is the cross-sectional area of the specimen; *t* is the flow duration; and *h* is the hydraulic head.

$$k = {}^{LQ}\!/_{Ath} \tag{3.5}$$

The volume of water passing through the specimen in the interval between readings is obtained through the difference in level in the base and top accumulators, observed in the graduated tubes. As the standard indicates, the volume adopted was the arithmetic mean between the inflow and outflow volumes. Unfortunately, it is not possible to measure the deformation of the specimen, thus, both *A* and *L* were considered constant during the test. The hydraulic head is determined by the difference between the stresses maintained at the base and at the top of the specimen and must be kept constant during the test. In this study, all tests were performed with

400 kPa at the base and 405 kPa at the top. The hydraulic head was maintained constant for all tests at a value of 5. In addition to the readings from the graduated tubes, the test temperature was also measured and the hydraulic conductivity was corrected.

3.2.4 Compressibility test

The compressibility test was performed following the procedures of ASTM D2435 (ASTM, 2011), aiming to determine the magnitude and rate of consolidation of the iron ore tailings when restrained laterally and drained axially while subjected to incrementally applied controlled-stress loading. Time-deformation readings were conducted on all load increments. Successive load increments were applied after 100% primary consolidation was reached. This procedure provides the compression curve with explicit data to account for secondary compression, the coefficient of consolidation for saturated materials, and the rate of secondary compression. Measurements were made of the change in the specimen height and these data were used to determine the relationship between the effective axial stresses and void ratio or strain.

The molding of the specimens was performed with a mold of 5 cm in diameter and 2 cm in height. The preparation of the specimens was carried out through the same procedures presented on item 3.2.1 for the unconfined compressive strength specimens; however, using only one compaction layer. The strain rate was verified using linear variable differential transformers (*LVDT*). Data acquisition is performed by an acquisition board controlled by LabView ® software.

As for the procedure, the consolidometer was assembled in such a manner as to prevent a change in water content or swelling of the specimens. Porous disks and filters were utilized and prepared using the test water. Then, the ring was assembled with the specimen, porous disks, and filter screens in the consolidometer. After assembling, a setting load of about 5kPa was applied in the specimen; immediately after the application of the seating load, the deformation indicator was adjusted and the deformation reading was initiated. The standard loading schedule of this research was 50 kPa, 100 kPa, 200 kPa, 400 kPa, 800 kPa, 1600 kPa, 3200 kPa, and 6400 kPa. As for the unloading schedule, 1600 kPa, 400 kPa, and 100 kPa stresses were utilized. Figure 3.12 shows the abovementioned procedures.

Figure 3.12. Compressibility test: (a) oedometric specimen; (b) chamber and porous stone; (c) bottom filter paper allocation; (d) specimen allocation; (e) chamber ring allocation; (f) bottom filter paper allocation; (g) top cap allocation; (h) general view of the test; (i) saturated specimens; (j) linear variable differential transformer.

The calculation procedures are divided in to two groups, specimen physical properties and deformation and stress calculations.

For the specimen's physical properties, the following parameters should be calculated: the dry mass, initial and final water content, initial dry density, volume of solids, equivalent height of solids, initial and final void ratio, and initial and final degree of saturation. The dry mass of the specimen is calculated according to Equation (3.6), where *Md* is the dry mass of the specimen, M_{Tf} is the moist mass of the specimen after test, and w_{fp} is the water content wedge of specimen taken after test.

$$Md = {M_{Tf}}/{1+w_{fp}} \tag{3.6}$$

The initial and final water content are calculated through Equations (3.7) and (3.8), respectively; where w_o is the initial water content, w_f is the final water content, *Md* is the dry mass of the specimen, M_{Tf} is the moist mass of the specimen after test, and M_{To} is moist mass of the specimen before testing.

$$w_o = \frac{M_{To} - M_d}{M_d} \times 100 \tag{3.7}$$

$$w_f = \frac{M_{Tf} - M_d}{M_d} \times 100 \tag{3.8}$$

The dry density of the specimen in calculated in accordance with Equation (3.9); where ρ_d is the dry density of specimen, *Md* is the dry mass of the specimen, and V_o is the initial volume of the specimen.

$$\rho_d = {M_d}/{V_o} \tag{3.9}$$

The computation of the volume of solids is done through Equation (3.10); where V_s is the volume of solids, *Md* is the dry mass of the specimen, *G* is the specific gravity of the solids, and ρ_w is the density of water filling the pore space.

$$V_s = {M_d}/{G\rho_w} \tag{3.10}$$

The height of solids is defined considering that the cross-sectional area of the specimen is constant throughout the test, defined in accordance with Equation (3.11); H_s is the height of solids, V_s is the volume of solids, and A is the specimen area.

$$H_s = {V_s}/{A} \tag{3.11}$$

The initial and final void ratio are calculated following Equations (3.12) and (3.13); where e_o is the initial void ratio, e_f is the final void ratio, H_o is the initial specimen height, H_s is the height of solids, and H_f is the final specimen height.

$$e_o = \frac{H_o - H_s}{H_s} \times 100 \tag{3.12}$$

$$e_f = \frac{H_f - H_s}{H_s} \times 100 \tag{3.13}$$

Lastly, the initial and final degree of saturation are calculated in accordance with Equations (3.14) and (3.15); where S_o is the initial degree of saturation, M_{To} is moist mass of the specimen before testing, Md is the dry mass of the specimen, ρ_w is the density of water filling the pore space, A is the specimen area, H_o is the initial specimen height, H_s is the height of solids, and H_f is the final specimen height, M_{Tf} is the moist mass of the specimen after test, and S_f is final degree of saturation.

$$S_o = \frac{M_{To} - M_d}{A\rho_w(H_o - H_s)} \times 100 \tag{3.14}$$

$$S_f = \frac{M_{Tf} - M_d}{A\rho_w(H_f - H_s)} \times 100 \tag{3.15}$$

For the deformation and stress calculations, the following parameters were calculated: change in specimen height and void ratio. For each deformation reading, the change in specimen height was calculated according to Equation (3.16); where ΔH is the change in specimen height, d is the deformation reading at various times in test, d_o is the initial deformation reading, and d_a is the apparatus deformation correction. On the other hand, the void ratio was calculated according to Equation (3.17).

$$H = H_o - \Delta H \tag{3.16}$$

$$e = \frac{H - H_s}{H_s} \tag{3.17}$$

Finally, the total axial stress was calculated in accordance with Equation (3.18).

$$\sigma_a = \frac{P + M_a g}{A} \times 10 \tag{3.18}$$

Where σ_a is the total axial stress, P is the applied force, M_a is the mass of apparatus resting on specimen, A is the specimen area, and g is the acceleration due to gravity.

3.2.5 Triaxial compression test

The triaxial equipment utilized for the monotonic triaxial tests was developed at the Laboratory of Geotechnical Engineering and Environmental Geotechnology (*LEGG*) of Federal Universisity of Rio Grande do Sul (*UFRGS*), as depicted by Marques (2016). The equipment was dimensioned to reach confining stresses of 10 MPa; however, due to technical limitations, it can only fully operate at confining stresses of up to 4 MPa. Also, the equipment has voltage control and automated data acquisition; a schematic drawing of the equipment can be seen in Figure 3.13.

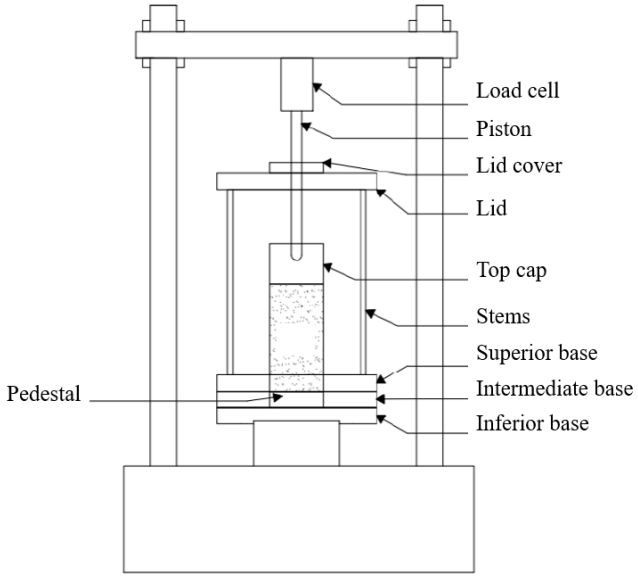

Figure 3.13. Schematic drawing triaxial test (Adapted from Marques, 2016).

Its operation consists in the application of a hydrostatic state of stress and an axial load on a cylindrical specimen of soil. The specimen is placed inside the test chamber, being surrounded by a latex membrane that creates an interface, allowing the application of two levels of stress on the specimen: the confining pressure ($\sigma 3$) and the back pressure (u). The chamber is then filled with water, on which pressure is applied, generating the confinement on the specimen. This stress acts in all directions, including the vertical direction. Back pressure is applied directly to the sample through the base pedestal or through the top of the sample (top cap). Finally, axial loading is applied by means of a piston that penetrates the chamber. The measurement of the applied load is carried out through a load cell connected to the piston. Dividing the force resulting from the axial loading by the area of the sample, the deviation stress or deviatory stress (q) is obtained; consisting of the difference between the axial stress ($\sigma 1$) and the radial ($\sigma 3$) applied to the specimen. Deflection stress is usually presented as a function of axial (εa) or distortional (εs) strain during loading (Figure 3.14a). Failure is reached when the deviator stress reaches its maximum value. The testing of specimens under different confining stresses, allows the determination of a failure envelope according to the Mohr-Coulomb criterion, through the tracing of the other Mohr circles (Figure 3.14b).

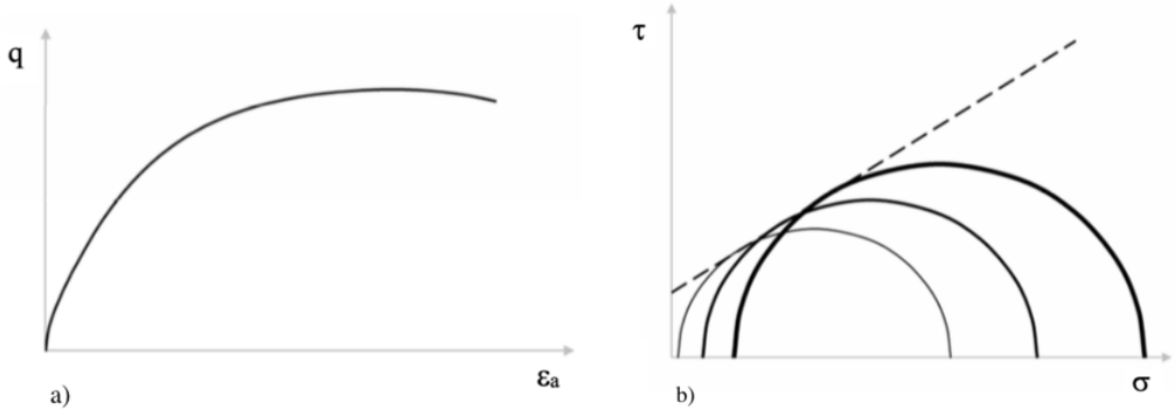

Figure 3.14. Triaxial compression (a) deviatory stress versus axial strain (b) Mohr circles (Adapted from Marques, 2016).

Although the name triaxial indicates three independent principal stresses, the specimens are actually subjected to a stress state in which two of the principal stresses are of equal magnitude ($\sigma 2$ and $\sigma 3$). The triaxial equipment developed by Marques (2016) was designed to perform tests both with specimens of 50 mm in diameter and 100 mm in height, and with of 100 mm in diameter and 200 mm in height. In the present research, only specimens of 50 mm in diameter and 100 mm in height were used. The equipment is composed of a triaxial chamber, pressure controllers, a system with servomotors, a mechanical jack controlled by a servomotor, a reaction system, instrumentation and a control and data acquisition system. Figure 3.15 shows an overview of the triaxial equipment developed by Marques (2016).

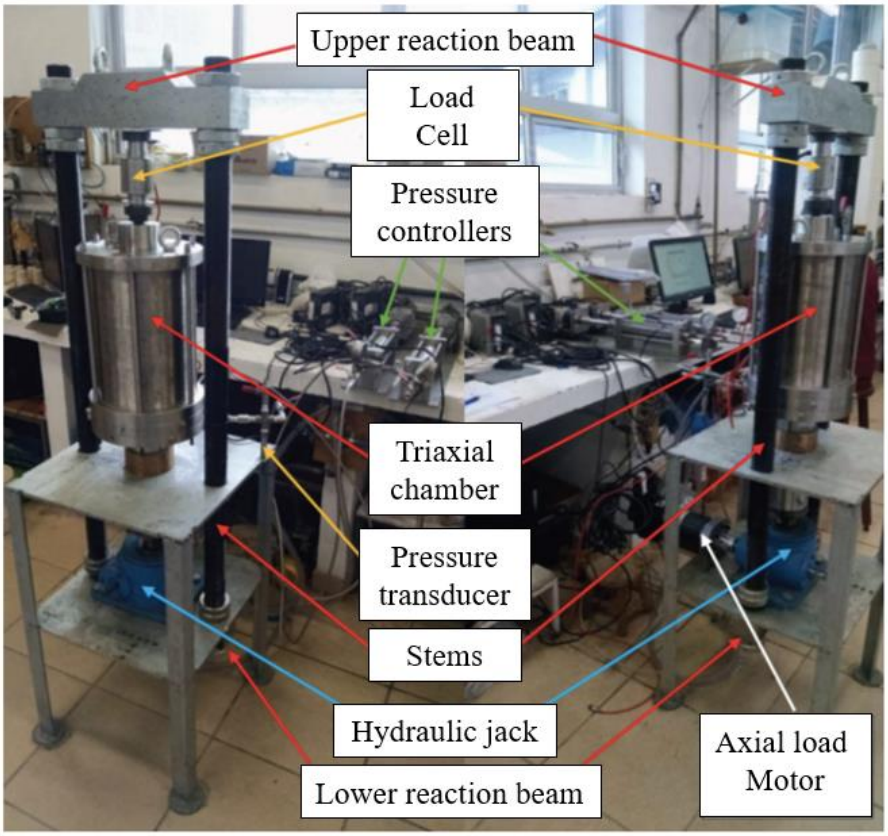

Figure 3.15. High stress triaxial test disposition (Adapted from Marques, 2016).

Axial loading is performed using a press that moves the triaxial chamber upwards, pressing the specimens against the piston. A load cell is installed between the piston and the reaction beam, which measures the load during loading. The upper reaction beam is connected, through two rods, to a lower reaction beam, providing the necessary reaction to the applied load. The mechanical jack responsible for the axial loading has a capacity of 20 tons. For the control of confining pressure and back pressure in pressure controllers and for the application of axial loading via a mechanical jack, there are three servomotors. The instrumentation allows data collection during the test. For this research, seven reading instruments are used in the triaxial equipment:

a) Two pressure transducers (for reading the confining stress and back pressure) of the ASHCROFT brand, which can read pressures between 0 and 2000 psi (approximately 14 MPa);
b) A linear displacement transducer of the brand GEFRAN, with 100 mm of travel, used to measure the external vertical displacement of the triaxial chamber;
c) A load cell with a maximum nominal capacity of 5 tones which measures axial force;
d) Three Hall effect gauges to measure internal strains (two axial and one radial).

For the control of servomotors and data acquisition, a Data Acquisition Board (*DAQ*) was used, which digitizes analog input signals. To facilitate the acquisition, analysis, presentation, and storage of instrumentation data, Marques (2016) also developed a virtual instrument in LabVIEW 2013 ®, which is a graphical programming language from National Instruments. Before executing any triaxial tests, all instruments of the triaxial equipment were recalibrated. The calibration constants are shown in Table 3.6.

Table 3.6: Calibration constants.

Instrument	Calibration constant
Confining stress transducer	1863.86
Backpressure transducer	1847.66
External strain gauge	-10.29
Load cell	27.65
Axial Hall effect gauge 01	3.94
Axial Hall effect gauge 02	-1.98
Radial Hall effect gauge 01	-1.87
Volumetric measurer	-2.69

The molding of triaxial test specimens followed the same procedures presented on item 3.2.1 for the unconfined compressive strength ones. As for the test procedure, the following steps were followed: (i) test assembling; (ii) percolation; (iii) saturation; (iv) consolidation; and (iv) shearing. The procedures adopted regarding the preparation and execution of the triaxial tests followed the principles described by the American Society for Testing and Materials [ASTM D7181 (2020), ASTM D4767 (2011)] and by Head (2006), in addition to usual methods based on experience at *LEGG/UFRGS*.

For the test assembling, a latex membrane was prepared with the necessary markings for the application of the internal instrumentation on the specimen. Because the top-cap inside the triaxial chamber was fixed, a split mold was used to apply the membrane to the specimen and then place it, together with the O-rings, under the pedestal and the top-cap. Then, a light suction (less than 10 kPa) was applied in order to verify the integrity of the membrane. After that, the internal instrumentation was installed, consisting of two axial strain gauges and a diameter gauge. Then, the triaxial chamber was placed with the help of a winch proceeding, immediately after, to the placement of the upper reaction, at the same time as the load cell was installed and the external axial gauge. After placing the chamber, it was no longer possible to have visual contact with the specimen, so its integrity was monitored by the software developed to control the triaxial equipment. Then, the initial data of the respective test were introduced, followed by

filling the triaxial chamber with water from the public supply (having no direct contact with the specimen). The aforementioned process can be seen in Figure 3.16.

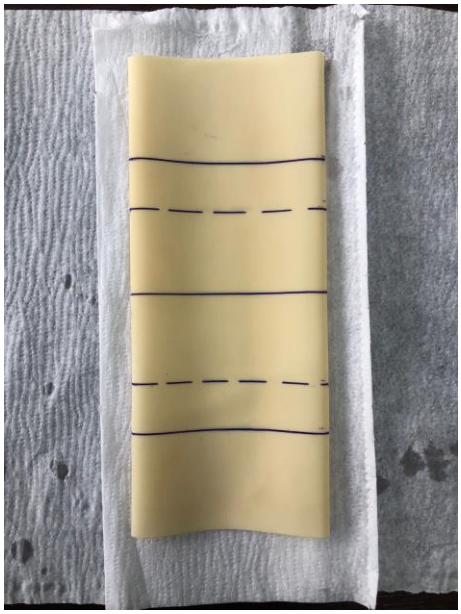

(a)

(b)

(c)

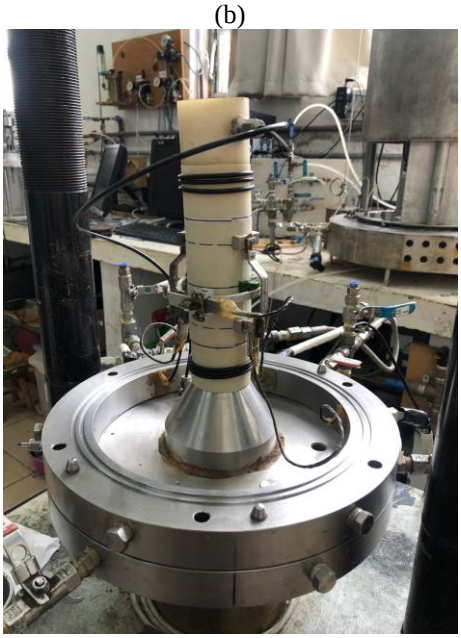

(d)

(e) (f)

(g) (h)

Figure 3.16. High stress triaxial test: (a) latex membrane marking; (b) specimen allocation on the membrane; (c) specimen allocation on the triaxial test; (d) internal sensors allocation; (e) chamber tow; (f) chamber allocation; (g) test disposition; (h) specimen after testing.

For the percolation step, carbon dioxide was utilized prior to water percolation to allow a faster dissipation of any air bubbles. To such a degree, all specimens were subjected to a confining stress of 35 kPa, while the back pressure was maintained at 15 kPa. Carbon dioxide percolation was maintained until at least 600 ml of CO_2 passed through the specimens. After that, water percolation could be initiated; this step was maintained until twice the void volume of each specimen was percolated (which was generally achieved in approximately 1 hour).

After percolation, the saturation phase of the tests was executed. The saturation process is standard procedure to ensure the dissolution of air bubbles in the sample. In this research, saturation was performed at a constant rate of 1.5 kPa/min, keeping an effective stress of 20 kPa, until a confining stress of 420 kPa and a back pressure of 400 kPa were reached. The degree of saturation was measured through the Skempton (1954) parameter *B* (Equation (3.19)); where $\Delta\sigma 3$ is the variation of the confining stress for a given increment of stress and Δu is the variation of back pressure measured as a function of confining stress variation. The closer the *B* value is to 1, the more saturated is the specimen.

$$B = \frac{\Delta\sigma 3}{\Delta u} \tag{3.19}$$

After saturation, the confining stress was applied according to the desired initial mean effective stress and the sample consolidation phase was started. The volumetric variation was measured to calculate the void ratio after consolidation. Consolidation was performed at a rate of 5 kPa/min in samples subjected to lower effective stresses (p' = 300 kPa) and at a rate of 15 kPa/min in samples subjected to higher effective stresses (p' = 3000 kPa). As a standard procedure, the consolidation phase was continued until all volumetric strains were constant.
As for the shearing phase, the loading rate (carried out under controlled deformation) was 1.0 mm/h. Area and membrane corrections were conducted in accordance with La Rochele et al. (1988).

3.2.6 Grain breakage analysis

The strength and stress-strain behavior of an element of soil is affected greatly by the degree to which crushing or particle breakage takes place during loading and deformation. For the type of deformation that primarily produces volume change, such as one-dimensional strain or isotropic compression, particle breakage adds to the reduction in volume. For the type of deformation where particles are moving past or around one another, such as triaxial compression or simple shear, crushing at sliding contacts or breakage of particles decreases the rate of dilation corresponding to a given principal stress ratio.
The most important factor affecting both shear strength and compressibility is the phenomenon of fragmentation undergone by a granular body when subjected to changes in its state of stresses, both during the uniform compression stage and during deviator load application. A similar fact is observed in one-dimensional compression tests.

To understand the physics of the strength and stress-strain behavior, it is important to define the degree to which the particles of an element of soil are crushed or broken. The amount of particle crushing that occurs in an element of soil under stress depends on the following parameters: (1) Particle size distribution; (2) particle shape; (3) state of effective stress; (4) effective stress path; (5) void ratio; (6) particle hardness (hardness of cementing material or weakest constituent of a particle and weakest particles of an element); and (7) the presence or absence of water.

Nakata et al. (1999) proposed a particle breakage factor *Bf*, as defined by Equation (3.20).

$$B_f = \frac{R}{100} \tag{3.20}$$

Where R is the percentage of particle finer, after testing, than the minimum particle size of the original sand, as shown in Figure 3.17. Bf is related to the minimum particle size of the initial grain size distribution and the survival probability – with the range from zero to unity corresponding to no particle breakage and breakage of every particle respectively.

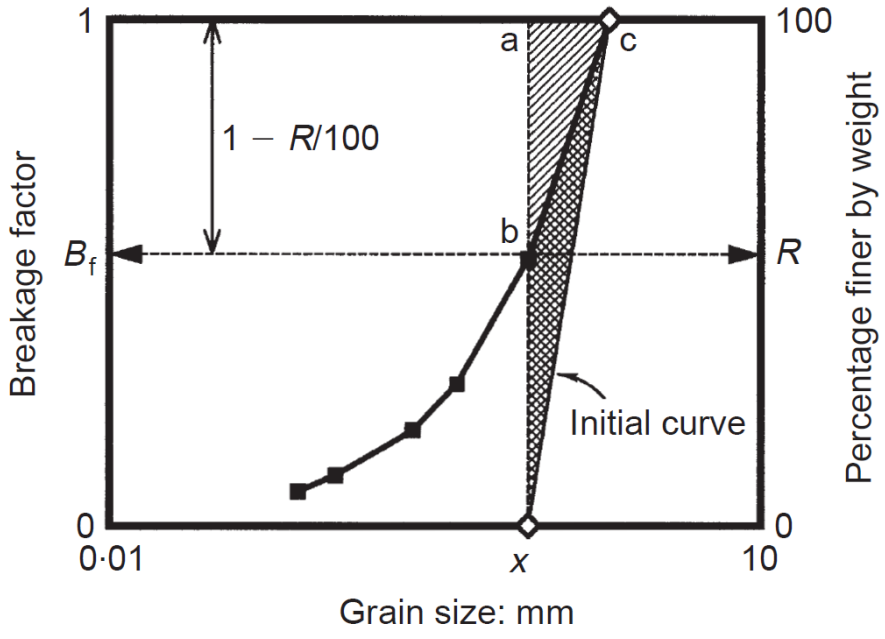

Figure 3.17. Definition of particle breakage factor Bf (Source: adapted from Nakata et al., 1999).

If the soil has an initial grading curve with a minimum particle size *x* before testing then a simple particle breakage factor Bf is proposed, where *Bf* is *R* = 100 and *R* is the percentage of

particles smaller, after testing, than the minimum particle size in the original sand as shown in Figure 3.17. This definition is similar to that proposed by Leslie (1963).

With that in mind, for this research, the grain breakage analysis proposed by Nakata et al. (1999) was applied to all specimens that were tested under high stress triaxial and compressibility regime. This analysis was conducted in order to investigate the influence of the studied variables on the grain size distribution of the material under different loading conditions. To this extent, additional grain size distribution tests were executed following the procedures of ASTM D7928 (ASTM, 2017a). In addition, a microscopic evaluation was also proposed, performed through a SEM-EDS mode, with electron beam of 20 kV voltage; with gold-coated samples (Quorum Q150 and JSM-6610 models).

3.3 RESEARCH APPROACH

These section provides information regarding the research approaches applied for the execution of this study. The variables of this research were divided in independent and dependent, with the first being related to the objective of the research, i.e., the study of the influence over the dependent variables (unconfined compressive strength, initial shear stiffness, hydraulic conductivity, compressibility, triaxial compression, and grain breakage analysis). The dependent variables can be also divided in two different groups: fixated and controlled. The following sections explore the application of the abovementioned concepts applied to this research.

3.3.1 Fixed variables

3.3.1.1 Unconfined compressive strength and initial shear stiffness tests fixed variables

For the unconfined compressive strength and initial shear stiffness tests, the fixed variables were: type of cement, cement content, curing period, and curing temperature.

High-initial strength Portland cement (type-III) was chosen as the stabilizing agent. This type of cement is associated with high strength values at low periods of time (developing more than 80% of the strength on the first seven days of curing). This is interesting from a practical viewpoint, as engineering problems tend to need fast solutions, especially regarding mining tailings. Besides, Davidson and Bruns (1960) reported significant economic and structural advantages in the utilization of type-III Portland cement when compared to type I conventional Portland cement for several engineering applications.

As for the cement content, an addition of 3% of high-initial strength Portland cement (type III) was utilized for the experimental program. This value was chosen based on previous researches on cemented tailings (Consoli et al., 2019; 2020; 2021; 2022).

A 7-days period was chosen as the research curing time, considering that high-initial strength Portland cement (type-III) was utilized for the experimental program. This type of cement is known for developing most of its cementitious reactions in the first 7 days of curing. Thus, this curing period can be considered as the most time-benefiting choice.

The temperature influence on cemented geotechnical materials has been extensively studied in the current literature (Alehyen et al., 2017; Consoli et al., 2014; Li, 1998; Marani and Madhkhan, 2021; Ouda and Gharieb, 2021; Vinai and Soutsos, 2019; Zhu et al., 2020), being known that increasing curing temperature accelerates the formation of cementitious reactions, consequently, improving the mechanical behavior. Considering that this research gap has already been explored, it was decided to set the curing temperature of this research at 23ºC, representing an average room temperature.

Table 3.7 presents a summary of the fixed variables for both the unconfined compressive strength and initial shear stiffness tests.

Table 3.7: Fixed variables unconfined compressive strength and initial shear stiffness tests

Fixed variable	Level
Type of cement	High-initial strength Portland cement
Cement content (%)	3
Curing period (days)	7
Curing temperature (°C)	23

3.3.1.2 Hydraulic conductivity test fixed variables

For the hydraulic conductivity tests, the fixed variables were: type of cement, curing period, curing temperature and hydraulic gradient. As for the reasoning behind the choices of type of cement, curing period, and curing temperature the same as exposed on item 3.3.1.1 applies.

On the other hand, the maximum hydraulic gradient was chosen based on ASTM D 5084. The standard states that the hydraulic gradient should be compatible with that likely to occur in the field (Table 3.8). The hydraulic conductivity of iron ore tailings is directly dependent of the grain size distribution and the processing of the material, as thoroughly discussed on Item 2.2.2.6.

Table 3.8: Maximum hydraulic gradient.

Hydraulic conductivity (m/s)	Recommended maximum hydraulic gradient
1×10^{-5} to 1×10^{-6}	2
1×10^{-6} to 1×10^{-7}	5
1×10^{-7} to 1×10^{-8}	10
1×10^{-8} to 1×10^{-9}	20
less than 1×10^{-10}	30

Source: ASTM D5084 (2016).

Nevertheless, for soils with low permeability it is usually necessary to apply substantially greater hydraulic gradients so that testing time will not be unduly prolonged. Considering the above-mentioned information, the hydraulic gradient was fixated in 5 for all permeability tests. A summary of the fixed variables of the hydraulic conductivity tests can be found in Table 3.9.

Table 3.9: Fixed variables hydraulic conductivity tests

Fixed variable	Level
Type of cement	High-initial strength Portland cement
Curing period (days)	7
Curing temperature (°C)	23
Hydraulic gradient	5

3.3.1.3 Compressibility test fixed variables

For the compressibility tests, the fixed variables were: the type of cement, curing period, curing temperature, and maximum applied stress. As for the reasoning behind the choices of type of cement, curing period, and curing temperature the same as exposed in Item 3.3.1.1 applies.

The maximum axial load utilized on the compressibility tests was 6.4MPa for all specimens, considering the limitations of the equipment, as well as, the weight availability in the laboratory. In addition, by utilizing a final loading of this magnitude (i.e., 6.4MPa), both low-stress and high-stress states would be encompassed. A summary of the fixed variables of the compressibility tests can be found in Table 3.10.

Table 3.10: Fixed variables compressibility tests

Fixed variable	Level
Type of cement	High-initial strength Portland cement
Curing period (days)	7
Curing temperature (°C)	23
Maximum applied stress (MPa)	6.4

3.3.1.4 Triaxial test fixed variables

For the triaxial compression tests, the fixed variables were: the type of cement, curing period, curing temperature, and triaxial condition. As for the reasoning behind the choices of type of cement, curing period, and curing temperature the same as exposed in Item 3.3.1.1 applies. Regarding the triaxial conditions, isotropic consolidation under triaxial compression was chosen, with basis on the basic characterization of the iron ore tailings. Table 3.11 presents the fixed variables for the triaxial compression tests.

Table 3.11: Fixed variables triaxial compression tests

Fixed variable	Level
Type of cement	High-initial strength Portland cement
Curing period (days)	7
Curing temperature (°C)	23
Triaxial conditions	Isotropically consolidated drained under triaxial compression

3.3.1.5 Grain breakage analysis fixed variables

For the grain breakage analysis, the fixed variables were the same as the ones exposed in Items 3.3.1.3 and 3.3.1.4; in other words, the analysis was conducted in all specimens of both oedometric and high confining stress triaxial tests.

3.3.1.6 Microscopic evaluation of the grain breakage analysis fixed variables

For the microscopic evaluation of the grain breakage analysis, the fixed variables can be represented by the specimen combination that resulted in the highest grain breakage, both for the oedometric and triaxial tests (see Items 4.6.1 and 4.6.2). In the case of this research, for both boundary conditions, this combination was represented by the specimens molded at the dry side of the compaction curve under the modified effort compaction energy.

3.3.2 Controlled variables

3.3.2.1 Unconfined compressive strength and initial shear stiffness tests controlled variables

For the unconfined compressive strength and initial shear stiffness tests, the controlled variables were: compaction energy, dry unit weight and moisture content.

The compaction effort is one of the most important factors influencing the compaction/densification of geotechnical materials. Two different compaction energies were explored in this research: standard [D698 (ASTM, 2021)] and modified [D1557 (ASTM, 2012)]. The standard energy can be defined as a light compaction while the modified energy as

a heavy one. Thus, standard energy is normally associated with simpler projects/designs while modified energy accounts for heavy machinery (e.g., larger trucks, higher traffic counts on highways, and bigger airplanes), which could produce higher compaction of soil. Along these lines, the understanding of the standard/modified energy relation can aid in geotechnical designs, by optimizing any decision-making process.

Regarding the dry unit weight and moisture content variables, 03 (three) different molding points were selected from each compaction curve, as shown in Figure 3.18. The main premise behind this choice was to study the influence of porosity and moisture content over different compaction energies.

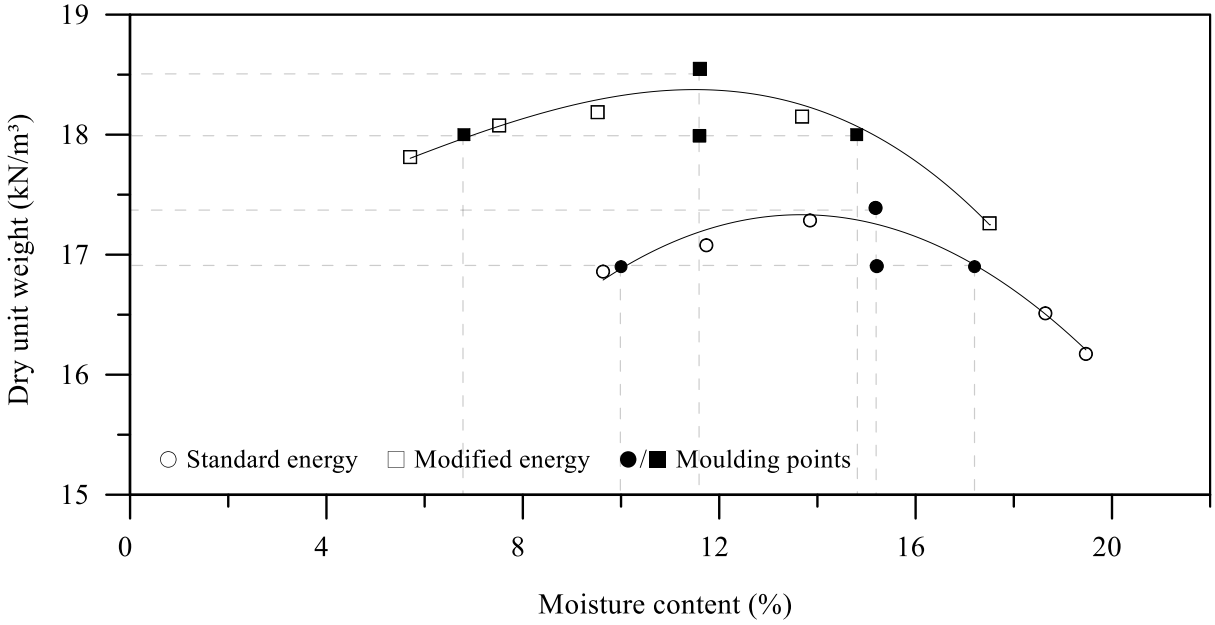

Figure 3.18. Compaction test – iron ore tailings

In both compaction curves, the first point to be selected was the optimum compaction one (i.e., maximum dry unit weight and optimum moisture content). Then, to explore the porosity effect, a reduction of 0.5 kN/m³ (~ 3% of the compaction degree) was applied to the maximum dry unit weight. As for the moisture content analysis, the reduced value of γ_d was extended to the center and both sides of the compaction curve (left and right), resulting in an optimum moisture content compaction point, a dry-side compaction point, and wet-side compaction point of the same density.

For the standard energy, the molding points were: (i) γ_d = 17.4 kN/m³ and ω = 15.2% (optimum moisture content at maximum dry unit weight); (ii) γ_d = 16.9 kN/m³ and ω = 15.2% (optimum moisture content at reduced dry unit weight); (iii) γ_d = 16.9 kN/m³ and ω = 10.0% (dry-side);

(iv) γ_d = 16.9 kN/m³ and ω = 17.2% (wet-side). On the other hand, for the modified energy, the molding points were: (i) γ_d = 18.5 kN/m³ and ω = 11.6% (optimum moisture content at maximum dry unit weight); (ii) γ_d = 18.0 kN/m³ and ω = 11.6% (optimum moisture content at reduced dry unit weight); (iii) γ_d = 18.0 kN/m³ and ω = 6.8% (dry-side); (iv) γ_d = 18.0 kN/m³ and ω = 14.8% (wet-side). Table 3.12 presents a summary of the controlled variables for the unconfined compressive strength and initial shear stiffness tests.

Table 3.12: Controlled variables unconfined compressive strength and initial shear stiffness tests

Controllable variable	Level	
Compaction energy	Standard	Modified
Dry unit weight (kN/m³)	17.4; 16.9	18.5; 18.0
Moisture content (%)	15.2; 10.0; 17.2	11.6; 6.8; 14.8

3.3.2.2 Hydraulic conductivity and compressibility tests controlled variables

For the hydraulic conductivity and compressibility tests, the controlled variables were: compaction energy, dry unit weight, moisture content, and cement content. Table 3.13 presents a summary of the controlled variables of both hydraulic conductivity and compressibility tests.

Table 3.13: Controlled variables hydraulic conductivity and compressibility tests

Controllable variable	Level	
Compaction energy	Standard	Modified
Dry unit weight (kN/m³)	17.4; 16.9	18.5; 18.0
Moisture content (%)	15.2; 10.0; 17.2	11.6; 6.8; 14.8
Cement content (%)	0; 3	

The compaction energy, dry unit weight, and moisture content variables were selected considering the same justifications presented in Item 3.3.2.1; as for the reasoning behind the cement content, the same as exposed in Item 3.3.1.1 applies.

3.3.2.3 Triaxial test controlled variables

For the triaxial compression tests, the controlled variables were: compaction energy, dry unit weight, moisture content, cement content, and confining stress. Table 3.14 depicts the controlled variables for the triaxial compression tests.

Table 3.14: Controlled variables triaxial compression tests.

Controllable variable	Level	
Compaction energy	Standard	Modified
Dry unit weight (kN/m³)	17.4; 16.9	18.5; 18.0
Moisture content (%)	15.2; 10.0; 17.2	11.6; 6.8; 14.8
Cement content (%)	0; 3	
Confining stress (kPa)	300; 3000	

The decision-making process behind compaction energy, dry unit weight, and moisture content variables can be found on item 3.3.2.1; while for cement content, justifications of Item 3.3.1.1 apply. As for the confining stress, two distinctive stresses were selected: 300kPa and 3000kPa. These stresses were selected considering that they represent stress levels that encompass both a low stress state and a high stress state of mining structures (e.g., tailing dams, dry stacking).

3.3.2.4 Grain breakage analysis controlled variables

For the grain breakage analysis, the controlled variables were: compaction energy, dry unit weight, moisture content, cement content, and test boundary condition. Table 3.15 presents a summary of the controlled variables of both hydraulic conductivity and compressibility tests.

Table 3.15: Controlled variables grain breakage analysis.

Controllable variable	Level	
Compaction energy	Standard	Modified
Dry unit weight (kN/m³)	17.4; 16.9	18.5; 18.0
Moisture content (%)	15.2; 10.0; 17.2	11.6; 6.8; 14.8
Cement content (%)	0; 3	
Test boundary condition	Oedometric condition; High stress triaxial condition	

The compaction energy, dry unit weight, and moisture content variables were selected considering the same reasoning presented on item 3.3.2.1; as for the reasoning behind the cement content, the same as exposed on item 3.3.1.1 applies. Finally, for the test boundary condition variable, the grain breakage analysis was conducted for both oedometric and high stress triaxial tests (p' = 3000 kPa), to evaluate the influence of one-dimensional consolidation (oedometric test) and multidimensional consolidation plus shearing (triaxial test) on the final grain size distribution. It is important to highlight that low confining stress triaxial specimens (p' = 300 kPa) will not be encompassed on the grain breakage analysis, considering that several authors (Einav, 2007a; Han and Hager, 1963; Tarantino and Hyde, 2005; Yu, 2017b) attest that this phenomenon is negligible for this stress level.

3.3.2.5 Microscopic evaluation of the grain breakage analysis controlled variables

For the microscopic evaluation, the controlled variables were: test boundary condition, cement content, and magnification, as shown in Table 3.16.

Table 3.16. Controlled variables microscopy evaluation.

Boundary condition	Cement content (%)	Magnification (times)
Oedometric	0	100; 500; 1,000; 2,000; 5,000
Oedometric	3	
Triaxial	0	
Triaxial	3	

Such as the case of Item 3.3.2.4, both oedometric and high stress triaxial conditions were selected to evaluate the effect of one-dimensional consolidation and multidimensional consolidation plus shearing on the final grain size distribution. Once again, low confining stress triaxial specimens (p' = 300 kPa) will not be encompassed on the grain breakage analysis, considering that several authors (Einav, 2007a; Han and Hager, 1963; Tarantino and Hyde, 2005; Yu, 2017b) attest that this phenomenon is negligible for this stress level. As for the magnification of the microscopic evaluation, the levels were chosen based on the ones commonly found on the analysis of grain breakage (Yu, 2021). Finally, the natural ore tailings were utilized as the control group for the microscopic evaluation.

4 RESULTS AND DISCUSSION

4.1 UNCONFINED COMPRESSIVE STRENGTH ANALYSIS

As mentioned on section 3.3.1.1, the unconfined compressive strength of the *IOTs* was only explored for the stabilized combinations (specimens with 3% cement content), considering that for unreinforced materials (i.e., specimens without any cement addition) any unconfined compressive strength (*UCS)* value would be originating from suction effects, not being representative of a real strength parameter.

Figure 4.1 and Table 4.1 present the *UCS* results for the stabilized *IOTs*. As stated in the method section (Item 3.2.1), *UCS* results were correlated with the porosity binder index; this index allows the unification of all experiments in a single relation, resulting in a rational dosage methodology for any cemented soil mixture, replacing trial and error conventional strategies that are normally laborious and time consuming. It is important to highlight that such equations are valid for the cemented mixtures studied herein and are only functional if the boundary conditions of the applied variables are ensured.

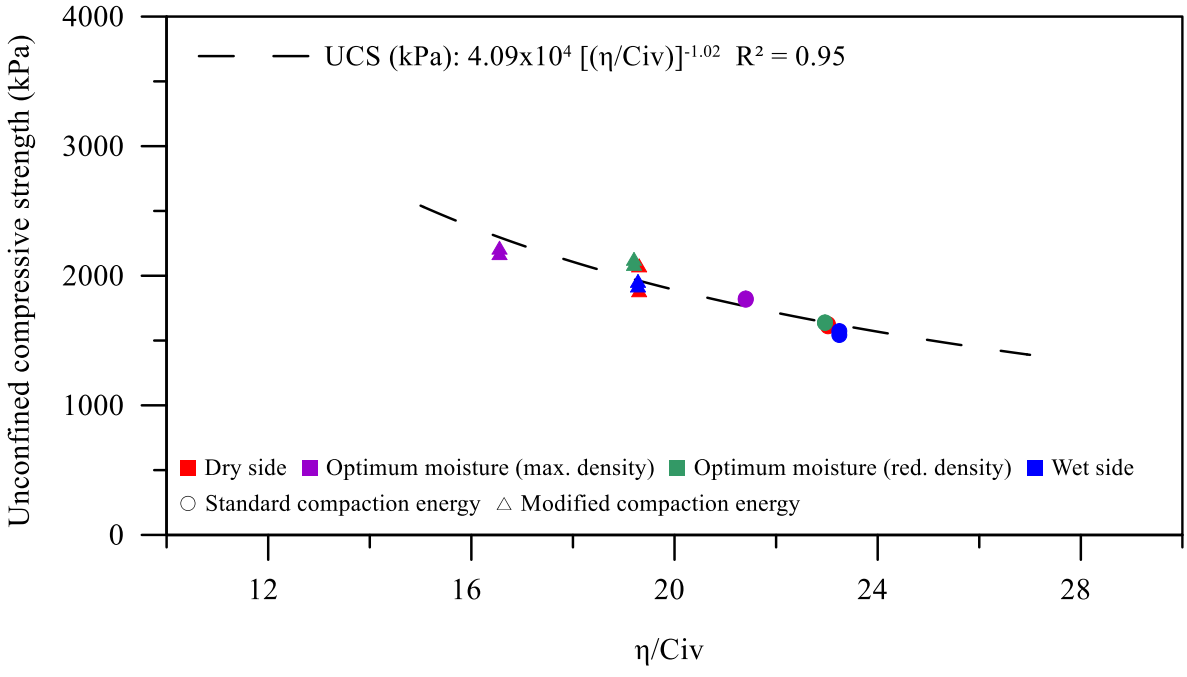

Figure 4.1. Unconfined compressive strength versus porosity/cement content index

Table 4.1. Unconfined compressive strength *IOTs* - summary

Compaction condition	Compaction energy	*η/Civ*	Unconfined compressive strength (kPa)
Dry side	Standard	23.02	1617.80

Compaction condition	Compaction energy	η/Civ	Unconfined compressive strength (kPa)
Optimum moisture (max. density)	Modified	21.40	1819.61
Optimum moisture (red. density)		22.96	1637.65
Wet side		23.24	1557.78
Dry side		19.30	1983.61
Optimum moisture (max. density)		16.55	2195.35
Optimum moisture (red. density)		19.20	2110.75
Wet side		19.28	1942.49

In general, it is possible to see that increasing cement content and reducing porosity resulted in higher *UCS* values. The reduction in porosity induces a greater contact area between soil particles, intensifying interlocking and mobilizing friction, which increases strength; while the increase in binder content is linked to the increase in cementitious reactions, also contributing to strength development. This physical-chemical phenomenon has also been evidenced in several cemented geotechnical materials, such as Portland cement stabilized soils (Consoli et al., 2007, 2020a; Diambra et al., 2017; Festugato et al., 2018; Veloso Marques et al., 2014), pozzolan and lime stabilized soils (Beck Saldanha et al., 2019; Consoli et al., 2011a, 2016, 2017c, 2019a, 2020b), alternative cement stabilized soils (Consoli et al., 2018c; Corrêa et al., 2021), Portland cement stabilized mining tailings (Consoli et al., 2018b), and green stabilized mining tailings (Alam et al., 2019; Bruschi et al., 2021e).

Regarding the effect of the molding conditions, for both compaction energies, higher *UCS* was evidenced for specimens molded at the optimum moisture content (max. density), followed by specimens molded at the optimum moisture (red. density), dry-side, and the wet-side, respectively. This behavior shows that moisture content directly affects the development of *UCS*, indicating that the structure imparted by compaction is fundamental even after the development of the cementation bonds. This fact may be explained considering the coupled effect of the two main contributing factors on the shear strength of the stabilized geotechnical materials: the structure imparted by compaction (soil fabric), mainly density and packing, which predominates in the short-term, and the formation of a cementitious matrix, which predominates in the long-term. A similar behavior was also evidenced for other geotechnical materials (Beck Saldanha et al., 2019; Bruschi et al., 2021b; c; Consoli et al., 2011a, 2018a; Pereira dos Santos et al., 2022; Saldanha et al., 2021; Tonini de Araújo et al., 2021).

Adequate correlations between *UCS* and η/Civ index were evidenced, with a determination coefficient (R^2) of 0.95. This high value indicates the index viability to predict the *UCS* behavior

of cemented tailings, also corroborated by the studies of Bruschi et al. (2021b) and Consoli et al. (2017a) (Bruschi et al., 2021e; Consoli et al., 2017a).

$$\text{UCS (kPa)} = 4.09\times10^{4}\left[\left(\eta/_{\text{Civ}}\right)\right]^{-1.02} \quad (4.1)$$

Based on Equation (4.1), it is possible to choose the best combination of porosity and binder content for a project, without trial-and-error experiments. For instance, standard NBR 12253 (ABNT, 2012) states that the *UCS* for cemented soils should be at least 2.1 MPa for a pavement layer; with that in mind, a *η/Civ* value of 17.8 would already fulfill this requirement. Several other standards (American Association of State Highway and Transportation Officials (AASHTO), 2008; AUSTROADS, 2017; Junta Autonoma de Estradas (JAE), 1995; Portland Cement Association (PCA), 1992; United States Army Corps of Engineers (USACE), 1984) could also be applied, simply by entering the required strength on the Equations; this would result in the minimum *η/Civ* value, in which the engineer can determine the best and most economic combination (varying porosity and binder content) for the project.

As an example, porosity could be related to *in situ* machinery availability for soil-cement applications in civil engineering projects. Thus, the higher the compaction degree achieved by a machinery, the lower the porosity. Other considerations such as environmental impacts can also be considered when defining porosity and binder content; according to Da Rocha et al. (2016), higher compaction degrees result in lower environmental impacts when compared to the increase in chemical stabilizer content.

4.2 INITIAL SHEAR STIFFNESS ANALYSIS

Initial shear modulus results were also correlated with the *η/Civ* index, according to Figure 4.2 and Table 4.2. As observed for the *UCS* results, the initial shear stiffness increased with the decrease of the porosity/cement content index. This behavior was once again attributed to the greater contact area between soil particles, alongside the increase in cementitious reactions, which contributed to stiffness development.

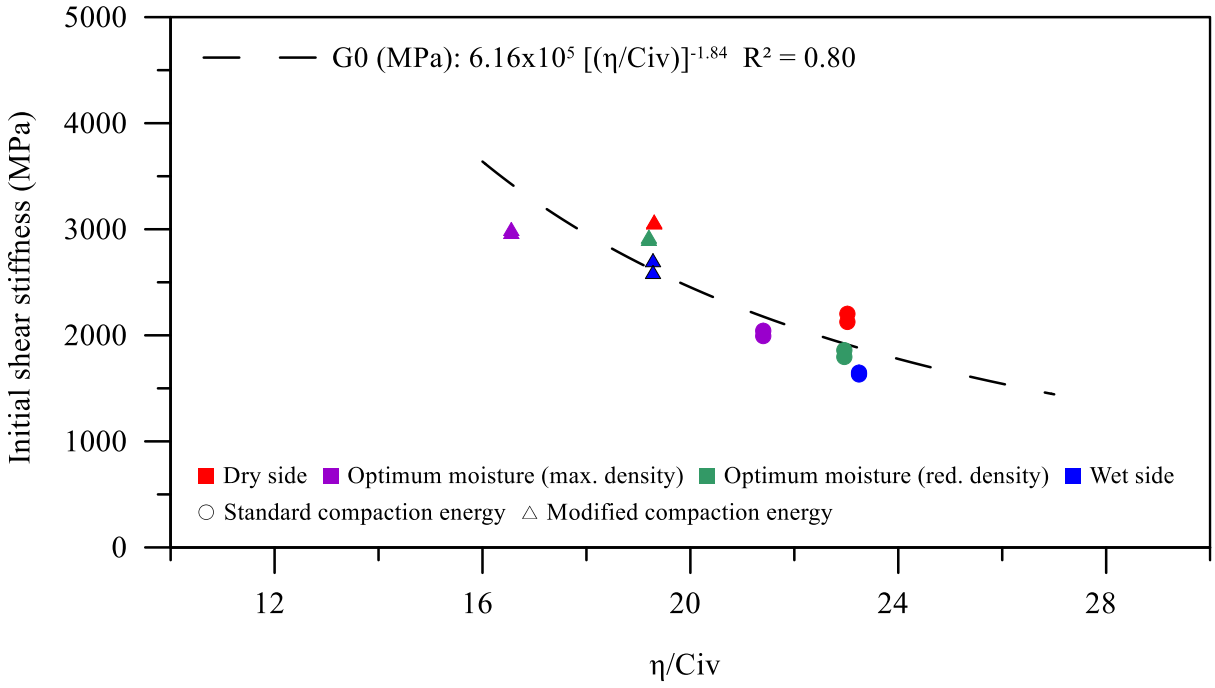

Figure 4.2. Initial shear stiffness versus porosity/cement content index

Table 4.2. Initial shear stiffness IOTs - summary

Compaction condition	Compaction energy	η/Civ	Initial shear stiffness (MPa)
Dry side	Standard	23.02	2164.24
Optimum moisture (max. density)		21.40	2017.61
Optimum moisture (red. density)		22.96	1827.44
Wet side		23.24	1639.28
Dry side	Modified	19.30	3068.34
Optimum moisture (max. density)		16.55	2988.81
Optimum moisture (red. density)		19.20	2919.61
Wet side		19.28	2652.92

Several authors (Bruschi et al., 2021e; Consoli et al., 2016, 2017b, 2020c; Corrêa-Silva et al., 2020; Rios et al., 2017) reported that stiffness can be simply and directly related to *UCS*, in which less porous samples with higher cement content result in higher values of initial shear stiffness. However, this behavior was not evidenced in this research; the highest initial shear stiffness values for both compaction energies were depicted for specimens molded on the dry-side of the compaction curve, followed by specimens molded at optimum moisture content (max. density), optimum moisture content (red. density), and finally wet-side of the proctor curve. This behavior indicates that stiffness of cemented iron ore tailings is not only dependent of void ratio and cement content, but is rather presented as a more complex phenomenon also influenced by the initial moisture content of the mixtures. Consoli et al. (2001) studied some

fundamental aspects of geotechnical behavior of cemented conventional soils, such as the short-term changes due to initial cementitious reactions and the influence of compaction parameters on strength and stiffness properties; the authors experimental evidences reflected similar findings to the ones presented in this research, in which specimens of lower initial moisture content resulted in higher stiffness when compared to wet-side and optimum moisture content specimens. This behavior was associated to the coupled effect of the two main contributing factors on the shear strength of the stabilized geotechnical materials: the structure imparted by compaction (fabric of the soil) which predominates in the short-term, and the formation of a cementitious matrix, which predominates in the long-term. The results of this research indicate that the findings of Consoli et al. (2001) also extent for non-conventional geotechnical materials, such as the case of mining tailings.

Finally, a fair correlation [Equation (4.2)] was identified between initial shear stiffness and the porosity/cement content index; with a determination coefficient (R^2) of 0.80. This elevated value, once again, indicates the viability of the index in predicting the stiffness of *IOTs* cemented mixtures, also corroborated by the work of Bruschi et al. (2021a; b).

$$\text{Initial shear stiffness (MPa)} = 6.16\times10^{5}\left[\left(\eta/_{Civ}\right)\right]^{-1.84} \quad (4.2)$$

4.3 HYDRAULIC CONDUCTIVITY ANALYSIS

The results of hydraulic conductivity are shown in Figure 4.3 and Table 4.3. Figure 4.3 also depicts a range for the different hydraulic conductivity classification levels of soils, as proposed by Lambe et al. (1979), for comparison purposes.

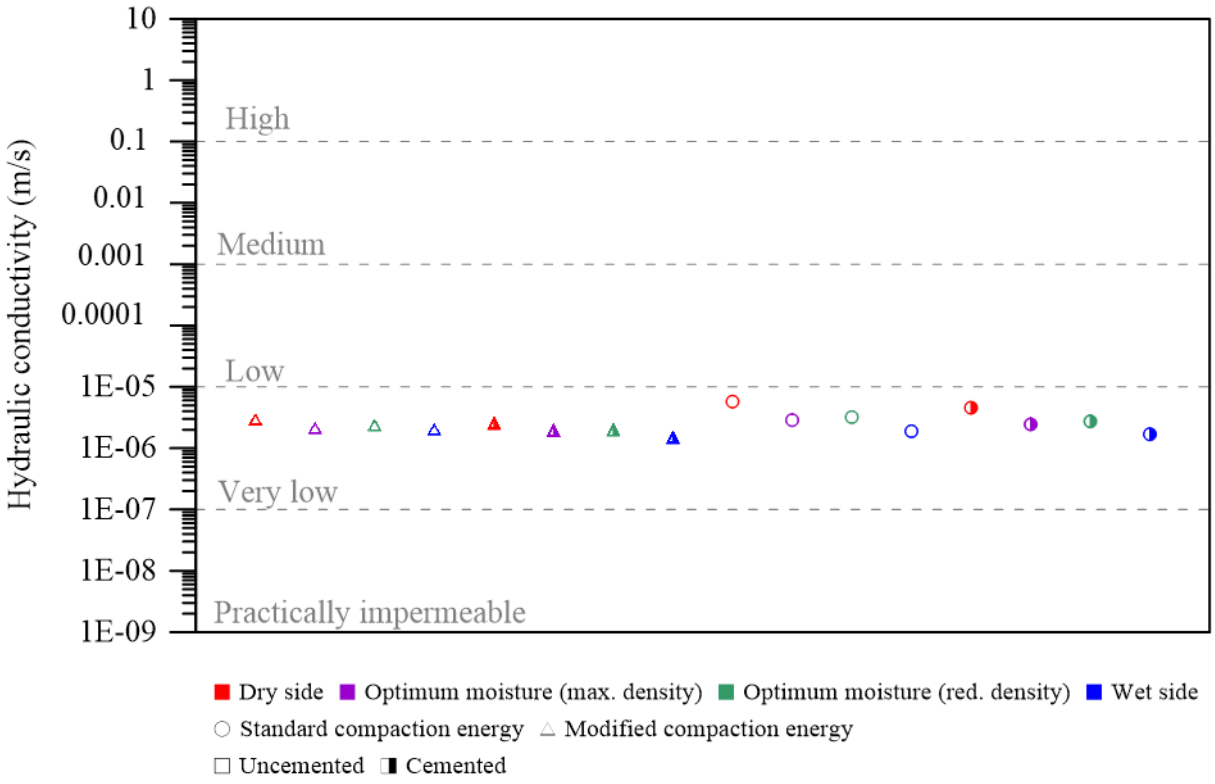

Figure 4.3. Hydraulic conductivity IOTs – graphic representation

Table 4.3. Hydraulic conductivity IOTs - summary

Compaction condition	Compaction energy	Cement content (%)	Hydraulic conductivity (m/s)
Dry side	Standard	0	5.76×10^{-6}
Optimum moisture (max. density)			2.87×10^{-6}
Optimum moisture (red. density)			3.21×10^{-6}
Wet side			2.03×10^{-6}
Dry side	Modified		2.94×10^{-6}
Optimum moisture (max. density)			2.13×10^{-6}
Optimum moisture (red. density)			2.37×10^{-6}
Wet side			1.89×10^{-6}
Dry side	Standard	3	4.57×10^{-6}
Optimum moisture (max. density)			2.45×10^{-6}
Optimum moisture (red. density)			2.74×10^{-6}
Wet side			1.69×10^{-6}
Dry side	Modified		2.56×10^{-6}
Optimum moisture (max. density)			1.97×10^{-6}
Optimum moisture (red. density)			2.01×10^{-6}
Wet side			1.51×10^{-6}

In general, all specimens resulted in similar hydraulic conductivity values, falling in the same permeability classification (i.e., very low permeability). This result was expected, considering that the specimens of this research were all in a dense state, with very low void ratios.

By analyzing the influence of compaction energy, the increase from standard to modified energy led to a decrease in hydraulic conductivity values. Soil permeability depends on multiple factors, among which the compactness plays a fundamental role. The aforementioned phenomenon can be associated with the reduction in void ratio with the increase of compaction energy; if the volume of voids in a soil mass increases, the flow path becomes wider and voids interconnectivity increases, hence increasing permeability. Attom (1997) studied the influence of different compaction energies (355, 987, 1637, and 2693 kJ/m³) on the hydraulic conductivity of soils; at optimum moisture contents, permeability decreased from 5.9 x 10^{-9} cm/sec to at 355kJ/m³ to 1.8 x 1ff 11 cm/sec at 2693 kJ/m³. Dry of optimum, permeability ranged from 9 x 10^{-9} to 5.37 x 10^{-7} cm/sec at 355 kJ/m³. At higher compaction energies (987 to 2693 kJ/m³) permeability decreased, ranging from 1 x 10^{-11} to 2.8 x 10^{-9} cm/sec. As compaction energy increases, the voids decrease, reducing permeability. Plotted against moisture content, permeability, at every energy level decreased from dry to optimum moisture contents and then increased beyond optimum. These conclusions are also affirmed by work previously performed by Lambe (1958) on fine grained materials.

When secluding the moisture content effect/influence, the increase in water presence led to a decrease in hydraulic conductivity for all combinations of compaction energies, initial moisture contents and cement contents. Normally, on the dry side of optimum moisture content the change in the value of permeability is large and rapid, but that on the wet-side of optimum water content the change (increase) in permeability is much less and at a much slower rate. If compacted on the dry side of optimum moisture content, soils are expected to present higher permeabilities, less susceptibility to shrinkage, but they will be more susceptible to swelling and will have higher absorption of water than soils compacted on the wet-side of the compaction curve. The values of permeability on the wet-side of optimum moisture content tend to increase with the addition of water, but this increase is at a much slower rate.

On the dry side of optimum moisture content the change in the value of permeability is large and rapid, but that on the wet-side of optimum water content the change (increase) in permeability is much less and at a much slower rate, such as the case of this research. Comparing permeability values on the wet and dry sides of optimum content moisture, a higher permeability for soils compacted dry of optimum than for soils compacted wet of optimum moisture content is found. Since the specimen compacted dry of optimum has a more random orientation, it has a greater number of large pores than the sample does with more nearly parallel

arrangement obtained from wet side compaction. The larger the individual pores for any given total pore area, the greater the flow, thus a high permeability.

When isolating the influence of cement content, it can be seen from the data presented in Figure 4.3 and Table 4.3 that the increase in cement content (0 to 3%) led to a decrease in hydraulic conductivity values. According to Ingles and Metcalf (1972), during the hydration process, cement hydrates are formed, followed by the increase in pH value and $Ca(OH)_2$ concentration can break the soil particles and free the silica and aluminum to join the calcium forming the second hydrate material. This will alter the modification of pores size and distribution. When the quantity of cement increases, the pores size decrease. Moreover, in the curing process, pores size can be minimized. Permeability will then decrease and soil - cement gains higher strength and stiffness. However, higher cement additions can also lead to an increase in soil permeability; in such cases, the pore size of soil-cement increases due to flocculation and agglomeration reaction. Hence, the permeability of the soil increases. In this research, the cement was only capable of reducing soil permeability, considering that the addition was only 3%.

The results shown in this section indicate that the *IOTs*, for all studied combinations (different compaction energies, initial moisture contents, and cement contents), present a behavior similar to the one found for conventional geotechnical materials, even though *IOTs* are an alternative geotechnical material.

4.4 COMPRESSIBILITY ANALYSIS

For the analysis of the compressibility results, the data was divided into three different subsections: uncemented analysis, cemented analysis, and uncemented versus cemented comparison. This division was created in order to facilitate the exposition of the results, as well as, the explanations regarding the evidenced behavior.

4.4.1 Compressibility: uncemented analysis

The compressibility test results for uncemented standard compaction energy specimens are shown in Figure 4.4. In general, all curves of Figure 4.4 show the classical pattern of a decreasing void ratio with increased stress during the loading stages up to 6.4 MPa, due to the fact that the interstitial fluid is expelled in response to the applied stress, and soil is rearranged

in a denser configuration resulting in a volume reduction and then a small rebound upon release of stress (Holtz and Kovacs 1981).

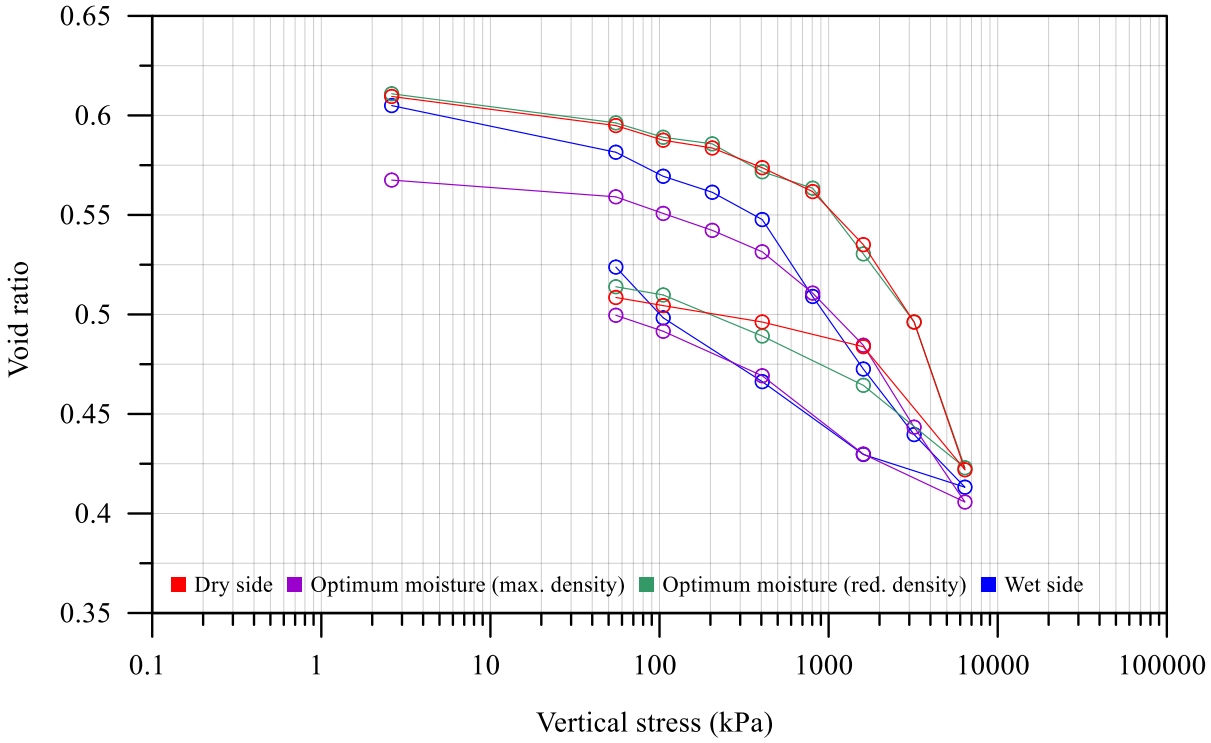

Figure 4.4. Compressibility results - standard energy - uncemented IOTs

Regarding the stress-strain behavior, specimens molded at optimum moisture (max. density) resulted in lower settlements, followed by specimens molded at optimum moisture (red. density), dry-side, and wet-side. Specimens molded at optimum conditions (max. density) presented a lower initial void ratio, which leaves less space for the rearrangement of soil particles, explaining the evidenced behavior. When comparing the moisture content influence for same initial void ratio specimens, it is possible to see that specimens molded at the optimum moisture (red. density) and dry-side, resulted in very similar settlements, with the latter being slightly less resistant; on the other hand, wet-side specimens resulted in higher settlements. This behavior is attributed to the soil fabric formed at the different molding conditions. At low moisture contents, the soil mass is normally stiffer and offers more resistance to compaction/load bearing. As the water content is increased, the soil particles get lubricated. The soil mass becomes more workable and the particles have closer packing. The dry density of the soil increases with an increase in the water content till the optimum water content in reached. At that stage, the air voids attain approximately a constant volume. With further increase in water content, the air voids do not decrease, but the total voids (air plus water)

increase and the dry density decreases. Thus, the higher dry density is achieved up to the optimum water content due to forcing air voids out from the soil voids. After the optimum water content is reached, it becomes more difficult to force air out and to further reduce the air voids.

The compressibility test results for uncemented modified compaction energy specimens are shown in Figure 4.5.

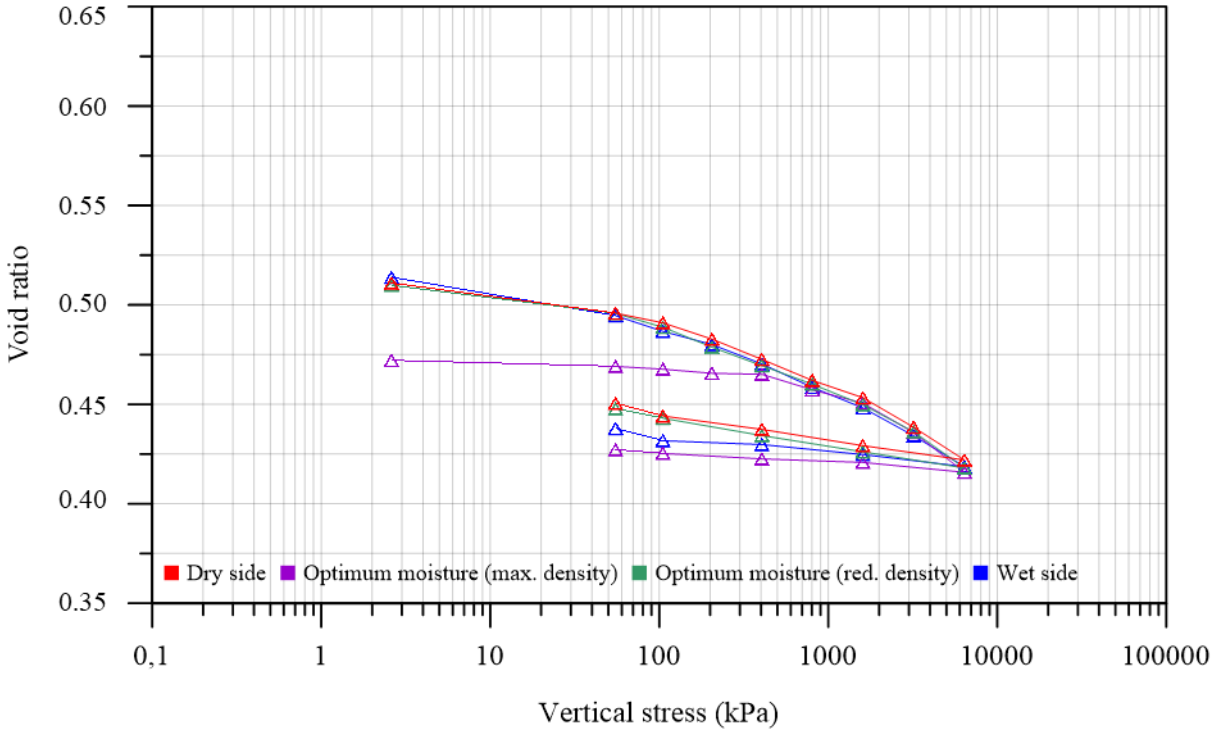

Figure 4.5. Compressibility results - modified energy - uncemented IOTs

The same behavior presented for the uncemented standard energy specimens was evidenced for the uncemented modified energy ones, in which a classical pattern of a decreasing void ratio with increased stress during the loading stages up to 6.4 MPa was shown. In addition, such as in the case of the standard energy, specimens molded at optimum moisture (max. density) resulted in lower settlements, followed by specimens molded at optimum moisture (red. density), dry-side, and wet-side. This behavior is once again associated with the soil fabric formed over distinctive molding conditions as thoroughly discussed in the last paragraphs.

When comparing both compaction energies for uncemented specimens, it is possible to see that the increase from standard to modified energy led to an improvement in the soil mechanical response, resulting in specimens with less variation in their void ratio over the studied stress range. This behavior is associated with the greater contact area between soil particles induced by the higher dry unit weight; this phenomenon intensifies interlocking and friction

mobilization, which in turn increases the strength of the mixtures. A considerable number of studies have analyzed the influence of compaction effort on the mechanical properties of earthen materials (Attom, 1997; Kouakou and Morel, 2009; Mesbah et al., 1999; Venkatarama Reddy and Jagadish, 1995). These studies agree that a higher compaction effort increases the dry density and, consequently, the stiffness and strength of the material. These studies also show that, for a given compaction effort, there is an optimum value of water content for which the highest density and the best mechanical properties are achieved, such as the case of this research. Finally, when comparing all uncemented tests, the minimum void ratios reached for stresses up to 6.4MPa were all similar, independent of the initial molding condition.

4.4.2 Compressibility: cemented analysis

The compressibility test results for cemented standard compaction energy specimens are shown in Figure 4.6. For all tested combinations a similar behavior was evidenced; the increase in stress (up to levels of 6.4MPa) led to a decrease in void ratio. The exhibited behavior is associated with the rearrangement of soil particles, creating a denser configuration resulting in a volume reduction and then a small rebound upon release of stress (unloading stages).

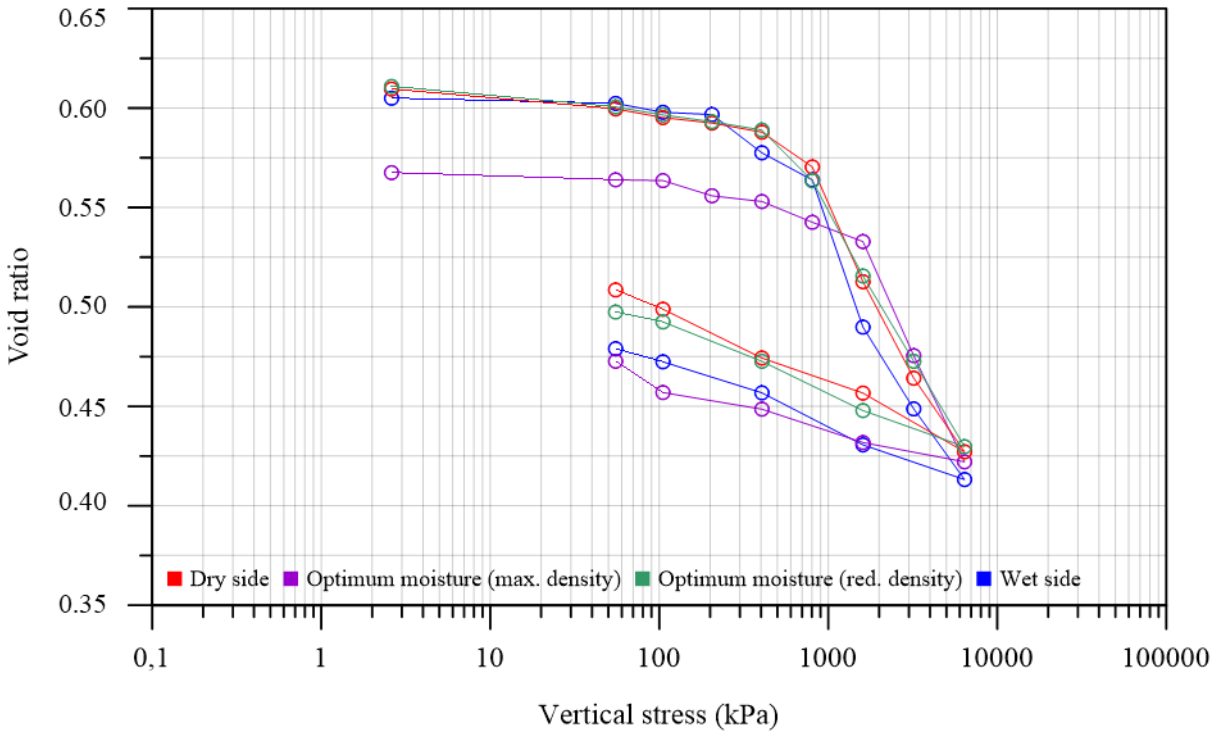

Figure 4.6. Compressibility results - standard energy - cemented IOTs

Regarding the initial moisture content influence, the cemented specimens for the standard compaction energy (Figure 4.6) resulted in a behavior analogous to the uncemented specimens.

That is, specimens molded at optimum moisture (max. density) resulted in lower settlements, followed by specimens molded at optimum moisture (red. density), dry-side, and wet-side. This attests that, although cement addition changes the soil fabric and structure, the moisture content influence on compressibility behavior still presents the same pattern; in which the increase in water content lubricates soil particles, increasing their workability and resulting in more compact arrangements. Thus, the density of the matrix increases with the increase of moisture content, until an optimum point is reached (air voids attain approximately a constant volume). From that point on, any further increase in water content leads to a decrease in density. After the optimum moisture content is reached, it becomes more difficult to force air out and to further reduce the air voids.

The same general behavior presented for the cemented standard energy specimens was evidenced for the cemented modified energy ones (Figure 4.7), with a classical pattern of a decreasing void ratio with increasing stress during the loading stages; behavior attributed to the densification of the soil structure with the increase in load application.

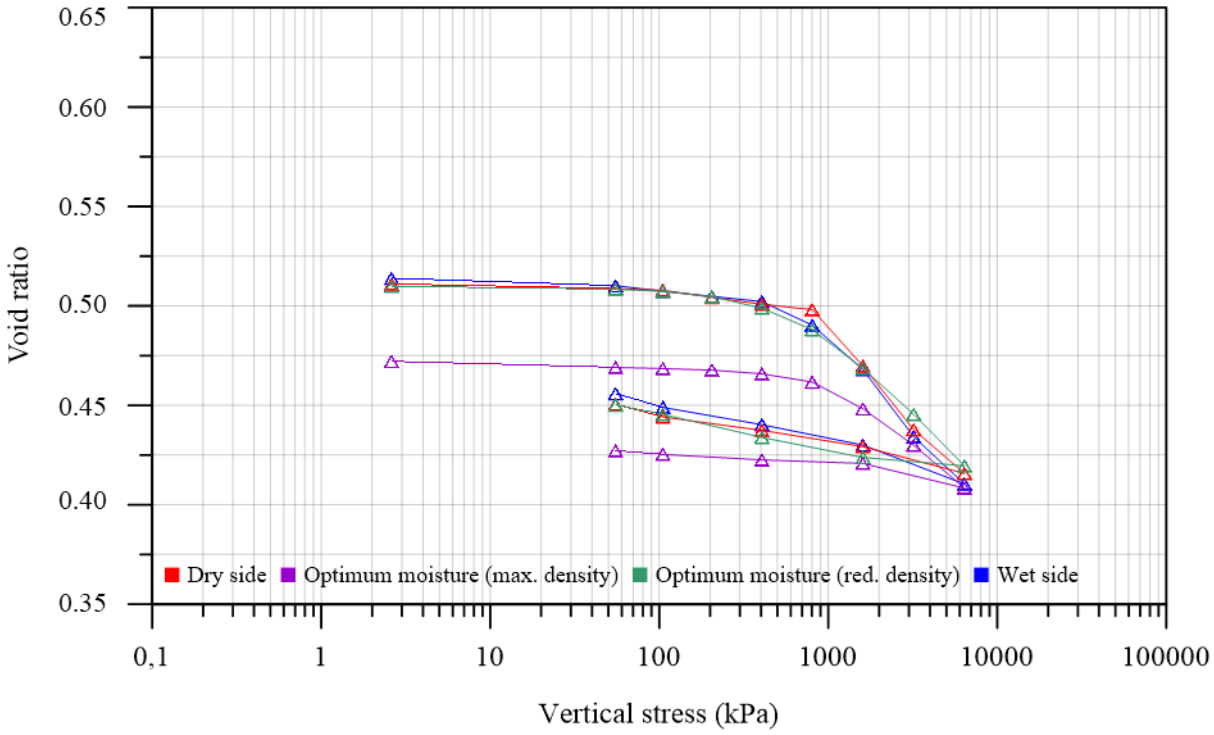

Figure 4.7. Compressibility results - modified energy - cemented IOTs

As for the influence of moisture content, once again, specimens molded at optimum moisture (max. density) resulted in lower settlements, followed by specimens molded at optimum moisture (red. density), dry-side, and wet-side. As for the same initial void ratio specimens, all

conditions resulted in extremely similar void ratios up to higher stress levels in which specimens molded at optimum moisture (red. density) had a slightly lower settlement when compared to dry-side and wet-side ones. The same reasoning exposed for the cemented standard energy specimens applies to this behavior; in which the soil fabric along the lubrication of the particles and the water expelling capability play vital roles on the settlement of the soil matrix.

Lastly, when comparing all cemented tests, the minimum void ratios reached at the last stress increment were all similar, independent of the initial molding condition. This indicates that even for cemented specimens, an indication of the critical state can be foreseen, alluding to the behavior presented on item 4.4.1.

4.4.3 Compressibility: uncemented versus cemented comparison

After analyzing the uncoupled effect of cementation, this section aims to discuss the results by comparing the data produced from uncemented and cemented mixtures. Figure 4.8 depicts the compressibility results for (a) uncemented specimens and (b) cemented specimens.

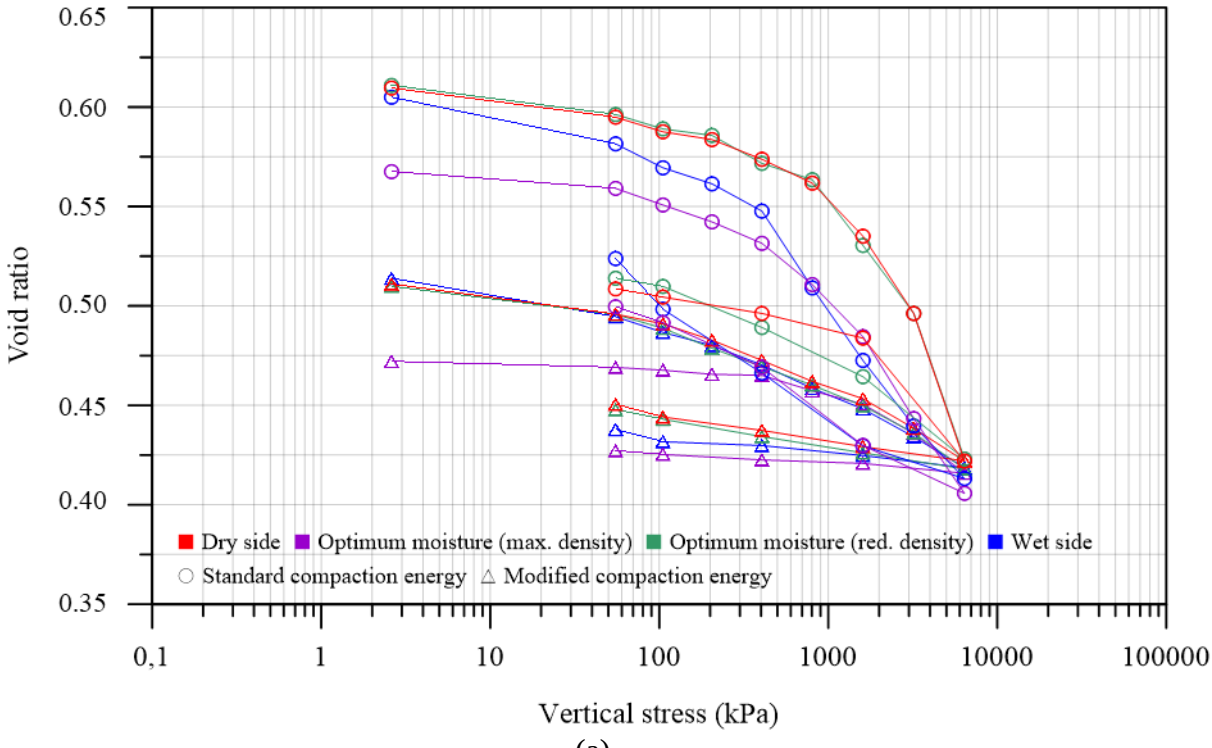

(a)

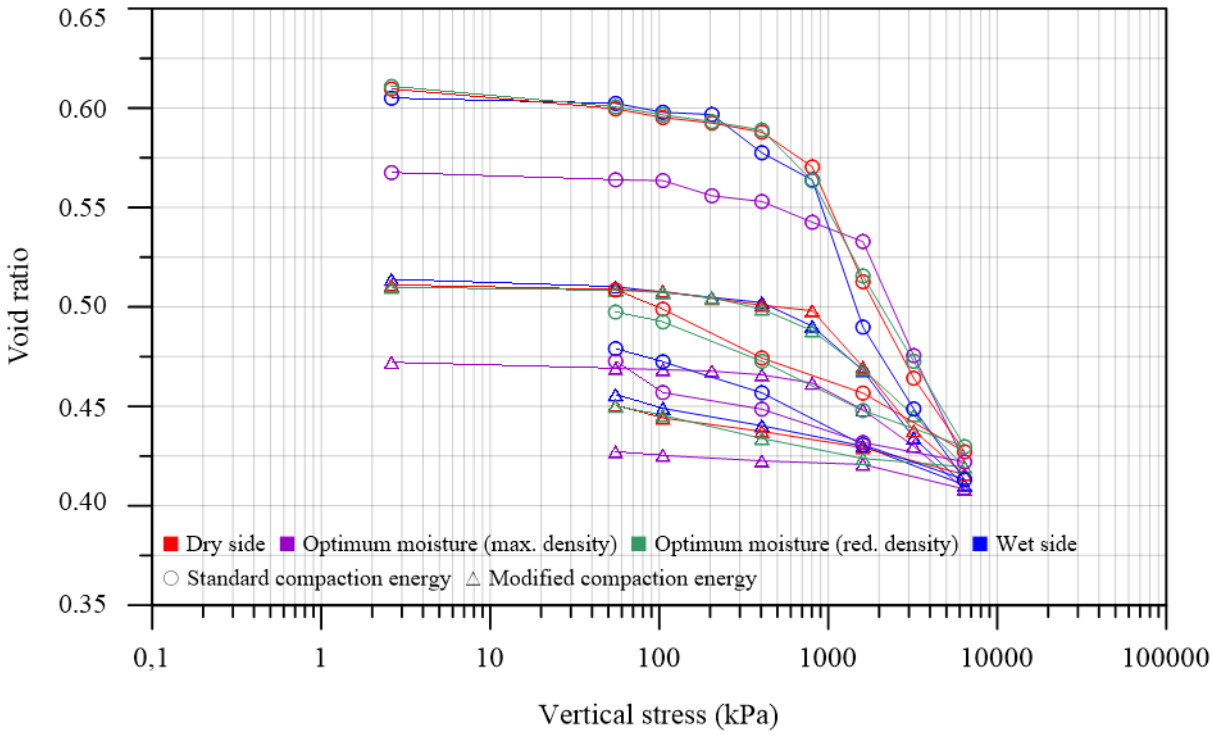

(b)

Figure 4.8. Compressibility results: (a) uncemented (b) cemented

By analyzing the data in Figure 4.8 it is clear that cement addition had a positive effect on the settlement of all specimens, independently of the initial molding conditions and molding energy. Higher the cement content, the greater the cementation-induced pre-consolidation stress, the more extended the reloading region, and the greater the vertical effective stress that can be sustained at a given void ratio. The increase in the pre-consolidation pressure and the shift of the compression curves to the higher vertical effective stress described are indications of the development of a stiffer soil structure with the treatment, when compared to uncemented specimens.

The structure is developed mainly as a result of the formation of the cement hydration products and their reactions with the soil particles. All these reactions are very sensitive to the chemical environment, especially the pH of the soil–cement system. As soon as cement gains access to water, formation of what are sometimes referred to in the soil cement literature (e.g., Aytekin and Nas, 1998; Broms, 1991; Consoli et al., 2018c; Eyo et al., 2021; Khadka et al., 2020; Suebsuk and Suksan, 2014; Tastan et al., 2011) as “primary cementitious products” starts. These include calcium silicate hydrate (*C–S–H*), calcium aluminate hydrate (*C–A–H*), and calcium hydroxide ($Ca(OH)_2$). Calcium silicate gel (*C–S–H*), which is formed from reaction of

the cement's tri-calcium silicate (*C3S*) and di-calcium silicate (*C2S*) with water, is the major source of the strength of the soil–cement mixture. Following these reactions, Ca^{2+} and OH^{-} ions are released into the pore water. The released OH– ions increase the pH of the pore water. Under high pH conditions, silica (SiO_2) and alumina (Al_2O_3) from the clay minerals are dissolved and combine with the released Ca^{2+} and OH^{-} ions to form "secondary" cementitious products (*C–S–H* and *C–A–H*). The amount of silica and alumina dissolved, and hence the amount of secondary cementitious products formed as a result of the reaction, are markedly dependent on the pH of the soil–cement system. Cemented specimens presented a lower variation of void ratios over the stress range until the 1MPa stress mark; from that point on the void ratios of the specimens tend to converge, indicating the initial breakage of the cementitious bonds and a possible indication of the critical state, alluding to the behavior presented on items 4.4.1 and 4.4.2.

4.5 TRIAXIAL COMPRESSION ANALYSIS

For the analysis of the triaxial compression results, the data was divided into two main subsections: overall stress-strain analysis and post-peak analysis. This division was created in order to facilitate the exposition of the results, as well as, the explanations regarding the evidenced behavior.

Regarding the initial condition of each sample, Table 4.4 presents the initial and post-consolidation void ratio values, as well as the value of effective confinement stress (initial *p'*) after consolidation.

Table 4.4. Initial and post consolidation void ratios triaxial testing

Specimen*	Initial void ratio	After consolidation void ratio
SD-DS-U-300	0.58	0.57
SD-OMM-U-300	0.54	0.53
SD-OMR-U-300	0.58	0.57
SD-WS-U-300	0.58	0.56
SD-DS-C-300	0.58	0.57
SD-OMM-C-300	0.54	0.53
SD-OMR-C-300	0.58	0.57
SD-WS-C-300	0.59	0.57
MO-DS-U-300	0.48	0.48
MO-OMR-U-300	0.44	0.43
MO-OMM-U-300	0.48	0.47
MO-WS-U-300	0.48	0.47
MO-DS-C-300	0.49	0.48
MO-OMR-C-300	0.44	0.43
MO-OMM-C-300	0.49	0.48
MO-WS-C-300	0.49	0.47

Specimen*	Initial void ratio	After consolidation void ratio
SD-DS-U-3000	0.58	0.43
SD-OMM-U-3000	0.54	0.43
SD-OMR-U-3000	0.58	0.43
SD-WS-U-3000	0.58	0.42
SD-DS-C-3000	0.58	0.43
SD-OMM-C-3000	0.54	0.43
SD-OMR-C-3000	0.58	0.43
SD-WS-C-3000	0.59	0.41
MO-DS-U-3000	0.48	0.41
MO-OMM-U-3000	0.44	0.40
MO-OMR-U-3000	0.48	0.42
MO-WS-U-3000	0.48	0.43
MO-DS-C-3000	0.49	0.41
MO-OMM-C-3000	0.44	0.41
MO-OMR-C-3000	0.49	0.42
MO-WS-C-3000	0.49	0.42

*W-X-Y-Z: Compaction energy [standard (SD) or modified (MD)]-Initial moisture content [dry side (DS), optimum moisture maximum density (OMM), optimum moisture reduced density (OMR), and wet side (WS)]-Cement content [uncemented (U) or cemented (C)]-Confining stress (300 or 3000).

4.5.1 Stress versus strain analysis

Aiming at a better understating of the exposed results, the stress versus strain analysis of the triaxial tests was divided into four subsections: (i) low confining stresses: standard compaction energy; (ii) low confining stresses: modified compaction energy; (iii) high confining stresses: standard compaction energy; and (iv) high confining stresses: modified compaction energy.

4.5.1.1 Low confining stresses: standard energy

The results of the uncemented low confining stress (p' = 300kPa) tests for the standard compaction energy are shown in Figure 4.9, in terms of deviatory stress (q) as a function of axial strain (εa).

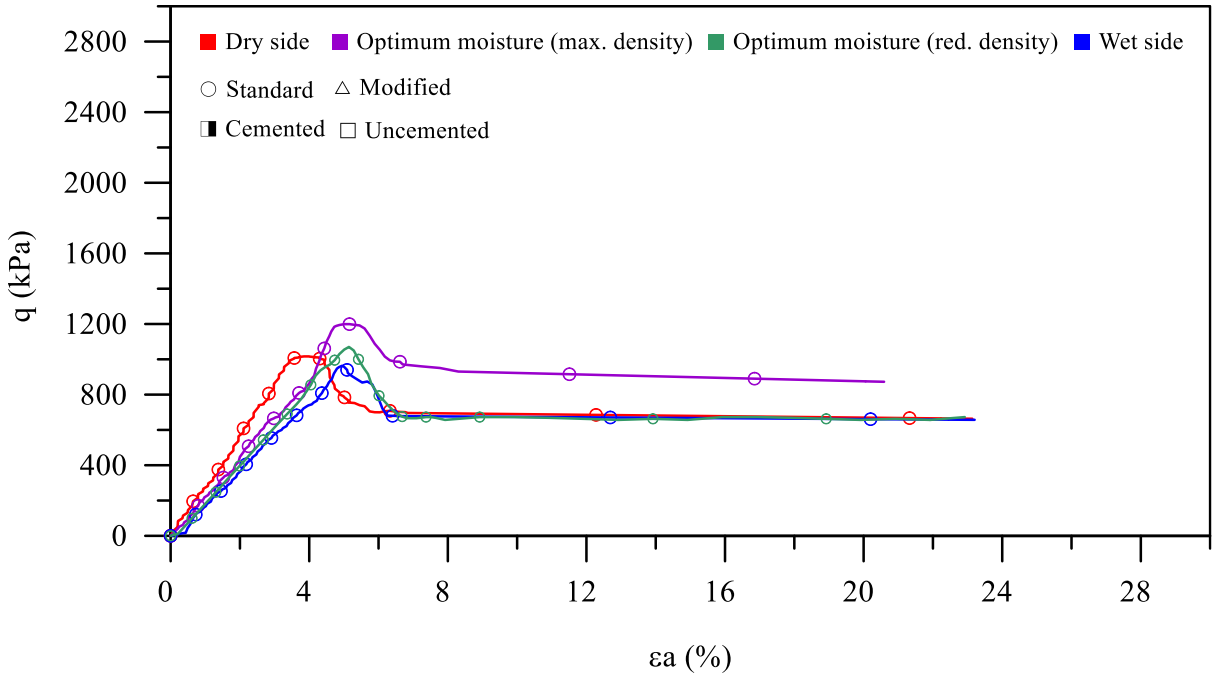

Figure 4.9. Stress-strain results for low confining stress standard compaction energy - uncemented specimens

As observed by Vick (1990), the characteristics of the stress-strain behavior of mining tailings are, in general, similar to those observed in soils of similar grain size distribution. For all specimens of the normal energy at low confining stresses (Figure 4.9), a classical strain-hardening behavior was evidenced until the peak of strength, followed by a strain-softening, with the strength of the *IOTs* generally reaching constant values between 5 and 20% strain. Post-peak reductions in shear stress are verified for samples subjected to low confining stresses. In these cases, the interlocking between the grains is not overcame by the consolidation stress and the sample exhibits a dilatant behavior during shearing, contrary to what happens for higher stresses.

The highest deviatory stress (q) value was evidenced for specimens molded at optimum moisture (max. density), followed by optimum moisture (red. density), dry-side, and wet-side ones. Considering that optimum moisture (max. density) specimens presented a slightly lower void ratio than the other combinations, a higher strength was expected. The reduction in porosity induces a greater contact area between soil particles, intensifying interlocking and mobilizing friction, which in turn increases strength.

When the void ratio influence is removed, it is possible to see that strength is directly affected by moisture content. In other words, the structure imparted by initial molding conditions is a fundamental aspect in *IOTs* geotechnical behavior. At low moisture contents, the soil mass is

normally stiffer and offers more resistance to shearing, this strength gain is evidenced until the optimum moisture content is reached. As the water content is further increased until the wet-side of the compaction curve is reached, the total void of the mixtures is highly increased, resulting in as impairment on strength. Finally, the peak for dry-side specimens was seen at lower strains, when compared to the other molding conditions. On the other hand, for optimum moisture content and wet-side specimens, the peak of strength was evidenced for similar strains. This behavior indicates that dry-side specimens present a higher stiffness, such as indicated on item 4.2. To further discuss on the stiffness behavior of low confining stress standard compaction energy uncemented specimens, the results presented in Figure 4.9 are now scaled down as shown in Figure 4.10.

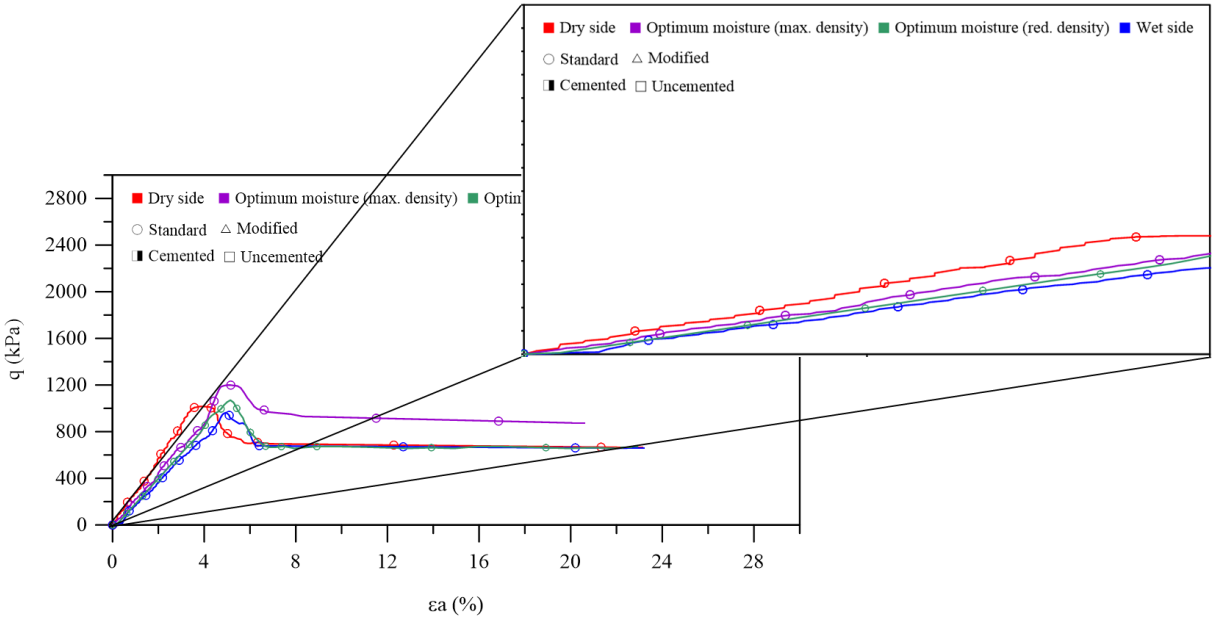

Figure 4.10. Scaled down stress-strain results for low confining stress standard compaction energy - uncemented specimens

From the data exposed on Figure 4.10 it is clear that the highest stiffest is evidenced for dry-side specimens (indicated by the inclination of the line), followed by specimens molded at optimum moisture (max. density), optimum moisture (red. density), and wet-side ones. This behavior indicates that stiffness cannot be simply and directly related to strength and initial void ratio, in other words, a more resistant specimen is not necessarily stiffer. Stiffness development was shown to be a more complex phenomenon involving not only the initial void ratio, but also other factors such as the initial moisture content and the soil fabric formed during the molding

procedures. Consoli et al. (2001) studied fundamental aspects of geotechnical behavior of conventional soils, depicting a similar behavior to the one found in this research; in which specimens molded at initial moisture contents below the optimum content resulted in a stiffer soil matrix, while specimens molded at the wet-side of the compaction curve resulted in the lowest stiffness values. The behavior was associated with the structure imparted by compaction, mainly density and packing (soil fabric) as well as the lubrication of the soil matrix particles, resulting from the different initial moisture content.

To further enhance the stiffness discussion, the triaxial data was also evaluated over the stiffness degradation in the shearing stage. For this purpose, Elasticity Theory was applied (Lambe and Whitman, 1979). The modulus of elasticity can be determined in two ways: through the tangent modulus (*Gtan*) and the secant modulus (*Gsec*). In this work, the determination of the tangent modulus was chosen, since, it represents a more reliable evaluation of the stiffness degradation. Thus, Figure 4.11 presents the shear modulus for low confining stress standard compaction energy of the uncemented specimens.

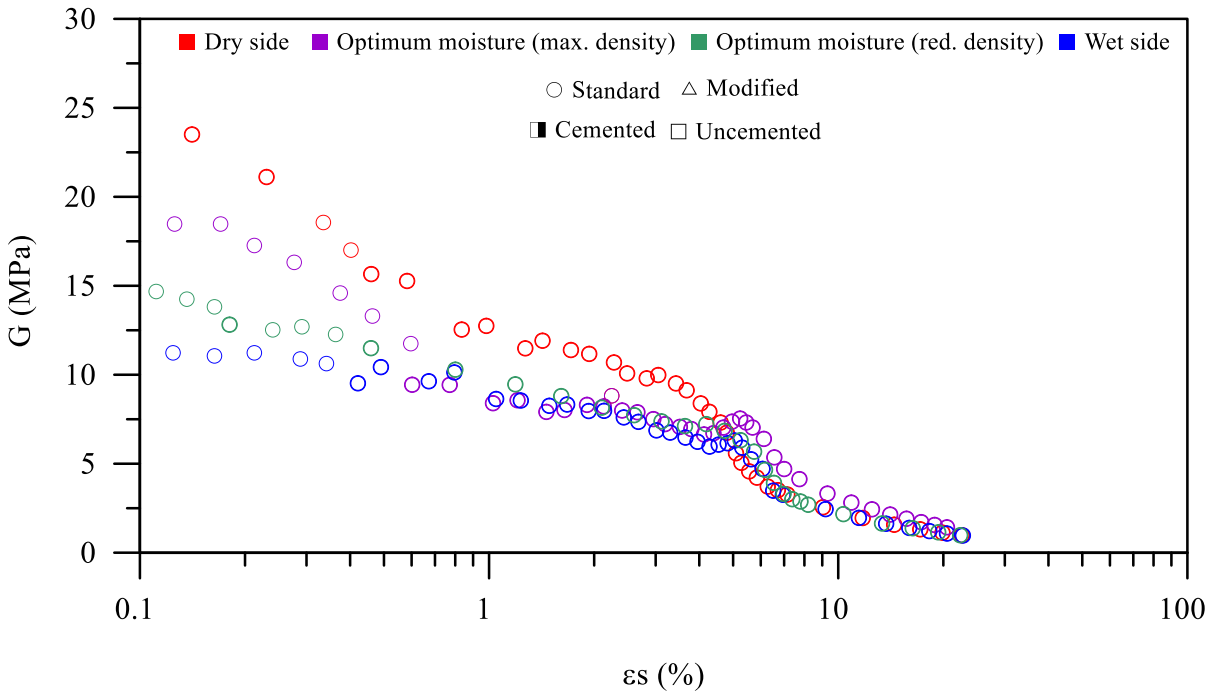

Figure 4.11. Shear modulus for low confining stress standard compaction energy - uncemented specimens

From the data shown in Figure 4.11 is possible to confirm the analysis conducted in Figure 4.10, regarding stiffness of the specimens; in which the highest stiffest is evidenced for dry-

side specimens, followed by specimens molded at optimum moisture (max. density), optimum moisture (red. density), and wet-side ones. In addition, a typical stiffness degradation behavior for conventional soils is shown, in which the increase in strain leads to a decrease in stiffness, as a result from the shearing of the specimen. The stiffness degradation behavior over shearing has also been attested by Åhnberg, (2007); Consoli et al. (2009); Hoyos et al. (2011); Lirer et al. (2011); Mmbando et al. (2023); Mousa et al. (2021).

The results of volumetric strain versus axial strain for uncemented specimens molded at standard compaction energy under low confining stress are shown in Figure 4.12.

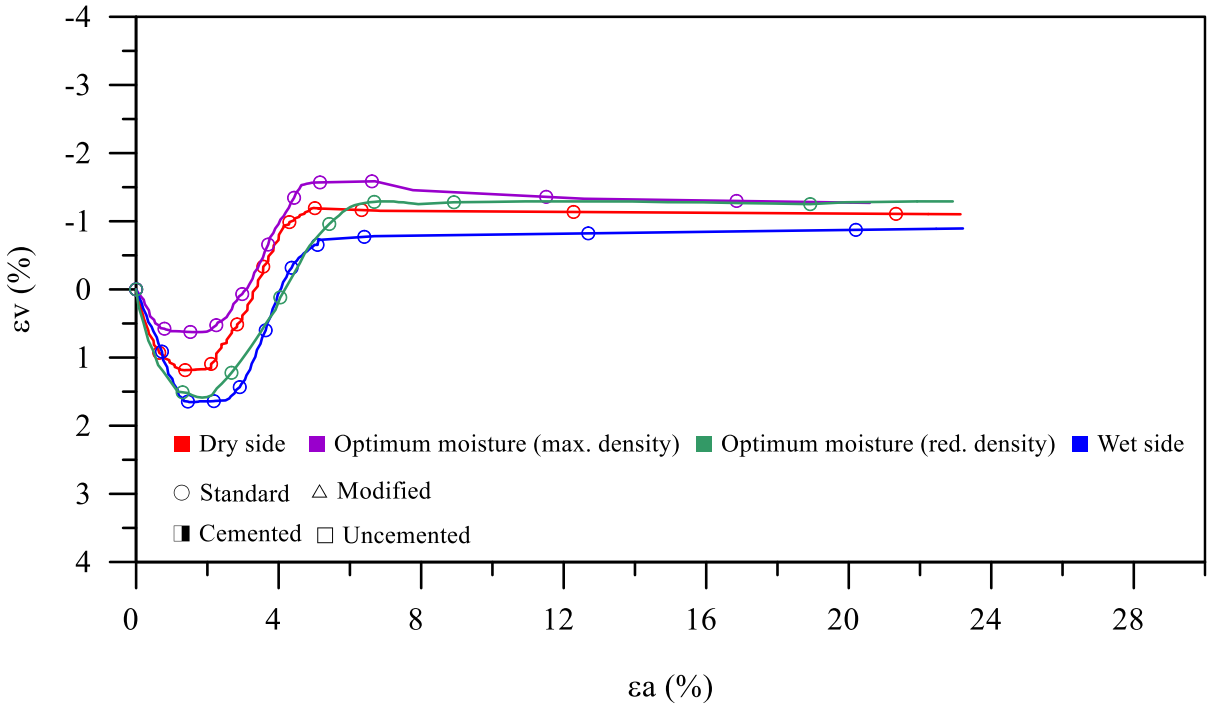

Figure 4.12. Volumetric versus axial strain for low confining stress standard compaction energy - uncemented specimens

All specimens depicted an initial compressive behavior, followed by an expansive one; this behavior is a typical conventional soil behavior for dense specimens, such as the case of this research. The initial compressive behavior is due to adjustment/accommodation of the soil particles, followed by the dilative behavior due to the interlocking of the grains.

Specimens molded at optimum moisture (max. density), resulted in lower compression and higher expansion when compared to the other studied combinations. This behavior can be associated with the lower initial void ratio of optimum moisture content specimens; considering

that these specimens presented a more compact initial matrix, particles had less space to accommodate resulting in an increased particle movement into a more close-packed array. When isolating the void ratio effect, dry-side specimens resulted in a less compressive and more dilative behavior. This is associated with the higher lubrication of the soil particles from the increased moisture content; in both optimum moisture (red. density) and wet-side arrangements the particles are able to more easily slide into the voids, allowing more compression and, consequently, less dilation.

After discussing the uncemented data, the results of the cemented low confining stress tests for the standard compaction energy are shown in Figure 4.13, in terms of deviatory stress (q) as a function of axial strain (εa).

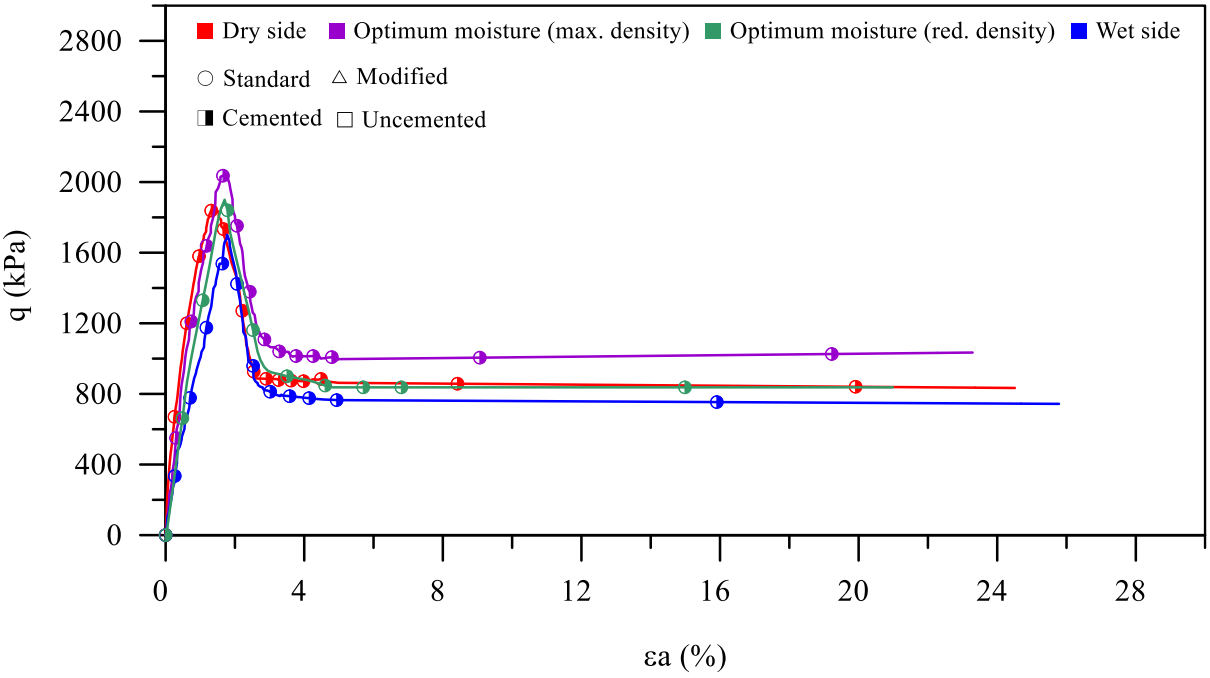

Figure 4.13. Stress-strain results for low confining stress standard compaction energy - cemented specimens

All cemented specimens, of the standard energy at low confining stresses (Figure 4.13), showed a pronounced peak point associated with the failure of the material. After that, the slope of the stress-strain curve decreased to a residual value in an axial strain. Once again, post-peak reductions in shear stresses were verified for specimens subjected to low confining stresses. It should be noted that the chemical stabilization of soils and the reactions and interactions between the soils and stabilizing materials contribute to the strength growth. Due to the pozzolanic reactions, cemented materials are formed, lead to increasing the bonds between the

soil grains, raising the strength. These series of chemical reactions result in the subsequent setting and hardening of the cemented soil mixture. Needle-like crystals of calcium sulfoaluminate hydrate, namely ettringite, are formed within a few minutes. The ettringite subsequently transforms to monosulfate hydrate after a time. Two hours after the start of the cementation process, large prismatic crystals of calcium hydroxide (*CH*) and very small crystals of calcium silicate hydrates begin to fill the empty pores previously occupied by water and air and the hydrated cement particles. Therefore, the major components formed components in the mixtures are: calcium silicate hydrate, calcium hydroxide, and calcium sulfoaluminate.

Such as in the case of uncemented specimens, the highest deviatory stress (q) value of cemented specimens was evidenced for specimens molded at optimum moisture (max. density), followed by optimum moisture (red. density), dry-side, and wet-side ones. This behavior was also associated with the initial void ratio of the optimum moisture (max. density) mixtures, in which a slightly lower void ratio is evidenced. The lower porosity induces a greater contact area between soil particles, intensifying interlocking and mobilizing friction, which in turn increases strength. When removing the void ratio influence and considering the initial moisture content for same void ratio specimens, optimum moisture (red. density) specimens resulted in higher deviatory stress values when compared to the other combinations. Lower moisture contents result in a more resistant soil fabric until the optimum moisture content is reached, from that point on the increase in moisture content results in a less stiff arrangement, with less strength capacity. Once again, the peak for dry-side specimens was evidenced at lower strains, when compared to the other molding conditions. On the other hand, for optimum moisture content and wet-side specimens, the peak of strength was evidenced for similar strains. This behavior indicates that dry-side specimens present a higher stiffness, such as indicated on item 4.2.

To further discuss on the stiffness behavior of low confining stress standard compaction energy cemented specimens, the results presented in Figure 4.13 were scaled down and are shown in Figure 4.14.

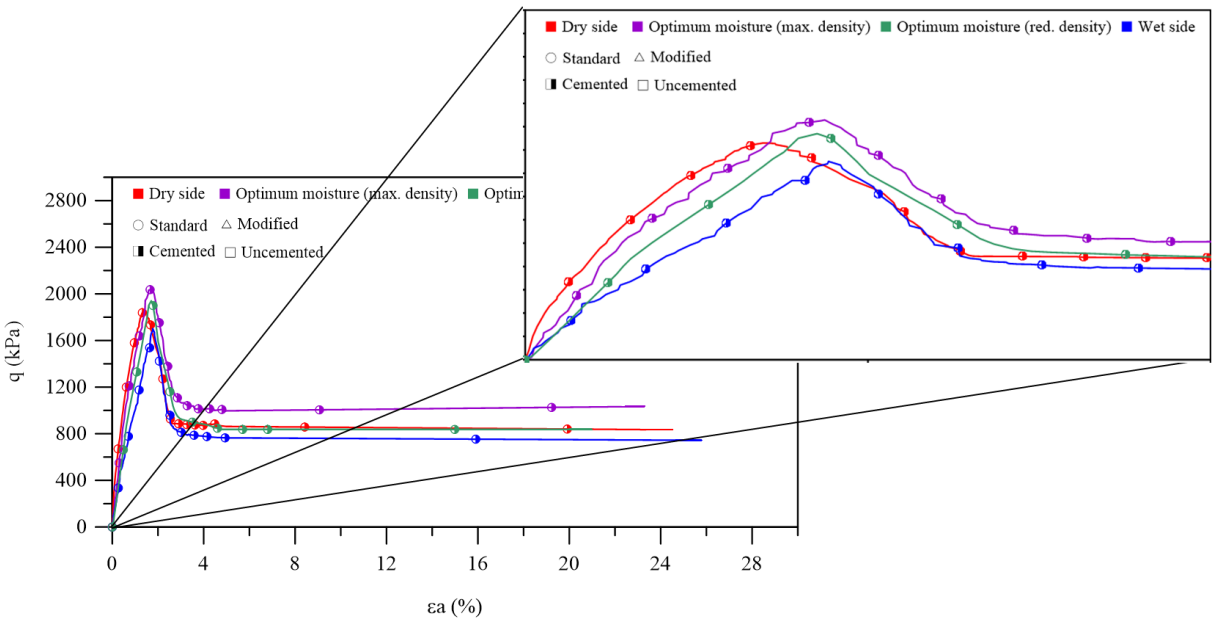

Figure 4.14. Scaled down stress-strain results for low confining stress standard compaction energy - cemented specimens.

Figure 4.14 indicates that the highest stiffest is evidenced for dry-side specimens (indicated by the inclination of the line), followed by specimens molded at optimum moisture (max. density), optimum moisture (red. density), and wet-side ones. This behavior is similar to the one presented for uncemented specimens, in which stiffness cannot be simply and directly related to strength and initial void ratio, but a rather complex phenomenon associated with the structure imparted by compaction (soil fabric), mainly density and packing as well as the lubrication of the soil matrix particles, resulting from the different initial moisture content.

To further enhance the stiffness discussion, the triaxial data was also evaluated over the stiffness degradation in the shearing stage, applying the Elasticity Theory (Lambe and Whitman, 1979) such as for the uncemented specimens. To this extent, Figure 4.15 presents the shear modulus of cemented specimens for low confining stress standard compaction energy.

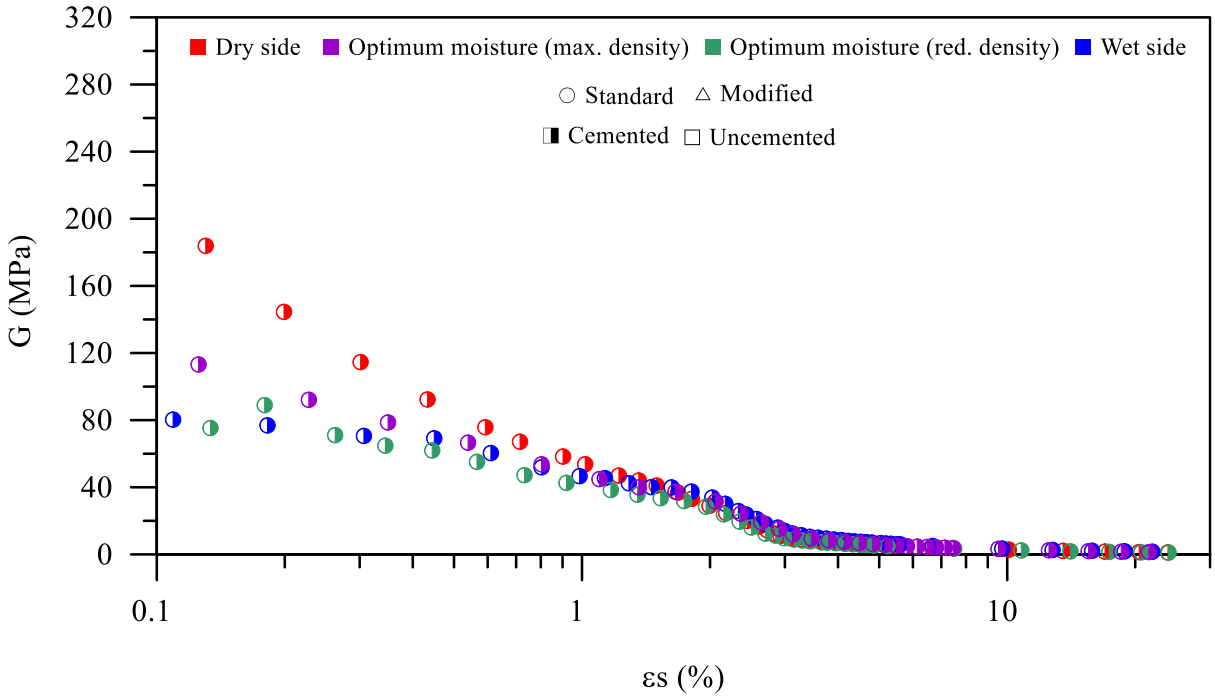

Figure 4.15. Shear modulus for low confining stress standard compaction energy - cemented specimens.

The results of Figure 4.15 attest for the analysis conducted in the stress-strain behavior regarding the stiffness of the specimens; thee highest stiffest is evidenced for dry-side specimens, followed by specimens molded at optimum moisture (max. density), optimum moisture (red. density), and wet-side ones. Furthermore, a typical stiffness degradation behavior for conventional soils is shown, in which the increase in strain leads to a decrease in stiffness, as a result from the shearing of the specimen. The stiffness degradation behavior over shearing has also been attested by Andreghetto et al. (2022); Consoli et al. (2009b); Corrêa-Silva et al. (2020); Jallu et al. (2020).

The results of volumetric strain versus axial strain for cemented specimens of standard compaction energy under low confining stress are shown in Figure 4.16.

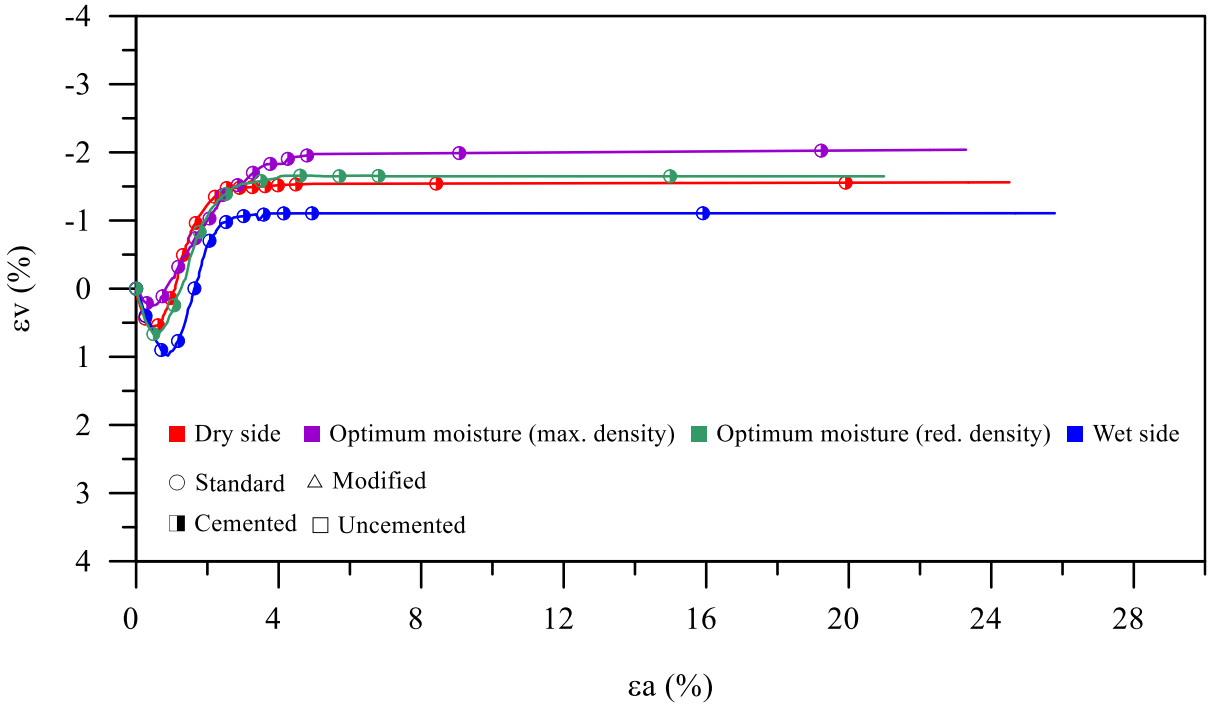

Figure 4.16. Volumetric versus axial strain for low confining stress standard compaction energy - cemented specimens.

Such as in the case of uncemented specimens, the cemented specimens resulted in an initial compressive behavior, followed by an expansive one, with this behavior being typical of dense geotechnical materials, such as the case of this research. The initial compressive behavior is due to adjustment/accommodation of the soil particles, followed by the dilative behavior due to the interlocking of the grains.

Comparing all molding conditions, specimens molded at optimum moisture (max. density) resulted in lower compression and higher expansion when compared to the other combinations. This behavior is once again associated with the lower initial void ratio of these specimens; in a more compact initial matrix, particles have less space to accommodate resulting in a more close-packed array, enhancing expansion. When comparing same initial void ratio specimens the contractive behavior was more prominent for specimens of high moisture content, while the dilative one presented higher magnitude for dry-side specimens. This contractive/dilative behavior is linked with the higher lubrication of the soil particles from the increase moisture content. On the wet-side of the compaction curve soil particles are able to more easily slide into the voids, allowing more compression and, consequently, less dilation.

4.5.1.2 Low confining stresses: modified energy

The results of the uncemented specimens under low confining stress (p' = 300kPa) tests molded at the standard modified compaction energy are shown in Figure 4.17, in terms of deviatory stress (q) as a function of axial strain (εa).

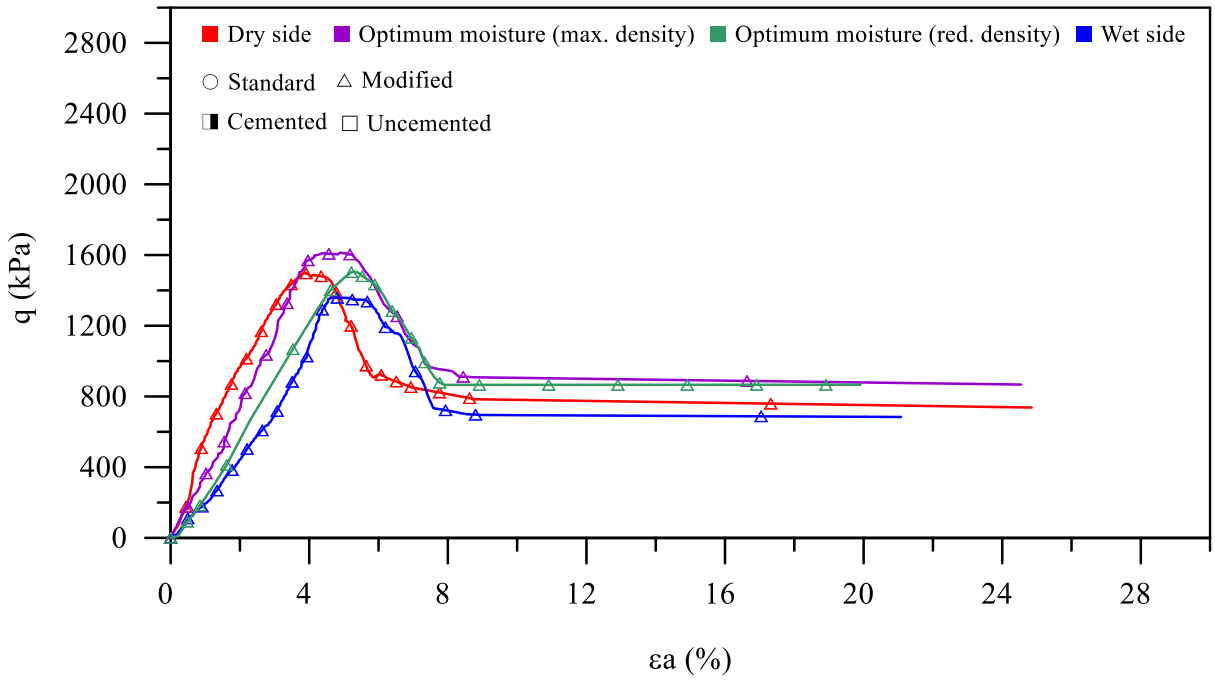

Figure 4.17. Stress-strain results for low confining stress modified compaction energy - uncemented specimens.

Similar to the behavior presented for the standard compaction energy (item 4.5.1.1), modified compaction energy specimens presented a classical strain-hardening behavior until the peak of strength was reached, from that point on a strain-softening behavior took place; the strength of the *IOTs* generally reaching constant values at approximately 10% of strain. These post-peak reductions are evidenced when the interlocking between the grains is not overcame by the consolidation stress and the specimens normally exhibit a dilatant behavior during shearing. As for the deviatory stress, the highest value was evidenced for optimum moisture (max. density) specimens, followed by optimum moisture (red. density), dry-side, and wet-side ones.

The aforementioned behavior was once again associated with the initial molding conditions of the samples, as thoroughly explained on items 4.1, 4.2, and 4.5.1.1; with the only noticeable difference being the magnitude of the values, in which modified compaction energy specimens resulted in higher stress values, due to the lower initial void ratios and, consequently, higher

friction mobilization between particles. Another important piece of information that can be extracted from Figure 4.17, is on the stiffness of the specimens (represented by the slope of the line). To better visualize this slope and discuss the stiffness, the results shown on Figure 4.17 were scaled down and are shown in Figure 4.18.

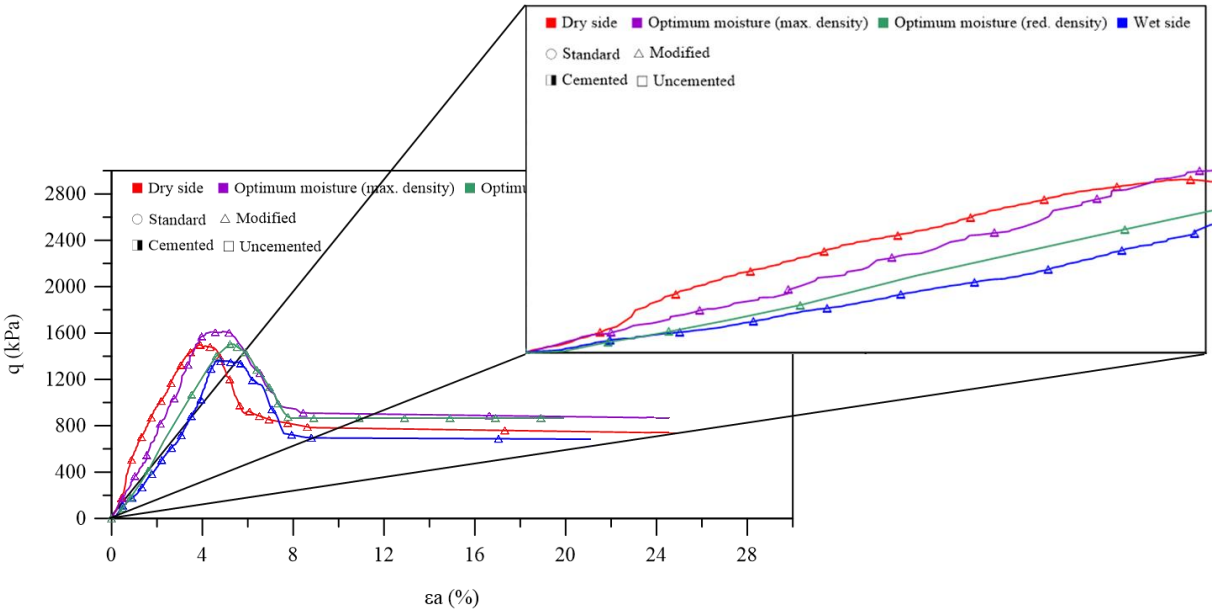

Figure 4.18. Scaled down stress-strain results for low confining stress modifiied compaction energy - uncemented specimens.

By analyzing Figure 4.18 it is clear that the highest stiffest is evidenced for dry-side specimens (indicated by the slope of the line), followed by specimens molded at optimum moisture (max. density), optimum moisture (red. density), and wet-side ones. This behavior indicates that even for different compaction energies, the same pattern is evidenced, in which stiffness cannot be simply and directly related to strength and initial void ratio. Stiffness of geotechnical materials is a rather complex phenomenon influenced by several initial molding conditions (e.g., initial moisture content). As stated by Consoli (2001), specimens molded at initial moisture contents below the optimum content resulted in a stiffer soil matrix, while specimens molded at the wet-side of the compaction curve resulted in the lowest stiffness values; this can be explained by the structure imparted in compaction, mainly density and packing as well as the lubrication of the soil matrix particles, resulting from the different initial moisture content.

In this sense, the triaxial data was also evaluated over the stiffness degradation in the shearing stage, applying the Elasticity Theory (Lambe and Whitman, 1979) based on the explanations

provided on item 4.5.1.1. Thus, Figure 4.19 presents the shear modulus of cemented specimens for low confining stress modified compaction energy.

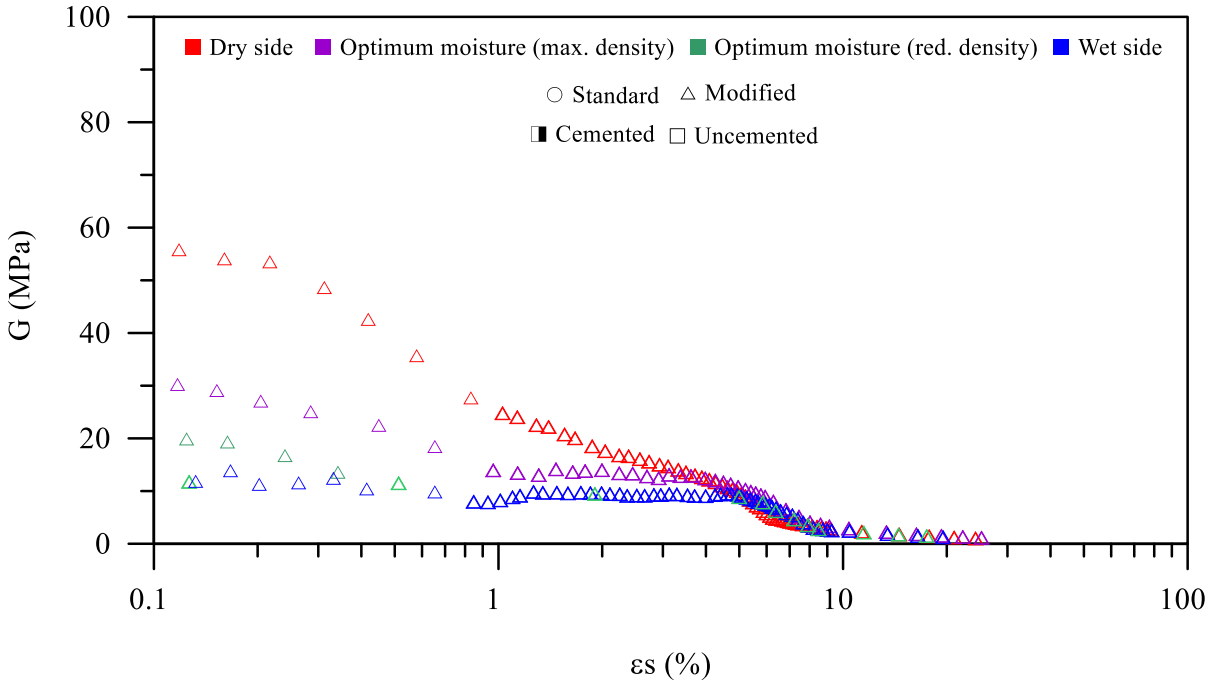

Figure 4.19. Shear modulus for low confining stress modified compaction energy - uncemented specimens.

The data shown in Figure 4.19 corroborates the analysis conducted in the stress-strain behavior regarding the stiffness of the specimen. In addition, a typical stiffness degradation behavior for conventional soils is shown, in which the increase in strain leads to a decrease in stiffness, as a result from the shearing of the specimen. The stiffness degradation behavior over shearing has also been attested by Åhnberg, (2007); Consoli et al. (2009); Hoyos et al. (2011); Lirer et al. (2011); Mmbando et al. (2023); Mousa et al. (2021). When comparing the influence of compaction energy, the only noticeable difference was the magnitude of the values, in which modified compaction energy specimens resulted in higher stiffness values, due to the lower initial void ratios and, consequently, higher friction mobilization between particles.

The results of volumetric strain versus axial strain for uncemented specimens molded at modified compaction energy under low confining stress are shown in Figure 4.12.

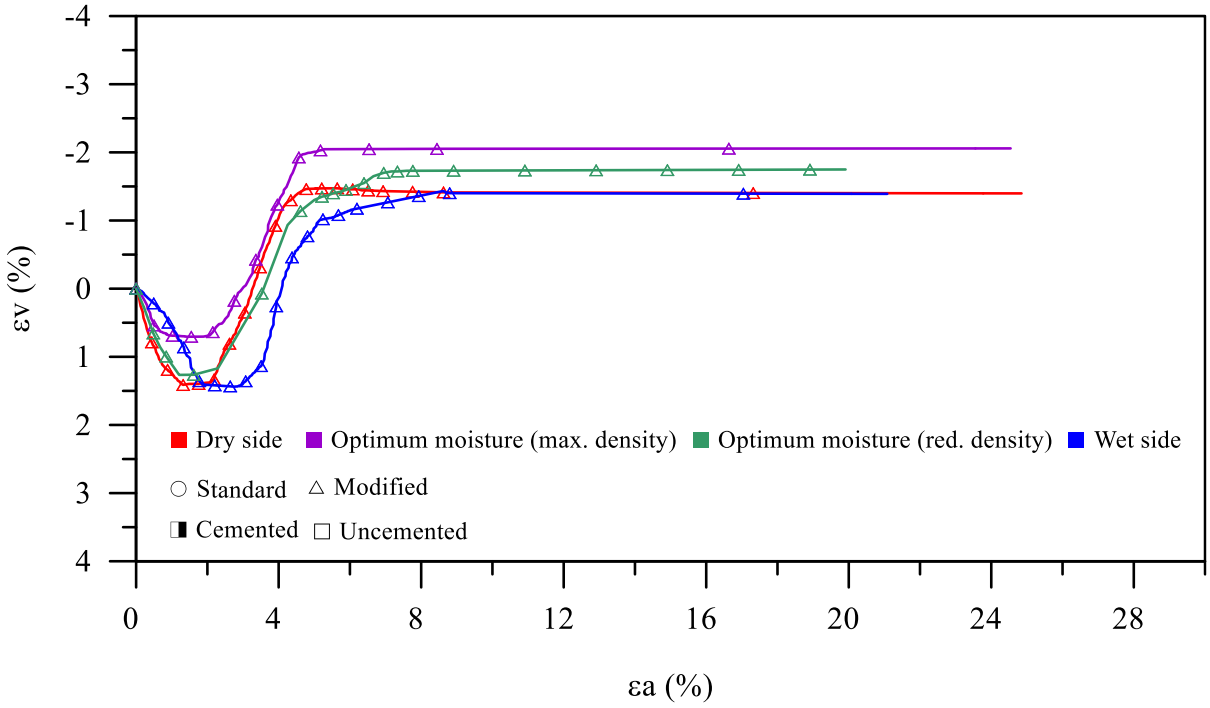

Figure 4.20. Volumetric versus axial strain for low confining stress modified compaction energy - uncemented specimens.

For all studied molding conditions, specimens were initially contractive, followed by a dilative behavior (which is a typical conventional soil behavior for dense specimens). The initial compressive behavior is due to adjustment/accommodation of the soil particles, followed by the dilative behavior due to the interlocking of the grains.

For the optimum moisture (max. density), specimens showed the least contractive and most dilative behavior; this can be explained by the lower initial void ratio of such specimens. A more compact initial structure leaves less space for particles to accommodate, in addition to resulting in a more close-packed array (higher dilation). By isolating the void ratio influence, specimens molded at the dry side of the compaction curve resulted in a less compressive and more dilative behavior when compared to wet-side specimens. This behavior can be explained by the higher lubrication of the soil particles from the increase moisture content; in wet-side arrangements the particles are able to more easily slide into the voids, allowing more compression and, consequently, less dilation.

Finally, when comparing the influence of compaction energy on the strain behavior, the only difference between specimens was the magnitude of the values, in which modified compaction energy specimens resulted in lower strain values due to the lower initial void ratios.

After discussing the uncemented data for the modified energy specimens, the results of the cemented low confining stress tests for the modified compaction energy are shown in Figure 4.21, in terms of deviatory stress (*q*) as a function of axial strain (*εa*).

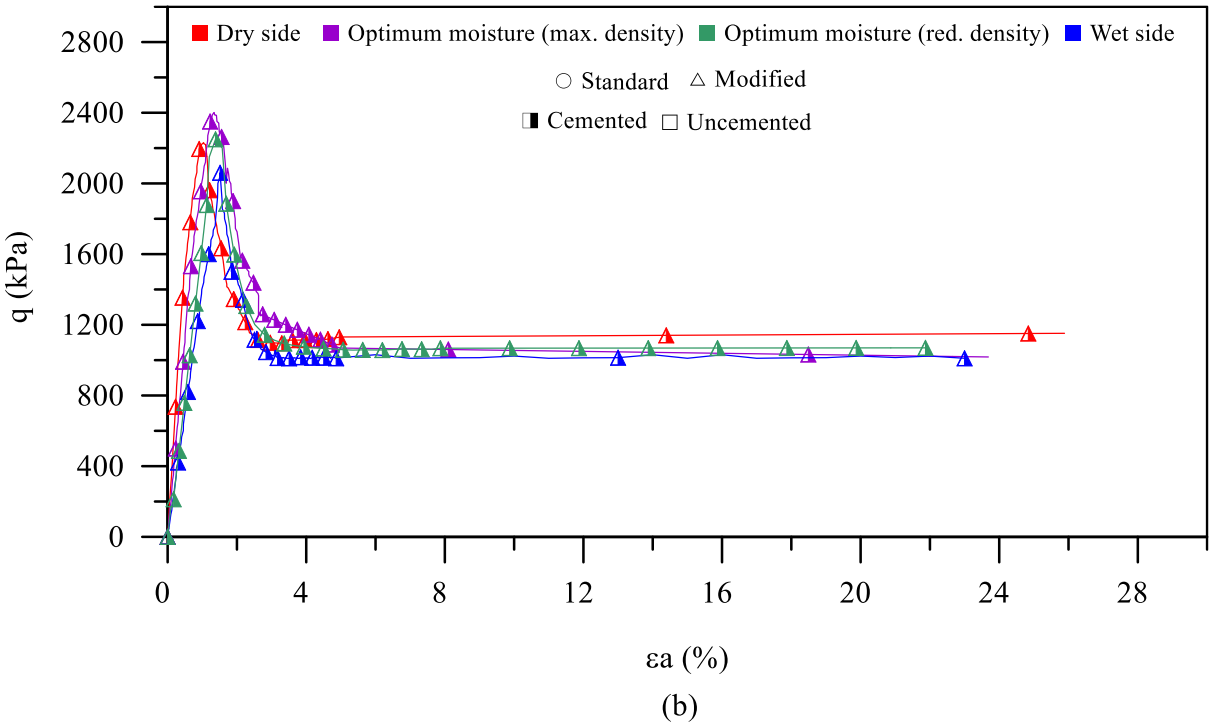

(b)

Figure 4.21. Stress-strain results for low confining stress modified compaction energy - cemented specimens.

In the stress-strain results (Figure 4.21), all specimens presented a pronounced peak point followed by a considerable strength reduction, this reduction being associated with the failure of the specimens. These post-peak reductions in shear stresses were verified for specimens subjected to low confining stresses; in such cases, the interlocking between the grains is not overcome by the consolidation stress and the sample exhibits a dilatant behavior during shearing. When comparing cemented and uncemented specimens, for the modified compaction energy, it is clear that the cement addition led to an improvement of the mechanical behavior (evidenced in the higher deviatory stress values). This improvement is associated with a series of chemical reactions resulting from the subsequent setting and hardening of the cemented *IOTs* mixture, thoroughly discussed in items 4.1, 4.2, 4.4, and 4.5.1.1.

Figure 4.21 also sheds light on the stiffness behavior of the mixtures, represented by the initial slope of the data. To facilitate the visualization and further discuss such information, the results shown in Figure 4.21 were scaled down and are depicted in Figure 4.22.

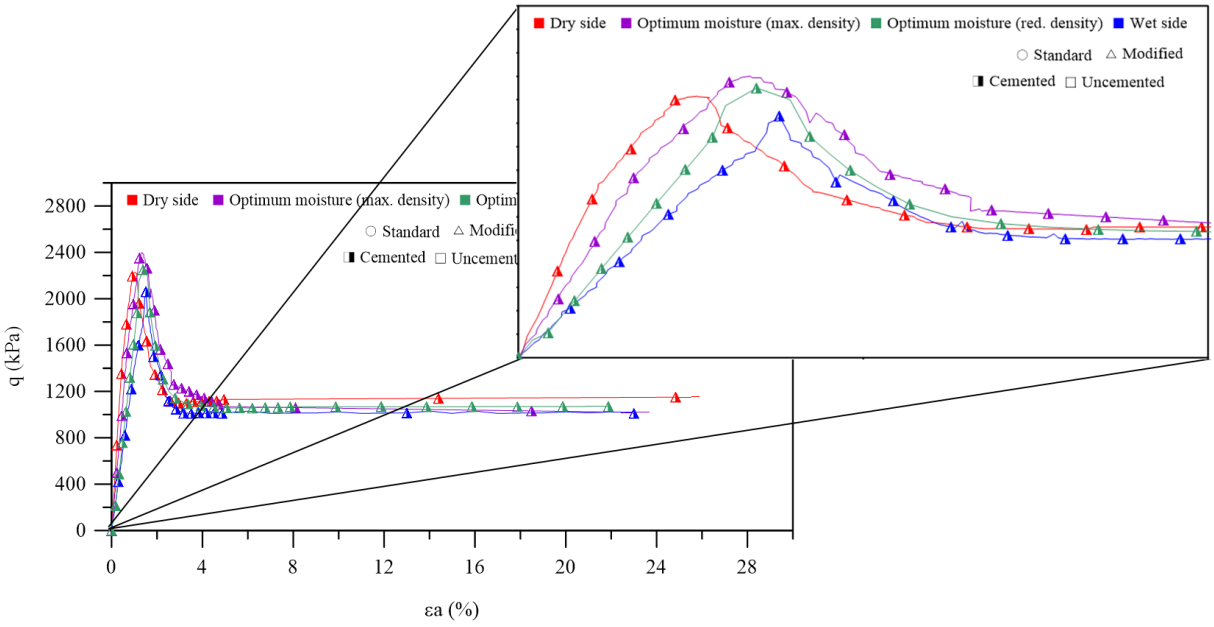

Figure 4.22. Scaled down stress-strain results for low confining stress modified compaction energy - cemented specimens.

Once again, the highest stiffest was evidenced for dry-side specimens (indicated by the slope of the line), followed by specimens molded at optimum moisture (max. density), optimum moisture (red. density), and wet-side ones. This behavior attests that regardless of the compaction energy (standard or modified) or the degree of cementation (0 or 3%) of the specimens, the same pattern is evidenced, indicating that stiffness is indeed a phenomenon that depends on the initial moisture content. The structure imparted in compaction plays a fundamental role on the generation of stiffness.

The triaxial data was also evaluated over the stiffness degradation in the shearing stage, applying the Elasticity Theory (Lambe and Whitman, 1979), in accordance with the presented in Item 4.5.1.1. In such a manner, Figure 4.23 presents the shear modulus of cemented specimens for low confining stress standard compaction energy.

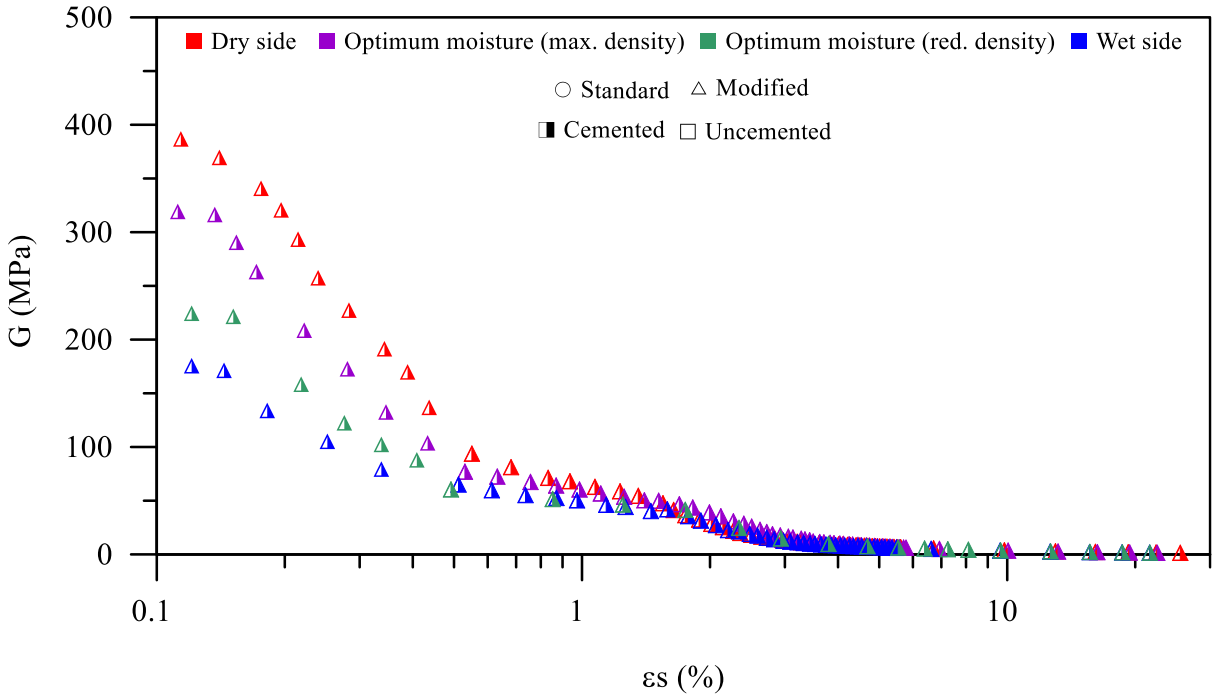

Figure 4.23. Shear modulus for low confining stress modified compaction energy - cemented specimens.

The results from Figure 4.23 attest to the aforementioned analysis for the stiffness behavior. Furthermore, a typical stiffness degradation behavior for conventional materials is evidenced, in which the increase in strain leads to a decrease in stiffness, as a result of the shearing of the specimen. Such a behavior has been thoroughly discussed in the beginning of this subsection. Finally, when comparing the influence of compaction energy, the only significant difference was the magnitude of the values, in which modified compaction energy specimens resulted in higher stiffness values, due to the lower initial void ratios and, consequently, higher friction mobilization between particles.

The results of volumetric strain versus axial strain for uncemented specimens molded at modified compaction energy under low confining stress are shown in Figure 4.24.

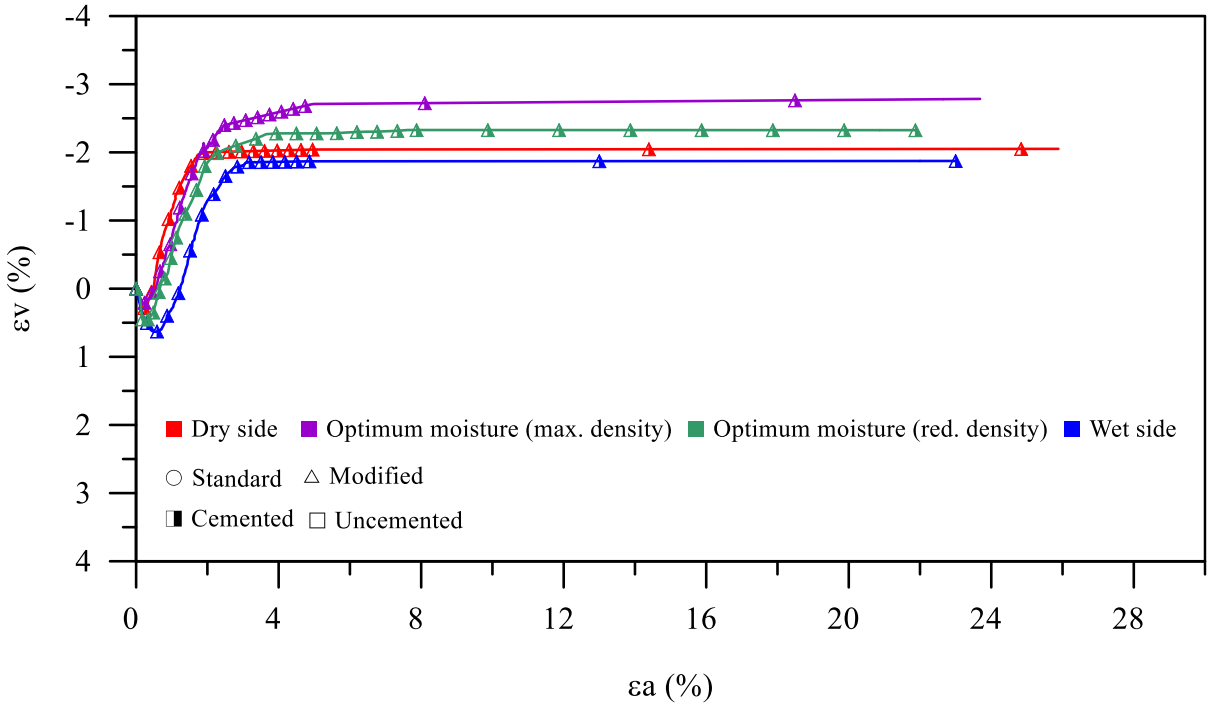

Figure 4.24. Volumetric versus axial strain for low confining stress modified compaction energy - uncemented specimens.

The strain behavior presented for the uncemented specimens was evidenced for the cemented ones, in which specimens were initially contractive, followed by dilative behavior. The initial compressive behavior is due to the adjustment/accommodation of the soil particles, followed by the dilative behavior due to the interlocking of the grains.

It is clear that cement addition results in a positive effect on the *IOTs* mechanical properties for both studied compaction energies. When cement is added to a geotechnical material, the chemical and physical properties are changed. Cement reduces the plasticity and water-holding capacity of the material while increasing its strength. The degree of stabilization depends upon the type of cement used, the type of geotechnical material, and some other factors such as water content, the proportion of mixing, degree of compaction, and curing.

Several studies can attest to this improvement behavior for conventional soils. Most previous studies have suggested that the addition of cement to granular soil (with a similar grain size distribution to *IOTs*) increases the soil's strength and, at the same time, makes its behavior more brittle. According to the Mohr–Coulomb Theory, the shear strength of a soil is a function of its adhesion and friction angle. While soil cementation is reported to increase soil adhesion, most studies have not reported a significant change in the friction angle of soil. Clough et al. (1981) studied the failure envelope of cementitious and non-cementitious soil and found the results to be parallel. Lade and Overton (1989) found the failure envelope of cementitious soil to be

curvaceous. By emphasizing the behavior friability of cementitious soil, Clough et al. (1981) showed that the peak strength of these soils occurs at low strains. Evidently, cementitious soil has more elastic hardness than non-cementitious soil. Leroueil and Vaughan (1990) declared the occurrence of the yield point as a hallmark of cementitious soils. Failure of cementitious soils is visible in different loading states, such as isotropic pressure, shear, and loading. It is very rare for cement bands among the grains to be reduced and destroyed after the yield point. It should also be noted that increasing the pressure of all-round diversion reduces the effect of cementation and, instead shifts the behavior from friability to a softer and transformable one. Molenaar and Venmans (1993) showed that the failure level for cementitious soil is increased by increasing the content and cement percentage. Therefore, it is possible to achieve higher levels of stress in cemented-treated geotechnical materials. More recently, similar behavior has also been attested for stabilized mining tailings, in the works of Bruschi et al. (2021c); Pereira dos Santos et al. (2022).

4.5.1.3 Low confining stresses: standard and modified energy tests unification

A unification/summary of the stress-strain behavior, for all specimens tested under low confining stresses, presented on Items 4.5.1.1 and 4.5.1.2, is depicted on Figure 4.25.

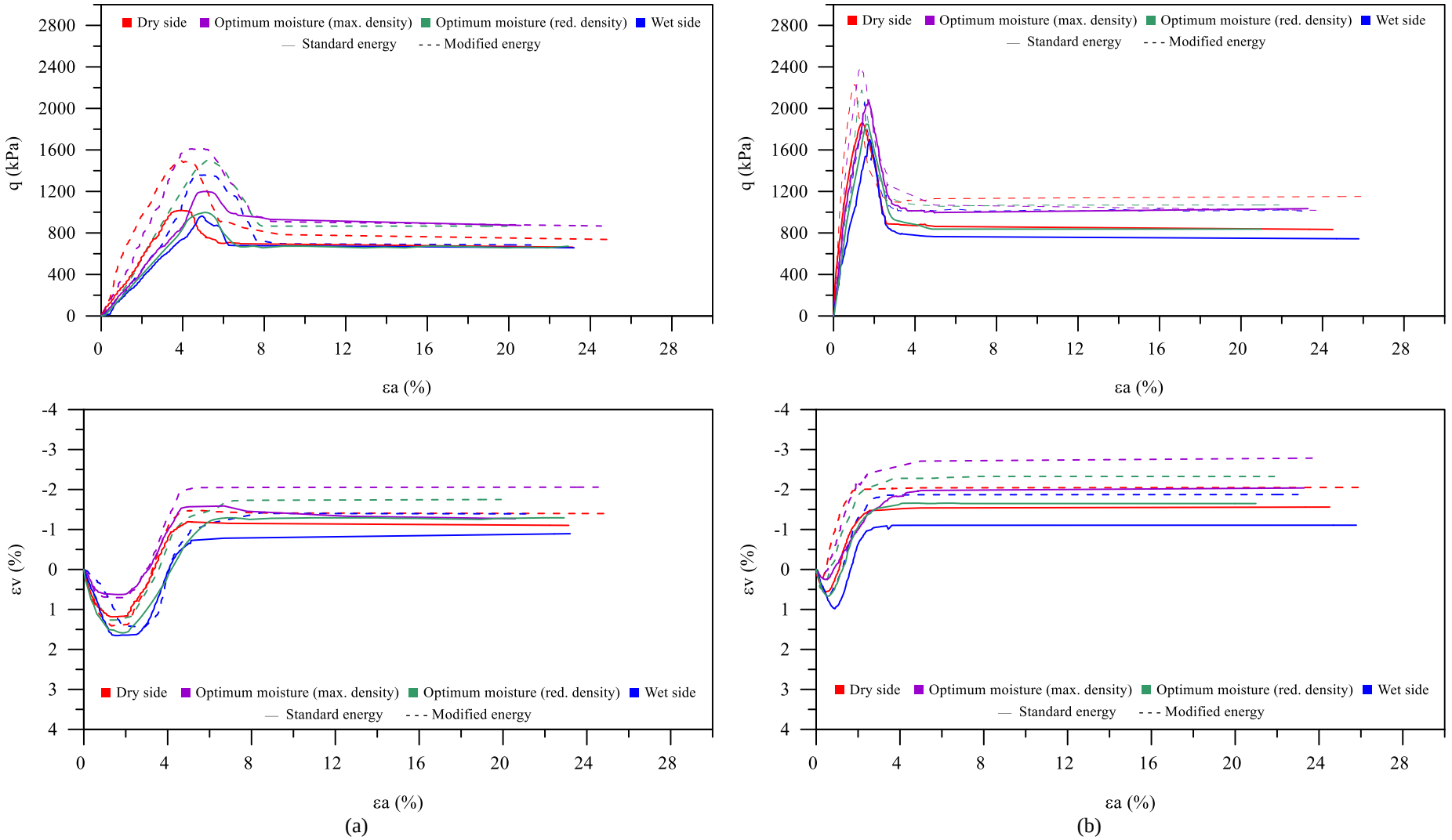

Figure 4.25. Summary of the stress-strain behavior of the low confining stress triaxial tests: (a) uncemented; (b) cemented.

The summarized data presented on Figure 4.25 aims to facilitate the reader's comprehension and comparison on the stress-strain behavior thoroughly discussed on Items 4.5.1.1 and 4.5.1.2. After this exposition, the next subsections present the analysis of the high confining stress triaxial tests.

4.5.1.4 High confining stresses: standard energy

The results of the uncemented high confining stress (p' = 3000kPa) tests for the standard compaction energy are shown in Figure 4.26, in terms of deviatory stress (q) as a function of axial strain (εa).

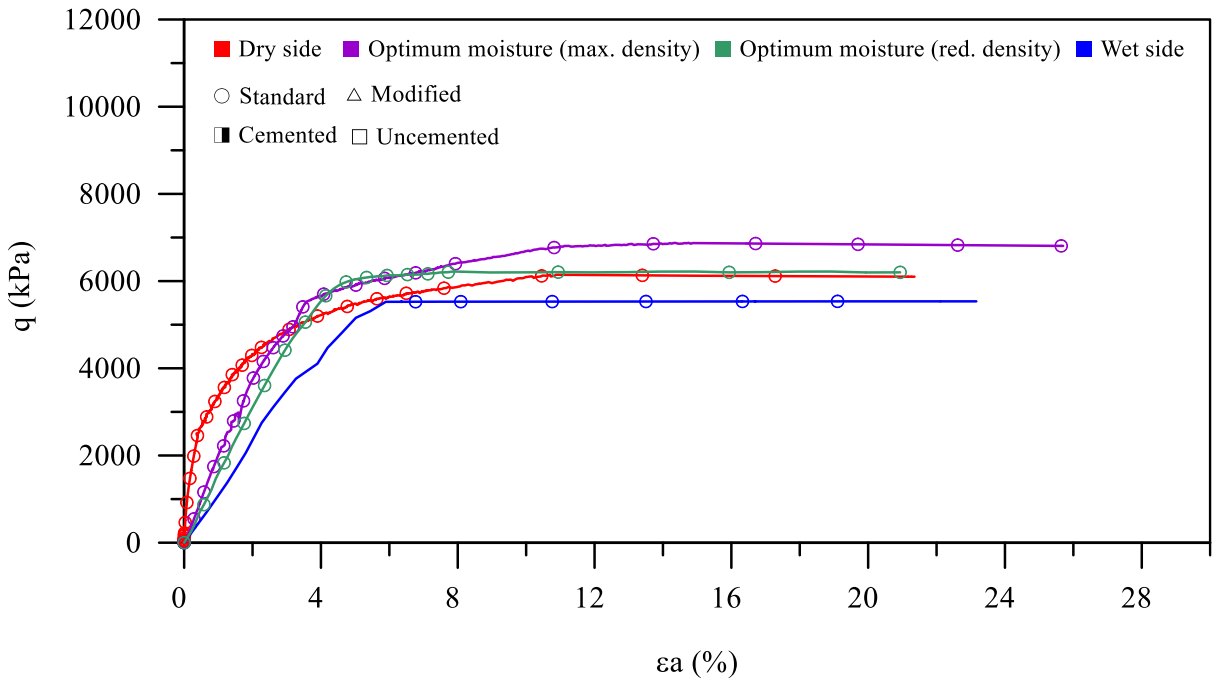

Figure 4.26. Stress-strain results for high confining stress standard compaction energy - uncemented specimens.

For all standard compaction energy uncemented specimens, tested under high confining stress, no pronounced peak of strength was evidenced, independently of the initial molding condition. Furthermore, constant values of strength were reached from 7-12% strain. This behavior is commonly depicted for high confining stresses results, in which the confining stress is such that the dilative behavior due to the interlocking of the grains is prevented.

Such as the case of the low confining stress specimens (items 4.5.1.1 and 4.5.1.2), the highest deviatory stress (q) of Figure 4.26 was seen for optimum moisture (max. density) specimens, followed by optimum moisture (red. density), dry side, and wet side ones; indicating that even

under high stresses (p' = 3000kPa) the initial molding conditions have a significant effect on the stress-strain behavior. Since optimum moisture (max. density) specimens had a slightly lower void ratio than the other combinations, the aforementioned behavior indicates that strength was more affected by the initial void ratio than by the moisture content. When the influence of void ratio is isolated and same void ratio specimens are compared, optimum moisture (red. density) specimens result in higher deviatory stress values, followed by the dry-side and wet-side ones, respectively. At the dry-side of the compaction curve it is expected a stiffer soil matrix to be formed, offering more resistance to shearing. In the compaction process, the increase in density corresponds to the elimination of air from the voids in the mixture. From a certain moisture content (wet-side of the compaction curve), compaction is no longer able to expel air from the voids as the degree of saturation is already high and the air is occluded (enveloped by water), resulting in a less resistant matrix to loading forces evidenced in the wet-side strength results.

The stiffness behavior can also be extracted from triaxial data, in which the stiffness of a specimen is represented by the slope of the results (see item 4.5.1.1). To facilitate the visualization and further discuss such information, the results shown on Figure 4.26 were scaled down and are depicted in Figure 4.27.

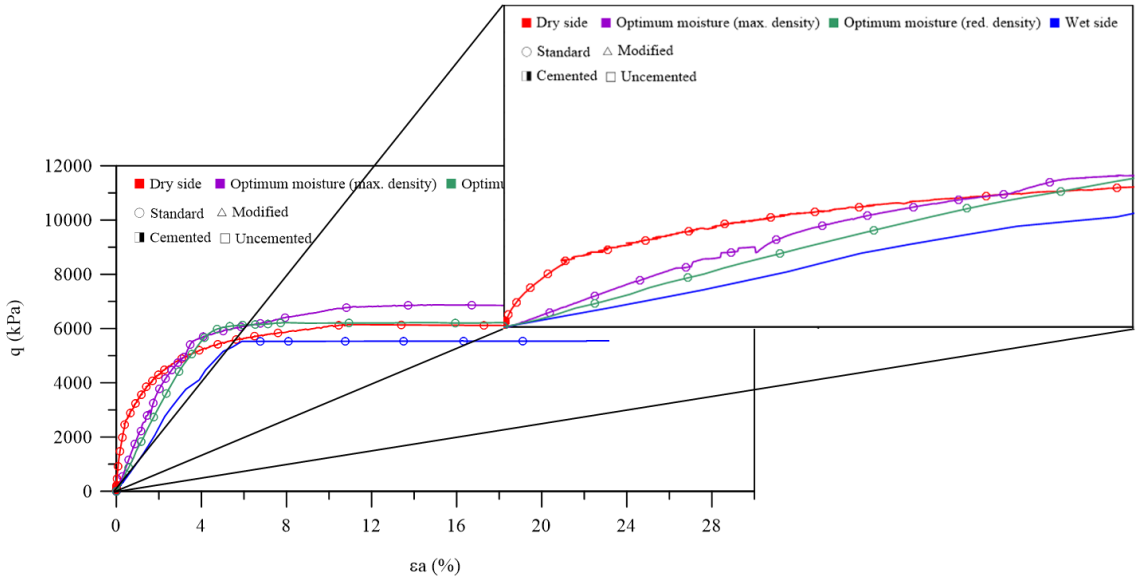

Figure 4.27. Scaled down stress-strain results for high confining stress standard compaction energy - uncemented specimens.

By analyzing the slope of all combinations, it is clear that the highest stiffest is evidenced for dry-side specimens, followed by optimum moisture (max. density), optimum moisture (red.

density), and wet-side ones; indicating the same pattern evidenced for low-confining stresses, in which stiffness cannot be simply and directly related to strength and initial void ratio. Other factors such as the initial moisture content should also be considered the decision-making process of an engineering design, specimens molded at initial moisture contents below the optimum content resulted in a stiffer soil matrix, while specimens molded at the wet-side of the compaction curve resulted in the lowest stiffness values; this can be explained by the structure imparted in compaction.

To attest the aforementioned information, the triaxial data was also evaluated over the stiffness degradation in the shearing stage, applying the Elasticity Theory (Lambe and Whitman, 1979) based on the explanations provided on item 4.5.1.1. Figure 4.28 presents the shear modulus of uncemented specimens molded at standard energy and tested under high confining stress.

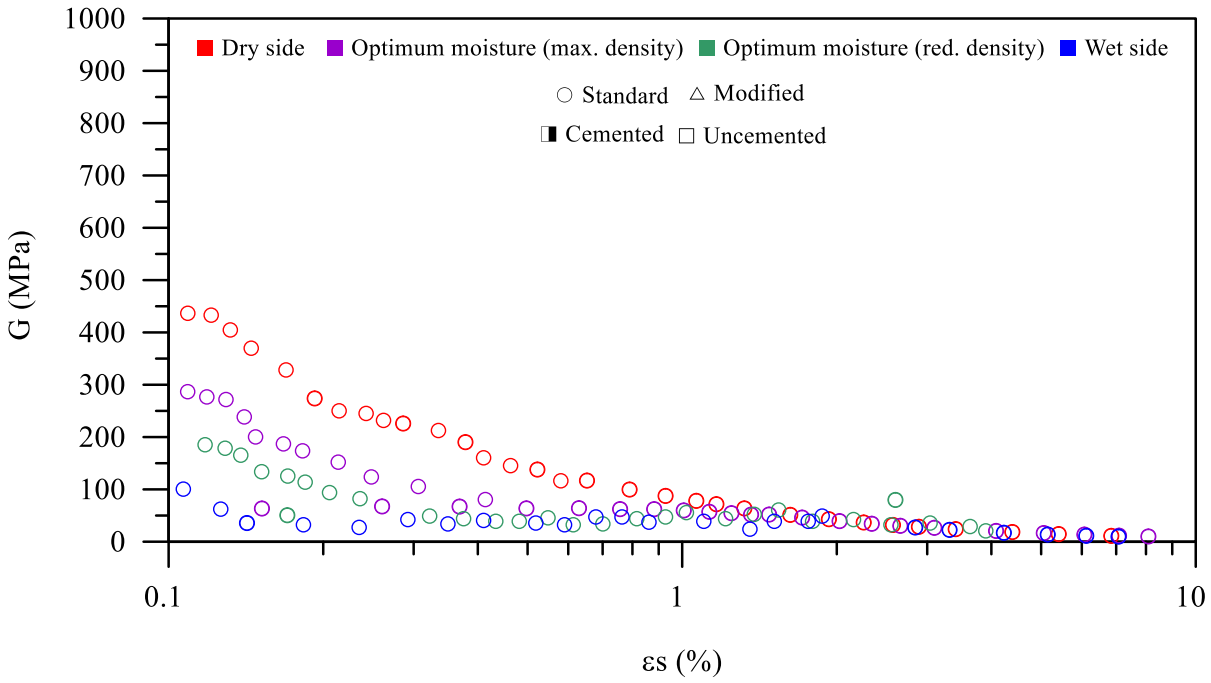

Figure 4.28. Shear modulus for high confining stress standard compaction energy - uncemented specimens.

Figure 4.28 shows indeed that the highest stiffest is evidenced for dry-side specimens. In addition, a typical stiffness degradation behavior for conventional soils is shown, in which the increase in strain leads to a decrease in stiffness, as a result of the shearing of the specimen. The stiffness degradation behavior over shearing has also been attested by Dutra (2021); Gonçalves (2021); Hoch (2023); Marques (2016).

The results of volumetric strain versus axial strain for uncemented specimens molded at standard compaction energy under low confining stress are shown in Figure 4.29.

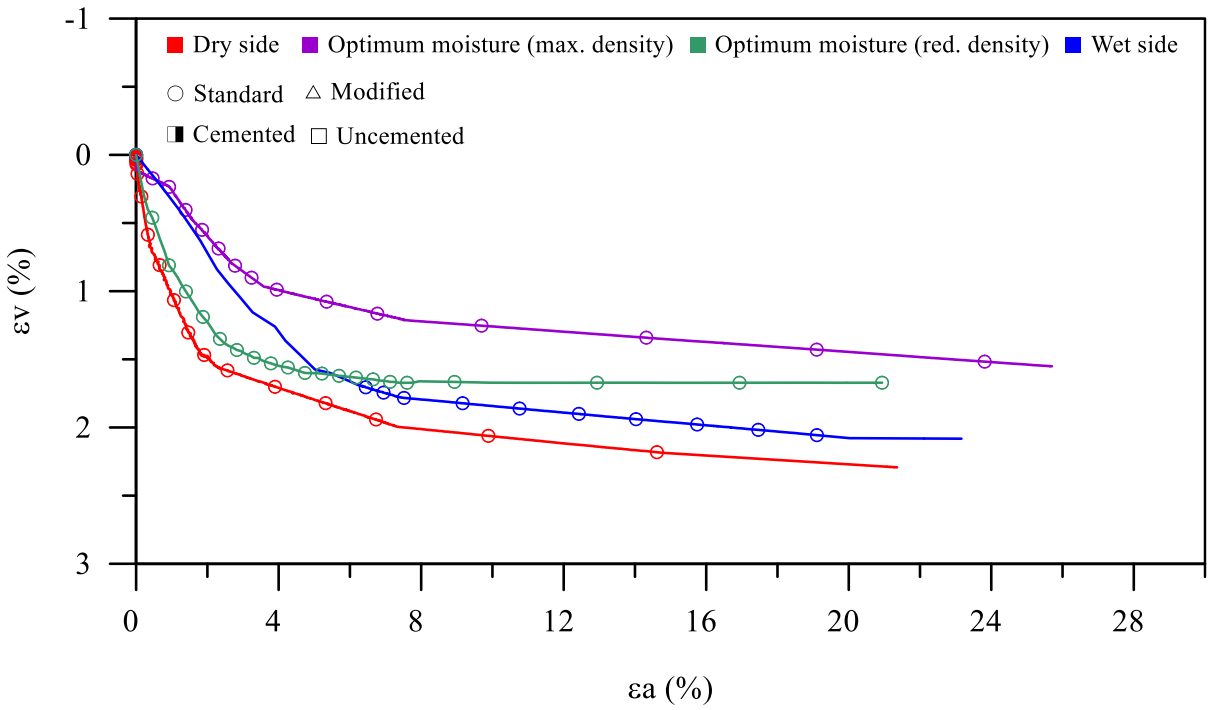

Figure 4.29. Volumetric versus axial strain for high confining stress standard compaction energy - uncemented specimens.

All specimens depicted a full compressive behavior; this behavior is associated to the high confining stress of the tests (p' = 3000kPa). Even though all specimens were initially in a dense state (i.e., dilative behavior is expected), the 3000kPa confining stress prevented the close-packed hexagonal array to happen, in other words, the confining stress influence was higher than the interlocking of the grains. Wet-side specimens resulted in higher compression when compared to the other combinations. This is associated with the higher lubrication of the soil particles from the increase moisture content; in wet-side arrangements the particles are able to more easily slide into the voids, allowing more compression. In addition, the lower initial void ratio (more compact initial matrix) of optimum moisture content specimens (max. density) left less space to particles to accommodate and, thus, lower compression was evidenced.

After discussing the uncemented data, the results of the cemented high confining stress tests for the standard compaction energy are shown in Figure 4.30, in terms of deviatory stress (q) as a function of axial strain (εa).

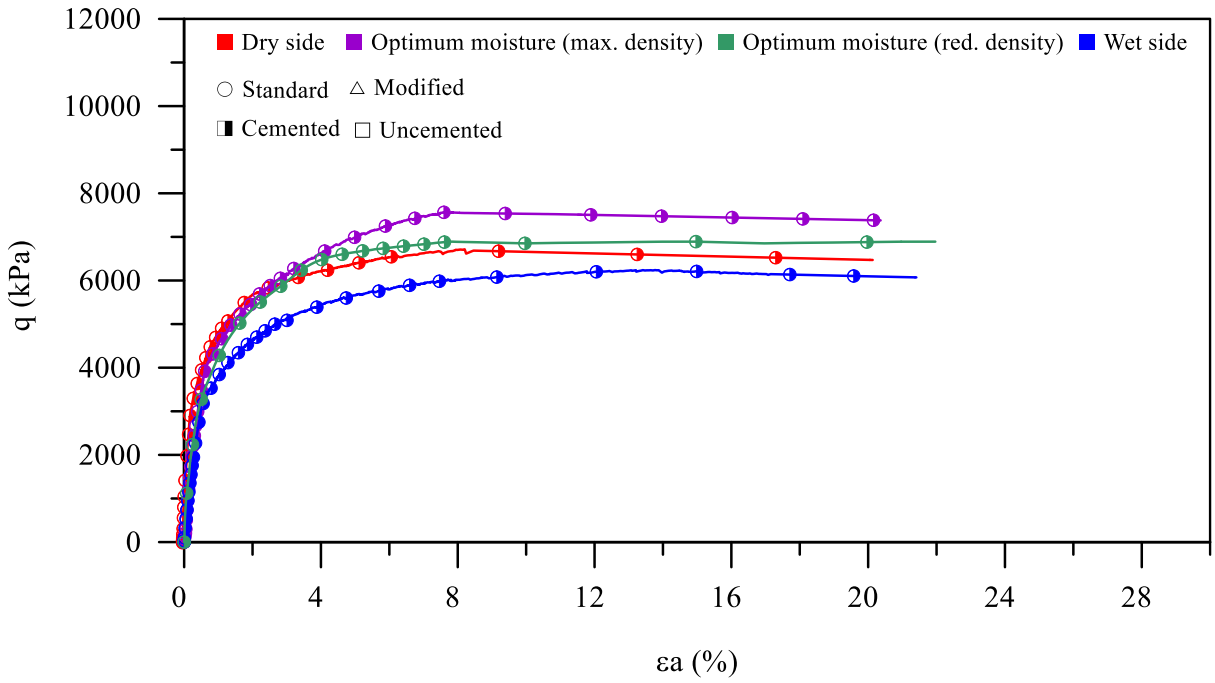

Figure 4.30. Stress-strain results for high confining stress standard compaction energy - cemented specimens.

Such as in the case of the uncemented specimens under high confining stress, the data of Figure 4.30 shows that no pronounced peak of strength was evidenced for the cemented specimens, independently of the initial molding condition. Furthermore, constant values of strength were reached from 7-12% strain. This behavior is commonly depicted for high confining stresses results, in which the confining stress is such that the dilative behavior due to the interlocking of the grains is prevented. The highest deviatory stress (q) value of cemented specimens was evidenced for optimum moisture content (max. density) specimens, followed by optimum moisture content (red. density), dry-side, and wet-side ones. This behavior was once again associated with the initial molding conditions and has been thoroughly explained on the aforementioned paragraphs and Items 4.2, 4.5.1.1, and 4.5.1.2.

As for the cement content influence on the stress-strain results, cemented specimens (Figure 4.26) presented an extremely similar behavior to uncemented ones (Figure 4.30), both in deviatory stress and axial strain. This behavior indicates that the cementation bonds may have been broken during the consolidation of the tests, considering that stress of 3000kPa were applied in this phase. This indicates that the stress state acting during the cementing process plays a fundamental role in the mechanical behavior of cemented *IOTs*. For cemented specimens to preserve the strength gain from cement addition under high confining stresses (i.e., stresses higher than the yield stress of the specimens), the curing process of such

specimens must be executed under stress (with at least the same stress level of the consolidation phase). Consoli et al (2000), indicate the existence of a coupled effect between curing condition and confining stress, that is, as the stress increases the more significant is the change in shear strength caused by curing under stress. This fact is probably related to the bonding degradation expected to occur during the application of isotropic confining stress in the specimens cured without stress and tested for confining stresses higher than their yield isotropic stresses. This behavior has also been attested by Dala Rosa et al (2009).

Such as the case of low confining stress specimens, the stiffness behavior (indicated by the slope of the data) of high confining stress ones was also analyzed in the triaxial test. To better visualize such data, the results shown on Figure 4.30 were scaled down and are depicted in Figure 4.31.

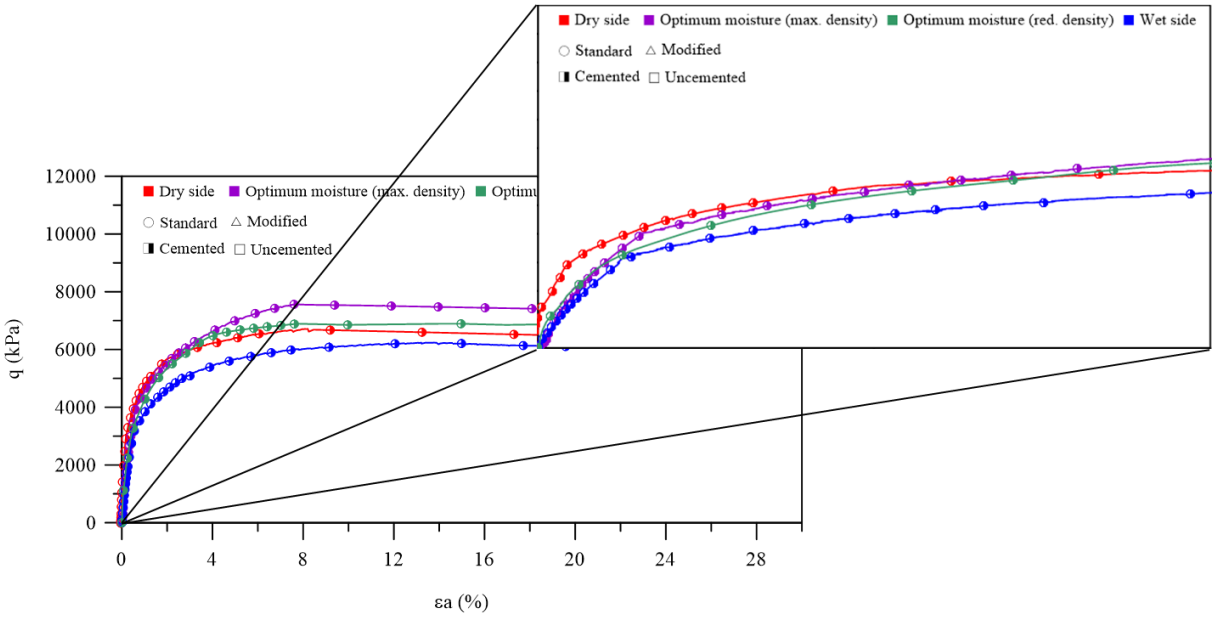

Figure 4.31. Scaled down stress-strain results for high confining stress standard compaction energy - cemented specimens.

The highest stiffest was evidenced for dry-side specimens, followed by optimum moisture content (max. density), optimum moisture content (red. density), and wet-side ones; indicating the same pattern evidenced for low-confining stresses. This phenomenon was once again associated with particle lubrication and density of the soil-cement matrix (soil fabric). To attest to the aforementioned suppositions, the triaxial data was also evaluated over the stiffness degradation in the shearing stage, applying the Elasticity Theory (Lambe and Whitman, 1979) based on the explanations provided in Item 4.5.1.1. Figure 4.32 presents the shear modulus of cemented specimens molded at standard energy and tested under high confining stress.

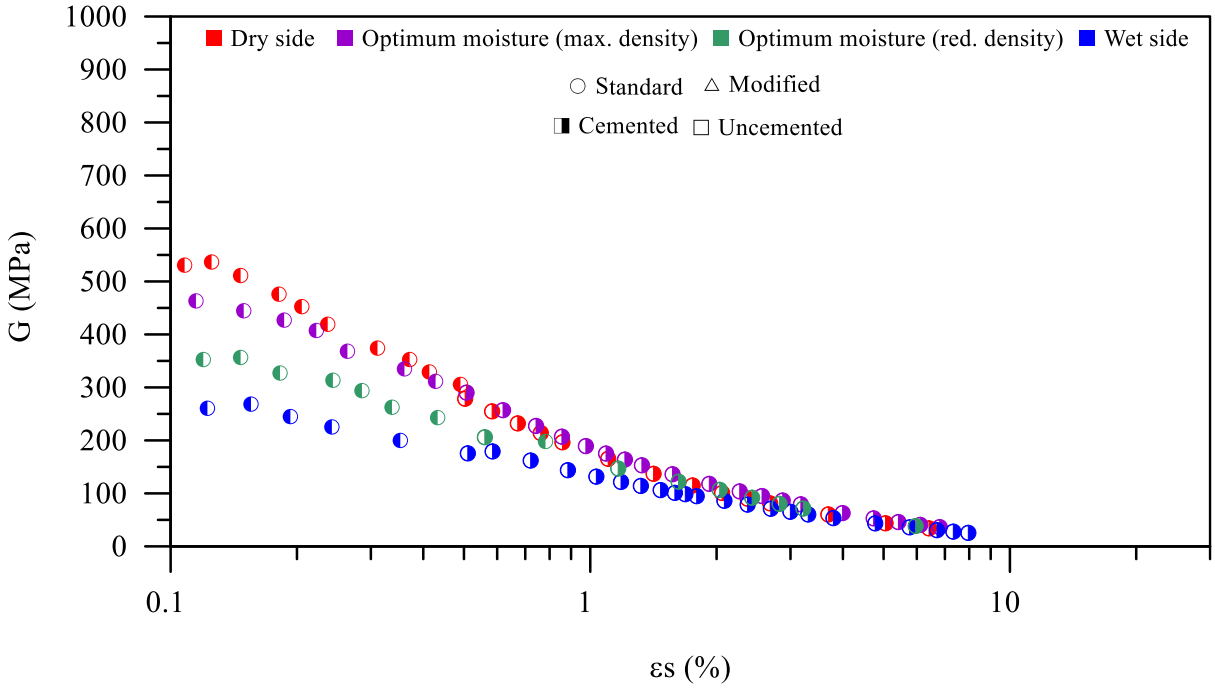

Figure 4.32. Shear modulus for high confining stress standard compaction energy - cemented specimens.

The data shown in Figure 4.32 attests the slope analysis conducted on the triaxial tests; in which, the highest stiffest is evidenced for dry-side specimens, followed by optimum moisture content (max. density), optimum moisture content (red. density), and wet-side ones. Furthermore, a typical stiffness degradation behavior for conventional soils is shown, in which the increase in strain leads to a decrease in stiffness, as a result from the shearing of the specimen. The stiffness degradation behavior over shearing has also been attested by Dutra (2021); Gonçalves (2021); Hoch (2023); Marques (2016). When comparing to the uncemented specimens molded at the same compaction energy, it is possible to see that the values of stiffness of cemented specimens were slightly higher. This indicates that even though cementation might have been broken during the consolidation phase of these specimens, some of the cementitious bound were still present, justifying the aforementioned increase in stiffness. After total degradation of the cementitious bonds, the material would behave like an uncemented geotechnical material and, as stated by Consoli et al. (2001), this degradation would not occur if specimens were cured under stress.

The results of volumetric strain versus axial strain for cemented specimens of standard compaction energy under low confining stress are shown in Figure 4.33.

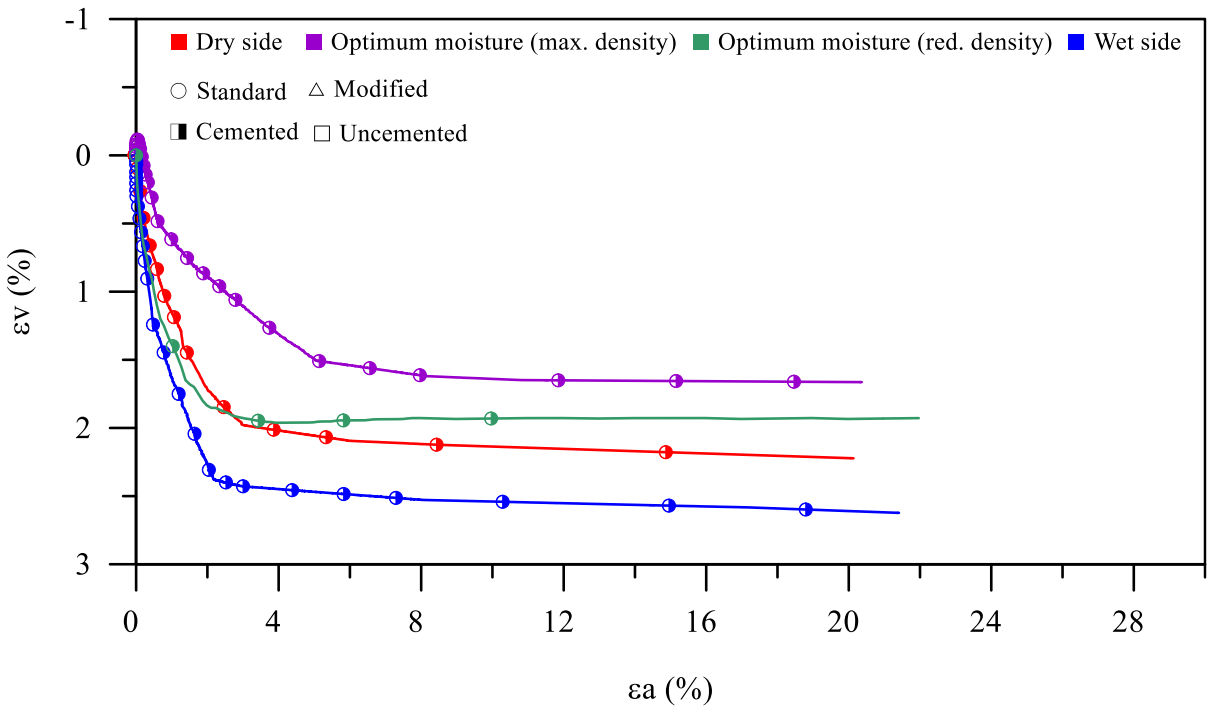

Figure 4.33. Volumetric versus axial strain for high confining stress standard compaction energy - cemented specimens.

Such as the case of uncemented specimens, the cemented specimens depicted a full compressive behavior, associated with the high confining stress of the tests (p' = 3000kPa); in which, the 3000kPa confining stress prevented the close-packed hexagonal array to happen.

4.5.1.5 High confining stresses: modified energy

The results of the uncemented specimens under high confining stress (p' = 3000kPa) tests molded at the standard modified compaction energy are shown in Figure 4.34, in terms of deviatory stress (q) as a function of axial strain (εa).

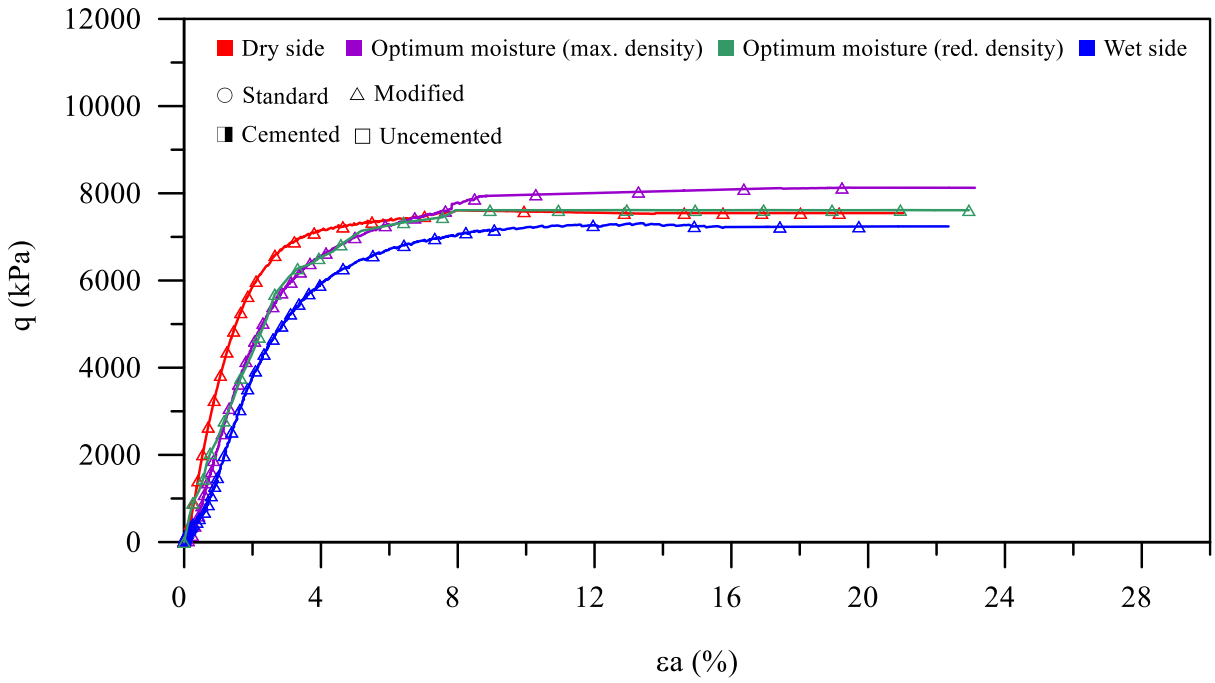

Figure 4.34. Stress-strain results for high confining stress modified compaction energy - uncemented specimens.

Similar to the behavior presented for the standard compaction energy (item 0), no pronounced peak of strength was evidenced for modified energy specimens; constant values of strength were reached from 8-14% strain. This behavior is commonly depicted for high confining stresses tests, in which the confining stress is such that the dilative behavior due to the interlocking of the grains is prevented.

Regarding the magnitude of the deviatory stress, the highest value was evidenced for optimum moisture content (max. density) specimens, followed by optimum moisture content (red. density), dry-side, and wet-side ones, alluding to the behavior presented on item 0. This significant different on the magnitude of strength values attests, once again, the influence of the initial molding conditions of the stress-strain behavior of stabilized *IOTs* under high confining stress.

When comparing the stress-strain behavior of the standard compaction energy for uncemented specimens (Figure 4.26) with the ones molded at modified compaction energy (Figure 4.34), the only difference on the general behavior is the magnitude of the values. Modified energy specimens present higher stress values due to the more compact initial matrix (lower void ratio) that mobilizes higher friction between *IOTs* particles.

The initial stiffness (represented by the initial slope of the test results) was also evaluated for the triaxial data; to ease the visualization of such parameters, the results shown on Figure 4.34 were scaled down and are shown in Figure 4.35.

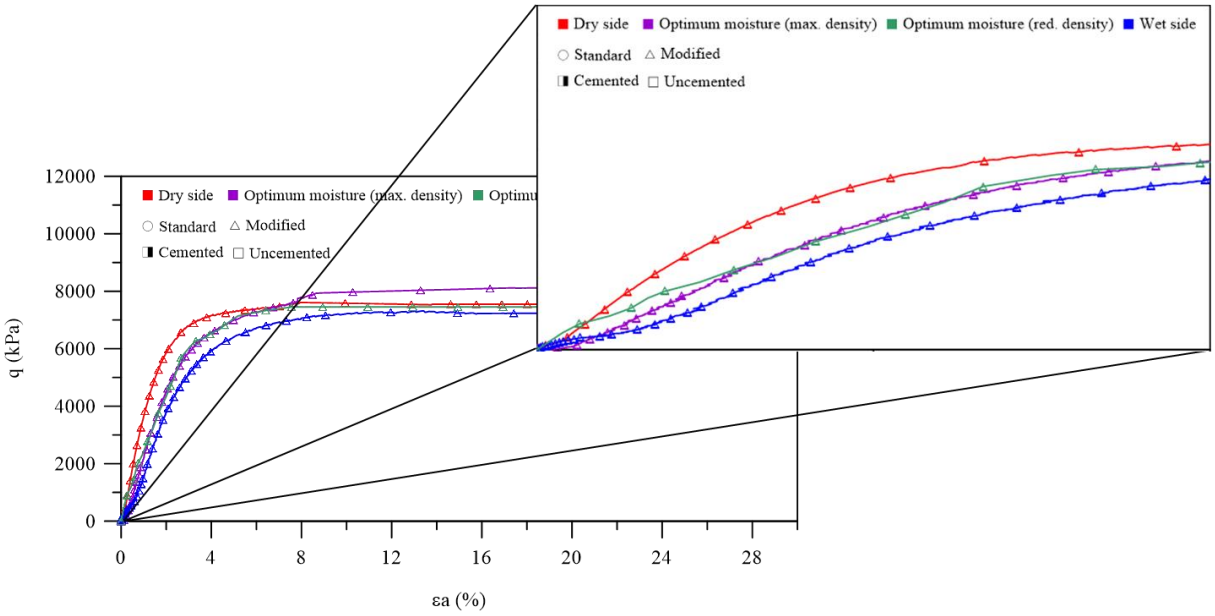

Figure 4.35. Scaled down stress-strain results for high confining stress modified compaction energy - uncemented specimens.

The highest stiffest was seen for dry-side specimens, followed by optimum moisture content specimens (max. density), followed by optimum moisture content specimens (red. density), and wet-side ones. This behavior once more indicates that stiffness presents the same pattern independently of the compaction energy. When molded in the dry side of the compaction curve, specimens result in a stiffer soil matrix, while specimens molded at the wet-side of the compaction curve resulted in the lowest stiffness values. This indicates that the structure imparted in compaction directly influences stiffness, especially regarding the density and packing (soil fabric), as well as, the lubrication of the soil matrix particles To this extent, the triaxial data was also evaluated over the stiffness degradation in the shearing stage, applying the Elasticity Theory (Lambe and Whitman, 1979) based on the explanations provided on item 4.5.1.1. Figure 4.36 presents the shear modulus of cemented specimens for low confining stress standard compaction energy.

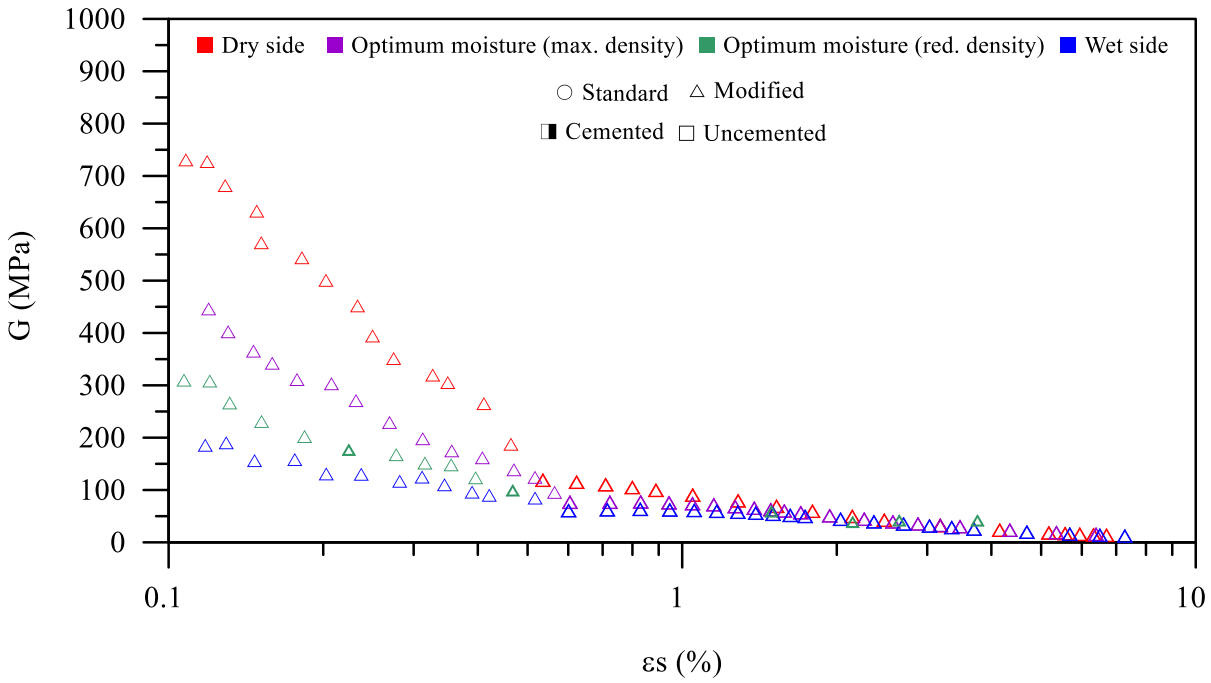

Figure 4.36. Shear modulus for high confining stress modified compaction energy - uncemented specimens.

Results from Figure 4.36 allude to the analysis conducted in the stress-strain behavior regarding the stiffness of the specimens. Furthermore, a conventional stiffness degradation behavior is shown, in which the increase in strain leads to a decrease in stiffness, as a result from the shearing of the specimen. The stiffness degradation behavior over shearing has also been attested by Dutra (2021); Gonçalves (2021); Hoch (2023); Marques (2016). Regarding the influence of the compaction energy, the only noticeable difference was the magnitude of the values, where modified compaction energy specimens resulted in higher stiffness values, due to the more compact soil matrix (lower void ratio).

The results of volumetric strain versus axial strain for uncemented specimens molded at modified compaction energy under low confining stress are shown in Figure 4.37.

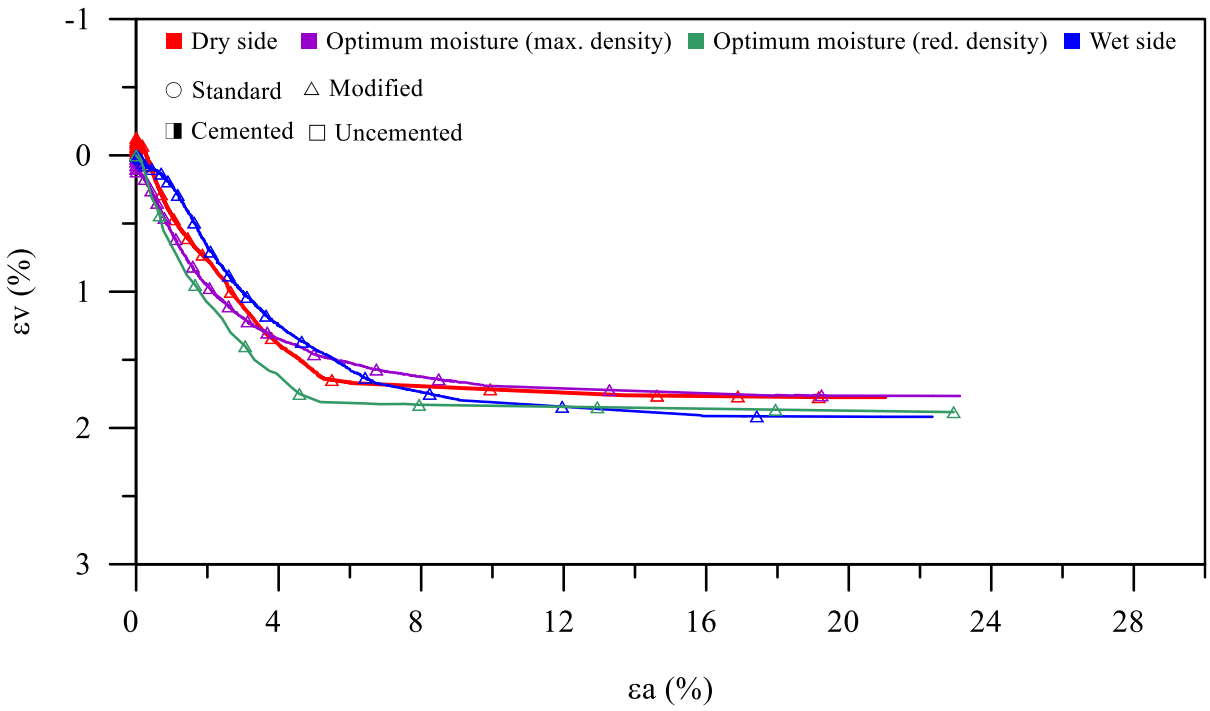

Figure 4.37. Volumetric versus axial strain for high confining stress modified compaction energy - uncemented specimens.

As expected, the specimens depicted a full compressive behavior, being associated to the high confining stress of the tests (p' = 3000kPa). This attests that the confining stress influence was higher than the interlocking of the grains, where the elevated confining stress prevented the close-packed hexagonal array. After the discussion of the uncemented data, the results of the cemented high confining stress tests for the modified compaction energy are shown in Figure 4.38, in terms of deviatory stress (q) as a function of axial strain (εa).

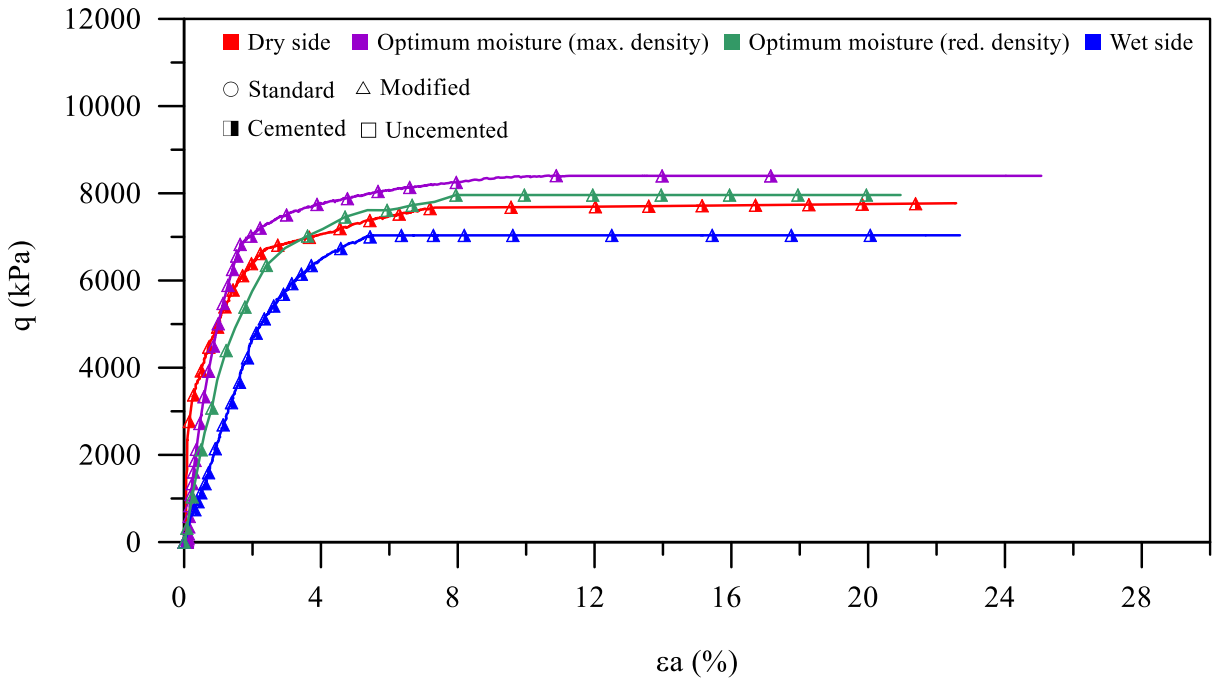

Figure 4.38. Stress-strain results for high confining stress modified compaction energy - cemented specimens.

Similar to the uncemented specimens, the strain-strain behavior showed no pronounced peak of strength for all of the studied combinations. In addition, constant values of strength were reached from 8-10% strain. The highest deviatory stress (*q*) value of cemented specimens was evidenced for optimum moisture content (max. density) specimens, followed by optimum moisture content (red. density), dry-side, and wet-side ones. This behavior is explained by the same reasoning presented for the uncemented specimens, as discussed on items 4.2, 4.5.1.1, and 4.5.1.2.

By analyzing the influence of cement content on the stress-strain results, the same pattern exposed for the standard compaction energy specimens is shown for the modified compaction energy specimens; in which values were extremely similar to same molding conditions specimens with 0% cement addition. This indicates that cementation may have also been broken during the consolation phase, considering that curing under stress was not applied (Consoli et al., 2007). In addition, other than the magnitude of the values, no expressive difference was evidenced when comparing the effect of molding energy.

In order to investigate the influence of the variables on the initial stiffness behavior, the data from the triaxial tests (Figure 4.38) were once again scaled down and are depicted in Figure 4.39.

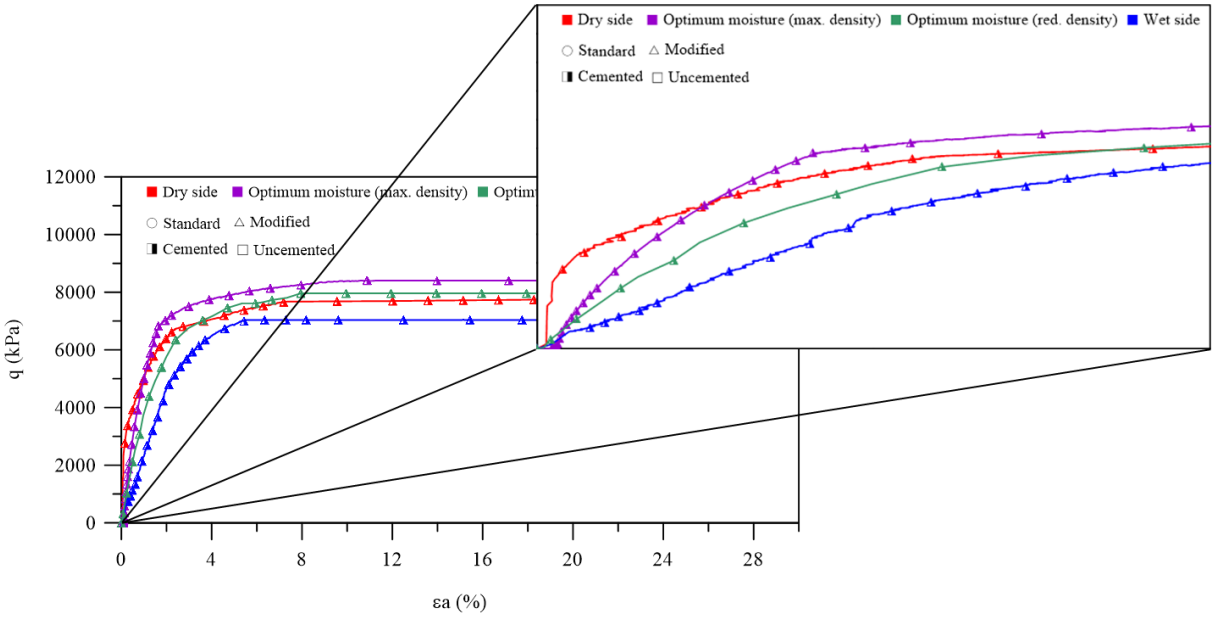

Figure 4.39. Scaled down stress-strain results for high confining stress modified compaction energy - cemented specimens.

The data shown in Figure 4.39 indicates that the highest stiffest (measured through the slope of the data) is evidenced for dry-side specimens, followed by optimum moisture content (max. density), optimum moisture content (red. density), and wet-side ones. Also, typical stiffness degradation behavior for conventional soils is shown, in which the increase in strain leads to a decrease in stiffness, as a result from the shearing of the specimen. Although for the stress-strain maximum values the cementitious bound appeared to be completely broken during the consolidation, Figure 4.32 indicates that the cement content had some effect on the development of initial stiffness; considering that slightly higher values of shear modulus were evidenced for the cemented specimens.

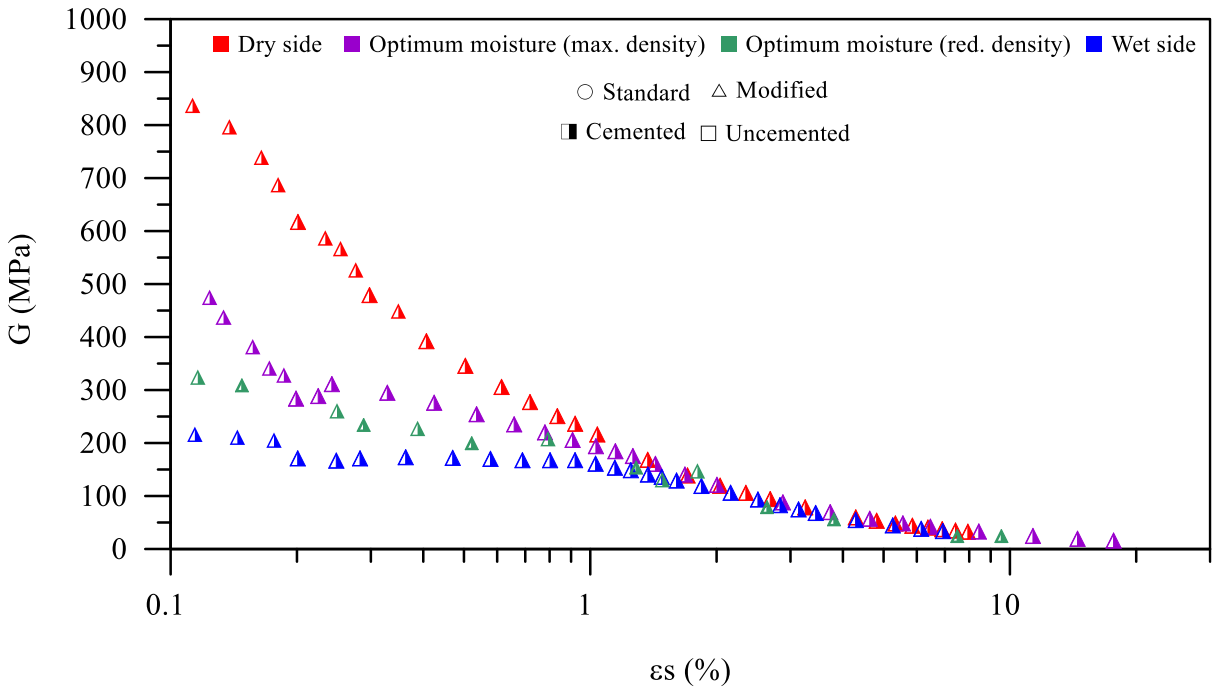

Figure 4.40. Shear modulus for high confining stress standard compaction energy - cemented specimens

The results of volumetric strain versus axial strain for cemented specimens of modified compaction energy under low confining stress are shown in Figure 4.41. Such as in the case of uncemented specimens, the cemented specimens depicted a full compressive behavior, associated with the high confining stress of the tests (p' = 3000kPa).

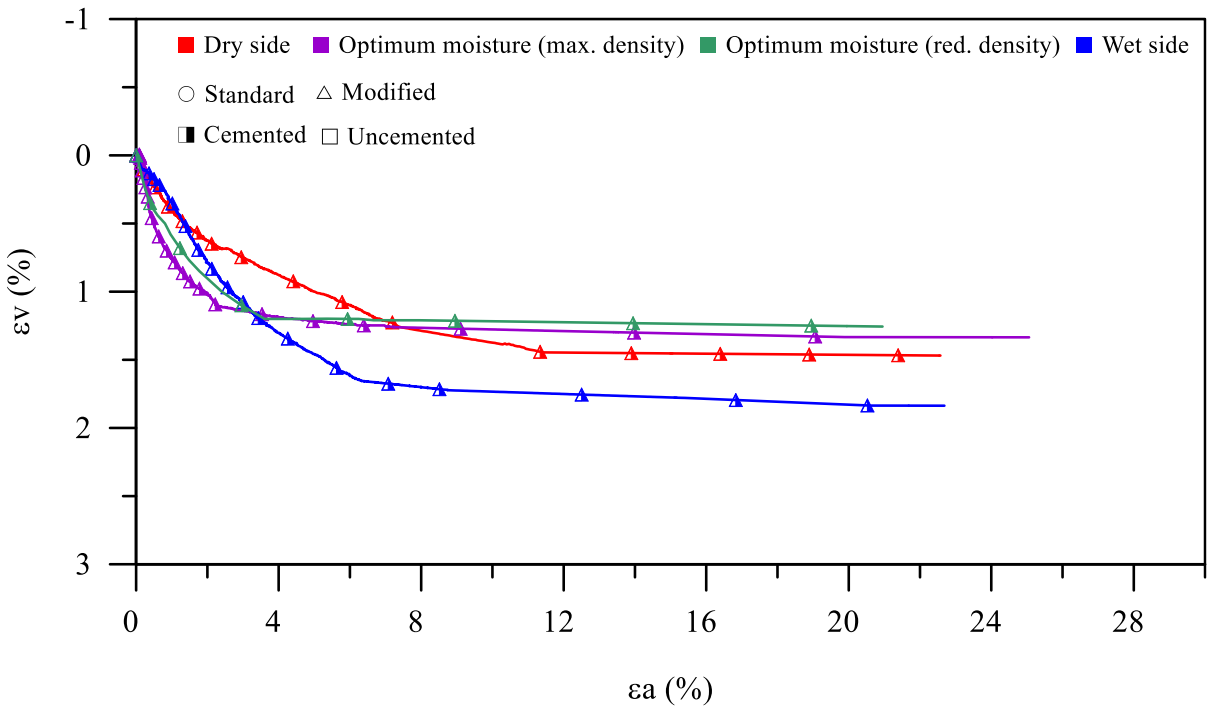

Figure 4.41. Volumetric versus axial strain for high confining stress standard compaction energy - cemented specimens.

From all the exposed discussion on the high confining stress subsections (items 0 and 4.5.1.5), it becomes clear that cement addition presents different effects for high confining stress specimens when compared to low confining stress ones. For lower confining stress cement addition results in a clear and measurable positive effect on the *IOTs* mechanical properties for both studied compaction energies. On the other hand, for high confining stresses, this improvement was only slightly seen on the initial shear modulus parameters. As previously stated, the degree of cementation depends upon the type of the cement used, the type of geotechnical material, and some other factors such as water content, proportion of mixing, degree of compaction and curing. Especially for high confining stresses, the curing conditions present one of the most significant factors; in order to maintain the strength gains from cement addition, specimens tested under high confining stresses (i.e., stresses higher than the yield stress of the specimens) must go over a curing process under stress. As indicated by Consoli et al (2000) for conventional geotechnical materials, as the stress increases the more significant is the change in shear strength caused by curing under stress. This fact is probably related to the bonding degradation expected to occur during the application of isotropic confining stress in the specimens cured without stress and tested for confining stresses higher than their yield isotropic stresses. Finally, the curing under stress process was not adopted in this research considering the difficulties related to the application of this technique in field conditions.

4.5.1.6 High confining stresses: standard and modified energy tests unification

Such as the case of the low confining stress triaxial tests, a unification/summary of the stress-strain behavior of the high confining stress triaxial tests (Items 0 and 4.5.1.5) has also been provided, as indicated in Figure 4.42.

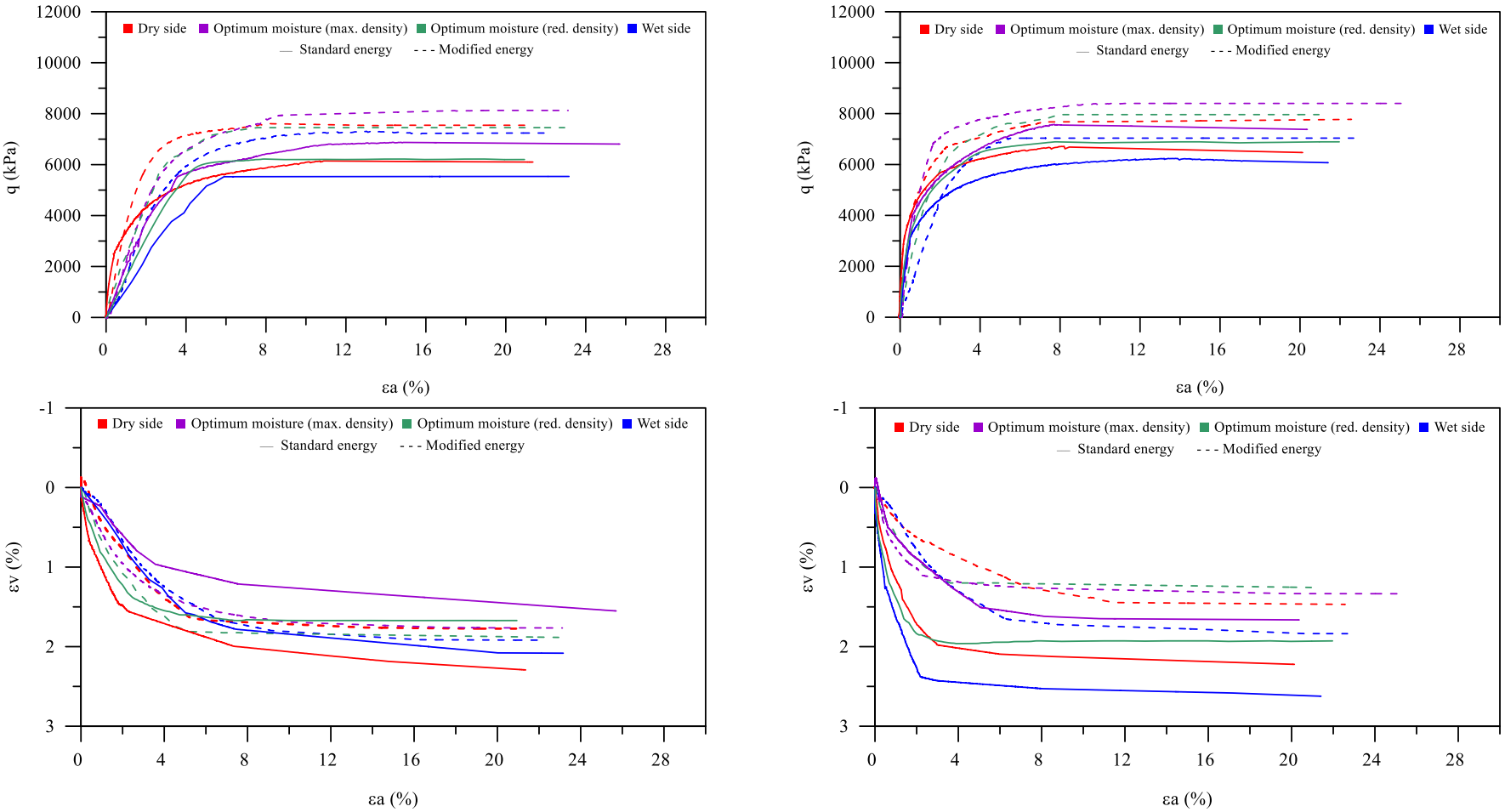

Figure 4.42. Summary of the stress-strain behavior of the high confining stress triaxial tests: (a) uncemented; (b) cemented.

The summarized data presented on Figure 4.42 aims to facilitate the reader's comprehension and comparison on the stress-strain behavior thoroughly discussed on Items 0 and 4.5.1.5. After this exposition, the next subsection explores the behavior of all triaxial tests (low and high confining stresses) under the light of a post-peak analysis.

4.5.2 Post-peak/end of test analysis

Figure 4.43 and Figure 4.44 present the post peak/end of test failure envelopes and respective strength parameters (i.e., effective friction angle and cohesive intercept) for the uncemented and cemented specimens, respectively. Although only two stress states were applied in this research (*p'* = 300kPa and *p'* = 3000kPa), the strength parameters could be estimated considering that in the critical state, the cohesive intercept must be zero, providing the third point for the failure envelope outline.

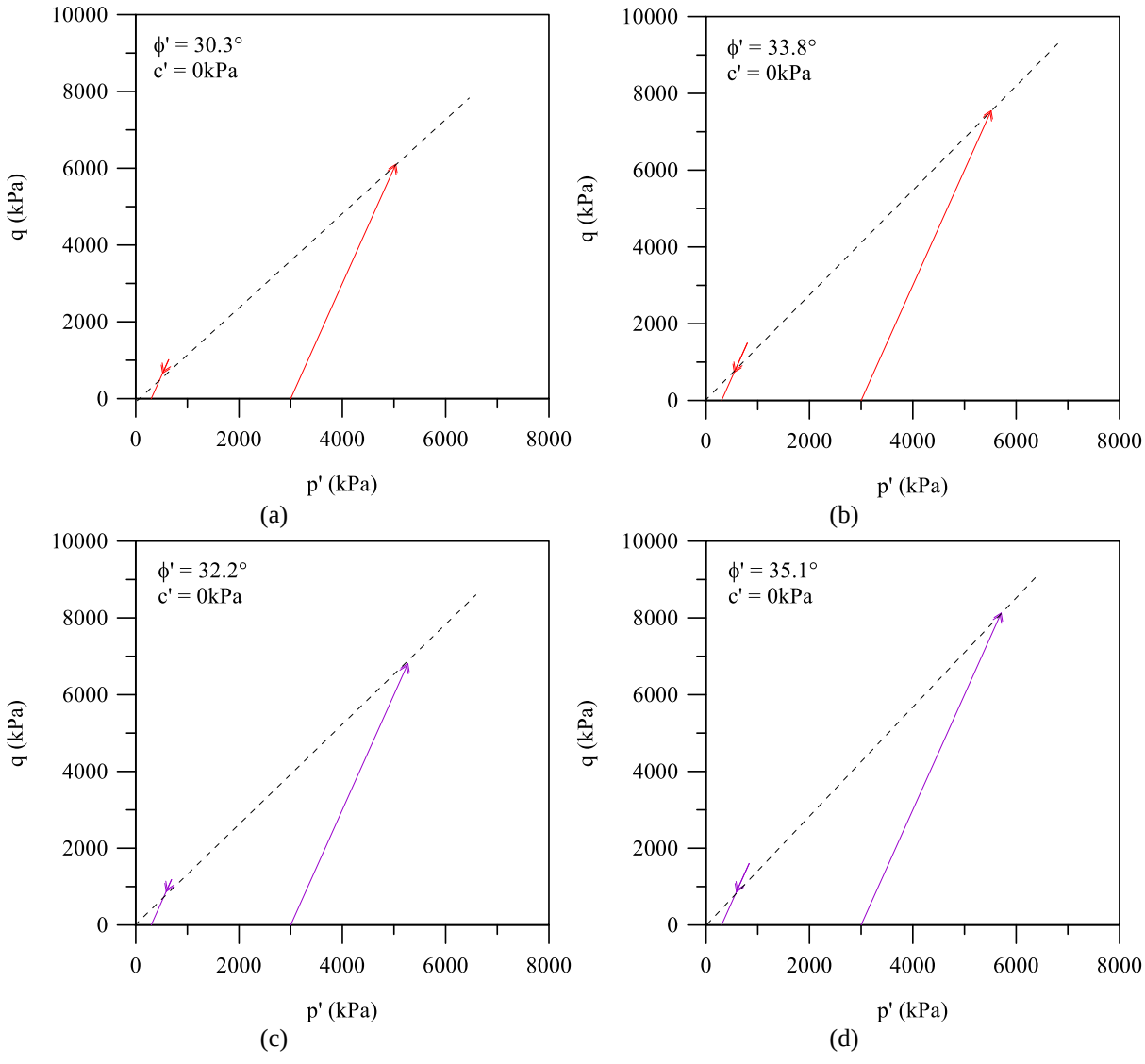

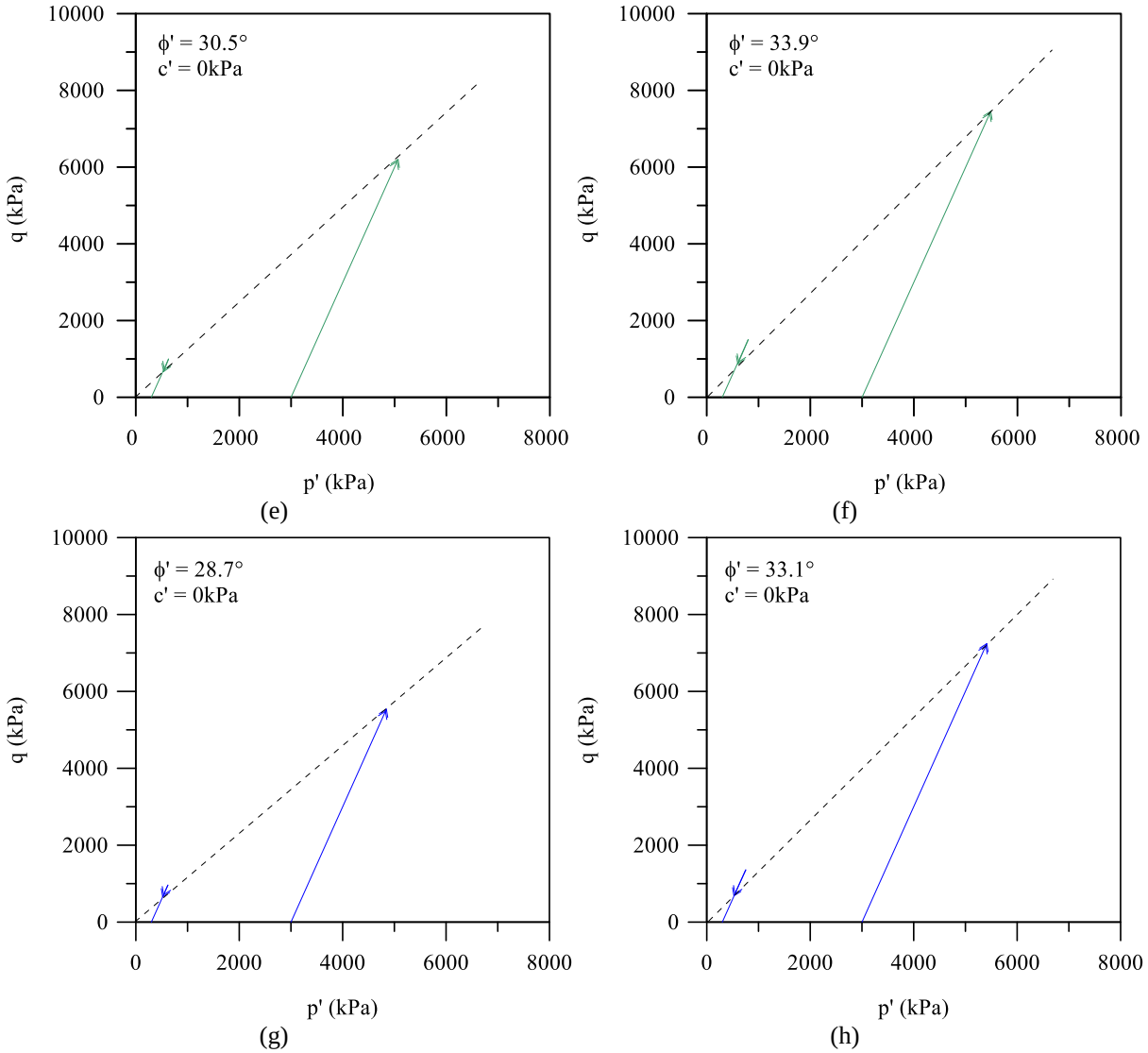

Figure 4.43. p'xq plane uncemented specimens: (a) standard energy-dry side; (b) modified energy-dry side; (c) standard energy- optimum moisture maximum density; (d) modified energy- optimum moisture maximum density; (e) standard energy-optimum moisture reduced density; (f) modified energy-optimum moisture reduced density; (g) standard energy-wet side; (h) modified energy-wet side

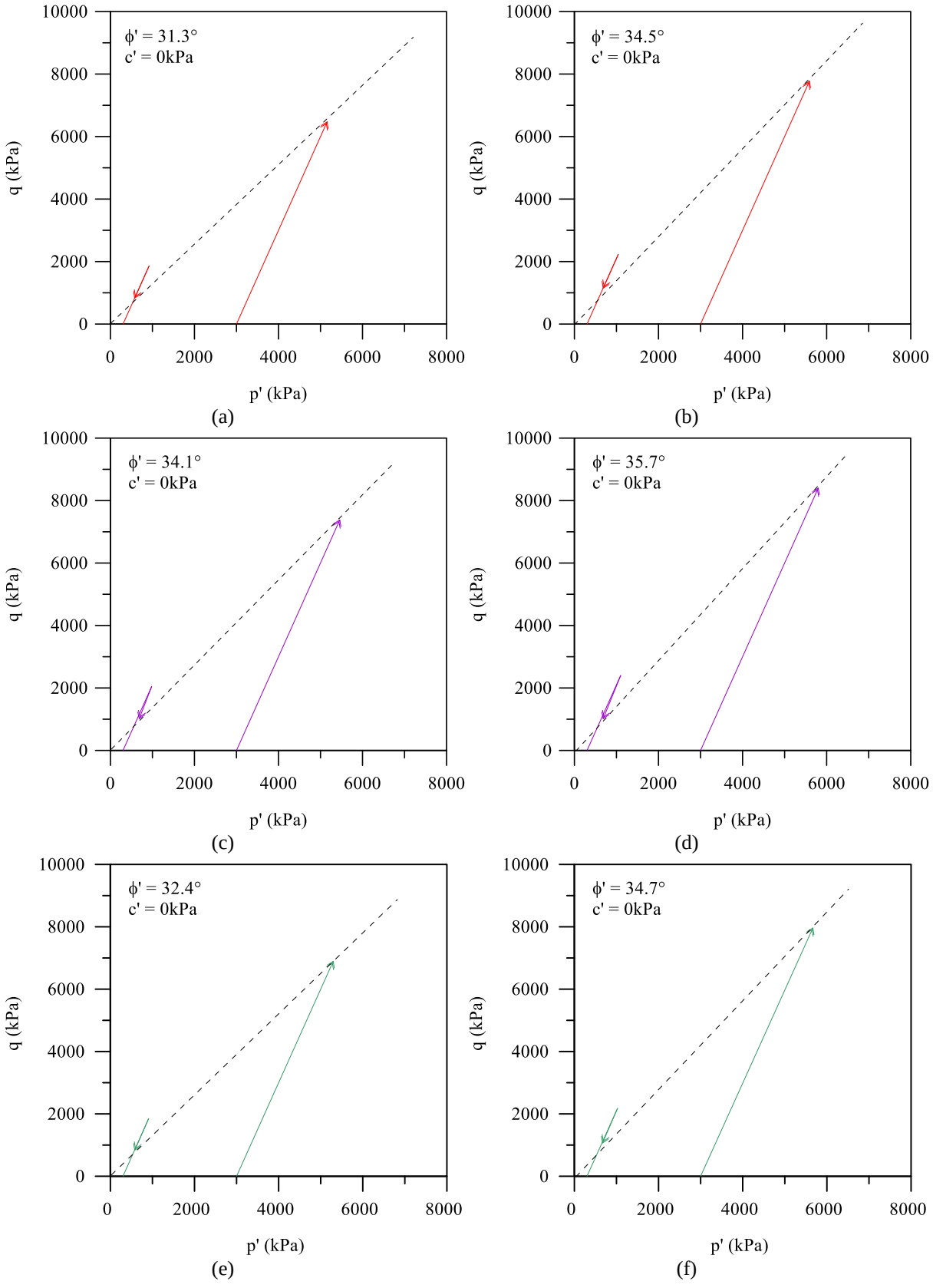
ϕ' = 31.3°
c' = 0kPa
q (kPa)
p' (kPa)
(a)
ϕ' = 34.5°
c' = 0kPa
q (kPa)
p' (kPa)
(b)
ϕ' = 34.1°
c' = 0kPa
q (kPa)
p' (kPa)
(c)
ϕ' = 35.7°
c' = 0kPa
q (kPa)
p' (kPa)
(d)
ϕ' = 32.4°
c' = 0kPa
q (kPa)
p' (kPa)
(e)
ϕ' = 34.7°
c' = 0kPa
q (kPa)
p' (kPa)
(f)

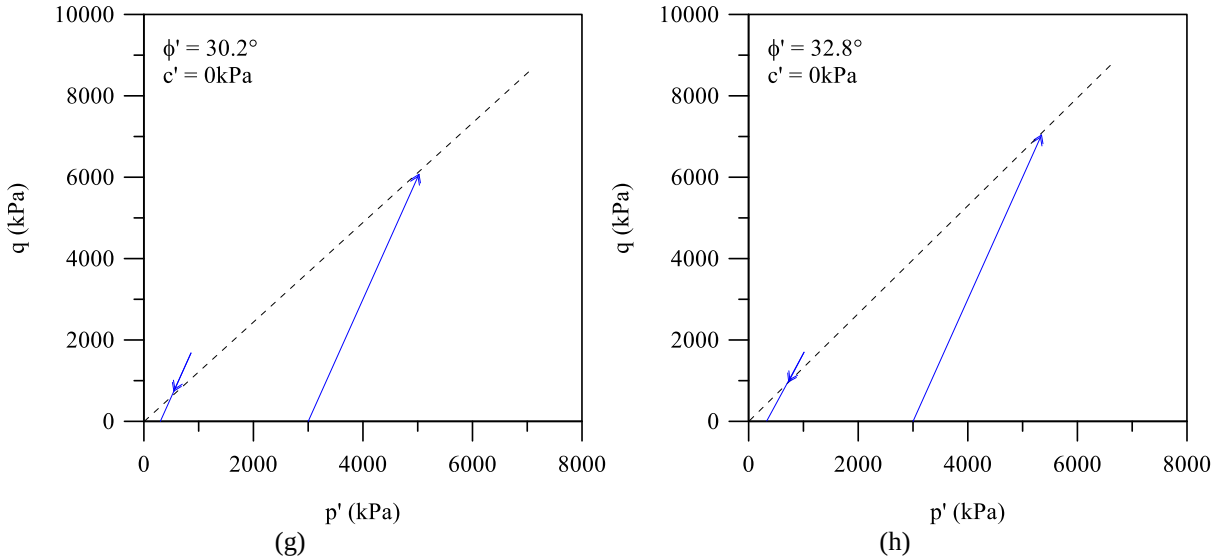

Figure 4.44. p'xq plane cemented specimens: (a) standard energy-dry side; (b) modified energy-dry side; (c) standard energy- optimum moisture maximum density; (d) modified energy- optimum moisture maximum density; (e) standard energy-optimum moisture reduced density; (f) modified energy-optimum moisture reduced density; (g) standard energy-wet side; (h) modified energy-wet side.

It is clear that for both cemented and uncemented specimens, the same pattern is evidenced; in which the highest effective friction angle (ϕ') was seen for optimum moisture content (max. density) specimens, followed by optimum moisture content (red. density), dry-side and wet-side ones, alluding to the behavior shown on item 4.5.1. Also, the increase in compaction energy also resulted in the increase of the strength parameters..

4.6 GRAIN BREAKAGE ANALYSIS

For the analysis of the grain breakage results, the data was divided into three main subsections: oedometric conditions, triaxial conditions, and microscopic evaluation. This division was created in order to facilitate the exposition of the results, as well as, the explanations regarding the evidenced behavior.

4.6.1 Oedometric conditions (OC)

Oedometer tests are designed to simulate the one-dimensional deformation and drainage conditions that soils experience in the field. In this test, specimens are restrained laterally and drained axially while subjected to incrementally applied controlled-stress loading, simulating a one-dimensional consolidation; in which, successive load increments are applied after 100% primary consolidation is reached. The results of the grain size distribution curves for the uncemented *IOTs* are shown in Figure 4.45.

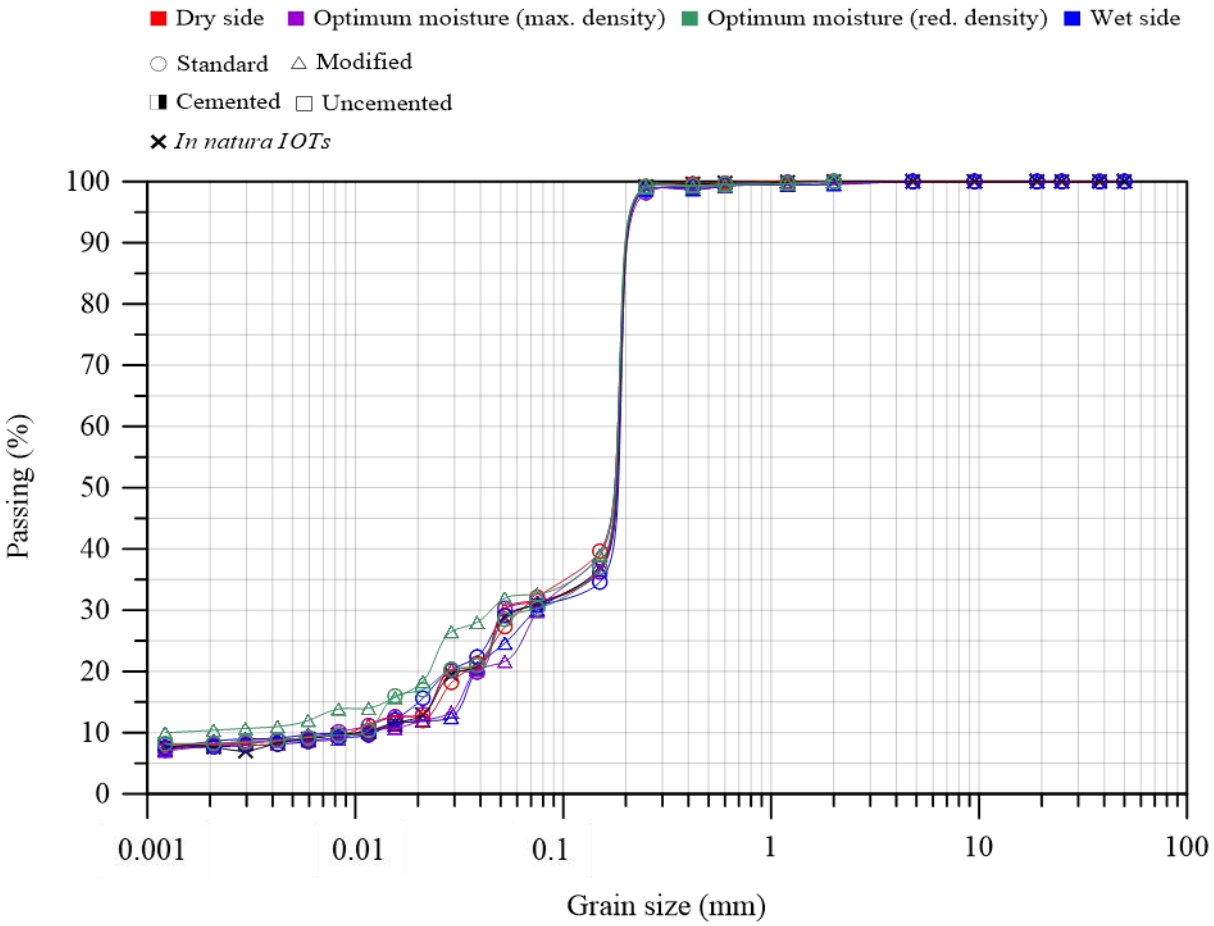

Figure 4.45. Grain size distribution uncemented IOTs - oedometric condition.

From the data exposed in Figure 4.45 it is possible to see that all uncemented specimens presented an extremely similar final grain size distribution to the natural *IOTs*. In general, the deformation of soil particle occurs as it is subjected to effective stress. With an increase of the energy imposed on soil particle, the micro-cracks in soil particle appear and develop gradually. Particle breakage occurs when the cracks in particle spread through the whole particle. In fact, the crushability of granular soil is mainly related to the physical nature and mechanical properties of soil, the stress-strain state on soil and the surrounding environment on soil.

The results demonstrate that the stress-strain state of the oedometric tests played a fundamental role in particle breakage, indicating that the consolidation state (represented by the oedometric condition) led to no significant change on the grain size distribution of the *IOTs*, independently of the initial molding condition. This behavior has also been attested for conventional soils, in which little or no breakage was evidenced during consolidation and significant breakage was seen during the shearing phase (Yu, 2017a; b; Yu and Su, 2016).

To further elucidate the influence of the oedometric conditions on the grain breakage analysis, the data was also evaluated in consonance with the method presented by Nakata (1999). Table 4.5 presents the grain breakage factor (*Bf*) for the uncemented oedometric test.

Table 4.5. Grain breakage factor uncemented specimens – oedometric condition.

Specimen*	Grain breakage factor (*Bf*)	Grain breakage (%)
SD-DS-U-OD	0.00	0.00
SD-OMM-U-OD	0.00	0.00
SD-OMR-U-OD	0.00	0.00
SD-WS-U-OD	0.00	0.00
MO-DS-U-OD	0.00	0.00
MO-OMM-U-OD	0.00	0.00
MO-OMR-U-OD	0.00	0.00
MO-WS-U-OD	0.00	0.00

*W-X-Y-Z: Compaction energy [standard (SD) or modified (MD)]-Initial moisture content [dry side (DS), optimum moisture maximum density (OMM), optimum moisture reduced density (OMR), and wet side (WS)]-Cement content [uncemented (U) or cemented (C)]-Test boundary condition [oedometric (OD) or triaxial (TX)].

The data exposed in Table 4.5 corroborates the previously mentioned behavior, in which uncemented specimens, under oedometric conditions (up to 6.4 MPa), present no grain breakage; considering that all grain breakage factors, as proposed by Nakata (1999), were zero (0% of the total grain breakage). This once again indicates, that for the *IOTs* of this research, the consolidation of the particles over high stresses results in no grain breakage, independently of the initial moisture content and compaction energy.

As for the cemented specimens, the results of the grain size distribution curves are shown in Figure 4.46.

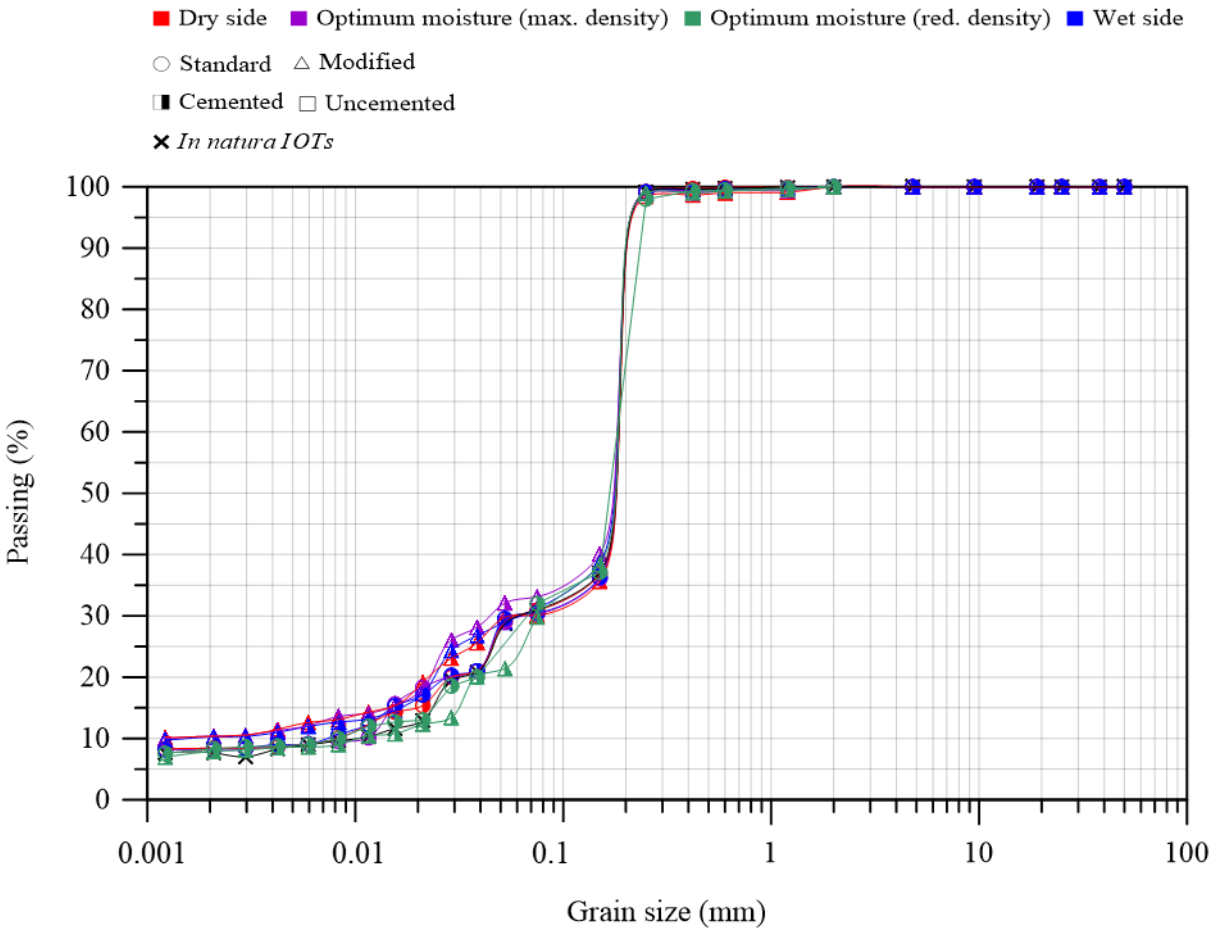

Figure 4.46. Grain size distribution cemented IOTs - oedometric condition.

Alluding to the behavior presented for the uncemented oedometric tests, all cemented specimens presented an extremely resembling final grain size distribution to the natural *IOTs*. It is expected soils to suffer deformation upon subjection to external stress. This stress may result in micro-cracks (especially in coarse-grained soils) that gradually increase with the increase in stress. Particle breakage is considered when the micro-cracks are spread through the whole soil particle. In the case of this research, for oedometric conditions, the results indicated that if any micro-cracks were formed in the cemented specimens, they were not capable of spreading to the whole particle, with no significant grain breakage occurring.

Regarding the influence of the molding conditions, no clear pattern could be extracted from the grain size distribution, only which cemented specimens resulted in a slightly finer grain size distribution. These results indicate, once more, that the stress-strain state is of great importance in the breakage of particles in *IOTs*, with the consolidation state imposed in the oedometric test not being capable of fully breaking the tailings grains. This behavior has been supported for conventional soils by several authors (e.g., Yu, 2017a; b; Yu and Su, 2016).

As stated initially, the data was also analyzed regarding grain breakage by means of the method presented by Nakata (1999). This analysis aimed to identify any possible patterns between the initial molding conditions and the final grain size distribution of the materials. Table 4.6 presents the grain breakage factor (*Bf*) for the cemented oedometric test.

Table 4.6. Grain breakage factor cemented specimens – oedometric condition.

Specimen*	Grain breakage factor (*Bf*)	Grain breakage (%)
SD-DS-C-OD	0.01	1.0
SD-OMM-C-OD	0.01	1.0
SD-OMR-C-OD	0.01	1.0
SD-WS-C-OD	0.01	1.0
MO-DS-C-OD	0.02	2.0
MO-OMM-C-OD	0.02	2.0
MO-OMR-C-OD	0.02	2.0
MO-WS-C-OD	0.02	2.0

*W-X-Y-Z: Compaction energy [standard (SD) or modified (MD)]-Initial moisture content [dry side (DS), optimum moisture maximum density (OMM), optimum moisture reduced density (OMR), and wet side (WS)]-Cement content [uncemented (U) or cemented (C)]-Test boundary condition [oedometric (OD) or triaxial (TX)].

From Table 4.6 it is clear that little breakage occurred for the cemented specimens, with a maximum grain breakage factor of 0.02 (representing 2% of the total grain breakage). Modified energy specimens resulted in higher grain breakage when compared to standard energy ones. This behavior is associated with the higher stiffness evidenced for modified specimens, resulting in a higher grain breakage. Nevertheless, the levels of grain breakage (maximum of 2%) evidenced for the cemented specimens can be seen as insignificant, considering that breakages lower or equal than 2% can be seen as the own variability of the grain size distribution test.

4.6.2 Triaxial conditions (TC)

Triaxial test conditions consist in the application of a hydrostatic state of stress and an axial load on a cylindrical specimen of soil. The specimen is placed inside the test chamber, being surrounded by a latex membrane that creates an interface, allowing the application of two levels of stress on the specimen: the confining pressure and the back pressure. The chamber is then filled with water, on which pressure is applied, generating the confinement on the specimen. This stress acts in all directions, including the vertical direction. Back pressure is applied directly to the sample through the base pedestal or through the top of the sample. Finally, axial loading is applied by means of a piston that penetrates the chamber. When compared to oedometric conditions, triaxial conditions are seen as more aggressive considering that both

consolidation and shearing phases involve multiaxial forces. In this sense, the results of the grain size distribution curves for the uncemented *IOTs* are shown in Figure 4.47.

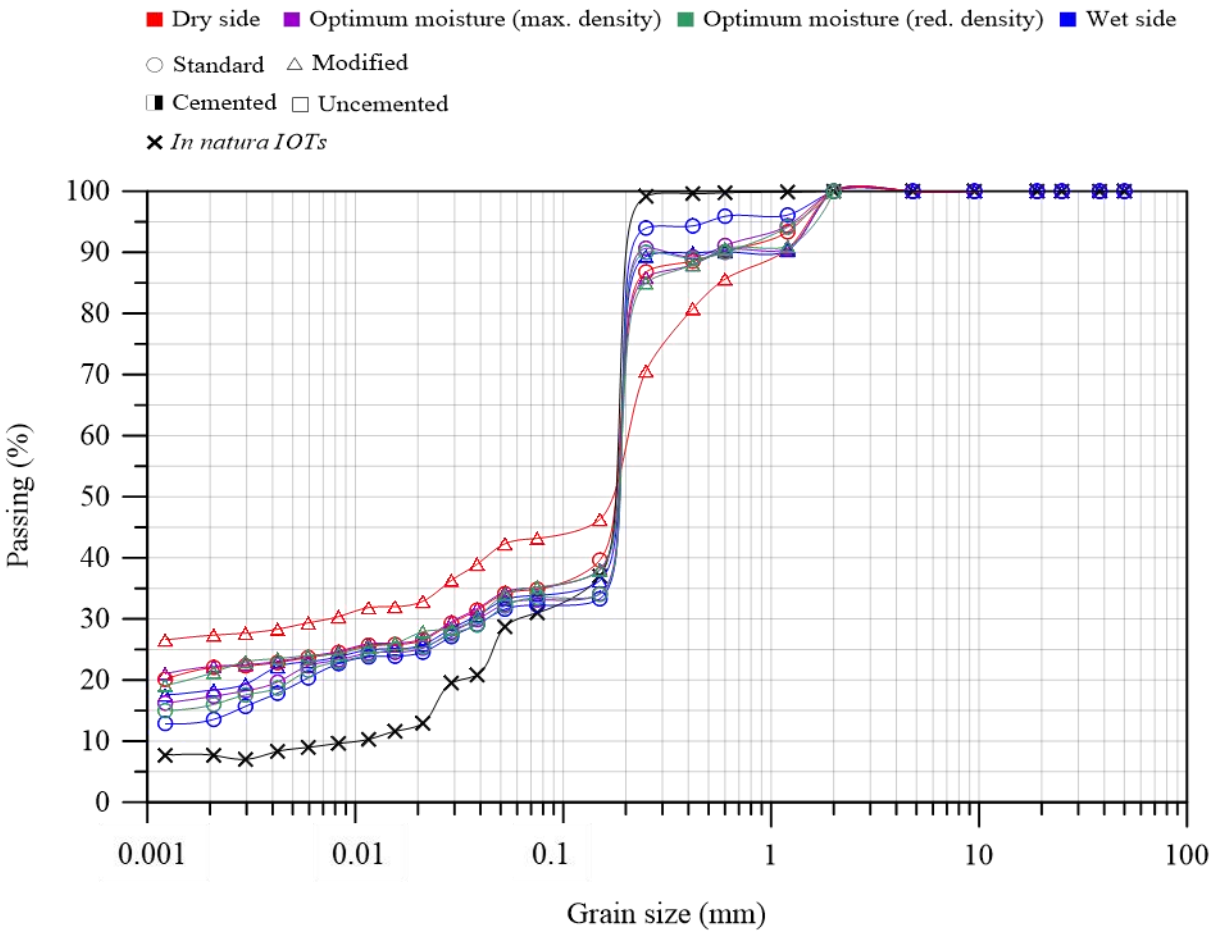

Figure 4.47. Grain size distribution uncemented IOTs – high stress triaxial condition.

Opposite from the behavior depicted from oedometric tests (Figure 4.46.), the grain size distribution of the uncemented specimens tested under triaxial conditions (Figure 4.47) resulted in significant changes in grain size distribution compared to the natural *IOTs*.

For the standard energy, the greatest grain breakages were evidenced for dry-side specimens, followed by optimum moisture content (max. density), optimum moisture content (red. density), and wet-side ones. This behavior was associated with the higher stiffness depicted for dry-side specimens, that present a more brittle failure mode. Brittle failure refers to the breakage of a material due to a sudden fracture. When a brittle failure occurs, the material breaks suddenly instead of deforming or straining under load. The fracturing or breaking can occur with only a small amount of load, impact force or shock. Brittle materials absorb less energy

before breaking or fracturing, despite the materials having a high strength. Brittle failure may also be known as brittle fracture. When materials reach the limit of their strength, they usually have the option of either fracturing or undergoing physical deformation. Materials exhibiting brittleness fail with little or no evidence of plastic deformation before the fracturing occurs.

In addition, as presented on items 4.2 and 4.5, the stiffness of *IOTs* be directly related to the structure imparted by compaction, mainly density and packing as well as the lubrication of the soil matrix particles, resulting from the different initial moisture contents. A similar pattern was evidenced for modified energy specimens, with the main difference laying on the magnitude of the values; in which modified energy specimens resulted in a higher alteration of the grain size distributions when compared to standard energy ones.

To further elucidate the influence of the triaxial conditions on the grain breakage analysis, the data was also evaluated in consonance with the method presented by Nakata (1999). Table 4.7 presents the grain breakage factor (*Bf*) for the uncemented triaxial test.

Table 4.7. Grain breakage factor uncemented specimens – triaxial condition.

Specimen*	Grain breakage factor (*Bf*)	Grain breakage (%)
SD-DS-U-TX	0.12	12.00
SD-OMM-U-TX	0.09	9.00
SD-OMR-U-TX	0.07	7.00
SD-WS-U-TX	0.05	5.00
MO-DS-U-TX	0.19	19.00
MO-OMM-U-TX	0.13	13.00
MO-OMR-U-TX	0.11	11.00
MO-WS-U-TX	0.10	10.00

*W-X-Y-Z: Compaction energy [standard (SD) or modified (MD)]-Initial moisture content [dry side (DS), optimum moisture maximum density (OMM), optimum moisture reduced density (OMR), and wet side (WS)]-Cement content [uncemented (U) or cemented (C)]-Test boundary condition [oedometric (OD) or triaxial (TX)].

The data exposed on Table 4.7 corroborates the previously mentioned behavior, in which the greatest grain breakages were evidenced for dry-side specimens, followed by optimum moisture content (max. density), optimum moisture content (red. density), and wet-side ones. Soil/water ratio significantly influences soil crushability. Under wet conditions, most of the soil pores are filled with water, and some of the water-filled pores resist external loads and protect the soil structure from damage. In the process of soil water absorption (wet soil), greater moisture makes it difficult to expel air from soil pores, increasing the confinement of air bubbles, resulting in an increase in soil elasticity. In addition, soil water acts as a lubricant within aggregates, which makes the soil sensitive to forces. Under dry soil conditions, forces act directly on soil particles, which destroy soil structure.

As for the cemented specimens, the results of the grain size distribution curves are shown in Figure 4.48.

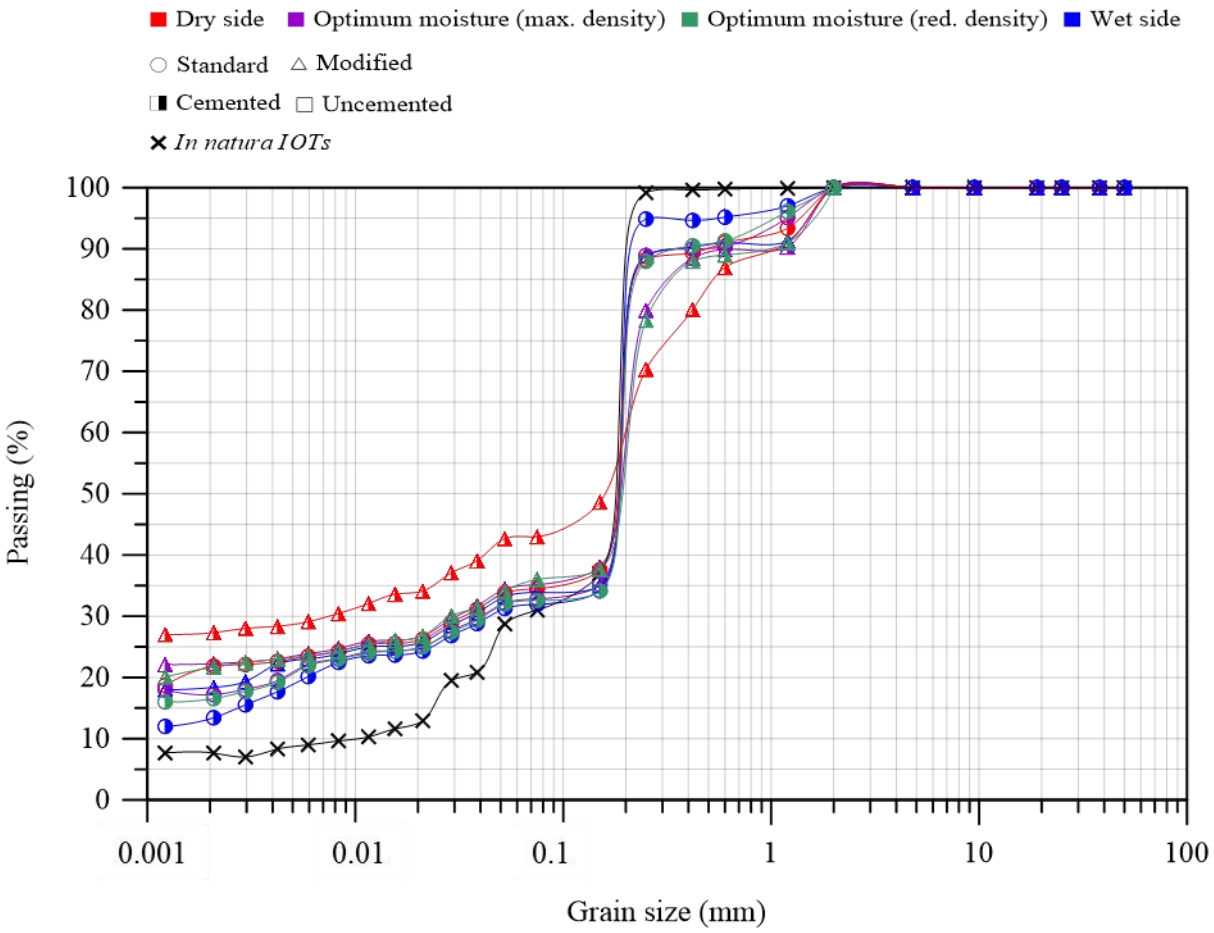

Figure 4.48. Grain size distribution cemented IOTs - triaxial conditions.

Alluding to the behavior presented for the uncemented triaxial tests, all cemented specimens resulted in significant changes in granulometry compared to the natural *IOTs*. For the standard energy, the greatest grain breakages were evidenced for dry-side specimens, followed by optimum moisture content (max. density), optimum moisture content (red. density), and wet-side ones. This behavior was once again associated with the higher stiffness and brittle behavior of the dry-side specimens, which represent phenomena directly related to the structure imparted by compaction, mainly density and packing as well as the lubrication of the soil matrix particles, resulting from the different initial moisture contents. A similar pattern was evidenced for modified energy specimens, with the main difference laying in the magnitude of the values; in which modified energy specimens resulted in a higher alteration of the grain size distributions when compared to standard energy ones. The increase in stress during shearing, in addition to

the rotation of the particles, results in micro-cracks (especially in coarse-grained soils) that gradually increase with the increase in stress. The evidenced particle breakage takes place when the micro-cracks are spread through the whole soil particle.

To further understand the abovementioned behavior, the grain breakage factor (*Bf*) of the cemented specimens was also calculated, in accordance with the method of Nakata et al. (1999). Table 4.8 presents the grain breakage factor (*Bf*) for the cemented triaxial tests.

Table 4.8. Grain breakage factor cemented specimens – triaxial condition.

Specimen*	Grain breakage factor (*Bf*)	Grain breakage (%)
SD-DS-C-TX	0.11	11.00
SD-OMM-C-TX	0.10	10.00
SD-OMM-C-TX	0.08	8.00
SD-WS-C-TX	0.04	4.00
MO-DS-C-TX	0.19	19.00
MO-OMM-C-TX	0.14	14.00
MO-OMR-C-TX	0.11	11.00
MO-WS-C-TX	0.10	10.00

*W-X-Y-Z: Compaction energy [standard (SD) or modified (MD)]-Initial moisture content [dry side (DS), optimum moisture maximum density (OMM), optimum moisture reduced density (OMR), and wet side (WS)]-Cement content [uncemented (U) or cemented (C)]-Test boundary condition [oedometric (OD) or triaxial (TX)].

Alluding to the behavior presented for the uncemented triaxial tests, for the cemented specimens the greatest grain breakages were evidenced for dry-side specimens, followed by optimum moisture content (max. density), optimum moisture content (red. density), and wet-side ones.

When comparing the cementation effect on grain breakage, no noticeable difference was evidenced, indicating that the cementation of the high confining stress specimens was indeed broken during the consolidation stage of the test. The general grain breakage behavior for the triaxial conditions further corroborated the premise that, under high stresses, shearing causes more particle breakage than consolidation (Yu, 2017a; b; Yu and Su, 2016) indicating that the rotation of angular particles play a fundamental role on the final grain size of the *IOTs*.

Particle breakage in granular geotechnical materials (such as the case of the *IOTs* of this research) is known to be dependent on particle strength, particle size and distribution, particle shape, density of particles, mineral composition of particles, presence or absence of water in soils, and even stress–strain state on particles. More particle breakage occurs under higher stress or larger strain (Wang et al., 2021). In granular soils, particle breakage may even continue with time in the creep form (McDowell and Khan, 2003).

It is physically plausible that particle breakage augments with increasing particle size due to the fact that larger particle would contain more flaws to be crushed in higher probability (McDowell et al., 1996). Nevertheless, some authors state that the fragmentation process in soil aggregation, larger particles would get cushioned to become more resistive to crushing by surrounding smaller particles so that the neighboring smaller particles are more likely to be crushed (Einav, 2007a; b). For this research, more particle breakage was evidenced in the denser samples; a similar behavior has been evidenced for conventional sands (Yu, 2017a; b; Yu and Su, 2016).

Furthermore, uniform soils have higher particle breakage than the well-graded soils with the same maximum particle size (Lee and Farhoomand, 1967). According to the increasing levels of particle damage, particle breakage can be defined as the grinding of particle surface, the breakage of an asperity of particle and the splitting of particle (Nakata et al., 2001). Particle breakage results in a new gradation of soil having a significant influence on the shearing and dilatancy mechanics of granular soil (e.g., Yu, 2017a; b; Yu and Su, 2016). Since the dilatancy phenomenon in granular materials was firstly mentioned by Reynolds (1885), the stress–dilatancy behavior of soil plays a very significant role in interpreting soil behavior: e.g., stress–dilatancy behavior (De Silva et al., 2014) and stress–dilatancy behavior in relation to particle breakage or fines content (e.g., Yu, 2017a; b; Yu and Su, 2016).

In the triaxial tests on the pre-crushed sands, particle breakage resulted in the change of strain–stress behavior in translation and rotation of the relation of the dilatancy factor and the effective principal stress ratio (Yu and Su 2016). In a great deal of triaxial tests on the pre-crushed sands, for a given initial void ratio, particle breakage impaired the peak state friction and dilatancy angles, but the peak-state basic friction angles (i.e., the difference between peak-state friction angle and peak-state dilatancy angle) of the pre-crushed sands were shown to experience an increase to a peak and then a decrease against the increase of particle breakage (Yu, 2017a; b; Yu and Su, 2016). In addition, particle breakage resulted in the reduction of the excess friction angles of the pre-crushed sands approximately in down concavity to a constant. Particle breakage impaired the dilatancy behavior of soil, resulting in a more contractive soil, i.e., causing the reduction of dilatancy angle and void ratio in the drained tests and the increase of excess pore water pressure in the undrained tests, which reveals the inherent influence of particle breakage on soil behavior (Yu, 2017a; b; Yu and Su, 2016).

In the investigation of the in situ tests and laboratory tests on the volcanic coarse-grained soils, particle breakage resulted in a more remarkable contractive behavior as well (Miura et al., 2003). In the direct shear tests on a carbonate sand, the apparent critical-state friction angle including frictional and clastic components was shown to increase with increasing the degree of particle breakage (Tarantino and Hyde, 2005). The phase–transformation– state stress ratio was revealed to decrease monotonically with decreasing state parameter (Murthy et al., 2007).

The influence of particle breakage on the stress–strain and dilatancy behavior has been presented under the drained and undrained conditions in triaxial compression and extension tests, as well as in one-dimensional compression and ring shear tests (Yu, 2017a; b; Yu and Su, 2016).

In general, the crushability of *IOTs* was mainly related to the physical nature and mechanical properties of the material, in addition to the initial molding conditions (moisture content and compaction energy) and the boundary conditions of the tests. To further corroborate the aforementioned behavior, the next section discusses the microscopic evaluation of the *IOTs* under the light of grain breakage analysis.

4.6.3 Microscopic evaluation (ME)

The microstructure evaluation and the semi-quantitative chemical composition were evaluated by a *SEM-EDS* mode. The *SEM* analysis was performed in the following conditions: backscattered electrons with a magnification of 100, 500, 1,000, 2,000, and 5,000 times and secondary electrons with magnification of 1,000, 2,000, and, 5000 times; electron beam of 20 kV voltage; with gold-coated samples (Quorum Q150 and JSM-6610 models). *ME* was conducted exclusively on specimens that presented the highest particle breakage from each test boundary condition (as shown in Items 4.6.1 and 4.6.2), while encompassing both cemented and uncemented specimens. In addition, the *ME* was also conducted on the natural material to create a control group for the analysis. A summary of the *ME* tests can be seen in Table 4.9.

Table 4.9. Microscopy evaluation: specimens and magnifications.

Specimen	Magnification (times)
Natural iron ore tailings[1]	100, 500, 1,000, 2,000, and 5,000
MO-DC-U-OD[2]	
MO-DC-C-OD[2]	
MO-DC-U-TX[2]	
MO-DC-C-TX[2]	

[1] Control group.

[2] W-X-Y-Z: Compaction energy [standard (SD) or modified (MD)]-Initial moisture content [dry side (DS)]-Test boundary condition [oedometric (OD) or triaxial (TX)].

To facilitate the comparison between the grain breakages of the tests, this analysis was also divided in two subsections, oedometric conditions and triaxial conditions.

4.6.3.1 ME: oedometric conditions

Figure 4.49 presents the results of microscopic evaluation of the uncemented iron ore tailings subjected to the oedometric test. In addition, the natural iron ore tailings are also presented to act as control group regarding the surface, roughness, and grain sizes comparisons.

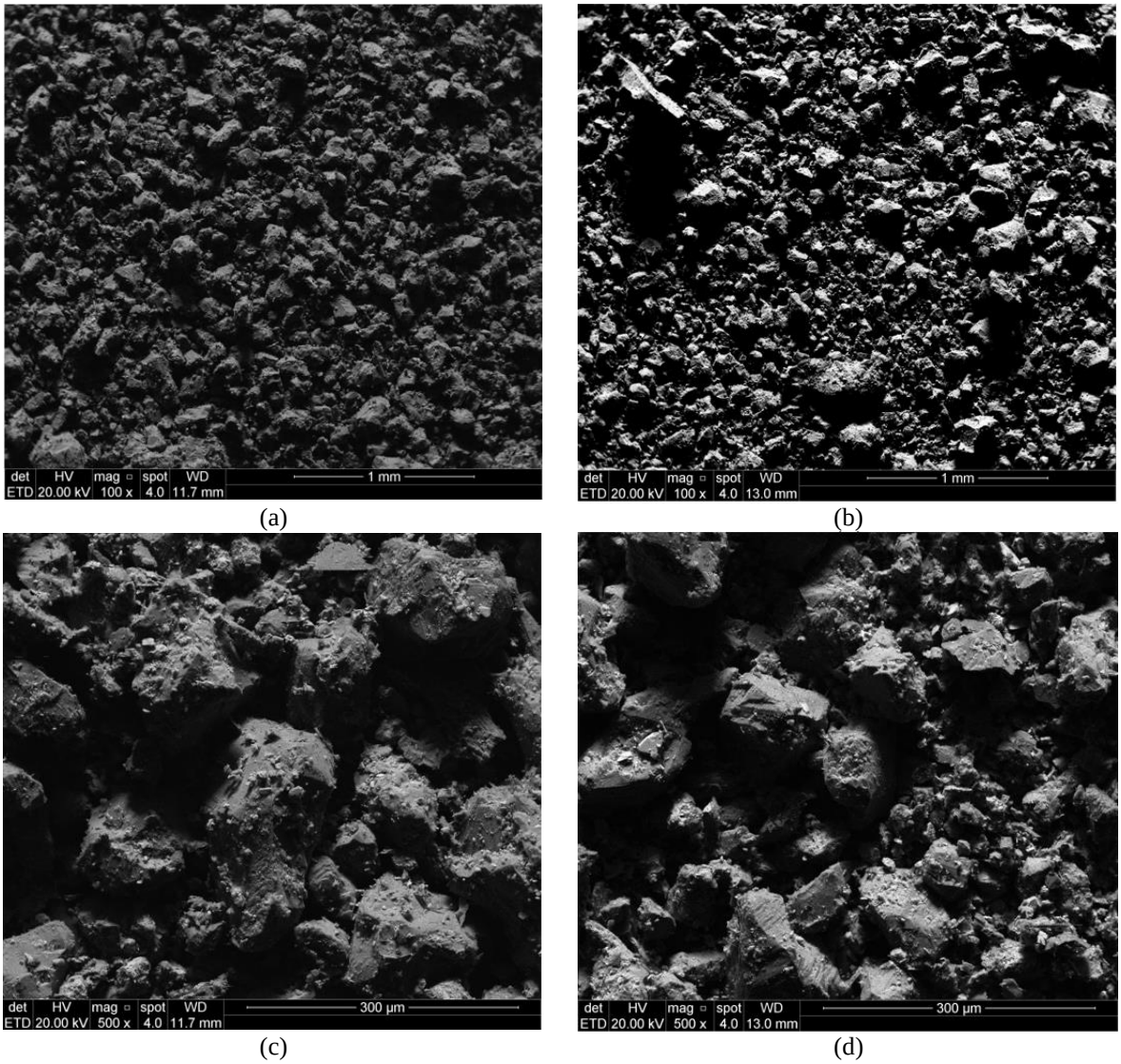

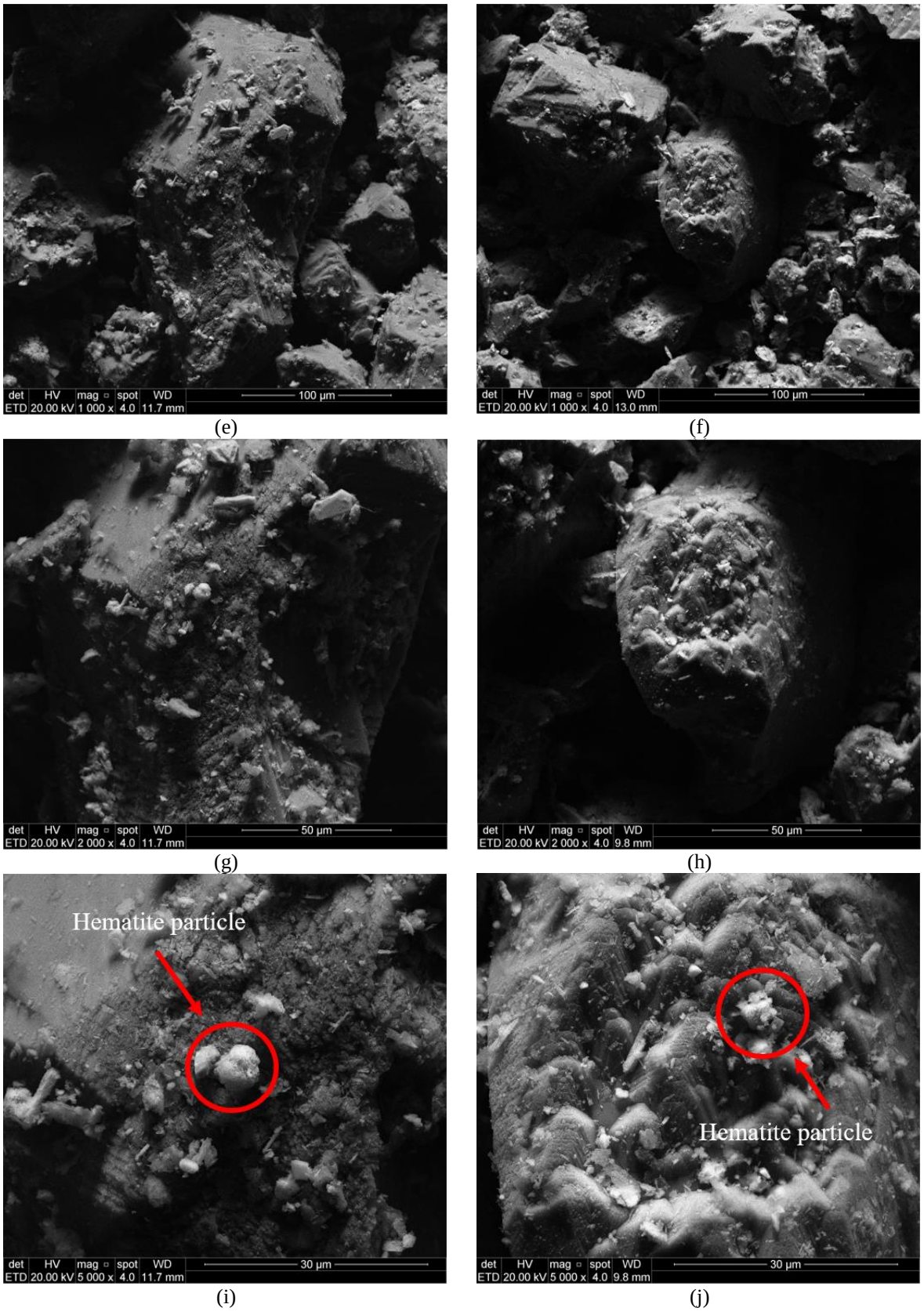

Figure 4.49. Scanning electron microscopy: (a) natural IOT – 100x; (b) Uncemented oedometric test – 100x; (c) natural IOT – 500x; (d) Uncemented oedometric test – 500x; (e) natural IOT – 1000x; (f) Uncemented oedometric test – 1000x; (g) natural

IOT – 2000x; (h) Uncemented oedometric test – 2000x; (i) natural IOT – 5000x; (j) Uncemented oedometric test – 5000x;

In general, it is possible to see that little or no alteration was evidenced on the uncemented oedometric test specimens, regarding their morphology, roughness, and particle size. For all magnifications, grains presented similar angularity, corroborating the results presented in Item 4.6.1, which indicated that no particle breakage occurred. This once again indicates that the one-directional consolidation state led to no significant change on the grain size distribution of the iron ore tailings. Finally, a typical behavior regarding the morphology evidenced: the presence of smaller agglomerated hematite particles on the surface of regular flat large quartz particles, similar to the one shown by several authors (Gou et al., 2019; Pinto et al., 2022; Reid et al., 2022; Reid and Fanni, 2022; Yu, 2021).

Figure 4.50 depicts the results of the microscopic evaluation of the cemented iron ore tailings subjected to oedometric testing. Also, the natural iron ore tailings are also presented to act as a control group regarding the morphology, roughness, and grain size comparisons.

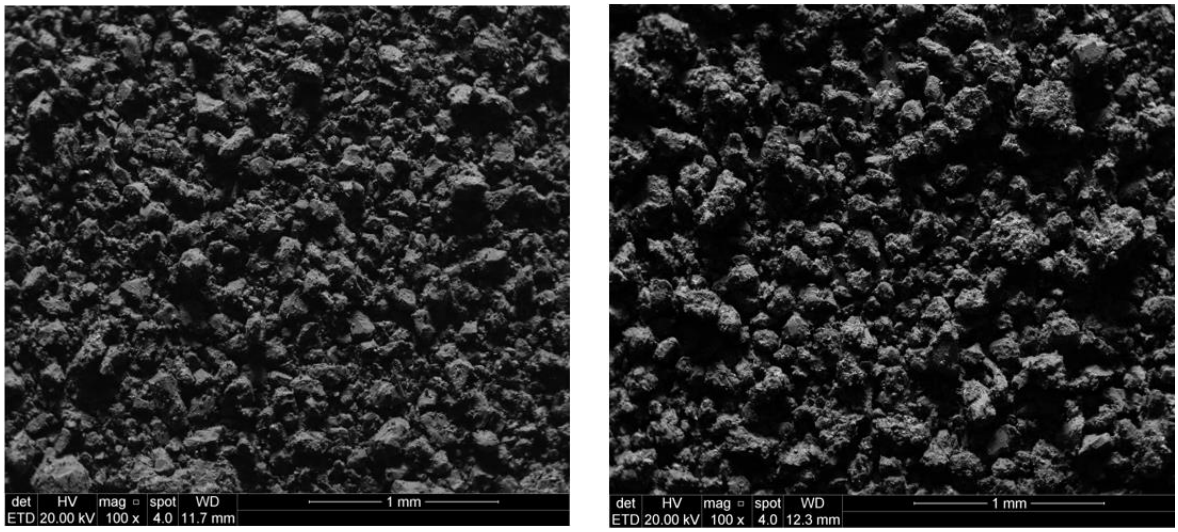

(a) (b)

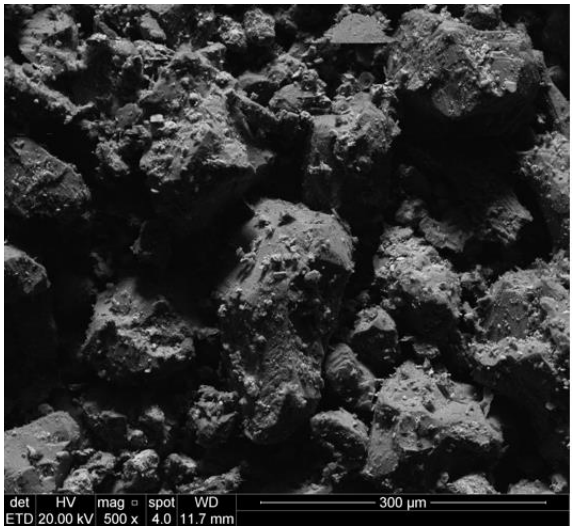
det HV mag spot WD
ETD 20.00 kV 500 x 4.0 11.7 mm
300 µm

(c)

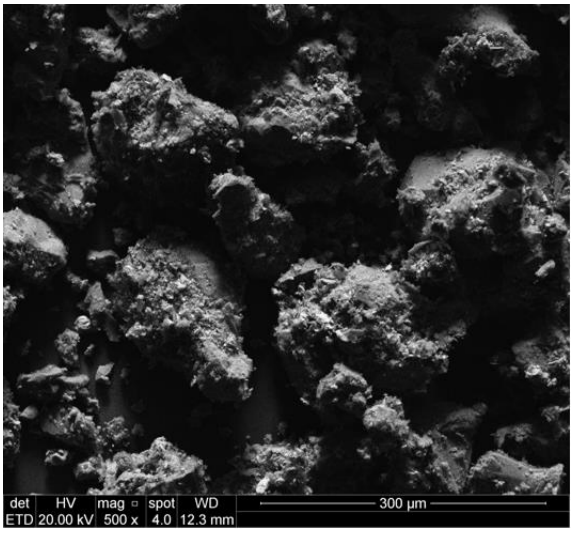
det HV mag spot WD
ETD 20.00 kV 500 x 4.0 12.3 mm
300 µm

(d)

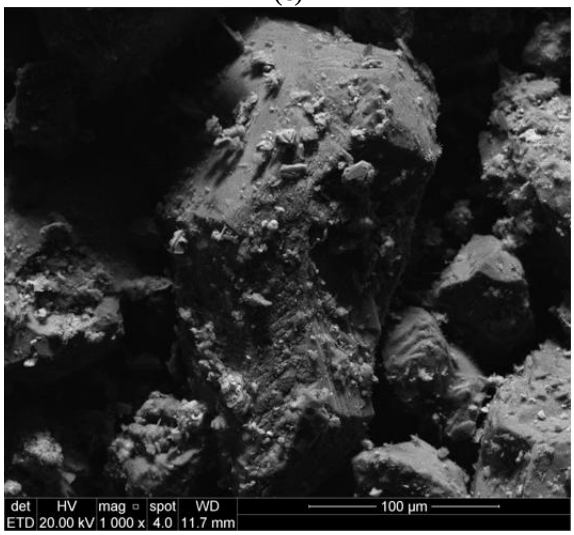
det HV mag spot WD
ETD 20.00 kV 1 000 x 4.0 11.7 mm
100 µm

(e)

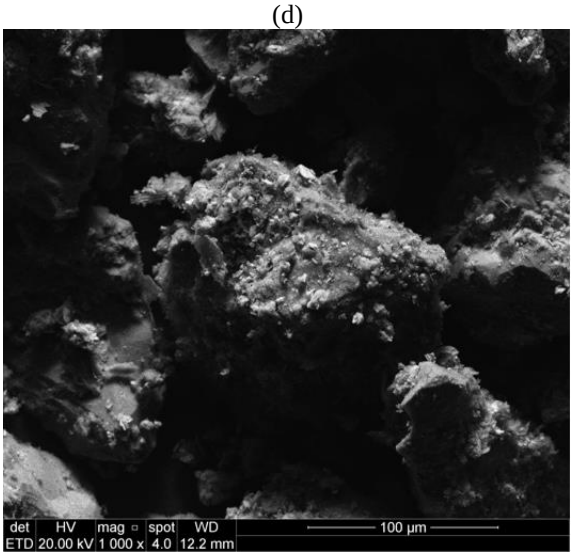
det HV mag spot WD
ETD 20.00 kV 1 000 x 4.0 12.2 mm
100 µm

(f)

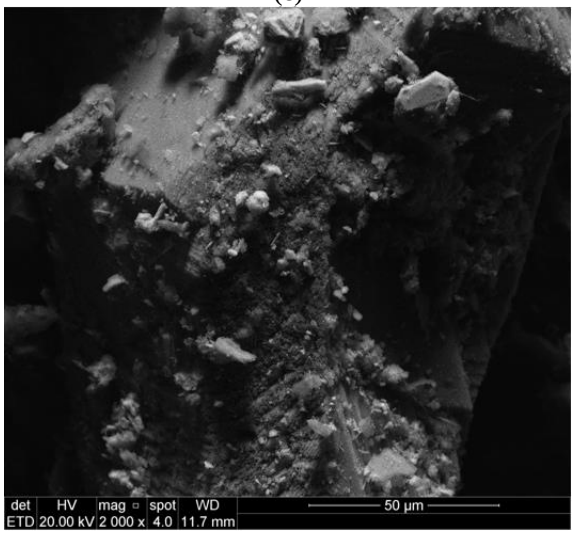
det HV mag spot WD
ETD 20.00 kV 2 000 x 4.0 11.7 mm
50 µm

(g)

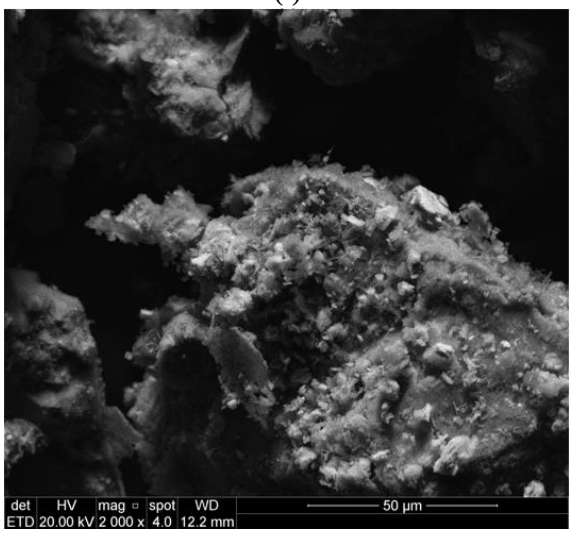
det HV mag spot WD
ETD 20.00 kV 2 000 x 4.0 12.2 mm
50 µm

(h)

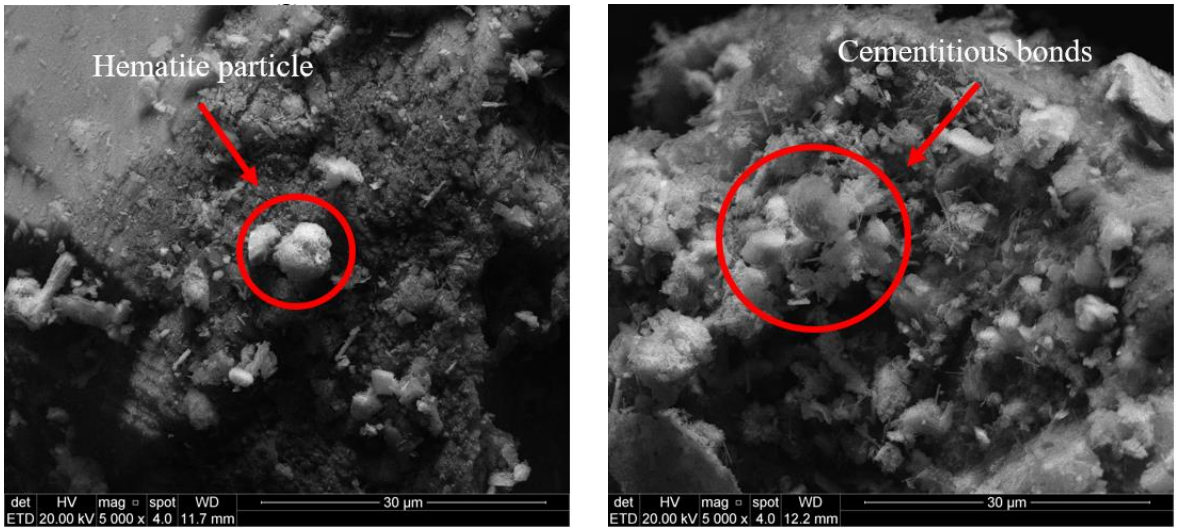

(i) (j)

Figure 4.50. Scanning electron microscopy: (a) natural IOT – 100x; (b) Cemented oedometric test – 100x; (c) natural IOT – 500x; (d) Cemented oedometric test – 500x; (e) natural IOT – 1000x; (f) Cemented oedometric test – 1000x; (g) natural IOT – 2000x; (h) Cemented oedometric test – 2000x; (i) natural IOT – 5000x; (j) Cemented oedometric test – 5000x;

For the cemented specimens under oedometric conditions (Figure 4.50), similar to what has been presented for the uncemented ones (Figure 4.49), little or no alteration was evidenced regarding their morphology, roughness, and particle size. The grains showed similar shapes and angularities, which in turn allude to the results discussed on Item 4.6.1. The microscopic evaluation further demonstrates that under oedometric conditions (even at high stresses up to 6.4MPa) no particle breakage is evidenced on *IOTs*. This behavior once again indicates, that the conditions imposed in the oedometric test (one-dimensional consolidation) are not severe enough to result in grain breakage, as also shown by Einav (2007b); Yu (2017a; b, 2021); Yu and Su (2016) for natural occurring materials. In general, both the natural and the tested material presented agglomerated hematite particles on the surface of regular flat large quartz particles. Finally, some sort of cementitious structure (represented by the little agglomerated particles forming clusters around the quartz particles) could be seen on the cemented specimens, even though some of the cementitious bonds may have been broken during the test.

4.6.3.2 ME: triaxial conditions

The results of the microscopic evaluation of the uncemented iron ore tailings subjected to high-stress triaxial testing are shown in Figure 4.51. Furthermore, the natural iron ore tailings are also presented in Figure 4.51 to create a control group regarding the morphology, roughness, and grain size of the tested specimens.

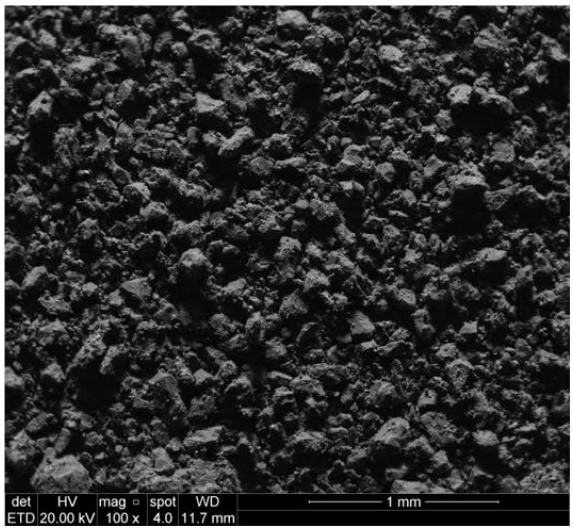
det HV mag spot WD
ETD 20.00 kV 100 x 4.0 11.7 mm
1 mm

(a)

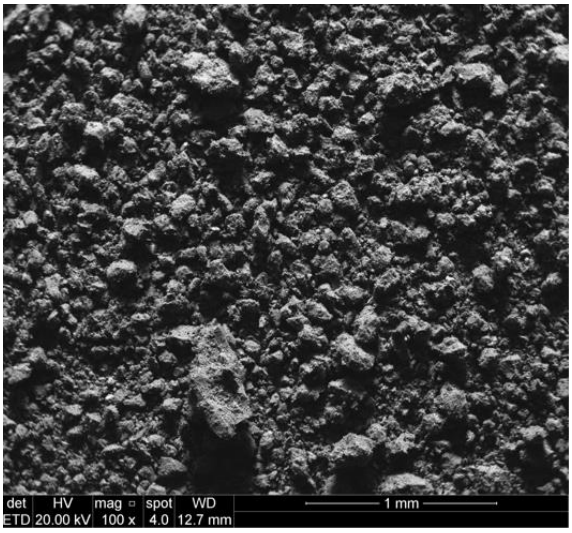
det HV mag spot WD
ETD 20.00 kV 100 x 4.0 12.7 mm
1 mm

(b)

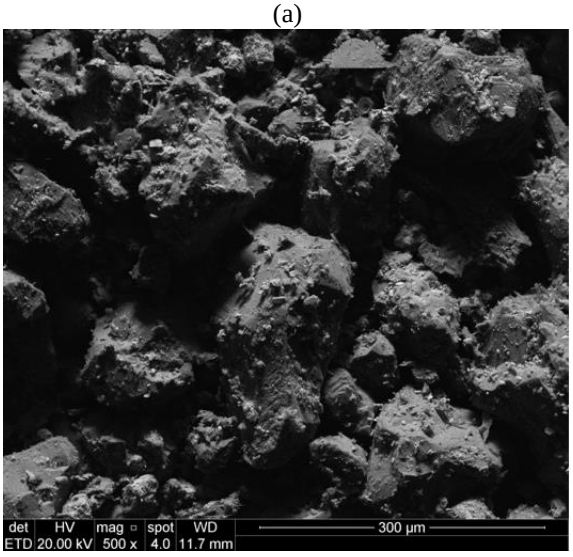
det HV mag spot WD
ETD 20.00 kV 500 x 4.0 11.7 mm
300 µm

(c)

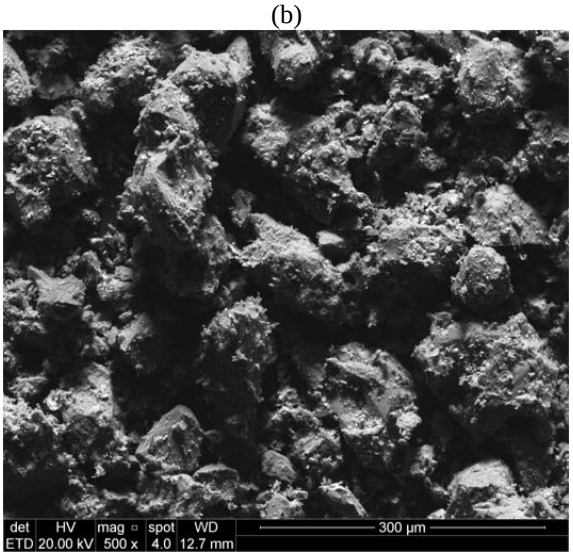
det HV mag spot WD
ETD 20.00 kV 500 x 4.0 12.7 mm
300 µm

(d)

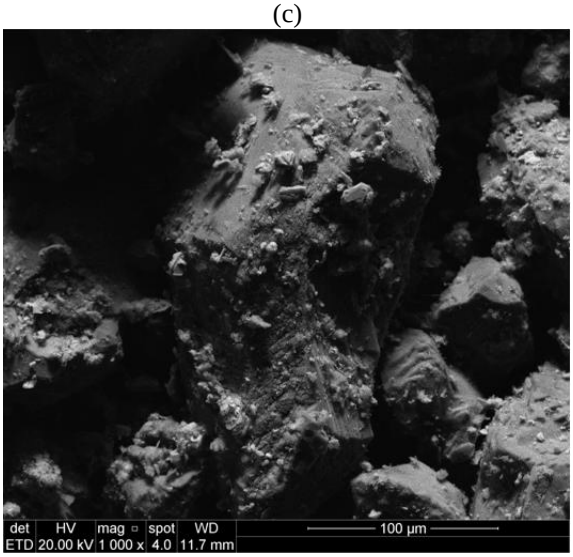
det HV mag spot WD
ETD 20.00 kV 1 000 x 4.0 11.7 mm
100 µm

(e)

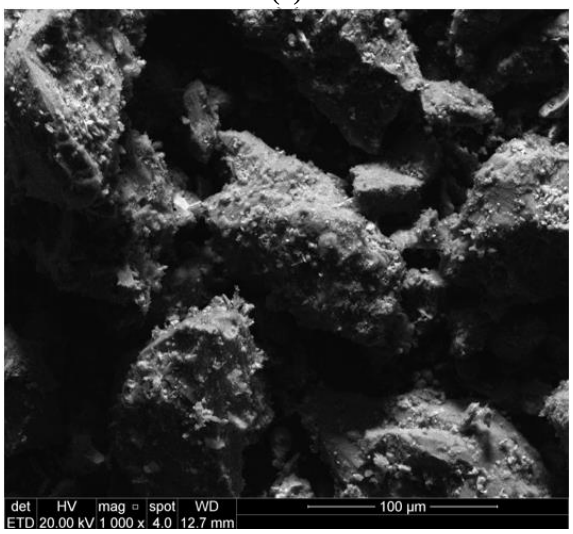
det HV mag spot WD
ETD 20.00 kV 1 000 x 4.0 12.7 mm
100 µm

(f)

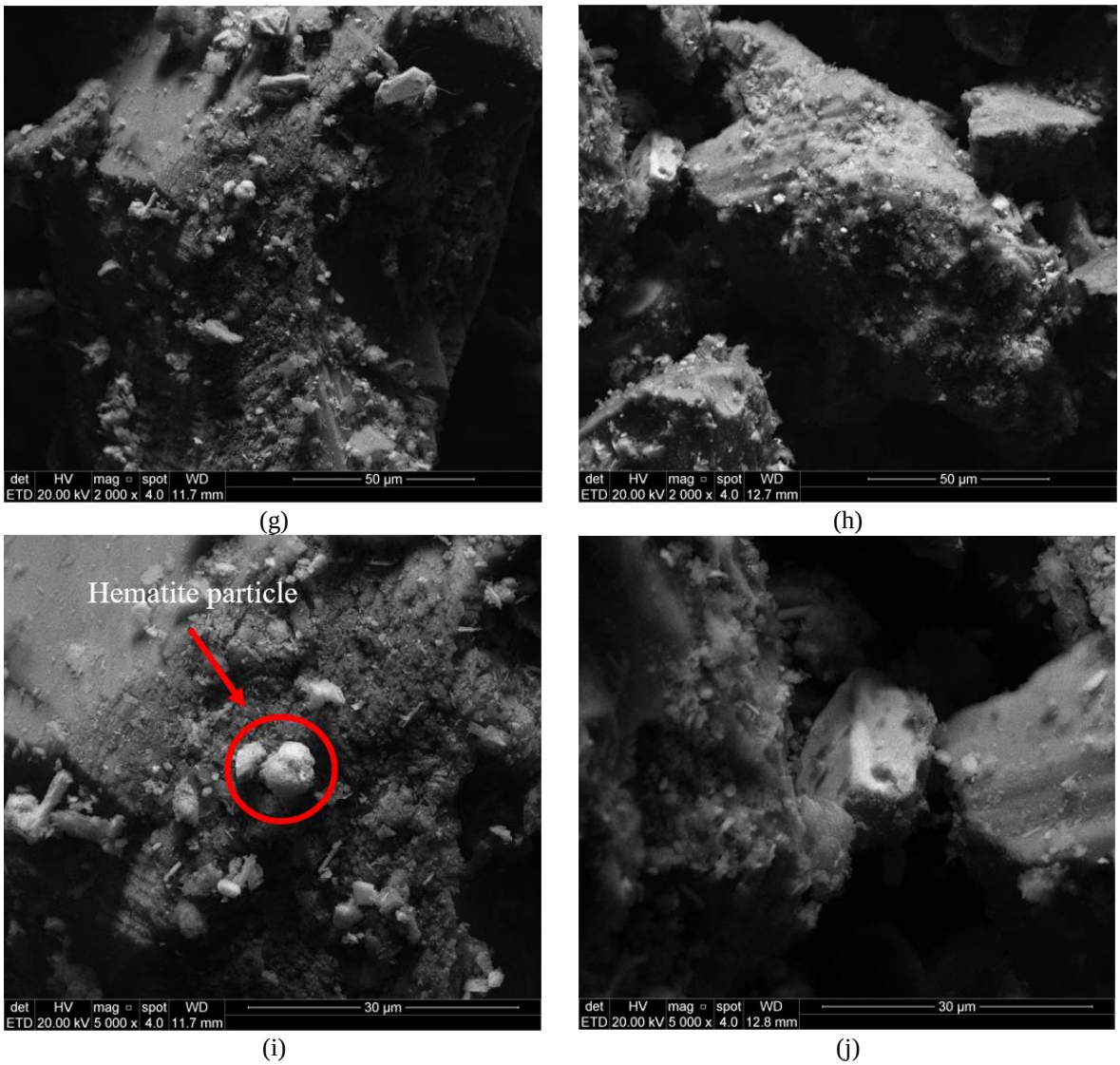

Figure 4.51. Scanning electron microscopy: (a) natural IOT – 100x; (b) Uncemented triaxial test – 100x; (c) natural IOT – 500x; (d) Uncemented triaxial test – 500x; (e) natural IOT – 1000x; (f) Uncemented triaxial test – 1000x; (g) natural IOT – 2000x; (h) Uncemented triaxial test – 2000x; (i) natural IOT – 5000x; (j) Uncemented triaxial test – 5000x;

In general, it is possible to see that the specimens that were tested under high-stress triaxial conditions presented rougher surfaces and less defined angular grains (indicating some level of grain breakage), when compared to the natural iron ore tailings. Especially from the 500 times magnification up, it is noted that the grain particles were directly affected by the test condition, with the specimens showing lower particle sizes, mainly agglomerates of micrometric particles (Figure 4.51d, f, h, j). This behavior indicates that, under high stresses, shearing causes more particle breakage than consolidation (Yu, 2017a; b; Yu and Su, 2016), in other words, the rotation of angular particles play a fundamental role in the final morphology of iron ore tailings.

Even though a large parcel of the grains was broken (up to 19%), clustered hematite particles were still evidenced over the quartz particles, indicating that most of the grain breakage occurred exclusively on the quartz particles.

Figure 4.52 presents the results for the cemented specimens under triaxial conditions, as well as, for the natural iron ore tailings.

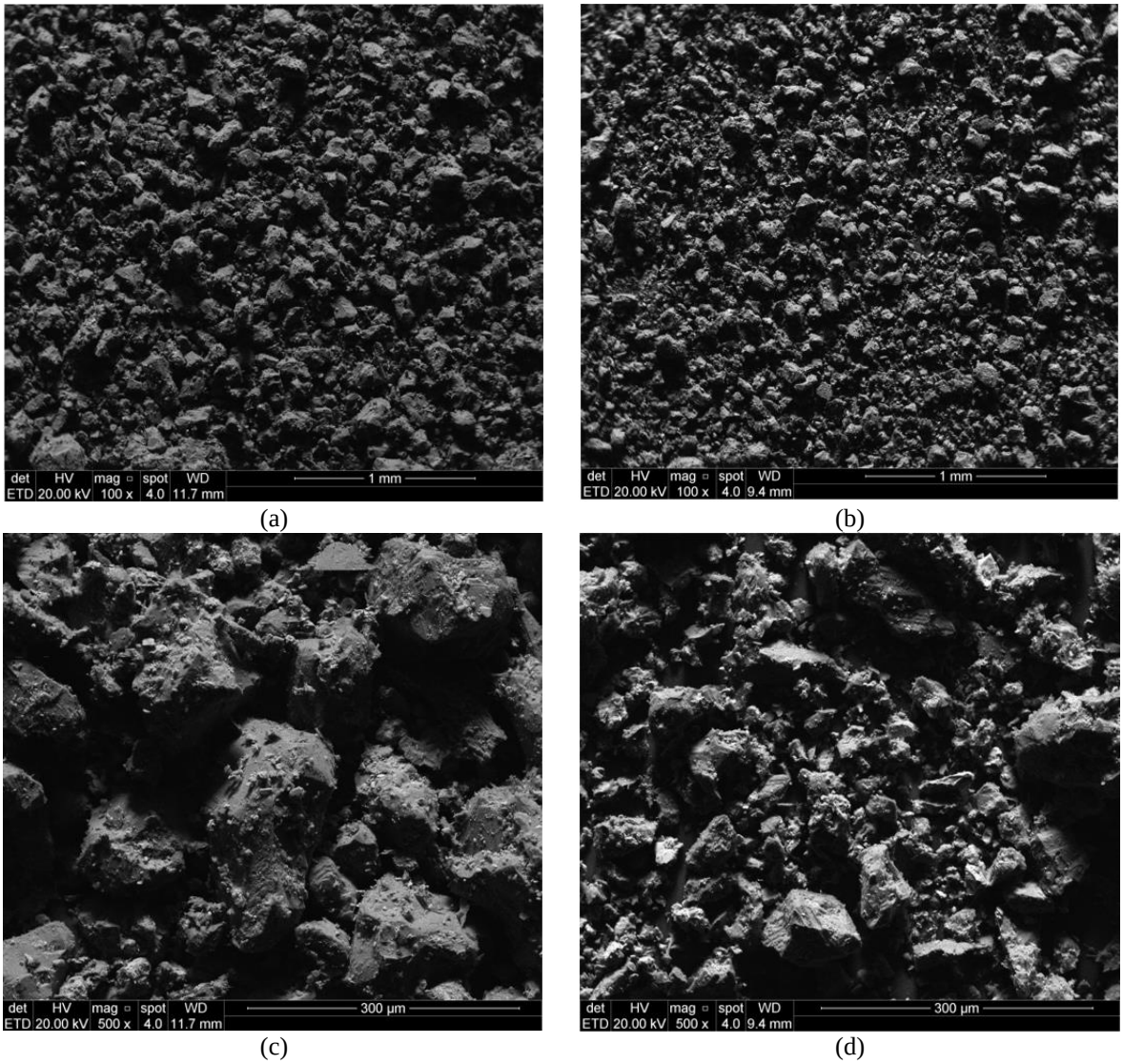

(a) (b)

(c) (d)

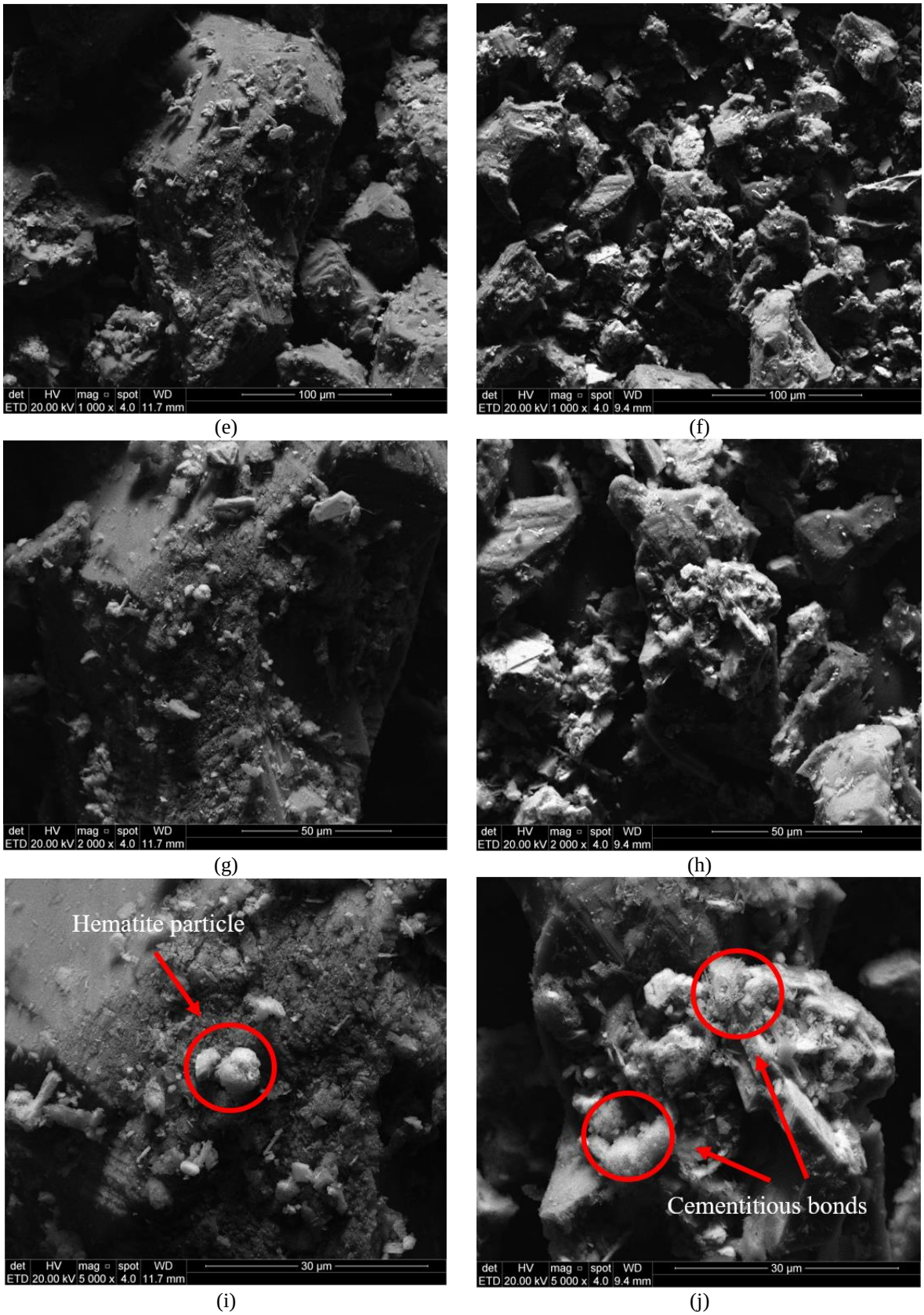

Figure 4.52. Scanning electron microscopy: (a) natural IOT – 100x; (b) Cemented triaxial test – 100x; (c) natural IOT – 500x; (d) Cemented triaxial test – 500x; (e) natural IOT – 1000x; (f) Cemented triaxial test – 1000x; (g) natural IOT – 2000x;

(h) Cemented triaxial test – 2000x; (i) natural IOT – 5000x; (j) Cemented triaxial test – 5000x;

The general behavior depicted on Figure 4.52 shows that similar to uncemented specimens, rougher surfaces and less defined angular grains were evidenced for the cemented specimens under triaxial conditions. This behavior is another indicative that most of the cementation was indeed broken during the consolidation phase of the triaxial test (p' = 3000 kPa), in which the iron tailings now behave like an uncemented material (see Items 2.3.5, 0, and 4.5.1.5). It is also noted that for all magnification of Figure 4.52, specimens showed lower particle sizes, (mainly agglomerates of micrometric particles) when compared to the natural material. Furthermore, it is plausible to assume that shearing of particles results in a higher particle breakage when compared to consolidation (both unidimensional and multidimensional). As previously stated, this behavior has also been attested by different authors (Yu, 2017a; b; Yu and Su, 2016) for conventional soils. Furthermore, clustered hematite particles were still evidenced over the quartz particles, indicating once more that most of the grain breakage occurred exclusively on the quartz particles. Finally, even though most of the cementitious structure was broken during the consolidation phase, some sort of cementitious structure (represented by the little agglomerated particles forming clusters around the quartz particles) was still evidenced on the cemented specimens.

5 CONCLUDING REMARKS

This research analyzed the influence of different molding conditions (i.e., dry side of the compaction curve, optimum moisture content, and wet side of the compaction curve) on the geomechanical behavior of both uncemented and cemented iron ore tailings under low (p' = 300kPa) and high confining stresses (p' = 3000kPa). To this extent, the following tests were executed: unconfined compressive strength, initial shear stiffness, hydraulic conductivity, compressibility, axial compression triaxial, and grain breakage analysis. With basis on the tests and analyses carried out during the development of this research, the following concluding remarks were taken:

a) **Regarding the characterization of the iron ore tailings**: The iron ore tailings presented a non-plastic behavior, and based on their grain size distribution they were classified as a silty sand. From the mineralogical composition analysis, it was possible to see that the material presented three crystalline phases: quartz, kaolinite, and hematite. Furthermore, the material was majorly composed of silicon, followed by iron and aluminum. Finally, it was possible to classify the iron ore tailings as an inert and non-hazardous waste (class IIB), in other words, a material that presents no harmful substances such as heavy metals or chemicals, not being chemically or biologically reactive.

b) **Regarding the unconfined compressive strength tests**: Increasing cement content and reducing porosity resulted in higher unconfined compressive strength values. The reduction in porosity induces a greater contact area between soil particles, intensifying interlocking and mobilizing friction, which increases strength; while the increase in binder content is linked to the increase in cementitious reactions, also contributing to strength development. Regarding the effect of the molding conditions, for both compaction energies, higher unconfined compressive strength was evidenced for specimens molded at the optimum moisture content (max. density), followed by specimens molded at optimum moisture content (red. density), dry-side and the wet-side, respectively. When the void ratio influence is removed, specimens molded at the optimum moisture content (red. density) still depicted the highest strength, showing that the structure imparted by compaction is fundamental (soil fabric) even after the development of the cementation bonds. This fact may be explained considering the coupled effect of the two main contributing factors on the shear strength of the stabilized

geotechnical materials: the structure imparted by compaction, mainly density, and packing, which predominates in the short-term, and the formation of a cementitious matrix, which predominates in the long-term. Finally, adequate correlations between unconfined compressive strength and η/Civ index were evidenced, indicating the possibility to choose the best combination of porosity and binder content for a project, without trial-and-error experiments.

c) **Regarding the initial shear stiffness tests**: Unlike the behavior depicted in literature for cemented geotechnical materials, stiffness could not be simply and directly related to unconfined compressive strength (in which less porous samples with higher cement content result in higher values of initial shear stiffness). The highest initial shear stiffness values were depicted for specimens molded on the dry-side of the compaction curve, for both compaction energies. This indicates that the stiffness of cemented soils is not only dependent on void ratio and cement content, but is rather presented as a more complex phenomenon also influenced by the initial moisture content of the mixtures This behavior was associated to the coupled effect of the two main contributing factors on the shear strength of the stabilized geotechnical materials: the structure imparted by compaction (soil fabric), mainly density, and packing, which predominates in the short-term, and the formation of a cementitious matrix, which predominates in the long-term.

d) **Regarding the hydraulic conductivity tests**: In general, all specimens resulted in similar hydraulic conductivity values, falling in the same permeability classification (i.e., very low permeability). The increase from standard to modified energy led to a decrease in hydraulic conductivity values. Soil permeability depends on multiple factors, among which the compactness which is itself linked to the density and the void ratio. When secluding the moisture content effect/influence, the increase in water presence led to a decrease in hydraulic conductivity for all combinations of compaction energies, initial moisture contents, and cement contents. If compacted on the dry side of optimum moisture content, soils are expected to present higher permeabilities, and less susceptibility to shrinkage, but they will be more susceptible to swelling and will have higher absorption of water than soils compacted on the wet-side of the compaction curve. The values of permeability on the wet-side of optimum moisture content tend to increase with the addition of water, but this increase is at a much slower rate. When isolating the influence of cement content, it can be seen that the increase in cement content (0 to 3%) led to a decrease in hydraulic conductivity values. For coarse-grained

materials (large grain sizes) the cement binds the soil particles, which decreases the average pore size, reducing the hydraulic conductivity.

e) **Regarding the compressibility tests**: For all tested combinations a similar behavior was evidenced, in which the increase in stress (up to levels of 6.4MPa) led to a decrease in void ratio. The exhibited behavior is associated with the rearrangement of soil particles, creating a denser configuration resulting in a volume reduction and then a small rebound upon release of stress (unloading stages). Specimens molded at optimum moisture content (max. density) resulted in lower settlements when compared to specimens molded optimum moisture content (red. density), dry and wet side of the compaction curve. This result can be correlated with the lower initial void ratio of optimum moisture content (max. density) specimens, which leaves less space for the rearrangement of soil particles. As for the other combinations, specimens molded at the optimum conditions (red. dry unit weight) and dry side, resulted in very similar settlements, with the latter being slightly less resistant; on the other hand, wet side specimens resulted in higher settlements. Cement addition had a positive effect on the settlement of all specimens, independently of the initial molding conditions and molding energy. Higher the cement content, the greater the cementation-induced pre-consolidation stress, the more extended the reloading region, and the greater the vertical effective stress that can be sustained at a given void ratio. The increase in the pre-consolidation pressure and the shift of the compression curves to the higher vertical effective stress described are indications of the development of a stiffer soil structure with the treatment when compared to uncemented specimens

f) **Regarding the axial compression triaxial tests under low stresses:** A classical strain-hardening behavior was evidenced until the peak of strength on the stress-strain analysis, followed by a strain-softening, with the strength reaching constant values at strains up to 20%. The highest deviatory stress value was evidenced for optimum moisture content (max. density) specimens, followed by specimens molded at optimum moisture content (red. density), dry-side and the wet-side, respectively. All specimens depicted an initial compressive behavior, followed by an expansive one; this behavior is a typical conventional soil behavior for dense specimens, such as the case of this research. The initial compressive behavior is due to the adjustment/accommodation of the soil particles, followed by the dilative behavior due to the interlocking of the grains. Optimum moisture content (max. density) specimens resulted in lower compression and

higher expansion when compared to the other combinations. This behavior can be associated with the lower initial void ratio of optimum moisture content specimens; considering that these specimens presented a more compact initial matrix, particles had less space to accommodate resulting in an increased particle movement into a more close-packed array. When isolating the void ratio effect and comparing the dry-side and wet-side specimens, dry side specimens resulted in a less compressive and more dilative behavior. The highest stiffest was evidenced for dry-side specimens, followed by optimum moisture content (max. density), specimens molded at optimum moisture content (red. density), and wet-side ones, respectively. This indicates that stiffness cannot be simply and directly related to strength and initial void ratio, in other words, a more resistant specimen is not necessarily stiffer. The behavior was associated with the structure imparted by compaction (soil fabric), mainly density and packing as well as the lubrication of the soil matrix particles, resulting from the different initial moisture content. As for the influence of compaction energy, higher the compaction energy higher the strength and stiffness values. Finally, the cemented specimens followed the aforementioned behavior/pattern, however with higher strength and stiffness values

g) **Regarding the axial compression triaxial tests under high stresses:** No pronounced peak of strength was evidenced on the stress-strain analysis, independently of the initial molding condition, with the strength reaching constant values at strains up to 15%. The highest deviatory stress value was evidenced for optimum moisture content (max. density) specimens, followed by specimens molded at optimum moisture content (red. density), dry-side and the wet-side, respectively; indicating that even under high stresses the initial molding conditions have a significant effect on the stress-strain behavior. All specimens depicted a full compressive behavior; this behavior is associated with the high confining stress of the tests that prevented the close-packed hexagonal array to happen, in other words, the confining stress influence was higher than the interlocking of the grains. Wet-side specimens resulted in higher compression when compared to dry-side and optimum moisture content ones. This is associated with the higher lubrication of the soil particles from the increase moisture content; in wet-side arrangements the particles are able to more easily slide into the voids, allowing more compression. In addition, the lower initial void ratio (more compact initial matrix) of optimum moisture content specimens left less space for particles to accommodate and, thus, lower compression was evidenced. The highest stiffest was evidenced for dry-side specimens, followed by optimum moisture content (max. density), specimens molded

at optimum moisture content (red. density), and wet-side ones. The behavior was once again associated with the structure imparted by compaction, mainly density and packing as well as the lubrication of the soil matrix particles, resulting from the different initial moisture content. As for the influence of compaction energy, higher the compaction energy higher the strength and stiffness values. The cemented specimens followed the aforementioned behavior/pattern, however with higher strength and stiffness values. Finally, regarding the cement content influence, cemented specimens presented an extremely similar behavior to uncemented ones, both in deviatory stress and axial strain. This behavior indicates that the cementation bonds may have been broken during the consolidation of the tests. In other words, the stress state acting during the cementing process plays a fundamental role in the mechanical behavior of cemented iron ore tailings. For cemented specimens to preserve the strength gain from cement addition under high confining stresses (i.e., stresses higher than the yield stress of the specimens), the curing process of such specimens must be executed under stress (with at least the same stress level of the consolidation phase).

h) **Regarding the grain breakage analysis for oedometric conditions:** All specimens presented an extremely similar final grain size distribution to the natural iron ore tailings. In general, the deformation of soil particle occurs as it is subjected to effective stress. With an increase in the energy imposed on soil particles, the micro-cracks in soil particles appear and develop gradually. Particle breakage occurs when the cracks in particles spread through the whole particle. The crushability of granular soil is mainly related to the physical nature and mechanical properties of soil, the stress-strain state of soil, and the surrounding environment on soil. The results demonstrate that the stress-strain state of the oedometric tests played a fundamental role in particle breakage, indicating that the consolidation state (represented by the oedometric condition) led to no significant change in the grain size distribution of the iron ore tailings, independently of the initial molding condition, compaction energy, and cementation.

i) **Regarding the grain breakage analysis for triaxial conditions:** When compared to oedometric conditions, triaxial conditions are seen as more aggressive considering that not only the consolidation is part of the triaxial process, but also shearing. The grain size distribution of the specimens tested under triaxial conditions resulted in significant changes in grain size distribution compared to the natural iron ore tailings. The greatest

grain breakages were evidenced for dry-side specimens, followed by optimum moisture content (max. density), optimum moisture content (red. density), and wet-side ones. This behavior was associated with the higher stiffness depicted for dry-side specimens, which present a more brittle failure mode. Brittle failure refers to the breakage of a material due to a sudden fracture. When a brittle failure occurs, the material breaks suddenly instead of deforming or straining under load. The fracturing or breaking can occur with only a small amount of load, impact force or shock. Brittle materials absorb less energy before breaking or fracturing, despite the materials having high strength. Brittle failure may also be known as brittle fracture. When materials reach the limit of their strength, they usually have the option of either fracturing or undergoing physical deformation. Materials exhibiting brittleness fail with little or no evidence of plastic deformation before the fracturing occurs. A similar pattern was evidenced for modified energy specimens, with the main difference laying in the magnitude of the values; in which modified energy specimens resulted in a higher alteration of the grain size distributions when compared to standard energy ones. The cement addition showed little effect on particle breakage, considering that according to the triaxial test results, most of the cementation was broken during the consolidation phase of the triaxial test. In general, the crushability of *IOTs* was mainly related to the physical nature and mechanical properties of the material, in addition to the initial molding conditions (moisture content and compaction energy) and the boundary conditions of the test.

j) **Regarding the microstructural analysis of particle breakage for oedometric conditions:** in general, little to no alteration was evidenced on both uncemented and cemented specimens, regarding their morphology, roughness, and particle size when compared to the natural iron ore tailings. This corroborates that the one-directional consolidation state led to no significant change in the grain size distribution of the iron ore tailings. A typical behavior regarding the morphology evidenced: the presence of smaller agglomerated hematite particles on the surface of regular flat large quartz particles. Finally, some sort of cementitious structure (represented by the little agglomerated particles forming clusters around the quartz particles) could be seen on the cemented specimens, even though most of the cementitious bonds may have been broken during the execution of the oedometric test.

k) **Regarding the microstructural analysis of particle breakage for triaxial conditions:** for both the uncemented and cemented specimens, the morphology

indicated rougher surfaces and less defined angular grains (indicating some level of grain breakage) when compared to the natural iron ore tailings. The grain particles were directly affected by the test condition, with the specimens showing lower particle sizes, mainly agglomerates of micrometric particles. This behavior indicates that, under high stresses, a triaxial condition (shearing) causes more particle breakage than an oedometric one (one-dimensional consolidation); the rotation of angular particles plays a fundamental role on the final morphology of iron ore tailings. Even though a large parcel of the grains was broken during triaxial testing, clustered hematite particles were still evidenced over the quartz particles, indicating that most of the grain breakage occurred exclusively on the quartz particles. Finally, even though most of the cementitious structure was broken during the consolidation phase, some sort of cementitious structure (represented by the little agglomerated particles forming clusters around the quartz particles) was still evidenced on the cemented specimens.

5.1 SUGGESTIONS FOR FUTURE RESEARCH

In order to complement and continue the work carried out in this research, expanding knowledge on the effect of distinctive molding conditions on the geotechnical behavior of uncemented and cemented iron ore tailings under low and high confining stresses, the author suggests the following research topics:

a) Utilize iron ore tailings that went through different processing methods;

b) Utilize alternative types of cement;

c) Evaluate the triaxial behavior under undrained conditions;

d) Evaluate the triaxial behavior under cyclic loading conditions for both drained and undrained tests;

e) Evaluate the effect of different stress paths on the triaxial test;

f) Evaluate the critical state condition.

REFERENCES

ABNT. (2004). NBR 10005: Procedimento para obtenção de extrato de lixiviado de resíduos sólidos. Associação Brasileira de Normas Técnicas, 16.

ABNT. (2009). NBR 10006: Procedimento para obtenção de extreto de solubilizado de resíduos sólidos. Associação Brasileira de Normas Técnicas, 1–14.

ABNT. (2012). NBR 12253: Solo-cimento - Dosagem para emprego como camada de pavimento. Associação Brasileira de Normas Técnicas.

ABNT. (2018). NBR 5739: Concreto - Ensaio de compressão de corpos de prova cilíndricos. Associação Brasileira de Normas Técnicas.

Adiansyah, J. S., Rosano, M., Vink, S., & Keir, G. (2015). A framework for a sustainable approach to mine tailings management: disposal strategies. Journal of Cleaner Production, Elsevier Ltd, 108: 1050–1062.

Åhnberg, H. (2007). On yield stresses and the influence of curing stresses on stress paths and strength measured in triaxial testing of stabilized soils. Canadian Geotechnical Journal, 44(1): 54–66.

Alam, S., Das, S. K., & Rao, B. H. (2019). Strength and durability characteristic of alkali activated GGBS stabilized red mud as geo-material. Construction and Building Materials, Elsevier Ltd, 211: 932–942.

Aldaood, A. (2020). Impact of fine materials on the saturated and unsaturated behavior of silty sand soil. Ain Shams Engineering Journal, Faculty of Engineering, Ain Shams University, 11(3): 717–725.

Alehyen, S., Zerzouri, M., El Alouani, M., El Achouri, M., & Taibi, M. (2017). Porosity and fire resistance of fly ash based geopolymer. Journal of Materials and Environmental Science, 8(10): 3676–3689.

Almada, B. S., da Silva Silveira Melo, H., Duarte, M. S., Aguilar, M. T. P., Garcia, D. C. S., Silva, G. J. B., & dos Santos, W. J. (2022). Study of mechanical, durability and microstructural properties of cementitious composite with addition of different iron ore tailings from Brazil. Journal of Materials Research and Technology, 18: 1947–1962.

Alonso, S., & Palomo, A. (2001). Alkaline activation of metakaolin and calcium hydroxide mixtures: Influence of temperature, activator concentration and solids ratio. Materials Letters, 47(1–2): 55–62.

Alshawmar, F., & Fall, M. (2023). Investigation of drying and wetting effects on response of highly densified tailings to cyclic loadings: Shaking table test results. Soil Dynamics and

Earthquake Engineering, Elsevier Ltd, 166(December 2022): 107769.

American Association of State Highway and Transportation Officials (AASHTO). (2008). Laboratory Determination of Resilient Modulus for Flexible Pavement Design.

Andreghetto, D., Festugato, L., Miguel, G., & Silva, A. (2022). Automated true triaxial apparatus development for soil mechanics investigation. Soils and Rocks, 45(2): 1–10.

Araujo, A. C., Amarante, S. C., Souza, C. C., & Silva, R. R. R. (2003). Ore mineralogy and its relevance for selection of concentration methods in processing of Brazilian iron ores. Mineral Processing and Extractive Metallurgy, 112(1): 54–64.

Armstrong, M., Langrené, N., Petter, R., Chen, W., & Petter, C. (2019). Accounting for tailings dam failures in the valuation of mining projects. Resources Policy, Elsevier Ltd, 63(August): 101461.

ASTM. (2012). D1557: Standard Test Methods for Laboratory Compaction Characteristics of Soil Using Modified Effort (56,000ft-lbf/ft3 (2,700 kN-m/m3)). ASTM International, 1–14.

ASTM. (2014). D854 - Standard Test Methods for Specific Gravity of Soil Solids by Water Pycnometer. Astm D854.

ASTM. (2017a). D7928: Standard Test Method for Particle-Size Distribution (Gradation) of Fine-Grained Soils Using the Sedimentation (Hydrometer) Analysis. ASTM International.

ASTM. (2017b). D4318: Standard Test Methods for Liquid Limit, Plastic Limit, and Plasticity Index of Soils. ASTM International, 1–14.

ASTM. (2019). D8295: Standard Test Method for Determination of Shear Wave Velocity and Initial Shear Modulus in Soil Specimens using Bender Elements. American Society for Testing and Materials, 1–8.

ASTM. (2021). Standard Test Methods for Laboratory Compaction Characteristics of Soil Using Standard Effort (12 400 Ft-lbf/ft3 (600 KN-m/m3)). ASTM D698 - 12(2021), ASTM international, West Conshohocken, PA.

Atkinson, J. H. (2000). Non-linear soil stiffness in routine design. Géotechnique, 50(5): 487–508.

Attom, M. F. (1997). The effect of compactive energy level on some soil properties. Applied Clay Science, 12(1–2): 61–72.

Augusto, T. D. M., Chagas, P., Sangiorge, D. L., Mac Leod, T. C. D. O., Oliveira, L. C. A., &

Castro, C. S. De. (2018). Iron ore tailings as catalysts for oxidation of the drug paracetamol and dyes by heterogeneous Fenton. Journal of Environmental Chemical Engineering, Elsevier, 6(5): 6545–6553.

AUSTROADS. (2017). Guide to Pavement Technology Part 2: Pavement Structural Design.

Aytekin, M., & Nas, E. (1998). Soil stabilization with lime and cement. Teknik Dergi/Technical Journal of Turkish Chamber of Civil Engineers, 9(1): 471–477.

Bahurudeen, A., Kanraj, D., Gokul Dev, V., & Santhanam, M. (2015). Performance evaluation of sugarcane bagasse ash blended cement in concrete. Cement and Concrete Composites, Elsevier Ltd, 59: 77–88.

Bazaluk, O., Petlovanyi, M., Lozynskyi, V., Zubko, S., Sai, K., & Saik, P. (2021). Sustainable Underground Iron Ore Mining in Ukraine with Backfilling Worked-Out Area. Sustainability, 13(2): 834.

Beck Saldanha, R., Reddy, K. R., & Cesar Consoli, N. (2019). Influence of sodium chloride on leaching behavior of fly ash stabilized with carbide lime. Construction and Building Materials, Elsevier Ltd, 227: 116571.

Bedin, J., & Schnaid, F. (2007). Piezocone in silty tailing materials. Studia Geotechnica et Mechanica, 29(1–2): 151–162.

Bedin, J., & Schnaid, F. (2010). Estudo das Propriedades Geotécnicas de Resíduos de Mineração através de ensaios de laboratório.

Benzaazoua, M., Bussière, B., Demers, I., Aubertin, M., Fried, É., & Blier, A. (2008). Integrated mine tailings management by combining environmental desulphurization and cemented paste backfill: Application to mine Doyon, Quebec, Canada. Minerals Engineering, 21(4): 330–340.

Berger, K. C. (2017). Study of Tailings Management Technologies. The Mining Association of Canada, (October): 1–164.

Bin-Shafique, S., Edil, T. B., Benson, C. H., & Senol, A. (2004). Incorporating a fly-ash stabilised layer into pavement design. Proceedings of the Institution of Civil Engineers - Geotechnical Engineering, 157(4): 239–249.

Boger, D. V. (2013). Rheology of Slurries and Environmental Impacts in the Mining Industry. Annual Review of Chemical and Biomolecular Engineering, 4(1): 239–257.

Broms, B. B. (1991). Stabilization of Soil with Lime Columns. Foundation Engineering Handbook, Springer US, Boston, MA, 833–855.

Brouwers, H. J. H. (2011). A hydration model of Portland Cement using the work of Powers

and Brownyard. (2011): 154.

Brunori, C., Cremisini, C., Massanisso, P., Pinto, V., & Torricelli, L. (2005). Reuse of a treated red mud bauxite waste: studies on environmental compatibility. Journal of Hazardous Materials, 117(1): 55–63.

Bruschi, G. J., Fante, F., Tonini de Araújo, M., Dias Macedo, G., & Ruver, C. A. (2021a). Analysis of different failure criteria to evaluate bauxite tailings mechanical behavior through numerical modelling. Soils and Rocks, 44(1): 1–10.

Bruschi, G. J., Santos, C. P. dos, Araújo, M. T. de, Ferrazzo, S. T., Marques, S., & Consoli, N. C. (2021b). Green stabilization of bauxite tailings: A mechanical study on alkali-activated materials. Journal of Materials in Civil Engineering, in press.

Bruschi, G. J., Santos, C. P. dos, Ferrazzo, S. T., Araújo, M. T. de, & Consoli, N. C. (2021c). Parameters controlling loss of mass and stiffness degradation of green stabilized bauxite tailings. Proceedings of the Institution of Civil Engineers - Geotechnical Engineering, 1–21.

Bruschi, G. J., Santos, C. P. Dos, Ferrazzo, S. T., Araújo, M. T. De, & Consoli, N. C. (2021d). Parameters controlling loss of mass and stiffness degradation of "green" stabilised tailings. Proceedings of the Institution of Civil Engineers - Geotechnical Engineering, 1–9.

Bruschi, G. J., dos Santos, C. P., Tonini de Araújo, M., Ferrazzo, S. T., Marques, S. F. V., & Consoli, N. C. (2021e). Green Stabilization of Bauxite Tailings: Mechanical Study on Alkali-Activated Materials. Journal of Materials in Civil Engineering, 33(11): 06021007.

Burris, L. E., Alapati, P., Moser, R. D., Ley, M. T., Berke, N., & Kurtis, K. E. (2015). Alternative cementitious materials: Challenges and opportunities. American Concrete Institute, ACI Special Publication, 1–10.

Cadore, D. E., Angulski da Luz, C., & Farias de Medeiros, M. H. (2019). An investigation of the carbonation of alkaline activated cement made from blast furnace slag generated by charcoal. Construction and Building Materials, Elsevier Ltd, 226: 117–125.

Carmignano, O., Vieira, S., Teixeira, A. P., Lameiras, F., Brandão, P. R., & Lago, R. (2021). Iron Ore Tailings: Characterization and Applications. Journal of the Brazilian Chemical Society, 32(10): 1895–1911.

Chen, X., Shi, X., Zhou, J., Yu, Z., & Huang, P. (2020). Determination of mechanical, flowability, and microstructural properties of cemented tailings backfill containing rice straw. Construction and Building Materials, Elsevier Ltd, 246: 118520.

Chen, Y., Zhang, Y., Chen, T., Liu, T., & Huang, J. (2013). Preparation and characterization of red porcelain tiles with hematite tailings. Construction and Building Materials,

Elsevier Ltd, 38: 1083–1088.

Cheng, Y., Huang, F., Li, W., Liu, R., Li, G., & Wei, J. (2016). Test research on the effects of mechanochemically activated iron tailings on the compressive strength of concrete. Construction and Building Materials, Elsevier Ltd, 118: 164–170.

CLAYTON, C. R. I. (2011). Stiffness at small strain: research and practice. Géotechnique, 61(1): 5–37.

Clough, G. W., Sitar, N., Bachus, R. C., & Rad, N. S. (1981). Cemented Sands under Static Loading. Journal of the Geotechnical Engineering Division, 107(6): 799–817.

Consoli, N. C., Bellaver Corte, M., & Festugato, L. (2012). Key parameter for tensile and compressive strength of fibre-reinforced soil–lime mixtures. Geosynthetics International, 19(5): 409–414.

Consoli, N. C., Bittar Marin, E. J., Quiñónez Samaniego, R. A., Heineck, K. S., & Johann, A. D. R. (2019a). Use of Sustainable Binders in Soil Stabilization. Journal of Materials in Civil Engineering, 31(2): 06018023.

Consoli, N. C., Carretta, M. D. S., Leon, H. B., Scheuermann Filho, H. C., & Tomasi, L. F. (2019b). Strength and Stiffness of Ground Waste Glass–Carbide Lime Blends. Journal of Materials in Civil Engineering, 31(10): 06019010.

Consoli, N. C., Carretta, M. S., Leon, H. B., Schneider, M. E. B., Reginato, N. C., & Carraro, J. A. H. (2020a). Behaviour of cement-stabilised silty sands subjected to harsh environmental conditions. Proceedings of the Institution of Civil Engineers - Geotechnical Engineering, 173(1): 40–48.

Consoli, N. C., Festugato, L., Filho, H. C. S., Miguel, G. D., Neto, A. T., & Andreghetto, D. (2020b). Durability Assessment of Soil-Pozzolan-Lime Blends through Ultrasonic-Pulse Velocity Test. Journal of Materials in Civil Engineering, 32(8): 04020223.

Consoli, N. C., Festugato, L., & Heineck, K. S. (2009a). Strain-hardening behaviour of fibre-reinforced sand in view of filament geometry. Geosynthetics International, 16(2): 109–115.

Consoli, N. C., Foppa, D., Festugato, L., & Heineck, K. S. (2007). Key Parameters for Strength Control of Artificially Cemented Soils. Journal of Geotechnical and Geoenvironmental Engineering, 133(2): 197–205.

Consoli, N. C., Leon, H. B., da Silva Carretta, M., Daronco, J. V. L., & Lourenço, D. E. (2019c). The effects of curing time and temperature on stiffness, strength and durability of sand-environment friendly binder blends. Soils and Foundations, 59(5): 1428–1439.

Consoli, N. C., Nierwinski, H. P., Peccin da Silva, A., & Sosnoski, J. (2017a). Durability and strength of fiber-reinforced compacted gold tailings-cement blends. Geotextiles and

Geomembranes, Elsevier Ltd, 45(2): 98–102.

Consoli, N. C., Prietto, P. D. M., Carraro, J. A. H., & Heineck, K. S. (2001). Behavior of Compacted Soil-Fly Ash-Carbide Lime Mixtures. Journal of Geotechnical and Geoenvironmental Engineering, 127(9): 774–782.

Consoli, N. C., Quiñónez, R. A., González, L. E., & López, R. A. (2017b). Influence of Molding Moisture Content and Porosity/Cement Index on Stiffness, Strength, and Failure Envelopes of Artificially Cemented Fine-Grained Soils. Journal of Materials in Civil Engineering, 29(5): 04016277.

Consoli, N. C., Quiñónez Samaniego, R. A., González, L. E., Bittar, E. J., & Cuisinier, O. (2018a). Impact of Severe Climate Conditions on Loss of Mass, Strength, and Stiffness of Compacted Fine-Grained Soils–Portland Cement Blends. Journal of Materials in Civil Engineering, 30(8): 04018174.

Consoli, N. C., Rosa, A. D., & Saldanha, R. B. (2011a). Variables Governing Strength of Compacted Soil–Fly Ash–Lime Mixtures. Journal of Materials in Civil Engineering, 23(4): 432–440.

Consoli, N. C., Samaniego, R. A. Q., & Villalba, N. M. K. (2016). Durability, Strength, and Stiffness of Dispersive Clay–Lime Blends. Journal of Materials in Civil Engineering, 28(11): 04016124.

Consoli, N. C., Silva, A. P. da, Nierwinski, H. P., & Sosnoski, J. (2018b). Durability, strength, and stiffness of compacted gold tailings – cement mixes. Canadian Geotechnical Journal, 55(4): 486–494.

Consoli, N. C., Da Silva Carretta, M., Festugato, L., Leon, H. B., Tomasi, L. F., & Heineck, K. S. (2020c). Ground waste glass–carbide lime as a sustainable binder stabilising three different silica sands. Géotechnique, 1–14.

Consoli, N. C., Silva, K. da, Filho, S., & Rivoire, A. B. (2017c). Compacted clay-industrial wastes blends: Long term performance under extreme freeze-thaw and wet-dry conditions. Applied Clay Science, Elsevier, 146(February): 404–410.

Consoli, N. C., Silva Lopes, L. da, Foppa, D., & Heineck, K. S. (2009b). Key parameters dictating strength of lime/cement-treated soils. Proceedings of the Institution of Civil Engineers - Geotechnical Engineering, 162(2): 111–118.

Consoli, N. C., Tonini de Araújo, M., Tonatto Ferrazzo, S., de Lima Rodrigues, V., & Gravina da Rocha, C. (2021). Increasing density and cement content in stabilization of expansive soils: Conflicting or complementary procedures for reducing swelling? Canadian Geotechnical Journal, 58(6): 866–878.

Consoli, N. C., Vendruscolo, M. A., Fonini, A., & Rosa, F. D. (2009c). Fiber reinforcement

effects on sand considering a wide cementation range. Geotextiles and Geomembranes, 27(3): 196–203.

Consoli, N. C., Vogt, J. C., Silva, J. P. S., Chaves, H. M., Scheuermann Filho, H. C., Moreira, E. B., & Lotero, A. (2022). Behaviour of Compacted Filtered Iron Ore Tailings–Portland Cement Blends: New Brazilian Trend for Tailings Disposal by Stacking. Applied Sciences, 12(2): 836.

Consoli, N. C., Winter, D., Leon, H. B., & Scheuermann Filho, H. C. (2018c). Durability, Strength, and Stiffness of Green Stabilized Sand. Journal of Geotechnical and Geoenvironmental Engineering, 144(9): 04018057.

Consoli, N. C., Zortéa, F., de Souza, M., & Festugato, L. (2011b). Studies on the Dosage of Fiber-Reinforced Cemented Soils. Journal of Materials in Civil Engineering, 23(12): 1624–1632.

Consoli, N. C., Zortéa, F., de Souza, M., & Festugato, L. (2011c). Studies on the Dosage of Fiber-Reinforced Cemented Soils. Journal of Materials in Civil Engineering, 23(12): 1624–1632.

Consoli, N., Da Rocha, C. G., & Silvani, C. (2014). Devising dosages for soil-fly ash-lime blends based on tensile strength controlling equations. Construction and Building Materials, Elsevier Ltd, 55: 238–245.

Coop, M. R., & Atkinson, J. H. (1994). Discussion: The mechanics of cemented carbonate sands. Géotechnique, 44(3): 533–537.

Corrêa-Silva, M., Miranda, T., Rouainia, M., Araújo, N., Glendinning, S., & Cristelo, N. (2020). Geomechanical behaviour of a soft soil stabilised with alkali-activated blast-furnace slags. Journal of Cleaner Production, 267: 122017.

Corrêa, B. R. S., Scheuermann Filho, H. C., Mattos, J. R. G., & Consoli, N. C. (2021). Compacted Ground Glass Particles—Carbide Lime Blends: An Environment Friendly Material. Geotechnical and Geological Engineering, 39(4): 3207–3219.

Cox, B., Innis, S., Mortaza, A., Kunz, N. C., & Steen, J. (2022). A unified metric for costing tailings dams and the consequences for tailings management. Resources Policy, Elsevier Ltd, 78(July 2021): 102862.

Cristelo, N., Castro, F., Miranda, T., Abdollahnejad, Z., & Fernández-Jiménez, A. (2021). Iron and Aluminium Production Wastes as Exclusive Components of Alkali Activated Binders—Towards a Sustainable Alternative. Sustainability, 13(17): 9938.

Cristelo, N., Coelho, J., Oliveira, M., Cesar Consoli, N., Palomo, Á., & Fernández-Jiménez, A. (2020). Recycling and Application of Mine Tailings in Alkali-Activated Cements and Mortars—Strength Development and Environmental Assessment. Applied Sciences, 10(6): 2084.

Cuccovillo, T., & Coop, M. R. (1999). On the mechanics of structured sands. Géotechnique, 49(6): 741–760.

D′Azeredo Orlando, M. T., Galvão, E. S., Sant′Ana Cavichini, A., Gabrig Turbay Rangel, C. V., Pinheiro Orlando, C. G., Grilo, C. F., Soares, J., Santos Oliveira, K. S., Sá, F., Junior, A. C., Bastos, A. C., & da Silva Quaresma, V. (2020). Tracing iron ore tailings in the marine environment: An investigation of the Fundão dam failure. Chemosphere, Elsevier Ltd, 257: 127184.

Dauce, P. D., Castro, G. B. De, Lima, M. M. F., & Lima, R. M. F. (2019). Characterisation and magnetic concentration of an iron ore tailings. Journal of Materials Research and Technology, Brazilian Metallurgical, Materials and Mining Association, 8(1): 1052–1059.

Davies, M. P. (2002). Tailings impoundment failures are geotechnical engineers listening? Geotechnical News, 20(3): 31.

Davila, R. B., Fontes, M. P. F., Pacheco, A. A., & Ferreira, M. da S. (2020). Heavy metals in iron ore tailings and floodplain soils affected by the Samarco dam collapse in Brazil. Science of The Total Environment, Elsevier B.V, 709: 136151.

Desogus, P., Manca, P. P. P., Orrù, G., & Zucca, A. (2013). Stabilization–solidification treatment of mine tailings using Portland cement, potassium dihydrogen phosphate and ferric chloride hexahydrate. Minerals Engineering, Elsevier Ltd, 45: 47–54.

Diambra, A., Festugato, L., Ibraim, E., Peccin da Silva, A., & Consoli, N. C. (2018). Modelling tensile/compressive strength ratio of artificially cemented clean sand. Soils and Foundations, Japanese Geotechnical Society, 58(1): 199–211.

DIAMBRA, A., & IBRAIM, E. (2015). Fibre-reinforced sand: interaction at the fibre and grain scale. Géotechnique, 65(4): 296–308.

Diambra, A., Ibraim, E., Peccin, A., Consoli, N. C., & Festugato, L. (2017). Theoretical Derivation of Artificially Cemented Granular Soil Strength. Journal of Geotechnical and Geoenvironmental Engineering, 143(5): 04017003.

Diana, W., Hartono, E., & Muntohar, A. S. (2019). The Permeability of Portland Cement-Stabilized Clay Shale. IOP Conference Series: Materials Science and Engineering, 650(1): 012027.

Duan, P., Yan, C., Zhou, W., & Ren, D. (2016). Fresh properties, compressive strength and microstructure of fly ash geopolymer paste blended with iron ore tailing under thermal cycle. Construction and Building Materials, Elsevier Ltd, 118: 76–88.

Duchesne, J., & Doye, I. (2005). Effectiveness of Covers and Liners Made of Red Mud Bauxite and/or Cement Kiln Dust for Limiting Acid Mine Drainage. Journal of

Environmental Engineering, 131(8): 1230–1235.

Dutra, M. R. (2021). Comportamento geomecânico de um rejeito de minério de ferro para baixas e altas tensões de confinamento.

Edraki, M., Baumgartl, T., Manlapig, E., Bradshaw, D., Franks, D. M., & Moran, C. J. (2014). Designing mine tailings for better environmental, social and economic outcomes: a review of alternative approaches. Journal of Cleaner Production, Elsevier Ltd, 84(1): 411–420.

Einav, I. (2007a). Breakage mechanics—Part I: Theory. Journal of the Mechanics and Physics of Solids, 55(6): 1274–1297.

Einav, I. (2007b). Breakage mechanics—Part II: Modelling granular materials. Journal of the Mechanics and Physics of Solids, 55(6): 1298–1320.

Etim, R. K., Eberemu, A. O., & Osinubi, K. J. (2017). Stabilization of black cotton soil with lime and iron ore tailings admixture. Transportation Geotechnics, Elsevier Ltd, 10: 85–95.

Eyo, E., Abbey, S., Oti, J., Ng'ambi, S., Ganjian, E., & Coakley, E. (2021). Microstructure and Physical-Mechanical Characteristics of Treated Kaolin-Bentonite Mixture for Application in Compacted Liner Systems. Sustainability, 13(4): 1617.

Fall, M., Célestin, J. C., & Han, F. S. (2009). Suitability of bentonite-paste tailings mixtures as engineering barrier material for mine waste containment facilities. Minerals Engineering, Elsevier Ltd, 22(9–10): 840–848.

Fan, Z., & Friedmann, S. J. (2021). Low-carbon production of iron and steel: Technology options, economic assessment, and policy. Joule, Elsevier, 5(4): 829–862.

Ferenczi, P. A. (2001). Iron ore, manganese and bauxite deposits of the northern territory. Northern Territory Geological Survey - Department of Business Industry & Resource Development, Darwin, Australia.

Fernandes, M. D. M. (2016). Mecânica dos solos - conceitos e princípios fundamentais. Oficina de Textos, São Paulo, Brasil.

Fernández-González, D., Ruiz-Bustinza, I., Mochón, J., González-Gasca, C., & Verdeja, L. F. (2017). Iron Ore Sintering: Process. Mineral Processing and Extractive Metallurgy Review, 38(4): 215–227.

Ferreira, H., & Leite, M. G. P. (2015). A Life Cycle Assessment study of iron ore mining. Journal of Cleaner Production, 108: 1081–1091.

Festugato, L., Menger, E., Benezra, F., Kipper, E. A., & Consoli, N. C. (2017). Fibre-

reinforced cemented soils compressive and tensile strength assessment as a function of filament length. Geotextiles and Geomembranes, 45(1): 77–82.

Festugato, L., Peccin da Silva, A., Diambra, A., Consoli, N. C., & Ibraim, E. (2018). Modelling tensile/compressive strength ratio of fibre reinforced cemented soils. Geotextiles and Geomembranes, Elsevier, 46(2): 155–165.

Filho, J. N. S., Da Silva, S. N., Silva, G. C., Mendes, J. C., & Peixoto, R. A. F. (2017). Technical and Environmental Feasibility of Interlocking Concrete Pavers with Iron Ore Tailings from Tailings Dams. Journal of Materials in Civil Engineering, 29(9): 1–6.

Fonteneau, L. C., Martini, B., & Elsenheimer, D. (2019). Hyperspectral imaging of sedimentary iron ores – beyond borders. ASEG Extended Abstracts, 2019(1): 1–5.

Fontes, W. C., Fontes, G. G., Costa, E. C. P., Mendes, J. C., Silva, G. J. B., & Peixoto, R. A. F. (2018). Iron ore tailings in the production of cement tiles: a value analysis on building sustainability. Ambiente Construído, 18(4): 395–412.

de Freitas, V. A. A., Breder, S. M., Silvas, F. P. C., Radino Rouse, P., & de Oliveira, L. C. A. (2019). Use of iron ore tailing from tailing dam as catalyst in a fenton-like process for methylene blue oxidation in continuous flow mode. Chemosphere, 219: 328–334.

Furlan, J. P. R., dos Santos, L. D. R., Moretto, J. A. S., Ramos, M. S., Gallo, I. F. L., Alves, G. de A. D., Paulelli, A. C., Rocha, C. C. de S., Cesila, C. A., Gallimberti, M., Devóz, P. P., Júnior, F. B., & Stehling, E. G. (2020). Occurrence and abundance of clinically relevant antimicrobial resistance genes in environmental samples after the Brumadinho dam disaster, Brazil. Science of the Total Environment, Elsevier B.V, 726: 138100.

Galitskaya, E. A., & Zhdaneev, O. V. (2022). Development of Electrolysis Technologies for Hydrogen Production in the Russian Federation. Ecology and Industry of Russia, 26(12): 57–63.

Galvão, J. L. B., Andrade, H. D., Brigolini, G. J., Peixoto, R. A. F., & Mendes, J. C. (2018). Reuse of iron ore tailings from tailings dams as pigment for sustainable paints. Journal of Cleaner Production, 200: 412–422.

Gama, F. F., Paradella, W. R., Mura, J. C., & de Oliveira, C. G. (2019). Advanced DINSAR analysis on dam stability monitoring: A case study in the Germano mining complex (Mariana, Brazil) with SBAS and PSI techniques. Remote Sensing Applications: Society and Environment, 16.

Garbarino, E., Orveillon, G., & Saveyn, H. G. M. (2020). Management of waste from extractive industries: The new European reference document on the Best Available Techniques. Resources Policy, Elsevier Ltd, 69(January): 101782.

Geymond, U., Ramanaidou, E., Lévy, D., Ouaya, A., & Moretti, I. (2022). Can Weathering of

Banded Iron Formations Generate Natural Hydrogen? Evidence from Australia, Brazil and South Africa. Minerals, 12(2): 163.

Gielen, D., Saygin, D., Taibi, E., & Birat, J. (2020). Renewables-based decarbonization and relocation of iron and steel making: A case study. Journal of Industrial Ecology, 24(5): 1113–1125.

Giri, S. K., Das, N. N., & Pradhan, G. C. (2011a). Magnetite powder and kaolinite derived from waste iron ore tailings for environmental applications. Powder Technology, Elsevier B.V., 214(3): 513–518.

Giri, S. K., Das, N. N., & Pradhan, G. C. (2011b). Synthesis and characterization of magnetite nanoparticles using waste iron ore tailings for adsorptive removal of dyes from aqueous solution. Colloids and Surfaces A: Physicochemical and Engineering Aspects, Elsevier B.V., 389(1–3): 43–49.

Godbout, J., Bussiere, B., Aubertin, M., & Belem, T. (2007). Evolution of cemented paste backfill saturated hydraulic conductivity at early curing time. Proceedings of the OttawaGeo2007, 2230–2230.

Gomes, L. E. de O., Correa, L. B., Sá, F., Neto, R. R., & Bernardino, A. F. (2017). The impacts of the Samarco mine tailing spill on the Rio Doce estuary, Eastern Brazil. Marine Pollution Bulletin, Elsevier, 120(1–2): 28–36.

Gomes, R. B., De Tomi, G., & Assis, P. S. (2016). Iron ore tailings dry stacking in Pau Branco mine, Brazil. Journal of Materials Research and Technology, Brazilian Metallurgical, Materials and Mining Association, 5(4): 339–344.

Gonçalves, R. R. S. M. (2021). Comportamento Geomecânico de Rejeito de Bauxita Sob Diferentes Condições de Confinamento e Carregamento.

Gore, M. S., Gilbert, R. B., McMillan, I., & Isovitsch Parks, S. L. (2016). Geotechnical Characterization of Compacted Bauxite Residue for Use in Levees. Geo-Chicago 2016, American Society of Civil Engineers, Reston, VA, 299–310.

Gou, M., Zhou, L., & Then, N. W. Y. (2019). Utilization of tailings in cement and concrete: A review. Science and Engineering of Composite Materials, 26(1): 449–464.

Guimarães, R. N., Moreira, V. R., Cruz, J. R. A., Saliba, A. P. M., & Amaral, M. C. S. (2022). History of tailings dam failure: Impacts on access to safe water and influence on the legislative framework. Science of The Total Environment, 852(September): 158536.

Halász, J., Hodos, M., Hannus, I., Tasi, G., & Kiricsi, I. (2005). Catalytic detoxification of C2-chlorohydrocarbons over iron-containing oxide and zeolite catalysts. Colloids and Surfaces A: Physicochemical and Engineering Aspects, 265(1–3): 171–177.

Hao, X., & An, H. (2022). Comparative study on transmission mechanism of supply shortage

risk in the international trade of iron ore, pig iron and crude steel. Resources Policy, Elsevier Ltd, 79(September): 103022.

He, C. (2000). Thermal stability and pozzolanic activity of raw and calcined mixed-layer mica/smectite. Applied Clay Science, 17(3–4): 141–161.

Helinski, M., Fahey, M., & Fourie, A. (2011). Behavior of Cemented Paste Backfill in Two Mine Stopes: Measurements and Modeling. Journal of Geotechnical and Geoenvironmental Engineering, 137(2): 171–182.

Herzog, A., & Mitchell, J. K. (1963). Reactions accompanying stabilization of clay with cement. Highway Research Record, (36): 146–171.

Hoch, B. Z. (2023). COMPORTAMENTO GEOMECÂNICO DE REJEITO DE MINERAÇÃO DE OURO SUBMETIDO A BAIXAS E ALTAS TENSÕES DE CONFINAMENTO SOB CARREGAMENTO MONOTÔNICO E CÍCLICO.

Hoyos, L. R., Puppala, A. J., & Ordonez, C. A. (2011). Characterization of Cement-Fiber-Treated Reclaimed Asphalt Pavement Aggregates: Preliminary Investigation. Journal of Materials in Civil Engineering, 23(7): 977–989.

Hu, L., Wu, H., Zhang, L., Zhang, P., & Wen, Q. (2017). Geotechnical Properties of Mine Tailings. Journal of Materials in Civil Engineering, 29(2): 04016220.

Hua, Y., Heal, K. V., & Friesl-Hanl, W. (2017). The use of red mud as an immobiliser for metal/metalloid-contaminated soil: A review. Journal of Hazardous Materials, Elsevier B.V., 325: 17–30.

Huang, Y., Chai, W., Han, G., Wang, W., Yang, S., & Liu, J. (2016). A perspective of stepwise utilisation of Bayer red mud: Step two—Extracting and recovering Ti from Ti-enriched tailing with acid leaching and precipitate flotation. Journal of Hazardous Materials, Elsevier B.V., 307: 318–327.

Islam, K., & Murakami, S. (2021). Global-scale impact analysis of mine tailings dam failures: 1915–2020. Global Environmental Change, Elsevier Ltd, 70(August): 102361.

Jallu, M., Arulrajah, A., Saride, S., & Evans, R. (2020). Flexural fatigue behavior of fly ash geopolymer stabilized-geogrid reinforced RAP bases. Construction and Building Materials, Elsevier Ltd, 254: 119263.

Jiang, H., Qi, Z., Yilmaz, E., Han, J., Qiu, J., & Dong, C. (2019). Effectiveness of alkali-activated slag as alternative binder on workability and early age compressive strength of cemented paste backfills. Construction and Building Materials, Elsevier Ltd, 218: 689–700.

Junta Autonoma de Estradas (JAE). (1995). Manual de Concepção e Pavimentos para a Rede Rodoviária Nacional. 56.

Khadka, S. D., Jayawickrama, P. W., Senadheera, S., & Segvic, B. (2020). Stabilization of highly expansive soils containing sulfate using metakaolin and fly ash based geopolymer modified with lime and gypsum. Transportation Geotechnics, Elsevier, 23(February): 100327.

Kiventerä, J., Golek, L., Yliniemi, J., Ferreira, V., Deja, J., & Illikainen, M. (2016). Utilization of sulphidic tailings from gold mine as a raw material in geopolymerization. International Journal of Mineral Processing, Elsevier B.V., 149: 104–110.

Klahold, P. A. (2013). Interpretação de ensaios de campo em solos com permeabilidade intermediária. Programa de Pós-Graduação em Engenharia Civil, Programa de Pós-Graduação em Engenharia Civil.

Kouakou, C. H., & Morel, J. C. (2009). Strength and elasto-plastic properties of non-industrial building materials manufactured with clay as a natural binder. Applied Clay Science, Elsevier B.V., 44(1–2): 27–34.

Krishnamurthy, K. V. (2022). Reserves and Resources of Iron Ores of India — A Perspective. Journal of the Geological Society of India, 98(5): 647–653.

Lade, P. V., & Overton, D. D. (1989). Cementation Effects in Frictional Materials. Journal of Geotechnical Engineering, 115(10): 1373–1387.

Lade, P. V., & Trads, N. (2014). The role of cementation in the behaviour of cemented soils. Geotechnical Research, 1(4): 111–132.

Lambe, T. W., & Whitman, R. V. (1979). Soil Mechanics. John Wiley & Sons, Inc., New York, United States.

Latt, K. M. M., & Giao, P. H. (2017). Prediction of permeability of cement-admixed soft clay using resistivity and time-domain IP measurements. Journal of Applied Geophysics, Elsevier B.V., 137: 92–103.

Lee, K. L., & Farhoomand, I. (1967). Compressibility And Crushing Of Granular Soil In Anisotropic Triaxial Compression. Canadian Geotechnical Journal, 4(1): 68–86.

Leroueil, S., & Vaughan, P. R. (1990). The general and congruent effects of structure in natural soils and weak rocks. Géotechnique, 40(3): 467–488.

Li, L. Y. (1998). Properties of Red Mud Tailings Produced under Varying Process Conditions. Journal of Environmental Engineering, 124(3): 254–264.

Li, Y.-Y., Zhang, T.-T., Jia, S.-B., Liu, J., Quan, X.-H., & Zheng, W. (2019). Mechanical

Properties and Leaching Characteristics of Geopolymer-Solidified/Stabilized Lead-Contaminated Soil. Advances in Civil Engineering, 2019: 1–8.

Lima, A. T., Bastos, F. A., Teubner, F. J., Neto, R. R., Cooper, A., & Barroso, G. F. (2020). Strengths and Weaknesses of a Hybrid Post-disaster Management Approach: the Doce River (Brazil) Mine-Tailing Dam Burst. Environmental Management, Springer US, 65(6): 711–724.

de Lima, R. E., de Lima Picanço, J., da Silva, A. F., & Acordes, F. A. (2020). An anthropogenic flow type gravitational mass movement: the Córrego do Feijão tailings dam disaster, Brumadinho, Brazil. Landslides, Landslides, 17(12): 2895–2906.

Lima, R. M. F., & Abreu, F. D. P. V. F. (2020). Characterization and concentration by selective flocculation/magnetic separation of iron ore slimes from a dam of Quadrilátero Ferrífero - Brazil. Journal of Materials Research and Technology, The Authors, 9(2): 2021–2027.

Lirer, S., Flora, A., & Consoli, N. C. (2011). On the Strength of Fibre-Reinforced Soils. Soils and Foundations, 51(4): 601–609.

Liu, B., Zhang, Y., Lu, M., Su, Z., Li, G., & Jiang, T. (2019). Extraction and separation of manganese and iron from ferruginous manganese ores: A review. Minerals Engineering, Elsevier, 131(248): 286–303.

Liu, Q., Liu, D., Liu, X., Gao, F., & Li, S. (2016). Research and application of surface paste disposal for clay-sized tailings in tropical rainy climate. International Journal of Mineral Processing, Elsevier B.V., 157: 227–235.

Lu, C., Yang, H., Wang, J., Tan, Q., & Fu, L. (2020). Utilization of iron tailings to prepare high-surface area mesoporous silica materials. Science of The Total Environment, Elsevier B.V, 736: 139483.

Lu, L. (2021). Iron Ore: Mineralogy, Processing and Environmental Sustainability. (Woodhead Publishing, ed.).

Lumbroso, D., McElroy, C., Goff, C., Collell, M. R., Petkovsek, G., & Wetton, M. (2019). The potential to reduce the risks posed by tailings dams using satellite-based information. International Journal of Disaster Risk Reduction, Elsevier Ltd, 38(January): 101209.

M. C. Duarte, G., & S. Lameiras, F. (2022). Challenges for the Destiny of Iron Mining Tailings in the Iron Quadrangle of Minas Gerais, Brazil. Revista Virtual de Química, 14(3): 552–559.

Ma, M. (2012). Froth Flotation of Iron Ores. International Journal of Mining Engineering and Mineral Processing, 1(2): 56–61.

Machado, I. F., & Figueirôa, S. (2022). Mining history of Brazil: a summary. Mineral Economics, Springer Berlin Heidelberg, 35(2): 253–265.

Magalhães, L. F. de, França, S., Oliveira, M. dos S., Peixoto, R. A. F., Bessa, S. A. L., & Bezerra, A. C. da S. (2020). Iron ore tailings as a supplementary cementitious material in the production of pigmented cements. Journal of Cleaner Production, Elsevier Ltd, 123260.

Malandraki, V., & Toll, D. (2000). Drained probing triaxial tests on a weakly bonded artificial soil. Géotechnique, 50(2): 141–151.

Malandraki, V., & Toll, D. G. (1996). The definition of yield for bonded materials. Geotechnical and Geological Engineering, (Springer, ed.), 14(1): 67–82.

Marani, A., & Madhkhan, M. (2021). Thermal performance of concrete sandwich panels incorporating phase change materials: An experimental study. Journal of Materials Research and Technology, Elsevier Ltd, 12: 760–775.

Marques, S. V. F. (2016). Comportamento de uma Areia Artificialmente Cimentada até Altas Tensões de Confinamento.

Matiolo, E., Couto, H. J. B., Lima, N., Silva, K., & de Freitas, A. S. (2020). Improving recovery of iron using column flotation of iron ore slimes. Minerals Engineering, Elsevier, 158(May): 106608.

McDowell, G. R., Bolton, M. D., & Robertson, D. (1996). The fractal crushing of granular materials. Journal of the Mechanics and Physics of Solids, 44(12): 2079–2101.

McDowell, G. R., & Khan, J. J. (2003). Creep of granular materials. Granular Matter, 5(3): 115–120.

Mcnab, B., Jankovic, A., David, D., & Payne, P. (2009). Processing of Magnetite Iron Ores – Comparing Grinding Options. Proceedings of Iron ore conference, (July): 27–29.

Mesbah, A., Morel, J. C., & Olivier, M. (1999). Comportement des sols fins argileux pendant un essai de compactage statique: détermination des paramètres pertinents. Materials and Structures, 32(9): 687.

Miura, S., Yagi, K., & Asonuma, T. (2003). Deformation-Strength Evaluation of Crushable Volcanic Soils by Laboratory and In-Situ Testing. Soils and Foundations, 43(4): 47–57.

Mmbando, E., Fourie, A., & Reid, D. (2023). Mechanics of an Iron Ore Tailings Exhibiting Transitional Behaviour. Geotechnical and Geological Engineering, Springer International Publishing, (0123456789).

Mobili, A., Telesca, A., Marroccoli, M., & Tittarelli, F. (2020). Calcium sulfoaluminate and

alkali-activated fly ash cements as alternative to Portland cement: study on chemical, physical-mechanical, and durability properties of mortars with the same strength class. Construction and Building Materials, Elsevier Ltd, 246: 118436.

Mohr, S., Giurco, D., Yellishetty, M., Ward, J., & Mudd, G. (2015). Projection of Iron Ore Production. Natural Resources Research, Springer US, 24(3): 317–327.

Molenaar, N., & Venmans, A. A. M. (1993). Calcium carbonate cementation of sand: A method for producing artificially cemented samples for geotechnical testing and a comparison with natural cementation processes. Engineering Geology, 35(1–2): 103–122.

de Moraes, S. L., & Ribeiro, T. R. (2019). Brazilian Iron Ore and Production of Pellets. Mineral Processing and Extractive Metallurgy Review, Taylor & Francis, 40(1): 16–23.

Morris, R. C. (1985). Genesis of Iron Ore in Banded Iron-Formation by Supergene and Supergene-Metamorphic Processes—A Conceptual Model. (ELSEVIER, ed.).

Mousa, E., El-Badawy, S., & Azam, A. (2021). Evaluation of reclaimed asphalt pavement as base/subbase material in Egypt. Transportation Geotechnics, Elsevier Ltd, 26(August 2020): 100414.

Murthy, T. G., Loukidis, D., Carraro, J. A. H., Prezzi, M., & Salgado, R. (2007). Undrained monotonic response of clean and silty sands. Géotechnique, 57(3): 273–288.

Mustafa, S., Luo, L., Zheng, B., Wei, C., & Christophe, N. (2022). Mineralogical and Chemical Changes after Reduction Roasting of Xinjiang Iron Ore, China. Metals, 12(2): 182.

Nakata, A. F. L., Hyde, M., Hyodo, H., & Murata. (1999). A probabilistic approach to sand particle crushing in the triaxial test. Géotechnique, 49(5): 567–583.

Nakata, Y., Hyodo, M., Hyde, A. F. L., Kato, Y., & Murata, H. (2001). Microscopic particle crushing of sand subjected to high pressure one-dimensional compression. Soils and Foundations, 41(1): 69–82.

Nath, H., Sahoo, P., & Sahoo, A. (2015). Characterization of Red Mud treated under high temperature fluidization. Powder Technology, Elsevier B.V., 269: 233–239.

Newson, T., Dyer, T., Adam, C., & Sharp, S. (2006). Effect of Structure on the Geotechnical Properties of Bauxite Residue. Journal of Geotechnical and Geoenvironmental Engineering, 132(2): 143–151.

Nierwinski, H. P. (2019). Caracterização e comportamento geomecânico de rejeitos de mineração. Universidade Federal do Rio Grande do Sul - UFRGS.

Nishijima, M., & Rocha, F. F. (2020). An economic investigation of the dengue incidence as a result of a tailings dam accident in Brazil. Journal of Environmental Management, Elsevier Ltd, 253(October 2019): 109748.

Niu, L., Zhang, J., Wang, Y., Kang, J., Li, S., & Shan, C. (2022). Iron ore granulation for sinter production: Developments, progress, and challenges. ISIJ International - Advance Online Publication Version.

Obenaus-Emler, R., Falah, M., & Illikainen, M. (2020). Assessment of mine tailings as precursors for alkali-activated materials for on-site applications. Construction and Building Materials, The Authors, 246: 118470.

Oboni, F., & Oboni, C. (2020). Tailings Dam Management for the Twenty-First Century. Tailings Dam Management for the Twenty-First Century, (Springer, ed.), Springer International Publishing, Cham.

Oliveira, T. M. de, Generoso, F. J., Silva, T. O. da, Sant'Anna, G. L., Silva, C. H. de C., & Pitanga, H. N. (2019). Geomechanical properties of mixtures of iron ore tailings improved with Portland cement. Acta Scientiarum. Technology, 41(1): 38038.

Ouda, A. S., & Gharieb, M. (2021). Behavior of alkali-activated pozzocrete-fly ash paste modified with ceramic tile waste against elevated temperatures and seawater attacks. Construction and Building Materials, Elsevier Ltd, 285: 122866.

Owen, J. R., Kemp, D., Lèbre, É., Svobodova, K., & Pérez Murillo, G. (2020). Catastrophic tailings dam failures and disaster risk disclosure. International Journal of Disaster Risk Reduction, 42: 101361.

Panda, I., Jain, S., Das, S. K., & Jayabalan, R. (2017). Characterization of red mud as a structural fill and embankment material using bioremediation. International Biodeterioration & Biodegradation, Elsevier Ltd, 119: 368–376.

Park, J., Kim, E., Suh, I., & Lee, J. (2021). A Short Review of the Effect of Iron Ore Selection on Mineral Phases of Iron Ore Sinter. Minerals, 12(1): 35.

Pereira dos Santos, C., Bruschi, G. J., Mattos, J. R. G., & Consoli, N. C. (2022). Stabilization of gold mining tailings with alkali-activated carbide lime and sugarcane bagasse ash. Transportation Geotechnics, 32(November 2021): 100704.

Pereira, O. C., & Bernardin, A. M. (2012). Ceramic colorant from untreated iron ore residue. Journal of Hazardous Materials, 233–234: 103–111.

Perumal, P., Niu, H., Kiventerä, J., Kinnunen, P., & Illikainen, M. (2020). Upcycling of mechanically treated silicate mine tailings as alkali activated binders. Minerals Engineering, Elsevier, 158(March): 106587.

Piciullo, L., Storrøsten, E. B., Liu, Z., Nadim, F., & Lacasse, S. (2022). A new look at the

statistics of tailings dam failures. Engineering Geology, 303(March): 106657.

Pinto, C. de S. (2006). Curso básico de mecânica dos solos. (M. Gregolin and A. T. Ávila, eds.), Oficina de Textos, São Paulo, Brasil.

Pinto, P., Milagre, L., Moreira, L., Rocha Junior, H., Salviano, A., Ardisson, J., Parreira, F., Teixeira, A. P., & Lago, R. (2022). Iron Recovery from Iron Ore Tailings by Direct Hydrogen Reduction at Low Temperature and Magnetic Separation. Journal of the Brazilian Chemical Society, 33(8): 969–977.

Portland Cement Association (PCA). (1992). Soil-Cement Construction Handbook.

Quiñónez Samaniego, R. A., Bruschi, G. J., Scheuermann Filho, H. C., Tonini de Araújo, M., Festugato, L., & Consoli, N. C. (2022). Effect of extended mellowing on strength and swelling behaviour of a high sulfated soil. Proceedings of the Institution of Civil Engineers - Ground Improvement, (May): 1–10.

Rajasekaran, G., & Narasimha Rao, S. (2002). Permeability characteristics of lime treated marine clay. Ocean Engineering, 29(2): 113–127.

Reddy, N. G., & Rao, B. H. (2016). Evaluation of the Compaction Characteristics of Untreated and Treated Red Mud. Geo-Chicago 2016, American Society of Civil Engineers, Reston, VA, 23–32.

Reid, D., & Fanni, R. (2022). A comparison of intact and reconstituted samples of a silt tailings. Géotechnique, 72(2): 176–188.

Reid, D., Fanni, R., & DiDonna, P. (2022). The effect of tamping conditions on undrained shear strengths of a non-plastic sandy silt tailings. Canadian Geotechnical Journal, 59(6): 783–795.

Reynolds, O. (1885). LVII. On the dilatancy of media composed of rigid particles in contact. With experimental illustrations. The London, Edinburgh, and Dublin Philosophical Magazine and Journal of Science, 20(127): 469–481.

Rios, S., Cristelo, N., Viana da Fonseca, A., & Ferreira, C. (2017). Stiffness Behavior of Soil Stabilized with Alkali-Activated Fly Ash from Small to Large Strains. International Journal of Geomechanics, 17(3): 04016087.

da Rocha, C. G., Passuello, A., Consoli, N. C., Quiñónez Samaniego, R. A., & Kanazawa, N. M. (2016). Life cycle assessment for soil stabilization dosages: A study for the Paraguayan Chaco. Journal of Cleaner Production, Elsevier Ltd, 139: 309–318.

Rout, S., Sahoo, T., & Das, S. (2013). Design of tailing dam using red mud. Open Engineering, 3(2): 316–328.

Ruan, Z., Wu, A., Bürger, R., Betancourt, F., Wang, Y., Wang, Y., Jiao, H., & Wang, S. (2021). Effect of interparticle interactions on the yield stress of thickened flocculated copper mineral tailings slurry. Powder Technology, 392: 278–285.

Rubinos, D., Spagnoli, G., & Barral, M. T. (2015). Assessment of bauxite refining residue (red mud) as a liner for waste disposal facilities. International Journal of Mining, Reclamation and Environment, 29(6): 433–452.

Saes, B. M., & Bisht, A. (2020). Iron ore peripheries in the extractive boom: A comparison between mining conflicts in India and Brazil. The Extractive Industries and Society, Elsevier, 7(4): 1567–1578.

Sahu, S. N., Meikap, B. C., & Biswal, S. K. (2022). Magnetization roasting of waste iron ore beneficiation plant tailings using sawdust biomass; A novel approach to produce metallurgical grade pellets. Journal of Cleaner Production, Elsevier Ltd, 343(September 2021): 130894.

Saldanha, R. B., da Rocha, C. G., Caicedo, A. M. L., & Consoli, N. C. (2021). Technical and environmental performance of eggshell lime for soil stabilization. Construction and Building Materials, Elsevier Ltd, 298: 123648.

Santos, R. S. P. dos, & Milanez, B. (2015). The Global Production Network for iron ore: materiality, corporate strategies, and social contestation in Brazil. The Extractive Industries and Society, Elsevier Ltd., 2(4): 756–765.

Schnaid, F. (2005). Geo-characterisation and properties of natural soils by in situ tests. Proceedings of the 16th International Conference on Soil Mechanics and Geotechnical Engineering: Geotechnology in Harmony with the Global Environment, Creative Commons, Millpress, Amsterdam, Netherlands.

Schnaid, F., Lehane, B. M., & Fahey, M. (2004). In situ test characterisation of unusual geomaterials. Proceedings ISC-2 on Geotechnical and Geophysical Site Characterization, Millpress, Rotterdam, Netherlands, 49–74.

Schnaid, F., Nierwinski, H. P., Bedin, J., & Odebrecht, E. (2014). On the Caracterization and Classification of Bauxite Tailings. Soil and Rocks, 37(January 2014): 277–284.

Schnaid, F., Nierwinski, H. P., Bedin, J., & Odebrecht, E. (2015). On the characterization and classification of bauxite tailings. Soils and Rocks, 37(3): 277–284.

Schnaid, F., Odebrecht, E., Sosnoski, J., & Robertson, P. K. (2016). Effects of test procedure on flat dilatometer test (DMT) results in intermediate soils. Canadian Geotechnical Journal, 53(8): 1270–1280.

Schoenberger, E. (2016). Environmentally sustainable mining: The case of tailings storage facilities. Resources Policy, Elsevier, 49: 119–128.

Segui, P., Safhi, A. el M., Amrani, M., & Benzaazoua, M. (2023). Mining Wastes as Road Construction Material: A Review. Minerals, 13(1): 90.

Servi, S., Lotero, A., Silva, J. P. S., Bastos, C., & Consoli, N. C. (2022). Mechanical response of filtered and compacted iron ore tailings with different cementing agents: Focus on tailings-binder mixtures disposal by stacking. Construction and Building Materials, 349(July): 128770.

Shackelford, C. D., Sevick, G. W., & Eykholt, G. R. (2010). Hydraulic conductivity of geosynthetic clay liners to tailings impoundment solutions. Geotextiles and Geomembranes, Elsevier Ltd, 28(2): 149–162.

Shipton, B., & Coop, M. R. (2015). Transitional behaviour in sands with plastic and non-plastic fines. Soils and Foundations, Elsevier, 55(1): 1–16.

da Silva, F. L., Araújo, F. G. S., Teixeira, M. P., Gomes, R. C., & von Krüger, F. L. (2014). Study of the recovery and recycling of tailings from the concentration of iron ore for the production of ceramic. Ceramics International, Elsevier, 40(10): 16085–16089.

Silva, J. P., Cacciari, P., Torres, V., Ribeiro, L. F., & Assis, A. (2022). Behavioural analysis of iron ore tailings through critical state soil mechanics. Soils and Rocks, 45(2): 1–13.

De Silva, L. I. N., Koseki, J., Wahyudi, S., & Sato, T. (2014). Stress-dilatancy relationships of sand in the simulation of volumetric behavior during cyclic torsional shear loadings. Soils and Foundations, Elsevier, 54(4): 845–858.

Singh, S., Ransinchung, G. D. R. N., Monu, K., & Kumar, P. (2018). Laboratory investigation of RAP aggregates for dry lean concrete mixes. Construction and Building Materials, Elsevier Ltd, 166: 808–816.

Soares Fortes, B. C., Villefort Teixeira, M. C., Pereira da Costa, S., Wagner, M. H., & Scotti, M. R. (2022). Post-disaster recovery plan for a rural settler's community affected by the Fundão dam tailings in Brazil. Journal of Rural Studies, 93(May): 55–66.

Souza Villar, L. F., Campos, T. M. P., Azevedo, R. F., & Zornberg, J. G. (2009). Influence of laboratory techniques on the geotechnical characterization of mining and industrial wastes. Proceedings of the 17th International Conference on Soil Mechanics and Geotechnical Engineering: The Academia and Practice of Geotechnical Engineering, M. Hamza et al. (Eds), ed., IOS Press, Alexandria, Egypt, 186–189.

Srivastava, M. ., Pan, S. ., Prasad, N., & Mishra, B. . (2001). Characterization and processing of iron ore fines of Kiriburu deposit of India. International Journal of Mineral Processing, 61(2): 93–107.

Srivastava, U., & Kawatra, S. K. (2009). STRATEGIES FOR PROCESSING LOW-GRADE IRON ORE MINERALS. Mineral Processing and Extractive Metallurgy Review, 30(4):

361–371.

Stević, D., Mihajlović, D., Kukobat, R., Hattori, Y., Sagisaka, K., Kaneko, K., & Atlagić, S. G. (2016). Hematite Core Nanoparticles with Carbon Shell: Potential for Environmentally Friendly Production from Iron Mining Sludge. Journal of Materials Engineering and Performance, 25(8): 3121–3127.

Suebsuk, J., & Suksan, A. (2014). Strength assessment of cement treated soil-reclaimed asphalt pavement (RAP) mixture. International Journal of GEOMATE, 6(2): 878–884.

Tarantino, A., & Hyde, A. F. L. (2005). An experimental investigation of work dissipation in crushable materials. Géotechnique, 55(8): 575–584.

Tastan, E. O., Edil, T. B., Benson, C. H., & Aydilek, A. H. (2011). Stabilization of Organic Soils with Fly Ash. Journal of Geotechnical and Geoenvironmental Engineering, 137(9): 819–833.

Terzaghi, K. (1943). Theoretical Soil Mechanics. John Wiley & Sons, Inc., New York, United States.

Terzaghi, K., Peck, R. B., & Mesri, G. (1996). Soil Mechanics in Engineering Practice. John Wiley & Sons, Inc., New York, United States.

Thistle, J., & Langston, N. (2016). Entangled histories: Iron ore mining in Canada and the United States. The Extractive Industries and Society, Elsevier Ltd., 3(2): 269–277.

Tishkov, C. V., Volkov, A. D., Kulakov, K. A., & Shchiptsov, V. V. (2022). Improvement of environmental and economic assessment methods of miningand processing of iron ore by corporations of the Arctic zone of the Russian Federation based on mathematical modeling. Mining Industry Journal (Gornay Promishlennost), (2/2022): 112–119.

Tonini de Araújo, M., Tonatto Ferrazzo, S., Jordi Bruschi, G., & Cesar Consoli, N. (2021). Mechanical and Environmental Performance of Eggshell Lime for Expansive Soils Improvement. Transportation Geotechnics, 31(2): 100681.

Trads, N., & Lade, P. V. (2014). The role of cementation in the behaviour of cemented soils. Geotechnical Research, (April).

United States Army Corps of Engineers (USACE). (1984). Soil Stabilization for Pavements Mobilization Construction.

Valenzuela, E. I., García-Figueroa, A. C., Amábilis-Sosa, L. E., Molina-Freaner, F. E., & Pat-Espadas, A. M. (2020). Stabilization of potentially toxic elements contained in mine waste: A microbiological approach for the environmental management of mine tailings. Journal of Environmental Management, 270(June): 110873.

Vallejo, M. N., & Dimitrakopoulos, R. (2019). Stochastic orebody modelling and stochastic long-term production scheduling at the KéMag iron ore deposit, Quebec, Canada. International Journal of Mining, Reclamation and Environment, Taylor & Francis, 33(7): 462–479.

Vasques Freitas, A. C., Belardi, R.-M., & Barbosa, H. de M. J. (2022). Characterization of particulate matter in the iron ore mining region of Itabira, Minas Gerais, Brazil. Atmósfera, 35(4): 781–802.

Vaughan, P. R., Maccarini, M., & Mokhtar, S. M. (1988). Indexing the engineering properties of residual soil. Quarterly Journal of Engineering Geology, 21(1): 69–84.

Veloso Marques, S. F., Consoli, N. C., & Almeida e Sousa, J. (2014). Testing Cement Improved Residual Soil Layers. Journal of Materials in Civil Engineering, 26(3): 544–550.

Venkatarama Reddy, B. V., & Jagadish, K. S. (1995). Discussion: The static compaction of soils. Géotechnique, 45(2): 363–367.

Vick, S. G. (1999). Design, and Analysis of Tailings Dams.

Vinai, R., & Soutsos, M. (2019). Production of sodium silicate powder from waste glass cullet for alkali activation of alternative binders. Cement and Concrete Research, Elsevier, 116(November 2018): 45–56.

Wagner, A. C., de Sousa Silva, J. P., de Azambuja Carvalho, J. V., Cezar Rissoli, A. L., Cacciari, P. P., Chaves, H. M., Scheuermann Filho, H. C., & Consoli, N. C. (2022). Mechanical behavior of iron ore tailings under standard compression and extension triaxial stress paths. Journal of Rock Mechanics and Geotechnical Engineering, Institute of Rock and Soil Mechanics, Chinese Academy of Sciences.

Wang, G., Wang, Z., Ye, Q., & Zha, J. (2021). Particle breakage evolution of coral sand using triaxial compression tests. Journal of Rock Mechanics and Geotechnical Engineering, Elsevier Ltd, 13(2): 321–334.

Wansbrough, V. C. (2014). Implications of Canadian Iron Ore Production. The Canadian Journal of Economics and Political Science, 16(3): 334–339.

Watson, A., Corser, P., Garces Pardo, E., Lopez Christian, T., & Vandekeybus, J. (2010). A comparison of alternative tailings disposal methods — the promises and realities. Proceedings of the First International Seminar on the Reduction of Risk in the Management of Tailings and Mine Waste, Australian Centre for Geomechanics, Perth, 499–514.

Wong, M. H. (1981). Environmental impacts of iron ore tailings-The case of Tolo Harbour, Hong Kong. Environmental Management, 5(2): 135–145.

Wong, M. H. (1985). Toxic effects of iron ore tailings and the response of watercress from tailings at high concentrations of Fe, Zn and Mn. Environmental Pollution. Series A, Ecological and Biological, 38(2): 129–140.

Wong, M. H., & Tam, F. Y. (1977). Soil and vegetation contamination by iron-ore tailings. Environmental Pollution (1970), 14(4): 241–254.

Wu, J., Yang, J., Ma, L., Li, Z., & Shen, X. (2016). A system analysis of the development strategy of iron ore in China. Resources Policy, Elsevier, 48: 32–40.

Xenidis, A., Mylona, E., & Paspaliaris, I. (2002). Potential use of lignite fly ash for the control of acid generation from sulphidic wastes. Waste Management, 22(6): 631–641.

Xiaolong, Z., Shiyu, Z., Hui, L., & Yingliang, Z. (2021). Disposal of mine tailings via geopolymerization. Journal of Cleaner Production, Elsevier Ltd, 284: 124756.

Yang, C., Cui, C., & Qin, J. (2015). Recycling of low-silicon iron tailings in the production of lightweight aggregates. Ceramics International, Elsevier, 41(1): 1213–1221.

Yellishetty, M., Ranjith, P. G., & Tharumarajah, A. (2010). Iron ore and steel production trends and material flows in the world: Is this really sustainable? Resources, Conservation and Recycling, Elsevier B.V., 54(12): 1084–1094.

Yi, Z., Sun, H., Wei, X., & Li, C. (2009). Iron ore tailings used for the preparation of cementitious material by compound thermal activation. International Journal of Minerals, Metallurgy and Materials, University of Science and Techonogy Beijing, 16(3): 355–358.

Yilmaz, E., & Fall, M. (2017). Paste Tailings Management. Paste Tailings Management, (E. Yilmaz and M. Fall, eds.), Springer International Publishing, Cham.

Yu, F. (2017a). Stress-dilatancy behavior of sand incorporating particle breakage. Acta Geotechnica Slovenica, 14(1): 55–61.

Yu, F. (2017b). Characteristics of particle breakage of sand in triaxial shear. Powder Technology, Elsevier B.V., 320: 656–667.

Yu, F. (2021). Particle breakage in granular soils: a review. Particulate Science and Technology, Taylor & Francis, 39(1): 91–100.

Yu, F., & Su, L. (2016). Particle breakage and the mobilized drained shear strengths of sand. Journal of Mountain Science, 13(8): 1481–1488.

Yüksek, S. (2022). Electroosmotic Dewatering of Iron Ore Tailings: A Laboratory Study to Improve Geotechnical Properties. Advances in Civil Engineering, (J. James, ed.), 2022: 1–12.

Yun, T. S., & Santamarina, J. C. (2005). Decementation, Softening, and Collapse: Changes in Small-Strain Shear Stiffness in k0 Loading. Journal of Geotechnical and Geoenvironmental Engineering, 131(3): 350–358.

Zhang, L., Ahmari, S., & Zhang, J. (2011). Synthesis and characterization of fly ash modified mine tailings-based geopolymers. Construction and Building Materials, Elsevier Ltd, 25(9): 3773–3781.

Zhang, S., Yi, B., Guo, F., & Zhu, P. (2022). Exploring selected pathways to low and zero CO2 emissions in China's iron and steel industry and their impacts on resources and energy. Journal of Cleaner Production, Elsevier Ltd, 340(January): 130813.

Zhang, W., Gu, X., Qiu, J., Liu, J., Zhao, Y., & Li, X. (2020). Effects of iron ore tailings on the compressive strength and permeability of ultra-high performance concrete. Construction and Building Materials, Elsevier Ltd, 260: 119917.

Zhao, X., Zhao, L., Yang, Q., Wang, Z., Cheng, A., Mo, L., & Yan, J. (2022). Permeability and Disintegration Characteristics of Composite Improved Phyllite Soil by Red Clay and Cement. Minerals, 13(1): 32.

Zheng, J., Gao, Z., He, H., Yang, S., & Sun, C. (2016). Efficient degradation of Acid Orange 7 in aqueous solution by iron ore tailing Fenton-like process. Chemosphere, Elsevier Ltd, 150: 40–48.

Zhu, Y., Li, Y., Si, C., Shi, X., Qiao, Y., & Li, H. (2020). Laboratory Evaluation on Performance of Fiber-Modified Asphalt Mixtures Containing High Percentage of RAP. Advances in Civil Engineering, 2020: 1–9.

Zhu, Y., Syndergaard, K., & Cooper, D. R. (2019). Mapping the Annual Flow of Steel in the United States. Environmental Science & Technology, research-article, American Chemical Society, 53(19): 11260–11268.

Zuccheratte, A. C. V., Freire, C. B., & Lameiras, F. S. (2017). Synthetic gravel for concrete obtained from sandy iron ore tailing and recycled polyethylterephtalate. Construction and Building Materials, Elsevier Ltd, 151: 859–865.